Aspects of Terahertz Reflection Spectroscopy

Kristensen, Mathias Hedegaard

DOI (link to publication from Publisher):
10.54337/aau561810826

Publication date:
2023

Document Version
Publisher's PDF, also known as Version of record

ASPECTS OF TERAHERTZ REFLECTION SPECTROSCOPY

BY
MATHIAS HEDEGAARD KRISTENSEN

DISSERTATION SUBMITTED 2023

AALBORG UNIVERSITY
DENMARK

Aspects of Terahertz Reflection Spectroscopy

Ph.D. Dissertation

Mathias Hedegaard Kristensen

Dissertation submitted June 26, 2023

Dissertation submitted: June 26, 2023

PhD supervisor: Assoc. Prof. Esben Skovsen
Aalborg University, Denmark

PhD committee: Prof. John Rasmussen (chair)
Aalborg University, Denmark

Prof. Frédéric Garet
Université Savoie Mont-Blanc, France

Prof. Valdas Pasiskevicius
KTH Royal Institute of Technology, Sweden

PhD Series: Faculty of Engineering and Science, Aalborg University

Department: Department of Materials and Production

ISSN (online): 2446-1636
ISBN (online): 978-87-7573-680-5

Published by:
Aalborg University Press
Kroghstræde 3
DK – 9220 Aalborg Ø
Phone: +45 99407140
aauf@forlag.aau.dk
forlag.aau.dk

Printed in Denmark by Stibo Complete, 2023

To my parents

English Abstract

In this thesis, the author study various aspects of terahertz (THz) spectroscopy conducted in reflection. After a brief introduction including both THz time-domain and frequency-domain spectroscopy, the main body focus on the application of THz spectroscopy for stand-off detection of explosives, which is followed by a chapter on THz generation through optical rectification (OR) in reflection. Finally, an outlook is given including a prospective direction of THz stand-off spectroscopy as well as future studies of THz OR in reflection.

In regard to THz stand-off detection, the methodology for how continuous-wave frequency-domain THz spectroscopy using multiple sources and detectors can be employed to increase the distance in stand-off measurements was explored. First, the radiation patterns state-of-the-art THz photomixer sources were characterized. Then, a stand-off CW THz spectrometer based on arrays of THz photomixer transmitters and receivers has been demonstrated. Using a reflecting sample, the stand-off distances could be increased to 10 m while retaining a 2:1 signal-to-noise ratio at 0.8 THz. However, the measurements were governed by the best performing transmitter/receiver pair. Subsequently, simple machine learning algorithms (MLAs) including principal component analysis and linear discriminant analysis were implemented for identification of explosives via their spectroscopic reflection characteristics. Excellent identification accuracies >99% were obtained even under unfavorable conditions. Additionally, it is shown that deconvolution of THz reflection spectra by a precise reference spectrum is redundant in regard to identification tasks based on MLAs.

Finally, THz generation through OR in reflection has been studied at normal incidence in the scope of future THz microscopy, *viz.* OR THz imaging, of opaque materials. First, a nonlinear plane wave model was established to analyze when generation in reflection is preferable. Secondly, experimental observations of a THz signal generated in reflection at the surface of a ZnTe crystal were demonstrated. Most importantly, it is found that the signal generated in reflection exhibits similar characteristics to a transmission signal but supports a larger bandwidth as it is not limited by dispersion and absorption losses from propagation inside the crystal.

Dansk Resumé

I denne afhandling studerer forfatteren forskellige aspekter af terahertz (THz) spektroskopi i et reflektionsformat. Først gives en introduktion, hvorunder THz tidsdomæne og frekvensdomæne spektroskopi kort beskrives. Hovedteksten er centreret omkring anvendelsen af THz spektroskopi til sporing af sprængstoffer på sikker afstand. Herefter findes et kapitel omhandlende generation af THz stråling via optisk ensretning i reflektion. Til sidst gives et bud på udsigterne for sporing af sprængstoffer ved hjælp af THz spektroskopi, samt et overblik over fremtidige studier indenfor THz genering ved optisk ensretning i reflektion.

I forhold til sporing af sprængstoffer undsøges det, hvordan frekvensdomæne THz spektroskopi med multiple THz sendere og modtagere kan udnyttes til at øge måleafstanden. Først kortlægges udstrålingsmønstrene af moderne THz antenner. Herefter demonstreres et THz frekvensdomæne spektrometer med multiple sendere og modtagere til målinger på lang afstand. Måleafstanden, hvor et signalstøjforhold på 2:1 ved 0,8 THz er bevaret, kunne øges til 10 m for en reflekterende prøve. Dog var målingerne domineret af det bedst ydende sender/modtager par. Endeligt implementeres simple maskinlæringsalgoritmer til identificering af sprængstoffer via deres spektroskopiske kendetegn i reflektion. Herunder principal komponent analyse og lineær diskriminant analyse. Sprængstoffer kunne identificeres korrekt i mere end 99% af tilfældene, selv under vanskelige forhold. Ydermere er affoldning af THz reflektionsspektrene med et nøjagtigt referencespektrum unødvendigt for korrekt identifikation ved hjælp af maskinlæring.

Til sidst studeres THz generation i reflektion via optisk ensretning under normalt indfald med henblik på THz mikroskopi af uigennemsigtige materialer. Først etableres en ulineær planbølgemodel for at analysere, hvornår generation i reflektion er favorabel. Dernæst observeres et THz signal genereret i reflektion på overfladen af en zinktellurkrystal eksperimentelt. Det erfares, at signalet genereret i reflektion indeholder samme information, som et signal genereret i transmission, men det understøtter samtidigt en større båndbredde, da det ikke begrænses af dispersion og absorptionstab fra udbredning gennem krystallen.

Contents

List of Appended Publications

Publication A

P. P. Cielecki, M. H. Kristensen and E. Skovsen, *Analysis and Classification of Frequency-Domain Terahertz Reflection Spectra using Supervised and Unsupervised Dimensionality Reduction Methods*, Journal of Infrared, Millimeter, and Terahertz Waves, 42, 1005 (2021).

Publication B

M. H. Kristensen, P. P. Cielecki and E. Skovsen, *Classification of Non-Referenced Terahertz Reflection Spectra using Machine Learning Algorithms*, submitted to APL Machine Learning, June 2023.

Publication C

P. P. Cielecki, M. H. Kristensen and E. Skovsen, *Database of frequency-domain terahertz reflection spectra for the DETRIS project*, Zenodo, (2021). DOI: 10.5281/zenodo.5079558.

Publication D

M. H. Kristensen, E. Herault, D. Zhai, E. Skovsen and J.-L. Coutaz, *Terahertz Generation through Optical Rectification in Reflection*, Journal of Applied Physics, 133, 173103 (2023).

Publication E

M. H. Kristensen, P. K. Kristensen, K. Pedersen and E. Skovsen, *Fourier Transform Second Harmonic Generation for High-Resolution Nonlinear Spectroscopy*, Optics Communication, 482, 126593 (2020).

Additional Contributions

M. H. Kristensen, P. P. Cielecki and E. Skovsen, *Classification of Terahertz Reflection Spectra using Machine Learning Algorithms*, 9th International Conf. on Optical Terahertz Science and Technology (2022). **Oral presentation**.

M. H. Kristensen, E. Herault, D. Zhai, E. Skovsen and J.-L. Coutaz, *Terahertz Generation through Optical Rectification in Reflection*, 9th International Conf. on Optical Terahertz Science and Technology (2022). **Poster presentation**.

M. H. Kristensen, P. P. Cielecki and E. Skovsen, *Classification of Terahertz Reflection Spectra using Machine Learning Algorithms*, 47th International Conf. on Infrared, Millimeter and Terahertz Waves (2022). **Oral presentation** and **proceeding paper**. DOI: 10.1109/IRMMW-THz50927.2022.9895909.

M. H. Kristensen, P. P. Cielecki and E. Skovsen, *Perspectives on Spectral Resolution in Continuous-Wave Terahertz Spectroscopy at Stand-off Distances*, 44th International Conf. on Infrared, Millimeter and Terahertz Waves (2019). **Poster presentation** and **proceeding paper**. DOI: 10.1109/IRMMW-THz.2019.8873947.

P. P. Cielecki, M. H. Kristensen and E. Skovsen, *Practical Guidelines for Continuous Wave Terahertz Spectroscopy - Perspectives and Challenges in Stand-off Detection*, 44th International Conf. on Infrared, Millimeter and Terahertz Waves (2019). **Poster presentation** and **proceeding paper**. DOI: 10.1109/IRMMW-THz.2019.8874043.

Preface

This present thesis is the result of my work as a PhD student at the Department of Materials and Production at Aalborg University from 2019 to 2023. The PhD scholarship was a part of the project *Detection of Explosives using Terahertz Radiation at Improved Stand-off distances* funded by Innovation Fund Denmark's (IFD) Grand Solutions program (grant no. IFD-7076-00017B) and MyDefence A/S. A five months research stay at IMEP-LAHC, UMR CNRS 5130, USMB, was facilitated at the invitation of Associate Professor Dr. Emilie Hérault from May 21, 2021.

Acknowledgments

Clearly, I could not have accomplished this incredible and sometimes chaotic journey all by myself. Therefore, I wish to send my gratitude and enormous thanks to everyone who has accompanied me during the trip.

The present thesis had not been possible without the guidance and funding acquired by my supervisor Esben Skovsen, for which I an truly grateful. Thank you for always having an open door and, not least, your continuous support. Moreover, I would like to express my sincere gratitude to all the colleagues in the Physics group at Skjernvej, who contributed to a pleasant work environment and who were always happy to celebrate our joint well-being! Especially, I would like to thank Christian Buhl Sørensen and Paweł Piotr Cielecki for creating a cheerful atmosphere in the office. I would also like to thank Peter Kjær Kristensen and Thomas Søndergaard for their practical and theoretical assistance, respectively, through out the years, and not least Peter Fojan for his insights into chemistry.

During my PhD studies, I visited Dr. Emilie Hérault at IMEP-LAHC, Université Savoie Mont-Blanc, France, to whom I owe a thousand thanks for the warm welcome and supervision – *Merci mille fois*. A huge thanks is also due to my good friends Raphaël Pederiva and Dongwei Zhai together with the rest of PHOTO group who made the stay even more pleasant.

Furthermore, I am extremely grateful for the mentoring by both Prof. Kjeld Pedersen and Prof. Jean-Louis Coutaz. Their knowledge about science and anecdotes have been invaluable and profoundly encouraging.

Finally, I would like to thank my dear friends and family for their support throughout this amazing journey. It goes without saying that I am forever indebted to my beloved Emma for her unconditional love, support and patience. Thank you!

Mathias Hedegaard Kristensen
Aalborg University, June 23, 2023

Chapter 1

Introduction

The terahertz (THz) frequency band spans the electromagnetic spectrum from the microwave to the far infrared region, slightly overlapping both regions. Within the community, the consensus is that terahertz spectral band ranges from 0.1 to 10 THz, even though the boundaries are yet to be clearly defined [1–3]. The wavelength λ of an electromagnetic wave is inversely proportional to its frequency ν, that is

$$\lambda = \frac{c}{\nu}, \tag{1.1}$$

where $c = 1/\sqrt{\varepsilon_o \mu_o}$ is the speed of light in vacuum[a] (ε_o and μ_o are respectively the permittivity and permeability of free space[b]). Thus, the THz band covers wavelengths from 30 μm to 3 mm. Photon energies $E = h\nu$ associated with THz frequencies lie between 0.41 and 41 meV (h is the Planck constant[c]). An equivalent thermodynamic temperature range can be established through $E = k_B T$ corresponding to roughly 5 - 500 K (k_B is the Boltzmann constant[d]). Let us notice that the thermal energy E_{th} at room temperature ($T = 300$ K) is approx. 26 meV, which translates to 6.3 THz. Therefore, thermal radiation and temperature are important factors when working in the THz domain, which often requires sophisticated experimental schemes.

The interactions of THz waves with matter are of great interest. The adjacent microwave and infrared regions are well-known for their spectroscopic techniques used to probe low-energy rotational transitions of molecular gases [4] and vibrational as well as rovibrational transitions of molecules [5], respectively. In the THz region, rotational transitions of molecules, torsional vibrations, and low-frequency vibrational modes involving large-amplitude

[a] $c \approx 2.998 \times 10^8$ m/s
[b] $\varepsilon_o \approx 8.854 \times 10^{-12}$ F/m and $\mu_o \approx 1.256 \times 10^{-6}$ N/A^2
[c] $h \approx 6.626 \times 10^{-34}$ J s $\approx 4.136 \times 10^{-15}$ eV s
[d] $k_B \approx 1.381 \times 10^{-23}$ J/K

motions of organic compounds through lattice vibrations in solids to intraband transitions in semiconductors and energy gaps in superconductors can be probed. [1, 2, 6] In fact, the rotational interaction strengths are 10^3 - 10^6 times stronger in the THz band relative to the microwave region [7], and in contrast to mid-infrared region, where polyatomic gases exhibit an abundance of modes leading to complex absorption bands and spectral convolution of different molecules with similar functional groups [8], the THz region offers specificity and selectivity [9]. Notably, liquid- and gas-phase polar molecules absorb THz waves strongly, however, polar gases do have transparent windows in between their absorption peaks. Dielectric media are in general transparent in the THz region. Nevertheless, pure crystals exhibit absorption peaks due to phonons, while impurities and localized vibrations in, *e.g.* , amorphous solids cause broadband attenuation. On the other hand, conductive materials like metals containing free charges act as almost perfect conductors. [1]

Obviously, the THz region has attracted much attention for its ability to probe such fundamental physical processes. However, while there are several ways to generate [10] and detect [11] THz radiation, the main challenge for THz spectroscopy has been the lack of compact and sufficiently powerful THz sources and sensitive detectors at spectroscopically relevant frequencies. Electronic THz sources emerging from the radio frequency (RF) side including, *e.g.* , backward-wave oscillators (BWO), Gunn diodes, and frequency multipliers, are generally narrowband, continuous-wave (CW), and to some extend tunable emitters. Typically, these sources operate well below 2 THz and can provide rather high output power up to tens or even hundreds of mW. Optical techniques include, *e.g.* , quantum cascade lasers (QCLs), optical parametric generators/oscillators (OPG/OPO), difference frequency generation (DFG) and optical rectification (OR) in nonlinear media as well as photoconductive (PC) antennas and photomixers. Together, these techniques allow for generation (and in most cases detection) of THz radiation in the form of coherent CW, narrowband quasi-CW (long pulses), and broadband ultrashort pulses. However, QCLs often require cryogenic cooling due to thermal noise and exhibit very limited tunability, while the nonlinear optical mixing processes cover a broad spectral range and can reach rather high power levels at the cost of complex laser systems. Though being regarded as optical techniques qua the use of near-infrared lasers, PC antennas and photomixers rely just as much on the control of photocarrier lifetimes and mobilities as well as antenna designs from the RF side. Their development has especially been driven by the attractive scientific and promising industrial applications of THz spectroscopy together with the advance of modern laser technology, which has led to compact and reliable pulsed and CW THz spectrometers have become commercially available in the recent years.

In the following sections, a brief introduction will be given of the two

most common methodologies, *viz.* THz time-domain spectroscopy and THz frequency-domain spectroscopy. Both of which have been employed in this work.

1 Terahertz Time-Domain Spectroscopy

For many years, THz spectroscopy was almost synonymous with THz time-domain spectroscopy (TDS). Hence, the technique is well-described in several textbooks [1–3, 12] and thorough reviews [6, 8, 13, 14] of its various aspects and applications. Thus, this section will only introduce the basics of the methodology. A traditional TDS setup is seen in Fig. 1.1. A mode-

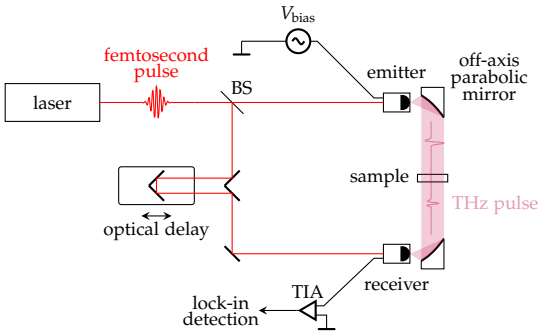

Fig. 1.1: Illustration of a traditional TDS setup.

locked laser delivers a train of femtosecond laser pulses, which is divided into a pump and a probe branch by a beam splitter (BS). The two beams are then incident on an emitter and receiver, respectively, to generate and detect THz waves. In this scheme, coherent sub-picosecond broadband THz pulses are generated. Typically, the THz electric field is detected, which requires a time resolution on the femtosecond scale much faster than any electronic receivers. Thus, equivalent time sampling is employed. This technique relies on the ultra-stable pulse trains delivered by mode-locked femtosecond lasers. An optical delay is implemented in the probe branch, which allow us to record the THz waveform step by step using a slow field detector. Let us notice that this allow us to retrieve the instantaneous amplitude as well as the instantaneous phase of the THz field.

Commercial systems[e] in particular employ PC antennas as sources and detectors of THz pulse. Frequency mixing through optical rectification (OR) in nonlinear crystals is another common way to generate broadband THz

[e]See for example TOPTICA Photonics AG, MenloSystems GmbH, Teravil Ltd. or TeraView Ltd.

pulses, which are then typically detected via electro-optic (EO) sampling. OR will be treated in more details in Chapter 3.

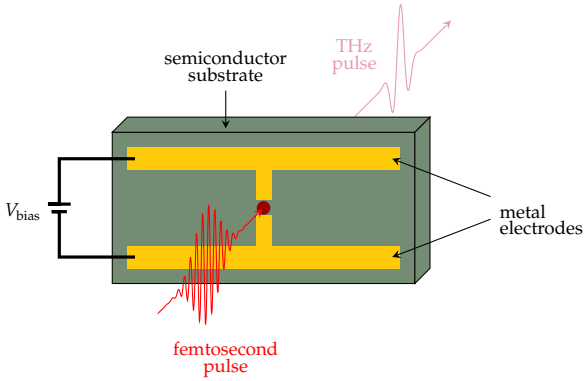

Fig. 1.2: Illustration of a PC antenna employed to generate broadband THz pulses.

PC antennas consist of a semiconductor slab with a pair of metal electrodes on top as illustrated in Fig. 1.2. By applying a bias voltage V_{bias} to the electrodes and exciting the semiconductor with a beam of light exhibiting photon energies larger than the bandgap, a time-varying photocurrent is generated. To generate and detect broadband THz radiation, ultrafast optical pulses and photoexcited free carrier lifetimes on the sub-picosecond scale are required. This is often met by 800-nm wavelength Ti:Sapphire mode-locked femtosecond lasers in combination with low-temperature grown GaAs substrates, respectively. Thereby, the acceleration and decay of the free carriers induce an electric dipole emitting electromagnetic pulses on the sub-picosecond scale. The resulting THz far-field is proportional to the time derivative of the photocurrent $i(t)$ [1], *i.e.*

$$E_{\text{THz}}(t) \propto \frac{\partial i(t)}{\partial t}. \tag{1.2}$$

It can be shown [1] that the THz spectral amplitude can be expressed

$$E_{\text{THz}}(\nu) \propto \nu \mu V_{\text{bias}} I_{\text{laser}}, \tag{1.3}$$

where μ is the electron mobility in the substrate and I_{laser} is the laser intensity. Thus, the PC substrate should also exhibit a high carrier mobility and a high breakdown field for optimized THz generation.

In a reverse scheme, PC antennas can be utilized to detect broadband THz pulses. Again, femtosecond pulses are impinged on the PC in the gap between the antenna electrodes to excite free photocarriers. In the presence of an incoming THz electric field, the free carriers are accelerated and a photocurrent flows between the electrodes. This current is proportional to the

THz field and can be measured using an ammeter connected to the electrodes. Similarly, if the incoming THz bias field is absent, the free carriers will recombine and no net current is measured between the electrodes. Typically, a lock-in amplifier is employed since the photocurrent to be measured is often on the nano-amp scale. The necessary modulation of the generated THz beam is then achieved by either modulating the emitter bias voltage or by chopping the optical pump or the THz beam. The THz-induced photocurrent is a convolution of the THz electric field and the response function of the PC switch $G(t)$, *i.e.*

$$i_{\mathrm{ph}}(t,\tau) \propto E_{\mathrm{THz}}(t-\tau)\int_0^\infty I_{\mathrm{laser}}(t-t')G(t')\,\mathrm{d}t', \tag{1.4}$$

where τ is the time delay between emission and detection. [1, 2] However, the electronics employed to measure the photocurrent are much slower, and we end up with a time-integrated signal

$$S(\tau) = \int_{-\infty}^{\infty} i_{\mathrm{ph}}(t,\tau)\,\mathrm{d}t \tag{1.5}$$

for which $G(t) = 0$ for $t < 0$ because of causality. Here, the THz waveform is obtained by scanning optical delay of the optical probe beam corresponding to τ. Taking the Fourier transform to obtain the spectrum of the recorded signal, we get

$$S(\nu) \propto G^*(\nu) I_{\mathrm{laser}} E^*_{\mathrm{THz}}(\nu), \tag{1.6}$$

where * denotes the complex conjugate. [1] Thus, short carrier lifetimes are crucial for broadband PC detectors in order to achieve a broad and flat response function $G(\nu)$. In modern TDS systems it is possible to achieve bandwidths up to 6 THz with approx. 1 GHz frequency resolution. Furthermore, high signal-to-noise ratios (SNRs) are inherent to THz-TDS measurements free of the thermal background due to the gated and coherent detection scheme. In fact, 100 dB dynamic range at 0.1 THz within a 200 ms integration is possible, even though, the average THz powers only reach up to 100 μW at best.

2 Terahertz Frequency-Domain Spectroscopy

Continuous-wave (CW) THz frequency-domain spectroscopy (FDS) by means of photomixing was first introduced by Brown *et al.* [15] in 1995. Fundamentally, photomixers are optoelectronic devices akin to the PC antennas employed in TDS. A monochromatic THz wave is generated in the photomixer illuminated by two CW lasers slightly offset in frequency. The THz frequency can then be scanned by tuning the frequency difference of the lasers. Typically, a second photomixer is coherently driven by the same lasers. Thus, like

in TDS, both the instantaneous amplitude and phase of the THz electric field can be obtained.

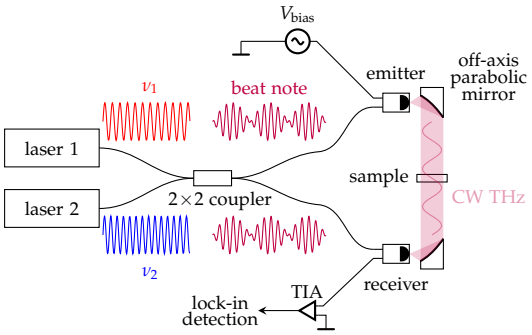

Fig. 1.3: Illustration of a typical CW THz spectrometer based on photomixers.

Modern CW THz spectrometers [16] are based on 1.5 μm distributed feedback (DFB) lasers designed for the telecom band and InGaAs photomixers. These systems offer tunability up to 2.75 THz using triple DFB lasers [17] and superior spectral resolution (<10 MHz). Furthermore, the spectrometers are very compact and robust thanks to the all fiber-coupled design. Typically, the emitters deliver 100 μW (10 μW) at 0.1 THz (0.5 THz). The coherent detection scheme together with lock-in detection yield a peak dynamic range of 90 dB. Fig. 1.3 illustrates such a commercial THz-FDS system. Here, a waveguide integrated photodiode (PD) antenna in reverse bias mode serves as a THz emitter. These devices are essentially high-speed PIN-structured PDs (an InGaAs/InGaAsP heterostructure grown on semi-insulating InP) developed for telecom applications, which have been optimized for THz generation, with bowtie antennas integrated on top of the diodes. Both high speed and high efficiency is achieved by the waveguide-coupled optical input, which allow for high absorption in the thin active layer. [18] The receiving photomixer is a highly engineered PC antenna for the 1.5 μm optical probe beam. A bowtie antenna with interdigitated finger electrodes in the PC gap is deposited on a 100-period InGaAs/InAlAs quantum well nanostructure stack grown on a InP substrate. All combined, this results in a high-speed PC receiver with low dark currents, improved sensitivity and an increased optical-THz interaction length. The two CW lasers emitting at slightly different frequencies ν_1 and ν_2 are combined in 50:50 fiber coupler to form an optical beat note. Subsequently, the resulting beat note is split and incident on the emitting and receiving photomixers, respectively. Let us assume that the lasers have equal electric field amplitudes $E_1 = E_2 = E_0$ and similar polarizations. Furthermore, we write the corresponding angular frequencies as $\omega_1 = \omega_0 - \Omega/2$ and $\omega_2 = \omega_0 + \Omega/2$. Here, $\Omega = \omega_2 - \omega_1$ is the THz frequency. Then, the

combined electric field can be written

$$E(t) = E_0 \cos(\omega_1 t) + E_0 \cos(\omega_2 t). \tag{1.7}$$

Thus, the laser intensity $I(t) = \frac{1}{2} c\varepsilon_0 |E(t)|^2$ at the photomixers writes

$$I(t) = I_{\text{laser}} \left[\cos^2(\omega_1 t) + \cos^2(\omega_2 t) + \cos(\Omega t) + \cos(2\omega_0 t) \right] \tag{1.8}$$

with $I_{\text{laser}} = \frac{1}{2} c\varepsilon_0 E_0^2$. At the emitting PIN diode, electron-hole pairs (*i.e.* , photoexicted free carriers) are generated in the intrinsic layer (depletion region) by the modulated laser intensity. However, the photocarrier response time is much slower than the oscillations at ω_1, ω_2 and $2\omega_0$. This means that the photocarrier density is proportional to time-averaged laser intensity

$$\langle I(t) \rangle = I_{\text{laser}} \left[1 + \cos(\Omega t) \right] \tag{1.9}$$

intergrated over an interval that is short compared to the THz period but longer than the optical periods.[1] Hence, the photocarriers only respond to the envelope of the intensity beat note, which is modulated at the THz frequency $\Omega \ll \omega_0$. The build-in electric field and/or the applied bias voltage V_{bias} facilitates a photocurrent by accelerating the free photocarriers to the diode contacts. Since the photocarrier density is modulated at the THz frequency Ω, the induced photocurrent $i(t)$ oscillates at this extact frequency. Similar to PC antennas, the photocurrent is converted into THz waves by the bowtie antenna. It follows that the radiated THz far-field is proportional to time derivative of the photocurrent $i(t)$ [1, 2], *i.e.*

$$E_{\text{THz}}(\Omega, t) \propto \frac{\partial i(t)}{\partial t} \propto I_{\text{laser}} \Omega \sin(\Omega t). \tag{1.10}$$

Like in TDS, the incoming THz field at the receiving (unbiased) PC antenna accelerates the induced photocarrier density, which is modulated by the optical beat in Eq. (1.9). Thus, the receiver photocurrent $i_{\text{ph}}(\tau, t, \Omega)$ is proportional to the product of the incoming THz field [Eq. (1.10)] and the optical beat [Eq. (1.9)], *i.e.*

$$i_{\text{ph}}(\tau, t, \Omega) \propto E_{\text{THz}}(\Omega, t + \tau) \langle I(t) \rangle , \tag{1.11}$$

where τ is the time delay between emission and detection.[1] The photocurrent is generally on the nano-amp scale and requires pre-amplification and lock-in detection, which is facilitated by modulation of the bias voltage. Therefore, the measured signal $S(\Omega, \tau)$ is the time-integrated photocurrent due to slow electronics. We have

$$S_{\text{ph}}(\Omega, \tau) = \lim_{T \to \infty} \int_0^T i_{\text{ph}}(\tau, t, \Omega) \, \mathrm{d}t \propto I_{\text{laser}}^2 \Omega \sin(\Omega \tau), \tag{1.12}$$

which can be expressed as

$$S_{\mathrm{ph}}(\Omega, \tau) \propto E_{\mathrm{THz}}(\Omega) \sin(\Omega\tau). \tag{1.13}$$

The time delay between the emission and detection of the THz wave is $\tau = \Delta L/c$, where

$$\Delta L = L_{\mathrm{E}} + L_{\mathrm{THz}} - L_{\mathrm{R}} \tag{1.14}$$

is the path difference between the emitter branch $L_{\mathrm{E}} + L_{\mathrm{THz}}$ and the receiver branch L_{R} of the interferometer. Here, L_{E} and L_{R} are the optical path lengths of the optical beat note to the emitter and receiver, respectively, and L_{THz} the length of the THz path. Hence, the measured signal in Eq. (1.13) depends on the THz amplitude E_{THz} and the phase difference between the THz wave and the optical beat note at the receiver

$$\Delta\phi = \Omega\tau = \frac{2\pi\nu}{c}\Delta L. \tag{1.15}$$

The amplitude and phase of the THz electric field can be determined by scanning the phase difference $\Delta\phi$.

One way is to modulate ΔL by means of fiber stretchers [19] in the optical path for a fixed THz frequency ν. This approach has the advantage that the spectrum can be obtained with an arbitrary effective resolution $\Delta\nu$, which is only limited by the spectral linewidth of the lasers $\delta\nu$ (typically a few MHz). Thus, this approach offers a very high frequency selectivity. Basically, fiber stretchers are piezo actuators wrapped by several tens of meters of appropriate fiber. The length of the wrapped fiber changes linearly with the voltage applied to the piezo. Typically, two fiber stretchers are installed in the emitter and detector branches, respectively. There are several reasons to employ such a symmetric setup [19]. Evidently, the length change x can be doubled (if one stretcher operate in reverse). The modulation frequency can be doubled as well if, *e.g.*, a sinusoidal voltage is applied. The symmetric setup also minimizes thermal drifts. Finally, ΔL can be kept small, which is can improve phase stability. Utilizing a sinusoidal voltage, the measured photocurrent varies as

$$S_{\mathrm{ph}} = A \sin\left(\frac{2\pi\nu}{c}x + \varphi\right). \tag{1.16}$$

Hence, we can retrieve the THz amplitude A and phase φ at a given frequency ν from a sinusoidal fit to the measured photocurrent.

However, the default approach in many commercial systems is to tune the THz frequency ν, while keeping the path difference ΔL fixed. The recorded signal S_{ph} thus oscillates as a function of ν with a period Δf determined by the path difference, *i.e.* $\Delta f = c/\Delta L$. The simplest way to retrieve the amplitude and phase of the THz field is by examining the extrema of oscillating

photocurrent signal. [20] However, in this analysis, the effective frequency resolution is limited the oscillation period (*i.e.*, $\Delta\nu = \Delta f/2$).

A more sophisticated method has been demonstrated by Vogt *et al.* [21, 22]. Here, the instantaneous amplitude $A(\nu)$ and instantaneous phase $\varphi(\nu)$ are retrieved via Hilbert transformation. It is assumed the incident THz field $E_{\text{in}}(t)$ interacts with a linear system with time response function $R(t)$ such that the output field is given by the convolution, *i.e.*

$$E_{\text{out}}(t) = \int_{-\infty}^{\infty} R(t-\tau)E_{\text{in}}(\tau)\,\mathrm{d}\tau. \tag{1.17}$$

In the frequency-domain, we can write

$$E_{\text{out}}(\omega) = \mathcal{F}\{E_{\text{out}}(t)\} = R(\omega)E_{\text{in}}(\omega), \tag{1.18}$$

where $\mathcal{F}$ denotes the Fourier transform. Since the time response of a physical system is causal, its frequency response will be an analytic signal, where its real and imaginary parts are linked by the Hilbert transform $\mathcal{H}$. [22] That is, a complex-valued signal with no negative frequency components. [23] As we showed above, the signal S_{ph} measured in THz-FDS is directly proportional to the real part of the frequency response $E_{\text{THz}}(\omega)$. Thus, we can obtain the analytic signal as [22]

$$S_{\text{a}}(\nu) = S_{\text{ph}}(\nu) + j\mathcal{H}\left\{S_{\text{ph}}(\nu)\right\}. \tag{1.19}$$

Let us recall that any complex number $z = x + jy$ can be represented in a polar form $z = |z|e^{j\phi}$ by its magnitude $|z|$ and phase ϕ. Thus, we can readily retrieve the spectral amplitude $A(\nu)$ and phase $\varphi(\nu)$ of the THz electric field from the analytic signal, *i.e.*

$$S_{\text{a}}(\nu) = A(\nu)\exp\left[i\varphi(\nu)\right]. \tag{1.20}$$

Notably, the spectral resolution is equal to the frequency step size and independent of the oscillation period, in contrast to the above-described method. Additionally, Kong *et al.* [24] have demonstrated that Fabry-Pérot interference in a spectrum caused by reflections in the experimental setup (*e.g.*, standing waves) can be filtered in the time-domain through Fourier transformation.

From Eq. (1.18) it is evident that the complete spectral response $R(\omega)$ of the system including any spectroscopic information is readily available if $E_{\text{in}}(\omega)$ is known. In terms of reflection spectroscopy, we measure the complex reflection coefficient [1]

$$\tilde{r}(\nu) = \frac{\tilde{E}_{\text{sam}}(\nu)}{\tilde{E}_{\text{ref}}(\nu)} = \frac{\tilde{r}_{\text{sam}}(\nu)}{\tilde{r}_{\text{ref}}(\nu)}e^{j4\pi\delta\nu/c}, \tag{1.21}$$

where we have exploited that $\tilde{E}_{\text{sam}} = \tilde{r}_{\text{sam}}\tilde{E}_{\text{inc}}$ and $\tilde{E}_{\text{ref}} = \tilde{r}_{\text{ref}}\,e^{-j4\pi\delta\nu/c}\tilde{E}_{\text{inc}}$. Here, $\tilde{E}_{\text{x}}$ with x = sam, ref, inc are the reflected electric fields from the front

surface of the sample and reference and the incident electric field, respectively. The exponential in the $\tilde{E}_{\text{ref}}$ accounts for any phase shift due to a misplacement δ of the reference compared to the position of the sample front surface. [1] Thus, any misalignment results in a mean linear slope $4\pi\delta/c$ in the measured phase spectrum as a function of frequency, which should be removed. In THz-FDS, the THz waves are most often linearly polarized and can freely be aligned in a s-polarized configuration. We can thus extract the complex refractive index $\tilde{n}(\nu) = n(\nu) + j\kappa(\nu)$ of the sample ($n(\nu)$ is the index of refraction and $\kappa(\nu)$ is the extinction coefficient) from the corresponding complex Fresnel reflection coefficient, *i.e.*

$$\tilde{r}_{\text{sam}} = \frac{\tilde{n}_1 \cos(\theta_{\text{i}}) - \tilde{n}_2 \cos(\theta_{\text{t}})}{\tilde{n}_1 \cos(\theta_{\text{i}}) + \tilde{n}_2 \cos(\theta_{\text{t}})}. \tag{1.22}$$

Here, $\tilde{n}_1$ and $\tilde{n}_2$ are the complex refractive indices of the surrounding medium (air) and the sample, respectively. Hence, $\tilde{n}_1 = n_{\text{air}} \approx 1$ and $\tilde{n}_2 = \tilde{n}(\nu)$. The subscripts i and t on θ refers to the angles of incidence and refraction, respectively. Typically, a perfectly reflecting sample is used in the reference measurement, hence, $\tilde{r}_{\text{ref}} \approx -1$. [2] Therefore, Eq. (1.21) can be written

$$\tilde{r} = -\tilde{r}_{\text{sam}} = \frac{\tilde{n}\cos(\theta_{\text{t}}) - \cos(\theta_{\text{i}})}{\cos(\theta_{\text{i}}) + \tilde{n}\cos(\theta_{\text{t}})} \tag{1.23}$$

with $\tilde{r}$ now being the phase corrected measured reflection coefficient. Rearranging Eq. (1.23), we get

$$\tilde{n}\cos(\theta_{\text{t}}) = \frac{1+\tilde{r}}{1-\tilde{r}}\cos(\theta_{\text{i}}). \tag{1.24}$$

Snell's law of refraction can be used to express the angle of refraction [25]

$$\theta_{\text{t}} = \arcsin\left(\frac{1}{\tilde{n}}\sin(\theta_{\text{i}})\right). \tag{1.25}$$

If we combine Eqs. (1.24) and (1.25) with the identity [26] $\cos(\arcsin(x)) = \sqrt{1-x^2}$ and solve for $\tilde{n}$, we obtain

$$\tilde{n} = \sqrt{\left(\frac{1+\tilde{r}}{1-\tilde{r}}\right)^2 \cos^2(\theta_{\text{i}}) + \sin^2(\theta_{\text{i}})}. \tag{1.26}$$

The measured reflection coefficient $\tilde{r} = |\tilde{r}|\exp[\Delta\varphi]$ is given by the relative amplitude spectrum

$$|\tilde{r}(\nu)| = \frac{A_{\text{sam}}(\nu)}{A_{\text{ref}}(\nu)} \tag{1.27}$$

and the phase spectrum

$$\Delta\varphi(\nu) = \varphi_{\text{sam}}(\nu) - \varphi_{\text{ref}}(\nu), \tag{1.28}$$

which are obtained from the Hilbert analysis in Eq. (1.20). Finally, we obtain the refractive index and the extinction coefficient from the real and imaginary parts of Eq. (1.26), *i.e.*

$$n = \mathrm{Re}\{\tilde{n}\} = \sqrt{\left(\frac{1-|\tilde{r}|^2}{1+|\tilde{r}|^2-2|\tilde{r}|\cos(\Delta\varphi)}\right)^2 \cos^2(\theta_\mathrm{i}) + \sin^2(\theta_\mathrm{i})} \tag{1.29}$$

and

$$\kappa = \mathrm{Im}\{\tilde{n}\} = \sqrt{\left(\frac{2|\tilde{r}|\sin(\Delta\varphi)}{1+|\tilde{r}|^2-2|\tilde{r}|\cos(\Delta\varphi)}\right)^2 \cos^2\theta_\mathrm{i} + \sin^2\theta_\mathrm{i}}. \tag{1.30}$$

In Fig. 1.4 we have applied this approach to extract the optical parameters from a sample of 80% α-lactose monohydrate by weight mixed with polyethylene. The reference sample was made of pure polyethylene. Clearly,

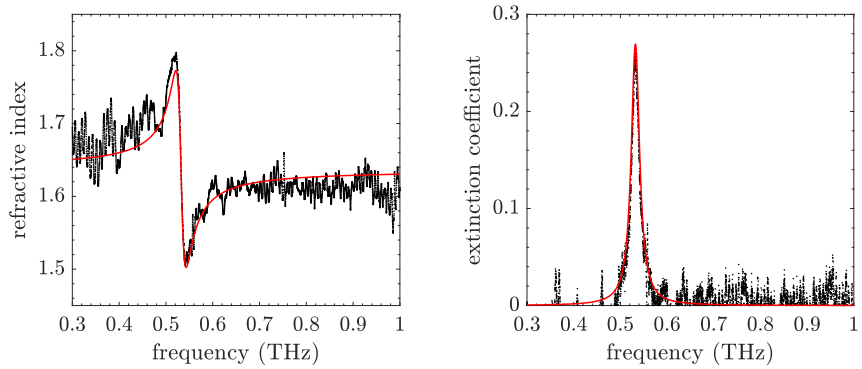

Fig. 1.4: The refractive index (left) and extinction coefficient (right) of an α-lactose sample obtained by Hilbert transform THz-FDS in reflection. The red line is a fitted Drude-Lorentz model.

there is a very good agreement between the experimental data and the fitted Drude-Lorentz model (red line). From the fit, we obtain the center frequency $\nu_c = 531.4$ GHz and linewidth $\gamma = 21.6$ GHz. These values are in excellent agreement with the results ($\nu_c = 530.4 \pm 0.5$ GHz and $\gamma = 25 \pm 1$ GHz) reported by Roggenbuck *et al.* [20] using a similar FDS system to measure α-lactose monohydrate in transmission, as well as the results reported by Brown *et al.* [27] using various THz techniques.

3 This Work

This thesis covers various aspects of THz reflection spectroscopy that overall can be divided into three parts.

The first two parts, described in Chapter 2, emphasize the work carried out in the framework of the project *Detection of Explosives using Terahertz Radiation at Improved Standoff-distances* (DETRIS). The project, funded by Innovation Fund Denmark (IFD), was conducted at Aalborg University in collaboration with the company MyDefence A/S. Further support was given by the Danish Ministry of Defence Acquisition and Logistics Organisation (DALO), who kindly gave access to explosive materials at the Danish Defence research facilities. In the first part, we explored how a CW THz spectrometer utilizing multiple photomixer sources and detectors can improve the distance in stand-off spectroscopy, while we in the second part demonstrated how simple machine learning algorithms can be implemented to reliably classify and identify explosives (and other compounds) from their spectral characteristics measured in reflection. The latter results have been summarized in Publication A and B together with the underlying database in Publication C necessary for the study.

In the third and final part, THz generation through OR in reflection was studied in collaboration with Dr. Jean-Louis Coutaz, Professor Emeritus, and Dr. Emilie Hérault, Associate Professor, from Université Savoie Mont-Blanc (USMB) in France. This work was initiated during my five months research stay at IMEP-LAHC, UMR CNRS 5130, USMB, from May 31 to October 29, 2021, and subsequently, continued at Aalborg University. Our first results presented in Publication D are discussed in Chapter 3.

Work has also been conducted within the topic of SHG spectroscopy. In Publication E, we reported a new characterization technique for high-resolution nonlinear spectroscopy with broadband femtosecond laser pulses, which combines Fourier transform (FT) spectroscopy and SHG to enable high spectral resolution within the spectral bandwidth of the input pulse. Thus, this allows for very broadband spectral coverage with high spectral resolution in a single scan without prolonging the scan duration if broadband laser pulses are utilized to excite the sample The FT-SHG method also benefits from high spectral reproducibility due to built-in calibration of the spectral axis by Connes' advantage compared to conventional techniques. To demonstrate the capabilities of the method, we resolved the strong and narrow exciton *X*-line of ZnO at 3.407 eV using much broader spectral bandwidth femtosecond laser pulses to excite the resonance. However, in order to keep the present thesis somewhat coherent, these results will not be discussed hereinafter.

Chapter 2

Terahertz Stand-Off Detection of Explosives

The DETRIS project evolved around three main conceptions given in the following hypotheses.

Hypothesis I *By shifting from time-domain spectroscopy based on broadband pulsed THz radiation to continuous-wave frequency-domain spectroscopy, which relies on a single tuneable frequency, all the emitted power can be concentrated within the transmissions windows of the water vapor absorption spectrum. Accordingly, this will reduce propagation losses and increase the stand-off distance.*

Hypothesis II *An array of THz photomixers in a multiple-input-multiple-output (MIMO) configuration will increase the emitted THz power and the directivity as well as the detection sensitivity by the number of array elements squared. This will improve the dynamic range (signal-to-noise ratio) of the THz spectrometer, and therefore, further increase the stand-off distance.*

Hypothesis III *Machine-learning algorithms can be developed and trained to identify the spectra of explosives under various conditions and will reduce the necessary signal-to-noise ratio required for identification of explosives. Furthermore, the algorithms should be able to recognize the spectra when masked by different barrier materials.*

A thorough discussion of Hypothesis I is given in Sec. 2, while Hypothesis II and III are treated in Sec. 3 and Sec. 4, respectively, including experimental results. However, before the hypotheses are investigated, we shall set the

scene by a State-of-the-Art review of *THz spectroscopy of explosives* and *THz stand-off spectroscopy* in the following section.

1 State-of-the-Art

With the introductory paper regarding security applications of terahertz technology [28] by Kemp *et al.* in the beginning of the millennium, stand-off detection of explosives using THz radiation quickly evolved to be one of the most desired research topics within national security and military defense. [29–33] Subsequently, underpinned by the joint work of researchers from fifteen NATO countries [34, 35] carried out from 2010 to 2015 under the Research and Technology Organisation (RTO) of NATO.

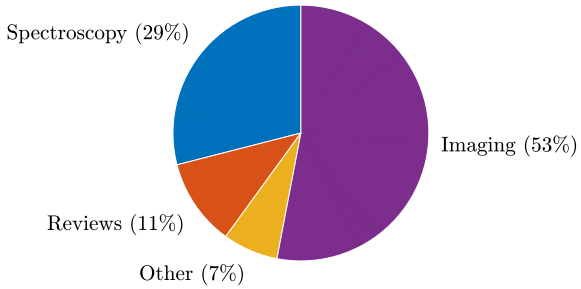

Fig. 2.1: Distribution of the bibliographic search of documents containing *'terahertz'* and *'stand-off'* or *'stand-off'* in the abstract, title, or keyword field categorized by the topics *'spectroscopy'*, *'imaging'*, *'review'*, and *'other'*.

A bibliographic search[a] of documents containing *'terahertz'* and *'standoff'* or *'stand-off'* in the abstract, title, or keyword field accumulates 306 results published from 1999 to 2021 omitting conference reviews. The distribution of the search results categorized in relation to *'spectroscopy'*, *'imaging'*, *'review'*, and *'other'* are seen in Fig. 2.1. More than half of these documents concern terahertz imaging, most without spectroscopic relevance, and thus, outside the scope of the DETRIS project. Less than one third of the results is related to spectroscopy.

1.1 Terahertz Spectroscopy of Explosives

In 2003, Kemp *et al.* first demonstrated detection of explosives using THz radiation in Ref. [28] by THz-TDS in transmission. Fig. 2.2 shows the

[a] `www.scopus.com`; as of 14 March 2022.

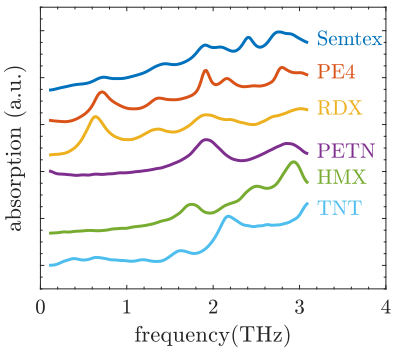

Fig. 2.2: Absorption spectra of common explosives measured in transmission. The spectra have been offset vertically for clarity. Adapted from Ref. [28].

THz absorption spectra of the common explosives TNT, HMX, PETN, RDX as well as commercial PE4 (RDX mixed with a plasticizer), and Semtex H (mixture of RDX, PETN and plasticizer) as presented in their paper. Let us notice that RDX and HDX set the lower and upper bounds of the spectral range of interest with respective absorption features around 0.8 and 2.8 THz. In the following years, Kemp *et al.* made significant advances including the first demonstration of reflection THz spectroscopy of explosives, as well as detection and identification of explosives using reflection terahertz pulsed spectroscopic imaging in combination with principal component analysis (PCA)[36, 37]. The group also conducted transmission measurements of possible confusion materials including foods (α-lactose monohydrate, vitamins, sugars, chocolate, and marzipan) and common medicines (asparin, paracetamol, and ibuprofen) as well as different barrier materials (cotton, wool, silk, vinyl, suede, polyester, nylon, leather, and cardboard).[29, 38, 39] Finally, they showed that it is possible to distinguish explosives from other substances such as D-tartaric acid by their reflection spectra, and explored the detection of explosives hidden behind multiple layers of cotton/polyester clothing.[39] Here, they found that since the clothing acted as a low-pass filter, it was necessary to study the reflectance derivative to recover the clear spectroscopic characteristics. Much of their work on THz stand-off detection and spectroscopy of explosives is summed up in Refs. [29, 40].

Soon after the first demonstration by Kemp *et al.* [28], several groups validated the results[41–43] and reported on THz absorption of other explosives and related compounds[43] including bio-agent simulants [44–46], and comparison studies of THz-TDS and Fourier transform infrared (FTIR) spectroscopy [36, 43]. Since then, various spectroscopic studies of explosives have been published [32, 37, 47–52]. Among these, density functional theory (DFT) calculations[47, 48, 52–54] were compared to the measured absorption spec-

tra, which showed that most of the characteristic spectral fingerprints below 3 THz originate from phonon modes, *i.e.* lattice vibrational modes, of the solid-state compounds. Furthermore, Yan *et al.* [55] have very recently shown that aging of RDX can be detected using THz-TDS, since its absorption peaks related to N-NO_2 bonds fractures as it ages.

The majority of the studies discussed above have been carried out in a transmission geometry, however, real-world applications like stand-off detection call for a reflection configuration, and especially, diffuse reflection measurements. Different studies have demonstrated specular reflection THz-TDS at stand-off distances of 1 m or less [39, 56–63], while Zhong *et al.* reported significant results on the detection of RDX by specular reflection TDS at standoff distances up to 30 m [64, 65]. It should however be noted that in this study, a collimated terahertz beam traveled 30 m back and forth with a pair of off-axis parabolic mirrors in close proximity of the sample to focus and collect the THz beam onto/from the sample. Thus, the setup did not resemble a true standoff geometry applicable in real-world security applications. Additionally, Zhong *et al.* combined THz-TDS with a large scale two dimensional imaging system, including a large ZnTe sensor crystal and a CCD camera, to perform reflective THz spectroscopic focal-plane imaging at 0.4 m stand-off distance. Using this setup they were able to identify and classify different explosives and bio-chemical materials by their derivative absorption spectra using PCA and a minimum distance classifier.[56, 65] In contrast, Liu *et al.* measured the diffuse reflection spectrum of a RDX pellet by TDS.[66] The absorbance was calculated by the Kramers-Kronig transform of the relative reflectance referenced to the spectrum of either Teflon or copper. Remarkably, the authors were able to distinguish the RDX from polyethylene and flour, even when covered by different barrier materials such as paper, polyethylene, leather, and polyester, by its 0.82-THz spectroscopic fingerprint in ambient conditions. Moreover, various studies have examined the effects of surface roughness on reflection spectra in THz spectroscopy [62, 67–70]

1.2 Atmospheric Propagation

One of the main challenges in THz stand-off detection is the required propagation through the atmosphere due to high absorption of THz radiation by the atmospheric water vapor. Because water absorption increases exponentially versus beam propagation distance, standoff detection at longer distances becomes even more challenging. In Ref. [32], Liu *et al.* investigated atmospheric propagation of THz waves. As seen in Fig. 2.3, they found several transparent windows between the strong absorption lines of water vapor, in which the atmospheric attenuation is minimal. In 2011, the group led by Grischkowsky further reported results on propagation of broadband THz pulses over long distances. They transmitted repetitive 0.5-ps broad-

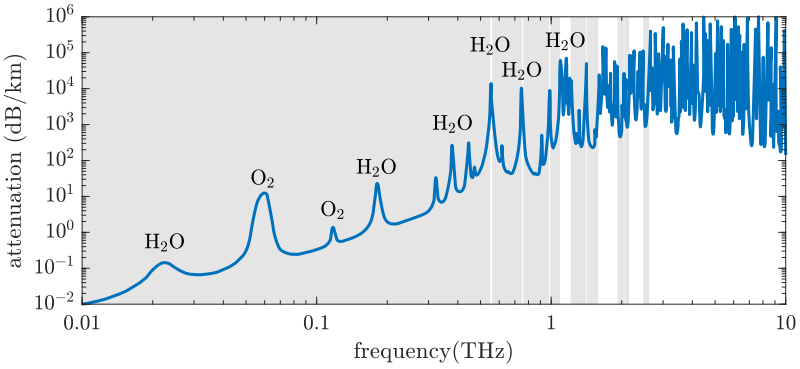

Fig. 2.3: Atmospheric attenuation of THz radiation at sea level in the range of 0.01 to 10 THz. Adapted from Ref. [71, 72]. The shaded areas indicate nine commonly attributed transmission windows.[32]

band THz pulses through 167 m of the atmosphere at 51 % relative humidity (RH).[73] However, such broadband THz pulses extend over several transmission windows. The THz power outside these windows is highly absorbed and, hence, the efficient THz power of the pulse is considerably reduced. Furthermore, sub-picosecond THz pulses are significantly prolonged by water vapor due to group velocity dispersion (GVD). After propagating 167 m, the initial 0.5-ps THz pulses were reshaped into 5-ps symmetric pulses at the leading edge followed by rapid oscillations to beyond 150 ps. Thus, the beneficial time-of-flight detection of pulsed THz systems is impossible at stand-off distances. A few years later, they demonstrated the propagation of broadband THz pulses through 137 m of dense artificial fog within a building.[74] The recorded THz pulses showed minimal additional distortion and attenuation in the presence of the fog, and as importantly, the transmission windows remain unaltered in the fog without frequency shifts or additional resonant lines. The same year, the groups of Grischkowsky and Jeon made a joint proof-of-concept demonstration of outdoor long-path THz-TDS atmospheric measurements between two buildings separated by 79.3 m.[75] The THz pulses were transmitted 9.5 m above ground level and travelled a 186 m path. Complex transmission spectra were acquired under different RH and weather conditions including clouds, rain falling at 3.5 mm/h, and snow falling at 2 cm/h. The spectral bandwidth spread to approx. 1 THz under outdoor weather conditions of 12.5% RH at 9.6°C (1.1 g/m^3 water vapor density (WVD)) and a wind velocity of 1.3 m/s, however, under more severe conditions the bandwidth was limited to approx. 0.5 THz. In 2017, they extended the long-path setup to a remarkably 910-m distance (883 m outdoor) retaining a 0.4 THz bandwidth.[76] More recently, the system was improved with a nanostructure plasmonic THz emitter PCA and a 1-m di-

ameter seven-mirror array reflector achieving a 141 dB SNR (1170:1).[77] This allowed recording of THz pulses at high WVD of up to 25.2 g/m^3. Furthermore, they measured for the first time the resonances of N_2O gas contained in a 1.5-m diameter balloon located 455 m away under atmospheric pressure in the 0.1-0.4 THz region. In recent time, the characterization of atmospheric transmission and dispersion of THz pulses is covered in the book chapter written by Jepsen *et al.* [78] in *THz Communications* (2022). Using ultrafast THz pulses, the atmospheric water vapor absorption across the 0.5-12 THz region measured in a laboratory atmosphere of 30% RH is presented.

1.3 Stand-Off Systems and Techniques

In the early years, Kemp and coworkers at TeraView Ltd. developed two prototype systems as they pursued the uses of THz technology for security applications[39, 79]. One of the systems was a stand-off THz detection setup that resembled a traditional single-point THz-TDS system as described in Chapter 1 with an additional rapid scanning delay stage, which allowed real-time operation at 15 Hz. Within the 1/15 s both acquisition and data processing to remove atmospheric water vapor absorption lines were performed. Long focal length off-axis parabolic mirrors were used to focus and collect the THz beam at a target distance of 1 m (2.4 m total THz path length). Using a perfectly reflecting target, they achieved >60 dB dynamic range and a spectral bandwidth from 0.1 to 3 THz. Furthermore, due to the depth of focus, they were able to track an object in a range greater than 150 mm from the focal plane by adjusting the long delay stage to center the THz pulse in the fast scan window.[79]

Meanwhile, the X.-C. Zhang, who chaired the task group behind the initial NATO report [34], and his team began studying THz generation and detection by optically generated plasma discharges in air (mixing of a femtosecond pulse and its second harmonic). A technique Zhang eventually pioneered, and which is now know as *THz air photonics*[80] (or *laser air photonics* [81]). However, generation of THz pulses via laser-induced plasma in gas was first observed in the 1990's by Hamster *et al.* [82, 83] and revived in 2000 by Cook *et al.* [84] and Löffler *et al.* [85]. First, Zhang's group systematically studied the basic generation mechanism [86], which they later expanded by a full quantum mechanical model[87, 88]. Shortly after, their initial study was followed by a theoretical analysis and experimental results of broadband detection of THz waves by a reciprocal four-wave mixing process, *viz.* electric-field-induced second-harmonic generation in laser-induced air plasma[89]. A technique they later termed *THz Air Biased Coherent Detection* (THz-ABCD). Noteworthy, they showed that extremely broadband THz pulses covering the entire THz region, only limited by the femtosecond pump pulse duration, can be achieved when air is used for both THz generation and detection in a

coherent detection scheme.[90, 91] Right from the beginning of their studies, stand-off THz spectroscopy was recognized as a feasible application[92, 93], which has since been a clear thread throughout their ongoing research and served to demonstrate and track the progress[94, 95]. Some of the main results include remote generation of intense THz pulses by propagating optical pulses over 100 m and focusing them locally [96], and stand-off THz generation in ambient air up to 30 m from the final optics[97, 98]. Impressive results have also been reported for THz remote sensing and standoff detection although being much more challenging, especially due to the strong atmospheric attenuation of THz frequencies. Even though air-plasma can be generated remotely forming the basis for the THz-ABCD technique, the THz-induced second-harmonic signal can only be detected in the forward propagating direction, and requires a high voltage local oscillator bias near the target if coherent detection is desired [89, 90]. Thus, THz-ABCD is not feasible in a stand-off configuration. To overcome these hurdles, Zhang *et al.* have proposed THz radiation enhanced emission of fluorescence (THz-REEF) [99, 100] and THz enhanced acoustics (THz-TEA) [101], in which the THz wave is indirectly detected through THz-induced changes in the plasma fluorescence and acoustics. Both techniques allow for omnidirectional collection of the signal and circumvents the problem of atmospheric absorption at THz frequencies, and thus, well-suited for stand-off spectroscopy. Especially, Stand-off detection at 30 m using THz-REEF has been demonstrated[98], while Clough *et al.* [102] have reported "all air-plasma" THz spectroscopy encoding the spectral THz signatures of different explosives into the fluorescence emitted from a bichromatic laser-induced plasma filament. Laser air photonics remain an active research topic by itself, and several reviews of their work can be found in Ref. [81, 103, 104] Finally, other groups have, *e.g.* , proposed optically-biased coherent detection (OBCD) [105] as a simpler counterpart to THz-ABCD and investigated THz generation in multiple laser-induced air plasmas [106].

In 2006, a research project was launched by Defence Research & Development Canada (DRDC) – Valcartier to study the feasibility of using THz radiation to detect and identify explosives and concealed weapons at stand-off distances [107]. The project was initiated by developing a compact TDS system to establish a THz transmission spectra database of commonly used explosives. Another task of the project was to develop a diffuse reflection TDS system based on OR in a large ZnTe crystal using a high-power laser. The initial work was made in collaboration with Advanced Laser Light Source (ALLS) at the Institut National de la Recherche (INRS) in Canada. Here, a beam of 30-fs laser pulses with 800 nm center wavelength and energies up to 40 mJ at 100 Hz repetition rate was used for generation of THz pulses with record-high (in 2006) pulse energies of 0.76 μJ and spectral bandwidth from 0.1 to 3 THz [107, 108]. A future step would be to combine the large

ZnTe crystal with their TW laser. This laser delivers 5 TW (250 mJ pulse energy and < 50 fs pulse duration) and was installed in a standard portable container including a class 100,000 clean room for ideal laser operation conditions [109]. However, due to the 10 Hz repetition rate of the TW laser, coherent detection would become very slow. It should be noted, that since then, tremendous progress has been made on the generation of high-power THz pulses through OR. For example, in recent times, high-power THz OR has been demonstrated in GaP reaching a maximum of 1.35 mW average THz power with a 6 THz bandwidth peaking at 2 THz [110], and in $LiNbO_3$ generating 66 mW average THz power with a bandwidth limited to approx. 2.5 THz [111], both driven by >100 W pump average power at 13.4 MHz repetition rate. Similar results have been reported using organic crystals such as HMQ-TMS [112, 113] achieving up to 1.38 mW broadband THz radiation of 6-THz bandwidth at 10 MHz repetition with average pump powers in the 10-W range. A thorough review of the recent development on intense laser-driving THz sources can be found in Ref. [114].

In continuation of the Canadian feasibility study of THz radiation for detection and identification of concealed explosives and weapons at stand-off distance [107], DRDC developed a new THz spectroscopy system for standoff detection based on an intra-cavity (IC) THz parametric oscillator (TPO)[115–117]. The rather compact TPO source used in the system was tunable from 0.75 to 2 THz emitting 10-ns pulses at a 50 Hz repetition rate with a <50 GHz linewidth and energies >30 nJ, resulting in a THz peak power greater than 3 W. Moreover, aside from the high spectral brightness and tunability, the THz output is highly collimated and exhibit an almost Gaussian beam quality. The detection scheme of this system relied on a 4.2 K liquid helium cooled bolometer. A full description of the ICTPO and the its operation is given in Ref. [118], while the prototype of the standoff system is described in Ref. [34, 118]. Let us notice that this scheme operates directly in the frequency-domain in contrast to all the above-mentioned methods. To demonstrate stand-off identification, the prototype system was used in the international experiment carried out under the first NATO task group [34] to detect and identify C4 hidden behind barrier materials at 8 m stand-off distance. The TPO was developed by M-Squared Ltd. [119], which since then has optimized and commercialized it as the *Firefly THz OPO* [120]. In this relation, it is worth noting that Piestrup *et al.* [121] first demonstrated a THz parametric oscillator based on a Lithium Niobate crystal in 1975. Then, the technique was stagnant until Kawase *et al.* [122] took it up in 1996 and later demonstrated THz spectral imaging of illicit drugs [123] using an updated compact and widely tunable TPO. Since then, THz spectroscopy and generation in the form of a TPO/TPG (terahertz parametric generator) [124–132] or via difference frequency generation (DFG) [133–141] in, *e.g.*, GaSe has been a widely studied topic. For example, Kawase's group have demonstrated a

multiwavelength injection-seeded (is) TPO for one-pulse spectroscopy[128] with >60 dB dynamic range using a high-power is-TPG with a peak power of 50 kW [126] and frequency tunability of 0.4 to 5 THz [128], and coherent detection by the inverse parametric conversion process in a second nonlinear crystal [142]. More recently, Takida *et al.* [132] were able to detect gas-phase methanol at trace concentrations of 0.2 ppm at the 1.48-THz transparent atmospheric window using an is-TPG source (tunable from 0.5 to 3 THz in 1-GHz frequency steps with maximum THz peak power of >50 kW and 100 Hz repetition rate) and a 1.8-m path length multipass cell, which lead to a prototype of a portable walk-through security screening system

The second NATO task group [35] was launched to investigate how THz technology could move from laboratory spectroscopy to stand-off detection in the field. One of the tasks within this framework was to compare different THz technologies and THz systems for detection and identification of explosives under field conditions. The resulting comparison study was also published elsewhere [143] in 2014. Several technologies including both broadband and narrowband pulsed THz spectroscopy as well as CW THz spectroscopy and electronic sources were considered. However, merely different TDS systems (two based on PC antennas and one EO-based) and a single electronic system were studied. The latter comprising an electronic frequency-modulated CW device and a microbolometer array detector. On this basis, it was concluded that TDS systems were the most promising candidates for stand-off detection because of their spectral bandwidth, although still being too complex for use in the field, while the electronic systems was recognized for its imaging applications.

As discussed in Chapter 1, direct frequency-domain THz spectroscopy can also be performed by means of monochromatic CW THz radiation via photomixing. Shimizu *et al.* [144] have developed on a system for stand-off gas sensing system including a photomixing transmitter[145] and a heterodyne superconductor-insulator-superconductor (SIS) mixer detector[146]. Finally, Shimizu *et al.* [147] demonstrated the performance of the stand-off spectrometer (operating in the 220-500 GHz region) by remote gas sensing experiments conducted in a full-scale simulated fire at approx. 8.6 m stand-off distance. Hereof the testing room, in which a metallic retroreflector bounced back the THz radiation, accounted for approx. 3.6 m of the total stand-off distance. Thus, they measured the transmission spectrum of the simulated fire and resulting smoke. The smoke appeared transparent to the THz radiation due to its micron-sized particles, and they were able to detect hydrogen cyanide at concentrations of 890 ppm, estimated from the measured absorption intensities.

Around the same time, Preu *et al.* [148] examined both spacial and temporal interference patterns of two independent photomixer sources driven by the same optical beat, and found that the coherence of the optical beams

is not affected by the internal structure of the photomixers and transfers directly to the THz beams. Hence, multiple photomixers are mutual coherent when driven by a common optical beat. Subsequently, Preu *et al.* simulated different array configurations of coherently driven free space THz sources for high brightness applications [149] such as stand-off sensing. Bauerschmidt *et al.* [150–152] followed up by experimentally demonstrating a four element emitter focal plane array (FPA) of individual, mutually coherent THz photomixers in a 1×4 and 2×2 configuration for stand-off imaging and spectroscopy. Each photomixer was equipped with a pair of lenses, and the focused THz beams were overlapped at a target distance of 4.2 m. The interference patterns as well as the transmission spectra of the 1×4 array and a single emitter were measured in the target plane using a Golay cell detector. Their measurements confirmed the theoretically square and inverse dependency on the number of sources of the peak intensity and the beam waist, respectively, as well as an excellent agreement to the expected interference patterns of the different array configurations.

In contrast, THz detector arrays in the context of synthetic aperture imaging have been explored by the group of J. F. Federici. Bandyopadhyay *et al.* [153] first studied the stand-off imaging properties of an interferometric array in the near-field region theoretically, and experimentally using a photomixer spectrometer by sampling the THz signal in different positions to emulate a detector array. Meanwhile, Sengupta *et al.* [57] measured C4 and gold by reflection THz-TDS, and synthesized THz images from the reflectance spectra to simulate interferometric detection.

Evidently, THz stand-off detection has primarily evolved from TDS and photonic techniques. However, a few electronic systems have been proposed as well. Mo *et al.* [154] have reported a nine-wavelength CW THz spectrometer for identification of explosive materials using three backward wave oscillator (BWO) sources covering the intervals from 0.18 to 0.26 THz, 0.2 to 0.38 THz, and 0.6 to 0.7 THz, respectively, and pyroelectric detector. To demonstrate the capabilities of the spectrometer, RDX, TNT, and 2,4-DNT were measured at nine frequencies between 0.21 and 0.7 THz, and were able to sucessfully identify and classify the sparse spectra using machine learning algorithms. Likewise, Richter *et al.* [155] have proposed a THz spectrometer based on THz quantum cascade lasers (QCLs) operating at different frequencies including a compact heterodyne hot electron bolometer detector for explosive detection and identification. Lastly and most recently, Chen *et al.* [156] have demonstrated wavelength beam-combining of four THz distributed-feedback QCLs, which could be promising for future monolithic THz QCL arrays for multi-spectral THz sensing at stand-off distances.

1.4 Hand-Held Devices

As mentioned, two prototype systems for security screening were developed at TeraView Ltd., of which we have already discussed one meant for stand-off detection at a distance. The second was a hand-held THz wand developed for people screening in close proximity including detection of both hidden weapons (both metallic and non-metallic) and explosives [39, 79]. The device was similar to the one described above but the optical pump and probe beams were coupled into fibers attached to the THz photoconductive (PC) antennas constituting the handheld THz transceiver head. Interestingly, the transceiver consisted of a single THz PC emitter, equipped with a silicon lens to produce a quasi-collimated output, surrounded by an assembly of six THz PC detectors, each with a silicon lens. The array of detectors could capture the THz signal reflected and scattered in multiple direction from the target. By analyzing the recorded signals from each detector independently, both spatial and spectroscopic information could be extracted The prototype achieved a dynamic range of approx 45 dB, spectral bandwidth up to 2 THz, and a 30 Hz scan rate[79], which allowed them to detect various materials in reflection including explosives behind two layers of leather[39].

In 2011, Schulkin *et al.* [157] at Zomega Terahertz Corporation presented a novel one-of-its-kind hand-held, point-and-shoot, batteri-driven THz spectrometer operating at 500 Hz for stand-off detection and identification of chemical compounds. With dimensions less than $26 \times 18 \times 9$ cm^3 and weighing less than 4.5 kg, the form factor of the spectrometer was similar to a cordless power drill. The spectroscopic identification was performed using standard correlation analysis to avoid the need for sample references. Using 50-ms integration times perfect classification of library samples including α-lactose, PABA, L-glutamic acid, and 2,4-DNT could be achieved at a distance of 7.5 cm.

1.5 Final Remarks

Besides the practical work with TeraView Ltd, Kemp also participated in the first technical NATO report[34], and reviewed the current progress, different challenges as well as future prospects and directions for THz technology in security applications[29, 158]. In conclusion, Kemp compiled his knowledge in the paper *Explosives Detection by Terahertz Spectroscopy – A Bridge Too Far?*[159], in which it was concluded that spectroscopic detection through barriers is unlikely in practice due to free space propagation loss, atmospheric absorption, barrier attenuation and scattering, and target reflectivity and/or scattering, while imaging at lower frequencies up to 1 THz (possibly multi-spectral) was deemed more promising for security applications. However, as discussed later in this thesis, the ongoing development of power-

ful monochromatic THz sources (*e.g.*, electronic sources or QCLs) combined with our machine learning based approach could allow for spectroscopic detection of explosives and hazardous substances at stand-off distances, even through barriers.

2 Continuous-Wave versus Pulsed Radiation

Hypothesis I claims that propagation losses can be reduced by employing CW FDS instead of pulsed TDS as all the emitted power can be concentrated within the atmospheric water vapor transmission windows. Here, it is implied that both approaches are conducted by optoelectronic techniques using photoconductive switches and photomixers, respectively. However, the conception behind such an idea is slightly wrong, which can be realized fairly easily by recalling that a broadband THz pulse can be regarded as a wave packet formed by the superposition of monochromatic waves of the frequencies in its spectrum. Hence, a THz pulse propagating through atmospheric water vapor is only absorbed at frequencies that coincide with the absorption lines of water vapor. In the time-domain, this can be observed as trailing oscillations to the main peak due to the absorbed waves of the respective frequencies. Thus, any difference of eligibility between a frequency-domain and a time-domain approach for stand-off spectroscopy is determined by the performance of the respective THz sources and detectors available in each approach. However, absolute power measurements of terahertz waves are not trivial and generally not available. Recently, Castro-Camus *et al.* [160] commented on the reliability of power measurements in the terahertz and discussed the challenges. Calibration of THz detectors can only be done at very few laboratories around the the world. For example, this is done by the THz radiometry group at Physikalisch-Technische Bundesanstalt (PTB), the German National Metrology Institute, using a far-infrared molecular gas laser emitting tunable monochromatic radiation from rotational transitions of the molecular gas [160]. For PC antennas and photomixers, the task is further complicated by the broad spectrum and/or low power of the emitted THz radiation. Therefore, different THz sources cannot readily be compared and, typically, THz spectrometers are characterized by system specific measures such as the amplitude of the detected signal or maximum achievable SNR. On top of that, a comparison of PC antennas and photomixers is often impeded by their respective pulsed and CW operation. Nevertheless, let us give a qualitative estimate of the performances of (commercially available) PC antennas compared to photomixers. Globisch *et al.* [161] have demonstrated absolute THz power measurements of a standard commercial TDS system using an ultrathin pyroelectric thin-film (UPTF) detector developed and calibrated by PTB. The UPTF detector exhibited a spectrally flat absorption of 50% from 0.1

to 5 THz. The diameter of the UPTF detector was 20 mm, which ensured that all of the incident THz radiation was captured Using a common InGaAs PC antenna as THz emitter, the authors measured the (average) THz power for various optical pump powers and emitter bias voltages. Similarly, a coherent PC antenna detector was employed to record the temporal THz waveforms for the same optical powers and bias voltages. Then, by calculating the time integral of the squared waveforms, a quantity proportional to the THz power was obtained. Noteworthy, Globisch *et al.* found an almost perfect agreement between the two means of measuring the THz power This imply that both detectors capture all of the incident beam. This is a quite remarkable finding, since the coherent PC detector has a very small active area between the electrodes (typically less than 50 μm wide). Thus, a strong focus of the THz beam is required, which is achieved by the attached hyper-hemispherical Si lens. This lens can be difficult to align and is often non-adjustable. Additionally, it doesn't focus the low and the high THz frequencies identically and some of these frequencies could potentially be coupled to the antenna electrodes. Furthermore, the sensitivity of such coherent detectors are not spectrally flat. All these considerations tend towards that only a lesser part of the incident THz radiation will be properly detected by the PC antenna. Nonetheless, the results reported by Globisch *et al.* indicate that these concerns are not so critical in a well aligned system. Commercial TDS systems employ PC emitters with average output power of typically 30-70 μW. [b] This value is averaged in time and integrated over the entire spectral bandwidth of the THz pulses from 0.1 to 6 THz. On the other hand, photomixers utilized in FDS systems are rated by their typical output power at some given frequencies or by their power spectrum. The red dots plotted in Fig. 2.4 show some typical power values of commercial photomixers. To give an estimate of the power spectrum of PC emitters employed in TDS systems, we recorded a THz waveform using our commercial TDS setup from Menlo Systems (Terasmart). The blue line on the left plot in Fig. 2.4 shows the resulting trace averaged over 1000 waveforms. From the recorded time-domain pulse, we can calculate its spectrum via the discrete Fourier transform. Let us square the magnitude of the resulting spectrum to get a quantity proportional to the THz power. A simple unitless distribution is obtained by normalizing the power spectrum such that it integrates to unity. For the sake of simplicity, let us suppose that the average THz power was 100 μW. Multiplying the normalized power distribution by this value, we obtain the spectrum given by the blue line in Fig. 2.4. As said, this is a crude estimate that sets the upper boundary of the THz power spectrum of PC emitters. Immediately, we see that CW photomixers reach power levels that are more than an order of magnitude higher. Thus, we can conclude that the maximum stand-off distance is expected to increase

[b] According to TOPTICA Photonics AG.

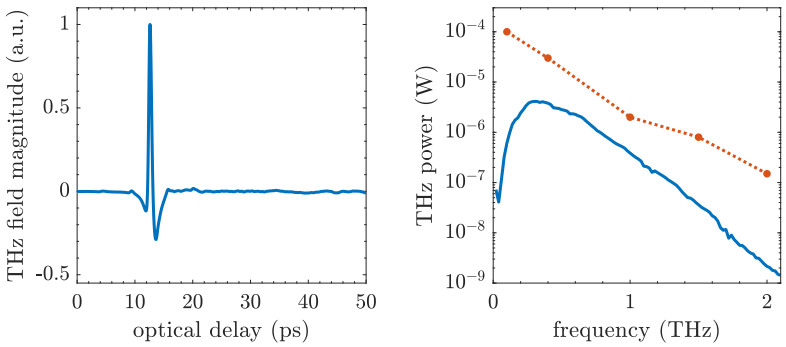

Fig. 2.4: THz waveform recorded using a commercial TDS system and its estimated power spectrum (blue) together with typical power levels in commercial FDS systems (red).

for current state-of-the-art FDS systems based on CW photomixers compared to TDS systems, even though Hypothesis I is slightly wrong, simply because of superior output power. It should however be emphasized that propagation losses (divergence, scattering *etc.*) will not be reduced.

3 Antenna Arrays

The first antenna array was built over 100 years ago by S. G. Brown in 1899. [162] Two monopole antennas where separated by half a wavelength and fed out of phase in order to increase the directivity. Likewise, an antenna array was utilized in the historical event when the pioneer G. Marconi transmitted the first wireless signals 2100 miles across the Atlantic.[163] A few years later, Prof. K. F. Braun at University of Strasbourg discovered the phased array and it's beam forming capabilities. [164] Finally, in 1909, Marconi and Braun shared the Nobel Prize in Physics for their contributions to the development of wireless telegraphy. [165]

Today, microwave phased arrays have become the backbone of modern wireless communication. Naturally, THz antenna arrays have been investigated as well in search for more powerful sources and sensitive detectors. As covered in Section 1, Preu and Bauerschmidt *et al.* investigated the interference between mutual coherent free standing photomixers[148, 149] and demonstrated a focal plane array emitter [150–152, 166], while Federici *et al.* [153] examined synthetic aperture imaging by THz detector arrays. However, THz antenna arrays were, in fact, already proposed in 2003 by Brown [167], who saw the advantage of moving THz photomixing to photoconductive InGaAs compatible with 1.5 μm lasers that benefit from fiber coupled optics and amplifiers. In particular, Brown proposed that on-chip fiber cou-

pled photomixer phased arrays could be realized, which would neglect the need for bulky silicon lenses, as we will see in the following. This idea was investigated experimentally a few years later, when Preu *et al.* [168] reported a 3×3 array based on LTG-GaAs photomixers with an appertaining microlens array for optical coupling, and Shimizu *et al.* [169] demonstrated a 3×1 array of 300-GHz microstrip antenna UTC photodiodes. More recently in 2022, Che *et al.* [170] fabricated an on-chip 4×1 array of InP/InGaAs UTC-PD photomixers with integrated 1×4 planar slot antennas for generation and beam combining/steering of both continuous and pulsed THz radiation up to 300 GHz. The generated continuous wave and pulsed output powers reached -12.87 dBm (52 μW) and -17.71 dBm (17 μW), respectively. This corresponded to gains of 12 dB and 10 dB relative to a single excited emitter. The lower output power in the pulsed operation was attributed to the bandwidth limitations of the slot antennas. Besides, various papers have been published on the topic from studies on array and lens arrangements [171] to a tutorial on the concepts of THz beamforming [172] and a review of the applications of THz beam steering [173].

3.1 Array Theory

Let us develop some basic equations of antenna arrays. Consider M oscillating electric dipoles with angular frequency ω distributed in the xy-plane as depicted in Fig. 2.5. At a given point in space $\vec{r}$ and time t, the electric field

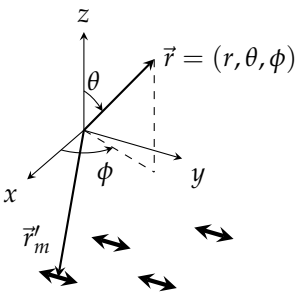

Fig. 2.5: Coordinate system for a collection of oscillating electric dipoles.

radiated by the mth dipole positioned at $\vec{r}_m$ can be written as

$$\vec{E}_m(\vec{r}, \vec{r}_m; t) = \vec{E}_{0,m}(\vec{r}, \vec{r}_m) e^{j\left(\vec{k}\cdot(\vec{r}-\vec{r}_m)-\phi_m\right)} e^{-j\omega t}, \tag{2.1}$$

where $\vec{E}_{0,m}(\vec{r}, \vec{r}_m)$ is the complex electric field amplitude, $\vec{k} = \omega/c\hat{k} = 2\pi/\lambda\hat{k}$ is the wave vector ($\hat{k}$ is the unit vector in the direction of propagation), and ϕ_m is the relative phase. Assuming there is no coupling between the dipoles, the total electric field radiated by the array $\vec{E}_{\text{total}}$ is the sum of the fields radiated

by the individual elements $\vec{E}_m$, *i.e.*

$$\vec{E}_{\text{total}}(\vec{r}) = \sum_{m=1}^{M} \vec{E}_{0,m}(\vec{r}, \vec{r}_m) e^{j\left(\vec{k}\cdot(\vec{r}-\vec{r}_m)-\phi_m\right)}. \tag{2.2}$$

Let us assume that the dipoles are identical, orientation included, thus exhibiting similar radiation patterns and equal power. Furthermore, we will only consider the far-field. That is, where the field components are transverse and the angular distribution is invariant to the radial distance from the source, which is generally defined to begin at the distance

$$r \geq \frac{2D^2}{\lambda} = \frac{2D^2\nu}{c} \tag{2.3}$$

from the source with $D > \lambda/2$ being the largest dimension of the source (the aperture).[174] With these assumptions, we can write $\vec{E}_{0,m}(\vec{r}, \vec{r}_m) = \vec{E}_0(\vec{r})$ and Eq. (2.2) writes

$$\vec{E}_{\text{total}}(\vec{r}) = \vec{E}_0(\vec{r}) \sum_{m=1}^{M} e^{j\left(\vec{k}\cdot(\vec{r}-\vec{r}_m)-\phi_m\right)}. \tag{2.4}$$

The sum

$$F(\vec{r}, \vec{r}_m) = \sum_{m=1}^{M} e^{j\left(\vec{k}\cdot(\vec{r}-\vec{r}_m)-\phi_m\right)} \tag{2.5}$$

describes the effect of the array and is, hence, referred to as the *array factor*. Constructive interference can be achieved in a point $\vec{r}$ if the phases of the radiated fields are equal up to an integer number n of 2π, given the polarizations are identical, *i.e.*

$$\vec{k} \cdot (\vec{r} - \vec{r}_m) - \phi_m = 2\pi n. \tag{2.6}$$

In this case, the array factor equals M and the total intensity $I_{\text{total}}(\vec{r}) = |\vec{E}_0(\vec{r})M|^2$ increases by M^2.

In antenna theory, $\vec{E}_{\text{total}}(\vec{r})$ and $\vec{E}_0(\vec{r})$ are called the *beam pattern* and *element pattern*, respectively. The fact that, in the far field, the beam pattern of an array is equal to the product of the element pattern at a reference point (typically Origo) and the array factor is an important result in antenna theory known as *pattern multiplication*.[174] The array factor is independent of the directional characteristics of the array elements and can thus be regarded as an array of isotropic point sources. Therefore, different array geometries can be studied optimized through the array factor and only then the total field is obtain by multiplying it with the actual element pattern. Typically, radiation patterns are described using a spherical coordinate system (r, θ, ϕ) with radial distance $r \in [0, \infty[$ from a fixed origin, polar angle $\theta \in [0, \pi]$, and azimuthal angle $\phi \in [0, 2\pi[$. Fig. 2.6(left) shows the normalized beam patterns of linear arrays of $M = 2$ (blue) and $M = 5$ (red) antennas equally

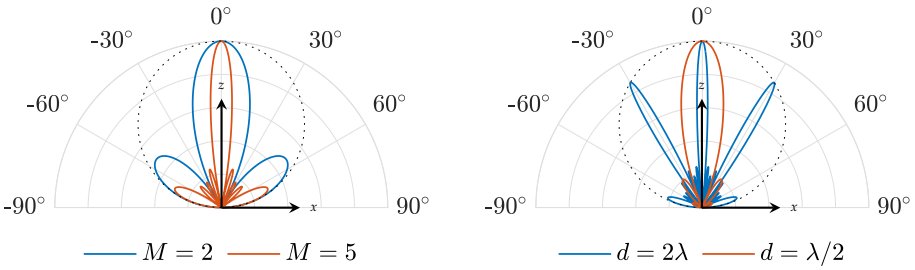

Fig. 2.6: - left - Beam pattern of a linear array along the x- axis with two elements (blue) and five elements (red), respectively, equally spaced by $d = \lambda$. - right - Beam pattern of a five element equally spaced linear array with $d = 2\lambda$ (blue) and $d = \lambda/2$ (red), respectively. In both plots, an element pattern $|\vec{E}_0| \propto \cos(\theta)$ is assumed (dotted, black line).

separated by $d = \lambda$ on the x-axis. An element pattern (dotted) equal to $\cos(\theta)$ has been chosen. The main lobe narrows while minor side lobes develop as the number of array elements is increased. In Fig. 2.6(left), the beam pattern of a $M = 5$ element equally spaced linear array along the x-axis with $d = 2\lambda$ (blue) and $d = \lambda/2$ is plotted. Compared to Fig. 2.6(right), we see that grating lobes (strong side lobes) develop as d is increased and, in particular, $d = \lambda/2$ produces a highly directional beam. Thus, various array configurations can be exploited to obtain certain beam patterns. In Fig. 2.7,

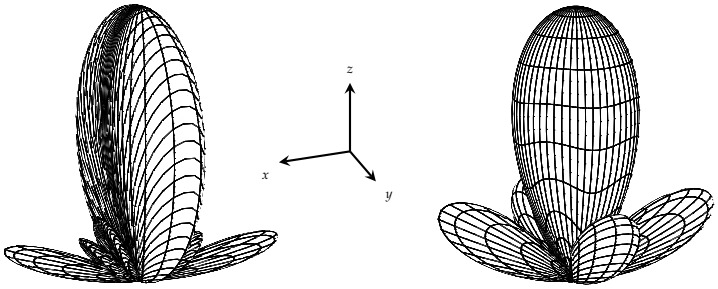

Fig. 2.7: Three-dimensional beam patterns of a 4×1 and a 2×2 array, respectively, with $d = \lambda$ and $|\vec{E}_0| \propto \cos(\theta)$.

the three-dimensional beam patterns of a 4×1 and a 2×2 array with element spacing $d = \lambda$ are shown. Evidently, the two-dimensional array confines the main lobe in both x- and y-directions resulting in a higher directivity. Another advantage of antenna arrays is beam steering. To exemplify this, let us consider an uniformly spaced $M = 4$ linear array (spaced by $d = \lambda/2$) with a linear phase gradient $\varphi_m = m\beta$ across the array. Additionally, we suppose

an element pattern $|\vec{E}_0| \propto \cos(\theta)$. This is plotted for various values of β in Fig. 2.8. Evidently, the beam pattern is shifted away from the broadside of

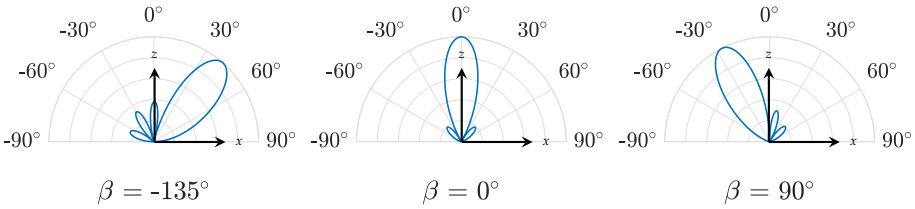

Fig. 2.8: The concept of beam steering by exciting the array elements with a linear phase gradient $\phi_m = m\beta$.

the array ($\beta = 0$) in the opposite direction of the phase shift β.

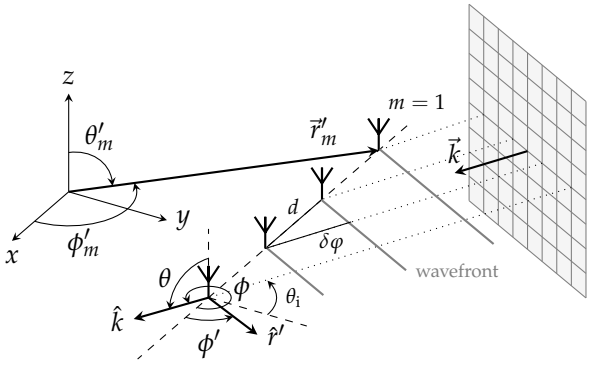

Fig. 2.9: Coordinate system for an array of receivers subject to an incoming plane wave.

Because of reciprocity, everything derived above for an array of transmitters is also true for an array of receivers. However, to get a better understanding of the operation of a detector array, let us consider a plane wave incident on a linear array of identical receiving elements as shown in Fig. 2.9. The plane wave model of the incoming electric field is a good approximation since the distance between the transmitting and the receiving array generally is much greater than the far-field limit. We choose the notation

$$\vec{E}(\vec{r};t) = \vec{E}(\vec{r})e^{-j\omega t} = E_0 e^{j\vec{k}\cdot\vec{r}} e^{-j\omega t}, \tag{2.7}$$

with wave vector $\vec{k} = \frac{\omega}{c}\hat{k}$ for the incoming plane wave in air. Since the receiving elements are identical, they possess an equal receive pattern $S_m(\theta,\phi) = S(\theta,\phi)$. The received electric field at mth antenna can then be expressed as

$$S_m(\vec{k},\vec{r}'_m) = S(\theta,\phi)E_0 e^{j\vec{k}\cdot\vec{r}'_m}. \tag{2.8}$$

The exponent can be written as $\vec{k} \cdot \vec{r}'_m = |\vec{k}||\vec{r}'_m| \cos(\alpha_m)$ with $\alpha_m = \phi - \phi'_m$ being the angle between the two vectors. However, we can choose the coordinate system such that the array elements line up along the x axis with the first antenna $m = 1$ located in Origo. Hence, we have $|\vec{r}'_m| = (m-1)d$ and $\phi'_m = 0$ implying $\alpha_m = \phi$. From Fig. 2.9, we see that $\phi = \theta_\mathrm{i} + \pi/2 + \pi$ and, hence, $\cos(\phi) = \sin(\theta_\mathrm{i})$. Thus, we arrive at $\vec{k} \cdot \vec{r}'_m = \frac{\omega}{c}(m-1)d\sin(\theta_\mathrm{i})$. Here, $d\sin\theta_i$ is the extra distance the wave has to travel to reach an adjacent antenna. It follows that the delay the mth antenna experience relative to the reference antenna $m = 1$ is $\tau_m = (m-1)d\sin(\theta_\mathrm{i})/c$, which corresponds to a phase shift $\delta\varphi_m = \omega\tau_m$. Hence, $\vec{k} \cdot \vec{r}'_m = \omega\tau_m = \delta\varphi_m$. Because the signal received at a given antenna gain a phase shift relative to the neighboring antennas, the signals are misaligned and cannot be added coherently and, consequently, there is no array gain achieved. However, in many cases it is possible to delay the signals independently and, hence, align the phases allowing coherent summation. This is done by multiplying the signals at the receivers by the complex weights w_m before summation. The total received signal can then be written as

$$S_\mathrm{total}(\theta,\phi) = E_0 S(\theta,\phi) F(\theta,\phi) \quad \text{with} \quad F(\theta,\phi) = \sum_{m=1}^{M} w_m e^{j\delta\varphi_m}. \tag{2.9}$$

To align the signals, the weights must be chosen as the complex conjugates of the phase shifts, *i.e.* $w_m = e^{-j\delta\varphi_m}$. Thus, the array factor $F(\theta,\phi)$ simply adds up to number of array elements M, and the total received signal is increased by a factor of M compared to a single antenna or M^2 in terms of power.

3.2 Summary of Results

As the starting point for the development of the multiple antenna THz spectrometer for detection at improved stand-off distances, we choose a TeraScan 1550 spectrometer from TOPTICA Photonics AG based on THz-FDS as described in Sec. 2. This was system was chosen because of its modular design and compatibility with the wealth of available telecom components including fiber optics and amplifiers. To accommodate multiple antennas, the TeraScan system was extended both in terms of optical and electronic parts. In the optical branch illustrated in Fig. 2.10, the output of each distributed feedback (DFB) laser was amplified by an erbium doped fiber amplifier (EDFA) from Keopsys to support the required power levels of four transmitter and four detector InGaAs photomixers, respectively. The EDFA outputs were then connected to a 2×2 fiber coupler, whose outputs were connected to a TOPTICA fiber stretcher designed for the TeraScan system. Finally, each output of the fiber stretcher were connected to a 1×4 coupler to supply the optical beat to each of the eight photomixers. The electrical wiring is illustrated in

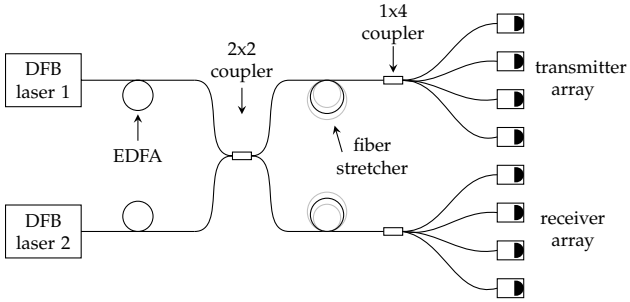

Fig. 2.10: Schematic of the multiple antenna THz-FDS setup in terms of optical components.

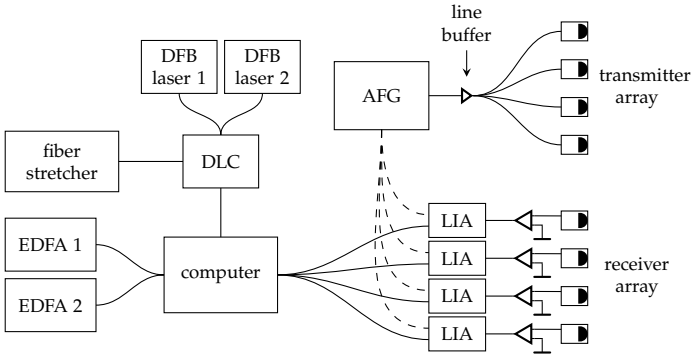

Fig. 2.11: Schematic of the multiple antenna THz-FDS setup in terms of electrical components.

Fig. 2.11. Normally, the FDS system is fully controlled by TOPTICA's DLC Smart digital control electronics including laser operation, bias voltage, lock-in detection *etc.* However, since each of the four detectors required a separate lock-in amplifier (LIA) and because of the higher load needed to be driven by the bias voltage, the DLC was just used to operate the DFB lasers and to control the fiber stretcher. Instead, a B&K Precision arbitrary function generator (AFG) was utilized in combination with a line buffer to supply the bias voltage to the photomixer emitters and to deliver a reference signal to the LIAs. The output current of each receiver was preamplified by a custom designed trans impedance amplifier and measured using a dual channel LIA, both from Femto Messtechnik GmbH. Finally, a computer with custom developed MATLAB software was employed to control the DLC as well as the EDFAs and to record the signals from the LIAs.

The array theory covered in Sec. 3 assumes that each array element (antenna) performs equally in terms of output power, radiation pattern *etc.* Thus, a natural first step toward a transmitting THz array was to characterize the individual THz emitters. The power spectra of four InGaAs THz emitters

adapted from the test reports made by the Fraunhofer Heinrich Hertz Institute (HHI) are shown in Fig. 2.12. All of the antennas perform within

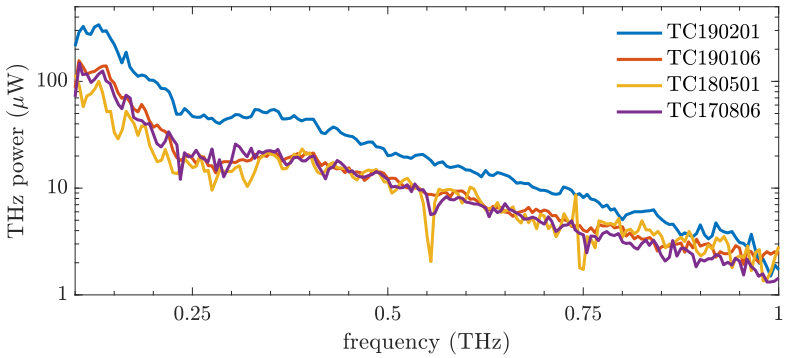

Fig. 2.12: The power spectra of the four THz photomixer transmitters adapted from the datasheets.

specs, however, one antenna (blue line) is clearly outperforming the remaining three in terms of output power. This antenna (TC190201) is from a newer batch compared to the rest. However, all four emitters have chips of the same design, and there has been no change in the production or assembly process.[c] The emitter InP chips (1.5 mm $\times$ 3 mm) are waveguide (WG) integrated PIN

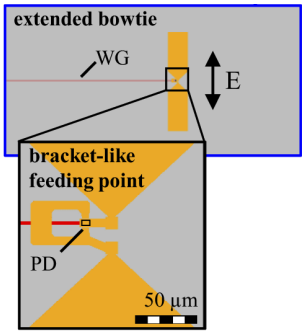

Fig. 2.13: Illustration of the bowtie antenna design of the THz photomixer transmitters. The sketch is adapted from Ref. [175].

photodiodes with an extended bow-tie antenna structure and a bracket-like feeding point as shown in Fig. 2.13. On the back, a hyper-hemispherical Si lens of 10-mm diameter is mounted to couple the THz waves into free space. Thus, the emitters are roughly 6.5 mm thick including the InP chip and Si lens.

[c]According to HHI. From a private correspondence with Dr. Anselm Deninger, Director Technical Sales Support, TOPTICA Photonics AG.

The next step was to characterize the radiation pattern of the individual THz emitters. Only a very few and recent studies [175, 176] have been published on the radiation patterns of PIN diode photomixers as employed in commercial THz-FDS systems. Particularly, we are interested in the far field as defined in Eq. (2.3). The aperture size of the PIN diode is approx. 1

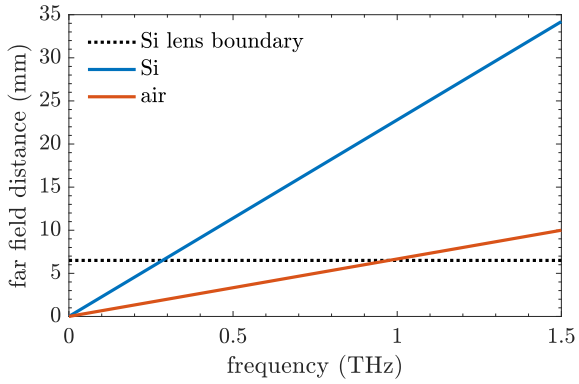

Fig. 2.14: The far field distance for Si and air at relevant frequencies calculated using Eq. (2.3). Adapted from Ref. [176].

mm corresponding to the size of the extended bow-tie antenna. As discussed by Smith *et al.* [176], the far field distance is longer in silicon since the THz wavelength $\lambda_{Si} = \lambda_0 / n_{Si}$ is shortened by the large refractive index $n_{Si} = 3.42$. Thus, the near field stretches beyond the silicon lens for frequencies above 0.3 THz as seen in Fig. 2.14. Smith *et al.* [176] propose that this effect causes the broadening of the central spot and added features they observe in their measurements. Therefore, the distance at which the radiation patterns are measured should be chosen larger than the far field distance at the largest frequency measured. In our experiment, the largest frequency is $\nu = 1.5$ THz and, hence, the distance should be greater than 35 mm (see Fig. 2.14). In the aforementioned studies, only the one-dimensional angular radiation profiles are mapped out for the E- and H-plane of the emitted THz field by rotating the THz emitter vertically relative to the detector. In particular, *"The radiation pattern of E- and H-plane are measured by orienting Tx and Rx with the respective polarization: for the E-plane, the orientation of the electric field E of emitter and receiver antenna are perpendicular to the rotation axis and for the H-plane, the magnetic field H is perpendicular to the rotation axis."* [175] As described by Smith *et al.* [176], the beam profile of an emitter can be mapped by either lateral or angular displacement of the emitter relative to the receiver. The former is preferable when mapping out a collimated beam, in which case the lateral profile and dimensions are preserved. On the other hand, the angular modality is optimal for the mapping of a divergent beam since the

emitter and receiver are equidistant for each measured value and the angular spread and variation are invariant. This approach naturally yields one-dimensional line scans, even though, several scans can be combined to form two-dimensional angular maps. In fact, even one-dimensional beam profiles can be non-intuitive and the exhibited beam features can be difficult to interpret. Nonetheless, because THz PIN diode emitters are divergent, Nellen *et al.* [175] and Smith *et al.* [176] mapped their beam patterns as a function of angular displacement but only for the two perpendicular directions. However, when the beam profile is only mapped in the perpendicular directions, potentially important information of the full pattern could be lost. In this study, we characterized the PIN diode emitters using an incoherent Schottky diode receiver, *i.e.* power detector, from TOPTICA mounted on an xy-stage, which was scanned laterally in two dimensions. Although, the recorded beam profiles will suffer from slight distortions due to small variations in distance and the angular dependency of the receiver, we gain a more complete two-dimensional image of the beam. For example, if the emitter is distanced $z = 100$ mm from a 50 mm $\times$ 50 mm image plane, then the optical path to the most distant pixels will at most be a few percentages longer relative to the center pixel. For the characterization, each emitter was placed in front of the Schottky diode at a distance z and oriented such that the THz electrical field is vertically polarized (E-plane parallel to the x axis). First, we tested

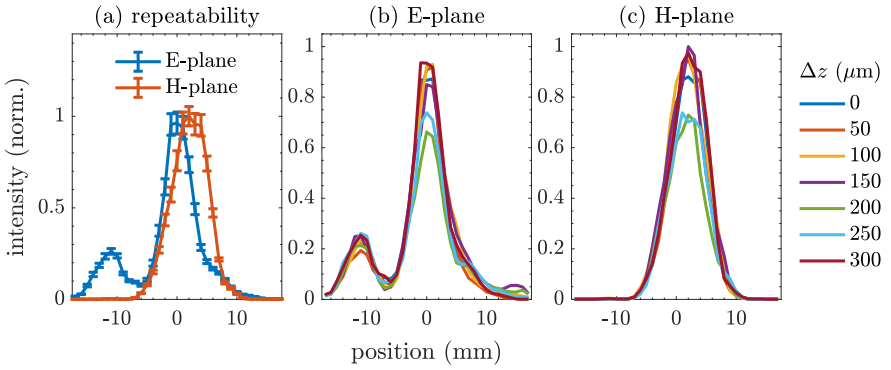

Fig. 2.15: Measurement repeatability test at $\nu = 0.5$ THz using the TC190201 antenna (a), and test of the influence of standing waves in the setup (b)-(c).

the measurement repeatability of our setup. Ten successive measurements where made of a single antenna at $z = 145$ mm, and the resulting means and standard deviations of the E- and H- plane, respectively, are shown in 2.15(a). Generally, the repeatability is good with the largest variance around the main peak. Furthermore, the overall beam profile in both the E- and H-plane are in good agreement with the results published in the recent studies

[175, 176]. Standing waves can arise between the emitter and the receiver and affect the measurements when dealing with CW THz radiation and is, thus, important to consider. The influence of standing waves was tested by scanning the distance to the detector over a 300 μm interval in steps of 50 μm between consecutive beam profile measurements at 0.5 THz. Thus, the interval corresponds to $\lambda/2$. The results for the E- and H-plane are shown in Fig. 2.15(b) and (c), respectively. There do seem to be a decrease in the peak value for $\Delta z = 200$ and 250 μm, which could be due to standing waves when the receiver is exactly in front of the emitter.

Subsequently, the radiation patterns were mapped out for a 35 mm $\times$ 35 mm area in 1 mm increments for 0.2 THz to 1.5 THz at a distance $z = 90$ mm. The resulting radiation patterns of the four emitters are shown in Fig. 2.16. The color scale of the maps has been normalized to that of the TC190201 antenna at the given frequency. At first sight, the beam diameter decrease from 0.2 THz reaching a minimum around 0.6$\sim$0.9 THz whereupon it increases up to 1.5 THz. Additionally, the beam patterns generally show irregularities at 0.4$\sim$0.5 THz and 1$\sim$1.2 THz. At higher frequencies, the patterns are mainly blurred due to the lower signal-to-noise ratio and the 1 mm step size. The asymmetric E-plane and H-plane beam profiles have previously been attributed by Nellen *et al.* [175] to the asymmetric feed point structure as seen in Fig. 2.13. In particular, the dimensions of the bracket structure equals $\lambda/4$ at 0.35 THz and, further, the extended bowtie was argued to act as a broad dipole producing frequency-dependent side lobes. However, a closer look at the beam patterns at 0.5-1 THz reveals weaker rings surrounding the main peaks. In Fig. 2.17, the dynamic range has been calculated to emphasize the pattern for each antenna at 0.7 THz. In all cases, an Airy-like pattern, *i.e.* a bright central spot (Airy disk) with concentric bright rings due to circular aperture diffraction, is seen. Notably, the Airy disk is approx. the same size for all antennas. Similarly, the dynamic range maps of the TC190201 antenna from 0.2 to 0.8 THz are shown in Fig. 2.18. Here, we can notice that the diameter of the central spot as well as the diameter of the concentric rings both decrease as the frequency increase. A possible explanation could be that the THz waves are diffracted by the circular aperture of the hyper-hemispherical Si lens.

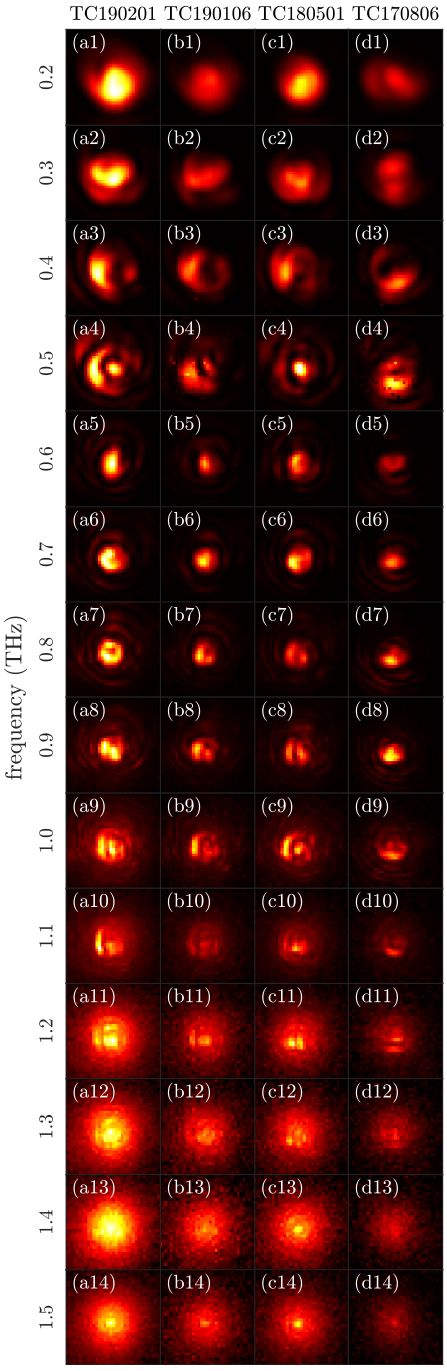

Fig. 2.16: The radiation pattern of the (a) TC190201, (b) TC190106, (c) TC180501 and (d) TC170806 antennas at frequencies from 0.2 to 1.5 THz. Each map covers 35 mm $\times$ 35 mm in 1 mm increments and is measured at $z = 90$ mm in front of the antennas.

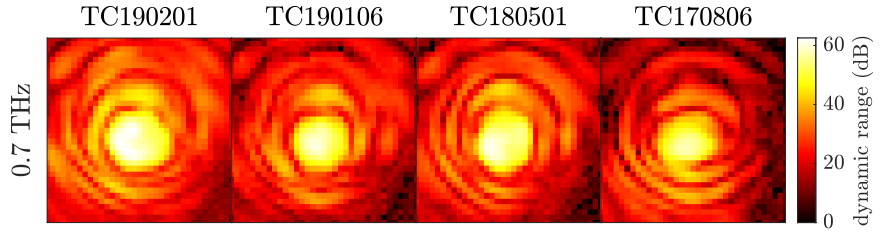

Fig. 2.17: Dynamic range of the antenna patterns (34 mm × 34 mm in 1 mm increments) at ν =0.7 THz, measured at $z = 90$ mm.

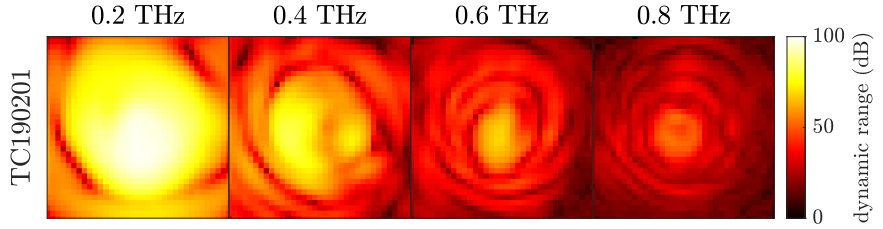

Fig. 2.18: Dynamic range of the TC190201 antenna patterns (34 mm × 34 mm in 1 mm increments) at frequencies $\nu = 0.2$, 0.4, 0.6 and 0.8 THz, measured at $z = 90$ mm.

The minima of an Airy pattern far from the aperture occur at the angle

$$\sin\theta \approx m\frac{\lambda}{d} \tag{2.10}$$

measured from the direction of the incoming light, where d is the diameter of the aperture and $m = 1.220, 2.233, 3.238$ gives the first three minima [177]. The diameter of the Airy disk should, hence, be inversely proportional to the frequency $\nu = c/\lambda$. Therefore, we plot the diameter of the central spot versus frequency in Fig. 2.19. The values for each antenna have been normalized to the value at 0.2 THz. Evidently, the central spot diameter follows a clear ν^{-1} trend for all antennas, which indicates that the THz beam indeed is diffracted by a circular aperture. The aperture diameter d can be estimated from the minima in the Airy pattern. The left hand side of Eq. (2.10) is $\sin\theta = r/\sqrt{z^2 + r^2} \approx r/z$, where r is the radius from the center of the Airy disk. If the two first consecutive minima are separated by $\Delta r = r_2 - r_1$, we have

$$d \approx (m_2 - m_1)\frac{cz}{\nu\Delta r} = 1.013\frac{cz}{\nu\Delta r} \tag{2.11}$$

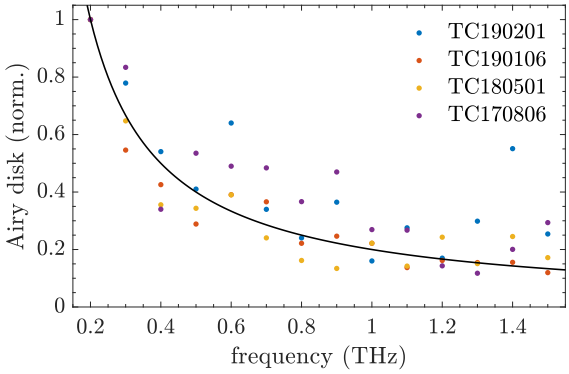

Fig. 2.19: Estimated Airy disk diameter as a function of frequency of the four THz emitters normalized to the value at 0.2 THz. The black curve is the theoretical ν^{-1} dependency of the Airy disk.

for $r \ll z$. Fig. 2.20 shows the beam profile in the E-plane of the TC180501

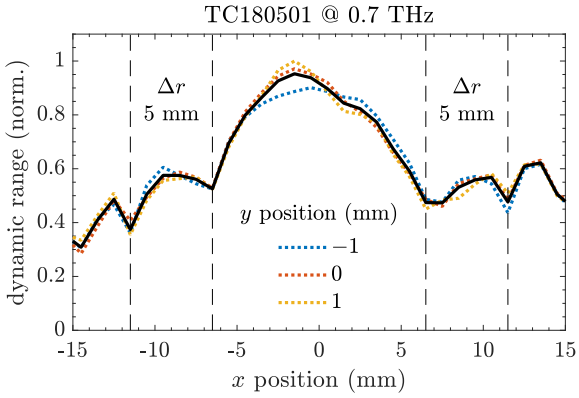

Fig. 2.20: The E-plane beam profile of the TC180501 antenna measured at 0.7 THz for the three center pixel rows corresponding to $y = -1, 0, 1$ mm (dotted lines) together with the average (black).

antenna measured at 0.7 THz. The black curve is the average of the three center pixel rows corresponding to $y = -1, 0, 1$ mm (dotted lines). First and second minima occurs at approx. ± 6.5 mm and ± 11.5 mm resulting in $\Delta r = 5$ mm. Inserting these numbers in Eq. (2.11), we get $d \approx 8$ mm. This crude estimate is, *e.g.* , limited by the 1-mm step size and, thus, only serves to give an order of magnitude of the aperture. The aperture diameter is approx. equal to that of the 10-mm Si lens. Therefore, it seems obvious that the radiated THz waves are diffracted by the overall device aperture leading to

an Airy pattern, which can be interpreted as side lobes when examined only in the E- and H-plane.

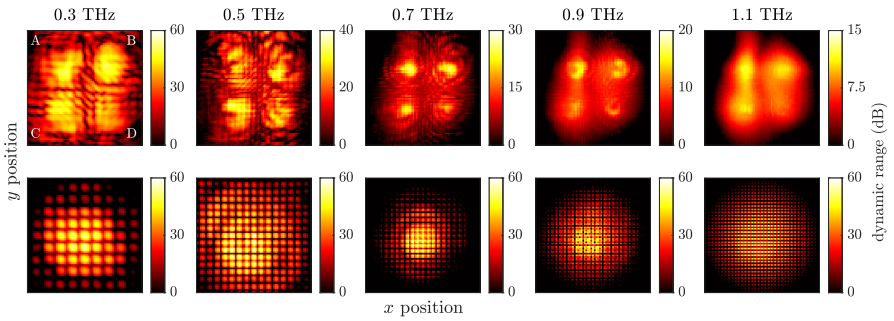

Fig. 2.21: The top row shows the recorded beam patterns in dB of the 2×2 array at different frequencies from 0.3 to 1.1 THz measured at $z = 90$ mm over an area of 75 mm × 75 mm. A, B, C, D refers to the TC190601, TC190201, TC170806, and TC180501 antennas, respectively. The second row displays the calculated beam pattern using array theory and the mean radiation pattern of the four emitters at a given frequency.

Next, the four emitters were arranged side by side in a 2×2 array. The photomixer devices are 25 mm in diameter and, hence, the distance between two adjacent antennas is approx. $d = 25$ mm (center-to-center). The array beam pattern was mapped in a 75 mm by 75 mm area at $z = 90$ mm for various frequencies. The resulting images are shown in the top row of Fig. 2.21. For comparison, the bottom row of Fig. 2.21 shows the predicted beam patterns using Eq. (2.4). Here, $\vec{E}_0(\vec{r})$ has been taken as the normalized mean of the individual antenna patterns and interpolated to a higher resolution, while the array factor has been weighted by the maximum value of the radiation pattern of each antenna. Interference is clearly present in the measured beam patterns showing a decreasing fringe spacing with increasing frequency. At 1.1 THz the fringes are washed out due to limited spacial resolution of 1 mm. The main resemblance between the measured and the predicted patterns is the checkered pattern due to destructive interference. Unexpectedly, the individual emitters TC190601, TC190201, TC170806 and TC180501 are easily distinguished in the four quadrants A-D, respectively. Thus, the expected array gain of 4^2 is absent in the measurements. A reason may be the quite different radiation patterns of the array elements. Nevertheless, both the measured and calculated beam patterns are rather inconvenient for stand-off spectroscopy because of their inhomogeneity. Besides the complex individual radiation patterns, this is also caused by the large array spacing $d \gg \lambda$, which results in grating lobes.

Instead, we turned our attention to focal plane arrays similar to the emitter arrays investigated by Bauerschmidt *et al.* [150–152]. The transmitting and receiving photomixers were each equipped with a custom made double con-

Fig. 2.22: Picture of the multiple-antenna setup and the perfectly reflecting sample (gold mirror) located 10 m away.

vex lens of ultra-high-molecular-weight polyethylene (UHMWPE) and configured in two 1×4 arrays, respectively, with $d = 12.5$ cm element spacing as seen in Fig. 2.22. The lenses had a focal length of $f = 100$ mm and where adjusted to focus the diverging THz beams at a distance $z = 10$ m in front of the setup. The optical axes of the array elements were coincided at an angle θ in the target point at $\vec{r} = \vec{\rho}$. To achieve constructive interference in the said point independent of the THz frequency, the emitters were displaced by Δs_m along their optical axis relative to the first emitter ($\Delta s_1 = 0$) to account for any differences in the THz paths modulo 2π. In fact, the relative phase should be chosen as $\vec{k} \cdot (\vec{\rho} - \vec{r}_m)$ corresponding to the differences in the THz path of the beams. However, since the optical fiber pigtails of the antennas vary, further corrections could be necessary. The resulting beam pattern at 0.9 THz normalized to the mean of the peak intensities of the individual emitters is seen in Fig. 2.23. We see an excellent inference pattern with vertical fringes due to the linear array configuration with a strong zero-order interference peak at $x = 0$ mm. Furthermore, the peak intensity is increased by a factor of 10 compared to the expected array gain of 4^2. The explanation of this difference is mainly to be found in the very different performance of the emitters. The peak intensity of the TC190201, TC170806, and TC180501 antennas measured only 68%, 16% and 10%, respectively, relative to the TC190601 antenna. Next, to test the effect of the receiver array, we put a reflecting sample (a 4" Si wafer with a 100-nm gold layer on top) in the target plane at $z = 10$ m. The optical axes of the receivers were aligned in pair with the ones of the corresponding transmitting elements, *viz.* RC190307 and TC170806; RC180402 and TC190201; RC190102 and TC190106; RC180501 and TC180501. As explained in Sec. 3, the received signals must be weighted to align their phases for coherent summation. This was achieved by scanning the phase of THz signals at a given frequency using the fiber stretcher. The

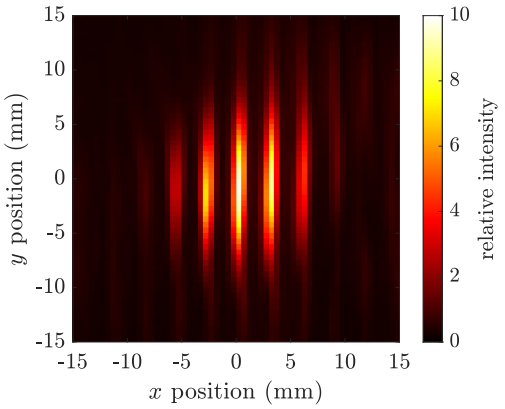

Fig. 2.23: Beam pattern of the 4×1 array in the target plane at $z = 10$ m. The THz intensity has been normalized to the mean peak intensity of the array elements.

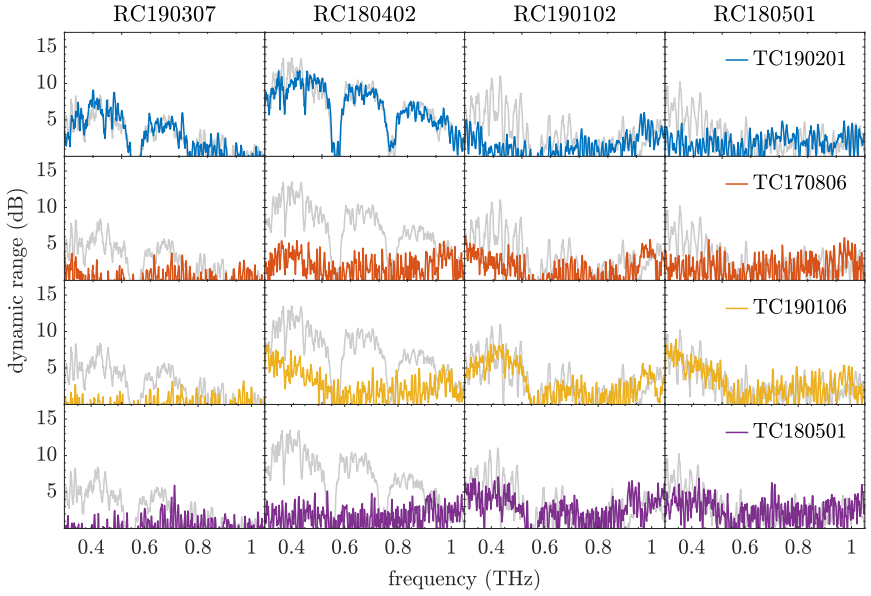

Fig. 2.24: Spectra of the individual emitters TCxxxxxx as recorded by the elements RCxxxxxx of the 4×1 receiver array. The gray continuous line is the measured spectra of the full emitter array.

maximum value of the phase scan was subtracted for each receiver and saved for the given measured frequency. In turn, the frequency was changed and the procedure was repeated until the desired spectrum was obtained. First, spectra were acquired for each of the individual elements of the transmitting

array, and then of the full transmitting array. Fig. 2.24 shows the resulting spectra received by the 4×1 array. The spectrum of the total transmitting array measured by each receiver is given in each plot (gray continuous line) for comparison. A moving average with a window size of 5 data points has been applied to each spectrum for clarity. The superior performance of the TC190201 emitter is clearly evident followed by TC190106. In particular, the TC190201/RC180402 pair retains a fairly good dynamic range considering the very long THz path of 20 m. The two absorption bands centered at roughly 0.55 THz and 0.75 THz are due to atmospheric water vapor. In contrast, the emitted THz signals of TC180501 and TC170806 are barely detected by the array. For both of the TC19xxxx antennas, the emitted signal is picked up by more than one element of the 4×1 receiver array. An explanation could be the rather complex and different radiation patterns of the emitters. However, the THz path from the emitter to the receiver array was greater than 20 m. Hence, one would expect only the strongest part of the radiation pattern to survive. Nonetheless, the beam sizes could be very different at the receiver array. Another possible explanation could be that the focal points of the individual elements, both emitters and receivers, were not exactly in target plane. However, the lenses were adjusted to give the largest possible signal. Let us notice the signal received at the RC180402 and RC190307 antennas are dominated by the TC190201 signal. Furthermore, there is no significant increase in the received signal when the full emitter array is employed compared to just the TC190201 antenna. A similar conclusion can be drawn for the RC190102, RC180501 and TC190106 antennas. In fact, the spectra recorded by the RC190102 and RC180501 antennas show oscillations that were only present when the full emitter array was operated. This indicates that the use of the emitter array could lead to undesired destructive inference at the receivers!

Hypothesis II claimed that an array of receivers will increase the detection sensitivity by the number of array elements squared. As we saw in Sec. 3, this is true in terms of power if the phases of the received signals can be coherently added. However, a CW THz spectrometer based on phase sensitive detection by employing secondary photomixers as receivers measures in fact the incoming electric field and not the power. Therefore, we should only expect the received signal to increase by a factor of M (number of array elements). Various strategies can be applied when the coherent output signals of the receivers are to be added. Some common schemes developed for wireless communication [178] are equal gain combining (EGC), maximum ratio combining (MRC) and selection combining (SC). The former EGC is merely a coherent summation of the signals. When we account for the number of receiver elements, it is simply the mean of the signals. Effectively, MRC is the weighted mean of the signals, where the each signal is weighted according to its SNR. Thus, MRC is more advanced and requires knowledge about the

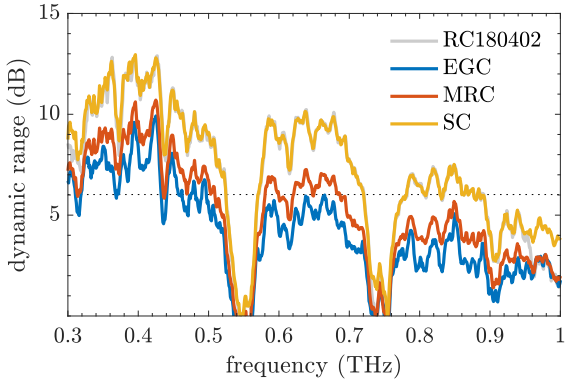

Fig. 2.25: Coherent combining schemes of the measured signals of the full emitter array at the four elements in the receiver array. The gray continuous line is the spectrum recorded by the RC180402 receiver for comparison. The dotted line indicates a SNR of 2.

SNR at each receiver prior to the summation. Here, the weights are chosen as the mean SNR over the given spectrum and normalized to 1. Lastly, in SC the receiving system switches to the receiver element, which receives the strongest signal, and the remaining $M-1$ elements are ignored. In our case, we choose the highest value of the dynamic range among the received signals at a given frequency. The results of the different approaches are seen in Fig. 2.25 together with the spectrum recorded by the RC180402 antenna (gray) using the full emitter array. The dotted line indicates a SNR of 2. Generally, we see a slight improvement of $\sim$1 dB using MRC versus EGC, whereas SC gains several dB compared to both. Further, we notice that the SC spectrum is more or less identical to single spectrum recorded by the RC180402 antenna due to the superior performance of the TC190201 emitter. In conclusion, we see no significant improvement in the dynamic range due to the receiver array, even though, we expected a $10\log(4) \approx 6$ dB improvement. This we mainly attribute to the large variation in the performance of the emitters.

4 Machine Learning

Machine learning (ML) is a field within artificial intelligence which can be employed for classification by the patterns exhibited by the data. A few important technical terms [179, 180] are needed when discussing ML algorithms (MLAs). First, the ML task is a *classification* problem, if it is to assign each input of the MLA to one of several discrete categories. This is in contrast to *regression*, where the output is one or several continuous variables. Second, the term *class* refers to the categories that the THz spectra can be divided into

(or classified to belong to) based on their spectroscopic characteristics. This could be the sample material or even the (discrete) concentration of a certain material in a given sample. Third, the data points in each class can be further specified using *labels*. For example, if the THz spectra are divided into different material classes, but within each class the spectra are measured at various (discrete) relative humidity (RH) percentages, then each spectrum of a certain material can be labeled according to the RH, and vice versa. Thus, labels allow us to differentiate the THz spectra. However, if there are no particular differences between the spectra within each class, the labels within each class are simply the same. Furthermore, in classification tasks, the model will map each input onto a class label. Finally, the term *feature* refers to an individual measurable property (*i.e.* a variable) of the observed phenomenon. In the task of classifying THz spectra, features are equivalent to the discrete frequency components constituting the spectra.

Generally, MLAs are said to be supervised or unsupervised if data class labels are included or not in the training of the algorithm. In particular, unsupervised MLAs analyze and cluster unlabeled datasets according to hidden patterns in the data, whereas supervised MLAs can be utilized to predict the class label of the input data. Further, MLAs can be utilized to reduce the number of features, while preserving relevant information, which can facilitate the classification task. Since THz spectra are multivariate data consisting of 100's or 1000's discrete frequencies, this is a very pertinent capacity. Additionally, THz reflection spectra depend on the refractive index of the sample and, hence, exhibit weak and broad absorption signatures compared to transmission spectra. Therefore, it can be very difficult for the programmer to define a model as is required in traditional knowledge-based algorithms. On the other hand, MLAs are data driven, and a given MLA develop and build the model of the system itself through data supplied in the training phase.

Researchers realized early on that MLAs would be beneficial for identification and classification of substances using THz spectroscopy. For example, Watanabe *et al.* [181] applied principal component analysis (PCA) to multispectral THz images to separate and obtain the spatial patterns of individual chemical components in a two-component sample, and further estimate their respective concentrations. Kawase *et al.* [123] then utilized this technique to demonstrate non-destructive inspection of illicit methamphetamine and MDMA hidden in mail envelopes. Soon after, Kemp's group picked up the technique and reported on detection and identification of RDX via THz-TDS imaging in reflection mode [37]. Furthermore, they investigated how PCA can be used to reduce the spectral dimensionality of multispectral THz images [36]. Since then several groups have implemented rather complex MLAs for classification of THz spectra including Bayesian models [182, 183], artificial neural networks [56, 184, 185], support vector machines [186–188],

and random forests [182, 184, 187]. Most recently, Park *et al.* [189] have reviewed the use of MLAs for THz-TDS and THz imaging, underpinning the importance of ML in THz applications.

4.1 Dimensionality Reduction

Dimensionality reduction methods (DRMs) are employed to lower the computational requirements of the MLAs and increase the learning speed. This is done by reducing the dimensionality of multivariate data while preserving most of the contained information. Further, DRMs help cluster data, which in turn allow for better classification results. The reduced dimensionality of the data also facilitate visualization that can support data interpretation. Hence, DRMs often serve as a preprocessing step prior to classification. Generally speaking, we can categorize DRMs in two branches, *viz.* feature selection and feature extraction. Feature extraction algorithms construct new

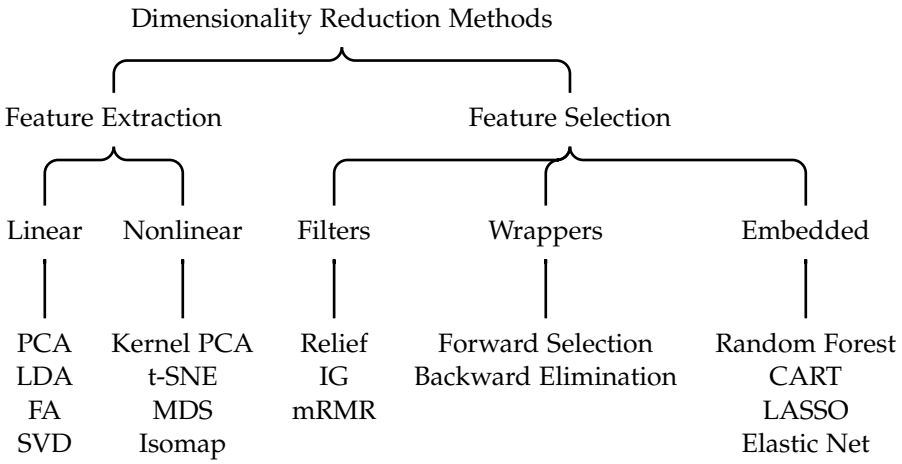

Fig. 2.26: Diagram of common dimensionality reduction methods.

features that are combinations of the original variables to form a lower dimensional space. These algorithms can either be linear or nonlinear and includes methods such as principal component analysis (PCA), linear discriminant analysis (LDA), factor analysis (FA), single value decomposition (SVD), t-distributed stochastic neighbor embedding (t-SNE), and multidimensional scaling (MDS). On the other hand, feature selection algorithms select a subset of the original variables that hold the most information of relevance and discard the remaining ones. These algorithms include filters such as the Relief algorithm, Information Gain (IG), and minimum redundancy maximum rel-

evance (mRMR) as well as wrappers using Forward Selection and Backward Elimination, which evaluate the relevance of a given variable using a preselected ML model. Finally, embedded ML as for example Random Forest, Classification And Regression Tree (CART), Least Absolute Shrinkage and Selection Operator (LASSO), and Elastic Net incorporate feature selection to the learning process. An overview of some common DRMs is given in Fig. 2.26. In this work, we restrict ourselves to two linear feature extraction methods, *viz.* PCA and LDA.

In the following, we will let X be our data matrix of size $N \times M$ such that each row n represents a THz spectrum S_n (observation), and each column m a discrete frequency component ν_m (variable), *i.e.*

$$X = \begin{bmatrix} S_1(\nu_1) & S_1(\nu_2) & \cdots & S_1(\nu_M) \\ S_2(\nu_1) & S_n(\nu_m) & \cdots & S_2(\nu_M) \\ \vdots & \vdots & \ddots & \vdots \\ S_N(\nu_1) & S_N(\nu_2) & \cdots & S_N(\nu_M) \end{bmatrix} \tag{2.12}$$

Principal Component Analysis projects the data onto a lower-dimensional space with the aim of maximizing the variance of the full data set disregarding any class information. Hence, it is a unsupervised technique, which focuses on revealing hidden patterns in the data. First, we assume that the variables $\vec{x}_m$ (columns of the data matrix X) have been standardized, *i.e.* each column has zero mean and unit variance.[190] We can construct a linear combination $\vec{y}$ of the individual variables, *i.e.*

$$\vec{y} = \sum_{m=1}^{M} w_m \vec{x}_m = X\vec{w}, \tag{2.13}$$

where $\vec{w}$ is a vector of constants $w_1, \ldots, w_M$. The PCA algorithm searches for the optimal weights $\vec{w}$ that maximizes the variance $\mathrm{var}(\vec{y})$, *i.e.*

$$\underset{\|\vec{w}\|=1}{\arg\max} \left\{ \mathrm{var}(\vec{y}) \right\}. \tag{2.14}$$

The constraint $\|\vec{w}\| = \vec{w}^{\mathsf{T}}\vec{w} = 1$ secures that the weights are normalized. Otherwise, the variance could attain an arbitrary large value for an optimal $\vec{w}$. The variance is calculated in the usual way:

$$\mathrm{var}(\vec{y}) = \frac{1}{N-1} \sum_{n=1}^{N} (y_n - \bar{y})^2 = \frac{\vec{y}^{\mathsf{T}}\vec{y}}{N-1}. \tag{2.15}$$

Here, it is implied that the data matrix X and, hence, all linear combinations $\vec{y}$ are mean-centered ($\bar{y} = 0$). T denotes transpose. The optimization task can

then be restated by combining Eqs. (2.13) - (2.15) as

$$\underset{\|\vec{w}\|=1}{\arg\max} \left\{ \vec{w}^{\mathsf{T}} \Sigma \vec{w} \right\} \tag{2.16}$$

using the covariance matrix $\Sigma = X^{\mathsf{T}} X/(N-1)$. The arg max denotes that we seek arguments or inputs, which maximize the function output. This is a standard problem in linear algebra solved by eigendecomposition [191, 192], but let us for the sake of clarity treat it in brief: (i) Form the Lagrangian function

$$\mathcal{L}(\vec{w}, \lambda) = \vec{w}^{\mathsf{T}} \Sigma \vec{w} - \lambda \left(\vec{w}^{\mathsf{T}} \vec{w} - 1 \right) \tag{2.17}$$

with Lagrange multiplier λ. (ii) Find its stationary points, *i.e.* its partial derivatives should be zero. This leads to

$$\Sigma \vec{w} - \lambda \vec{w} = 0 \quad \text{and} \quad \vec{w}^{\mathsf{T}} \vec{w} - 1 = 0. \tag{2.18}$$

The former is a eigenvalue problem, while the latter the imposed constraint. Since Σ is a $M \times M$ real symmetric matrix, it follows that exactly M real eigenvalues λ_m and corresponding orthogonal eigenvectors $\vec{v}_m$ exist.[192] The associated linear combinations $\vec{y}_m = X\vec{v}_m$ are the so-called *principal components* (PCs) of the data, whereas the elements of $\vec{y}_m$ and of $\vec{v}_m$ are respectively referred to as the PC *scores* and the PC *loadings*. In fact, the eigenvalues equal the variances of the principal components $\vec{y}_m$:

$$\mathrm{var}(\vec{y}_m) = \mathrm{var}(X\vec{v}_m) = \vec{v}_m^{\mathsf{T}} \Sigma \vec{v}_m = \lambda_m \vec{v}_m^{\mathsf{T}} \vec{v}_m = \lambda_m. \tag{2.19}$$

Furthermore, we see that any two PCs $\vec{y}_m$ and $\vec{y}_{m'}$ are uncorrelated:

$$\mathrm{cov}(\vec{y}_m, \vec{y}_{m'}) = \vec{v}_m^{\mathsf{T}} \Sigma \vec{v}_{m'} = \lambda_{m'} \vec{v}_m^{\mathsf{T}} \vec{v}_{m'} = 0, \tag{2.20}$$

where the last equality is due to the orthogonality of the eigenvectors. Thus, each PC explains an independent (uncorrelated) portion of the total variance. Now, let us assume that the eigenvectors are sorted in descending order of the eigenvalues such that $\vec{v}_1$ corresponds to the largest eigenvalue λ_1. Then $\vec{v}_1$ is the optimal solution resulting in a PC $\vec{y}_1$ with maximal variance λ_1. Equivalently, the successive eigenvectors represent the next orthogonal PCs along which the maximal proportion of the remaining variance in the data is captured, respectively. The overall variance can, hence, either be calculated as the sum of the variances of the original variables, *i.e.* the trace of the covariance matrix, or by summing the full range of eigenvalues. The quality of each PC can therefore be quantified by the amount of total variance it explains, *i.e.*

$$\frac{\lambda_m}{\sum_{m=1}^{M} \lambda_m}. \tag{2.21}$$

Finally, the dimensionality of the data set can be reduced by retaining only the most significant PCs, which account for most of the variance in the data. It can be useful to calculate the *captured variance*, *i.e.* the cumulative variance along each new feature normalized to the total variance, equivalent to the *proportion of explained variance* to aid the decision of how many PCs that should be kept.

Linear Discriminant Analysis is another common method for transforming data into a lower-dimensional space. In contrast to PCA, it is a supervised method meaning that class information is included to formulate the transformation constraints. In terms of THz spectroscopy, a class can be a different material or *e.g.* different concentrations of a material in a given sample. The naive idea of LDA is to utilize the extra information in the transformation to increase the separation of the class means and reduce the spread within each class. Thus, the optimization problem is to maximize the inter-class distances while minimizing the intra-class distances in the projection space. Let $\vec{s}_i$ represent the ith row of the data matrix X (the ith observation). The class information is included to label each observation $\vec{s}_i$ such that the data matrix X can be partitioned into c classes K_j of n_j observation:

$$X = \begin{bmatrix} K_1 \\ \vdots \\ K_c \end{bmatrix} \quad \text{with} \quad K_1 = \begin{bmatrix} \vec{s}_1 \\ \vdots \\ \vec{s}_{n_1} \end{bmatrix}, K_2 = \begin{bmatrix} \vec{s}_{n_1+1} \\ \vdots \\ \vec{s}_{n_2} \end{bmatrix}, \textit{etc.} \tag{2.22}$$

Further, we will denote the projections $\vec{y}_i = \vec{w}^\mathsf{T}\vec{s}_i$. Then, the separation of the different classes in the projection space can be quantified by the between-class scatter

$$\sum_{j=1}^{c} n_j(\vec{m}_j - \vec{m})^2, \tag{2.23}$$

where

$$\vec{m}_j = \frac{1}{n_j}\sum_{\vec{s}_i \in K_j} \vec{y}_i = \vec{w}^\mathsf{T}\vec{\mu}_j \quad \text{with} \quad \vec{\mu}_j = \frac{1}{n_j}\sum_{\vec{s}_i \in K_j} \vec{s}_i \tag{2.24}$$

is the jth class centroid in the projection space and

$$\vec{m} = \frac{1}{N}\sum_{j=1}^{c} n_j\vec{m}_j = \vec{w}^\mathsf{T}\vec{\mu} \quad \text{with} \quad N = \sum_{j=1}^{c} n_j \tag{2.25}$$

is the weighted mean of the projected centroids. $\vec{\mu}_j$ and $\vec{\mu}$ are the corresponding jth class and global centroids, respectively, in the original space. The

expressions in Eqs. (2.24)-(2.25) simplifies the between-class scatter as

$$\begin{aligned}\sum_{j=1}^{c} n_j(\vec{m}_j - \vec{m})^2 &= \sum_{j=1}^{c} n_j \left(\vec{w}^{\mathsf{T}}\vec{\mu}_j - \vec{w}^{\mathsf{T}}\vec{\mu}\right)\left(\vec{w}^{\mathsf{T}}\vec{\mu}_j - \vec{w}^{\mathsf{T}}\vec{\mu}\right)^{\mathsf{T}} \\ &= \sum_{j=1}^{c} n_j\, \vec{w}^{\mathsf{T}}\left(\vec{\mu}_j - \vec{\mu}\right)\left(\vec{\mu}_j - \vec{\mu}\right)^{\mathsf{T}}\vec{w} \\ &= \vec{w}^{\mathsf{T}} S_{\mathrm{B}} \vec{w}, \end{aligned} \tag{2.26}$$

where the between-class scatter matrix

$$S_{\mathrm{B}} = \sum_{j=1}^{c} n_j(\vec{\mu}_j - \vec{\mu})(\vec{\mu}_j - \vec{\mu})^{\mathsf{T}} \tag{2.27}$$

is calculated in the original space. Similarly, the spread of each projected class j can be quantified by the within-class scatter

$$\begin{aligned}\sigma_j &= \sum_{\vec{s}_i \in K_j} (\vec{y}_i - \vec{m}_j)^2 \\ &= \sum_{\vec{s}_i \in K_j} \left(\vec{w}^{\mathsf{T}}\vec{s}_i - \vec{w}^{\mathsf{T}}\vec{\mu}_j\right)\left(\vec{w}^{\mathsf{T}}\vec{s}_i - \vec{w}^{\mathsf{T}}\vec{\mu}_j\right)^{\mathsf{T}} \\ &= \vec{w}^{\mathsf{T}} S_j \vec{w}. \end{aligned} \tag{2.28}$$

Here the within-class scatter matrix of the jth class is given by

$$S_j = \sum_{\vec{s}_i \in K_j} (\vec{s}_i - \vec{\mu}_j)(\vec{s}_i - \vec{\mu}_j)^{\mathsf{T}} \tag{2.29}$$

The total within-class scatter of the projected classes is hence

$$\sum_{j=1}^{c} \sigma_j = \sum_{j=1}^{c} \vec{w}^{\mathsf{T}} S_j \vec{w} = \vec{w}^{\mathsf{T}} S_{\mathrm{W}} \vec{w} \tag{2.30}$$

with the total within-class scatter matrix

$$S_{\mathrm{W}} = \sum_{j=1}^{c} S_j \tag{2.31}$$

The task of LDA to maximize the distance between the projected class means and minimize the within-class variance is therefore equivalent to maximizing the ratio

$$\arg\max_{\vec{w}} \left\{ \frac{\vec{w}^{\mathsf{T}} S_{\mathrm{B}} \vec{w}}{\vec{w}^{\mathsf{T}} S_{\mathrm{W}} \vec{w}} \right\}. \tag{2.32}$$

This optimization problem is not bound, so we require the weights $\vec{w}$ to be of unit length, and since we are only concerned with directions, we introduce the constraint $\vec{w}^{\mathsf{T}} S_{\mathrm{W}} \vec{w} = 1$. Thus, we need to solve

$$\underset{\vec{w}^{\mathsf{T}} S_{\mathrm{W}} \vec{w}=1}{\arg\max} \left\{ \vec{w}^{\mathsf{T}} S_{\mathrm{B}} \vec{w} \right\}. \tag{2.33}$$

Using the same approach as for PCA, we define the Lagrangian function

$$\mathcal{L}(\vec{w}, \lambda) = \vec{w}^{\mathsf{T}} S_{\mathrm{B}} \vec{w} - \lambda \left(\vec{w}^{\mathsf{T}} S_{\mathrm{W}} \vec{w} - 1 \right) \tag{2.34}$$

and examine its stationary points

$$S_{\mathrm{B}} \vec{w} - \lambda S_{\mathrm{W}} \vec{w} = 0. \tag{2.35}$$

This is a generalized eigenvalue problem

$$S_{\mathrm{B}} \vec{w} = \lambda S_{\mathrm{W}} \vec{w}. \tag{2.36}$$

Given S_{W} is not singular, it is equivalent to

$$S_{\mathrm{W}}^{-1} S_{\mathrm{B}} \vec{w} = \lambda \vec{w} \tag{2.37}$$

Again, the optimal solution is the eigenvector $\vec{v}_1$ associated with the largest eigenvalue λ_1. However, at most $c-1$ eigenvectors exist because $\operatorname{rank}(S_{\mathrm{B}}) \leq c-1$ due to the fact that its columns are linearly dependent. Furthermore, $S_{\mathrm{W}}^{-1} S_{\mathrm{B}}$ is not necessarily symmetric, thus, the eigenvectors are not generally orthogonal. Consequently, the dimensionality of the original data matrix X is reduced to $k \leq c-1$ features by projecting it onto the eigenvectors. The projections $\vec{y}_k = X\vec{v}_k$ are the *linear discriminants* (LDs) comparable to the PCs of PCA. As mentioned above, it can be useful to calculate the captured variance. However, for LDA this quantity is not equivalent to the proportion of explained variance, since the eigenvalues are related to the between-class and within-class variance, and hence, reflect the robustness and the ability to discriminate between different classes. Lastly, we assumed that S_{W} is non-singular, which is often not true. A common simple solution is to regularize S_{W} by

$$S'_{\mathrm{W}} = S_{\mathrm{W}} + \beta I \tag{2.38}$$

with regularization parameter β and identity matrix I. Then by eigendecomposition, we have

$$S'_{\mathrm{W}} = Q \Lambda Q^{\mathsf{T}} + \beta I = Q(\Lambda + \beta I) Q^{\mathsf{T}}. \tag{2.39}$$

Here Q is the square matrix containing the eigenvectors and Λ the diagonal matrix of the eigenvalues.

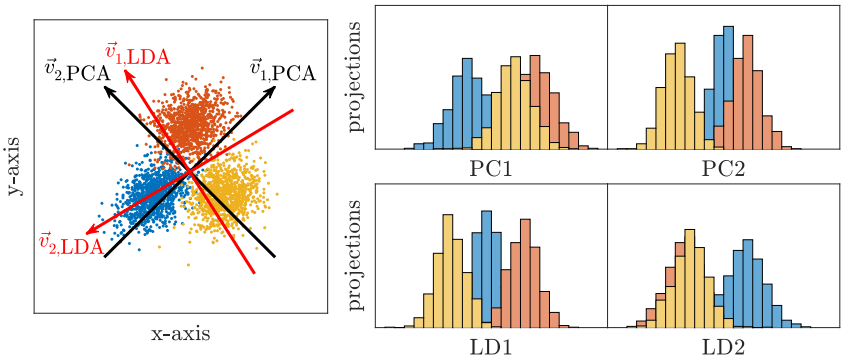

Fig. 2.27: Comparison of PCA and LDA performed on the same dummy data set of two variables and three classes.

To illustrate the difference of PCA and LDA, the two methods have been applied to a dummy data set of two variables containing three classes in Fig. 2.27 (left). Two eigenvectors of both algorithms are plotted together with the data points. The projections of the data onto the respective eigenvectors are plotted in Fig. 2.27 (right). As expected, the principal components PC1 and PC2 show a larger variance in the data compared to the discriminant components LD1 and LD2, while the latter exhibit the best separability.

4.2 Classification

As mentioned above, a trained ML classification algorithm predicts the class of some input data, *i.e.* it maps the input onto a set of predefined labels. Here, we will employ three different classification algorithms; one based on probabilities, one based on geometrical distance, and one based on hyperplanes.

The Bayes Classifier calculates the posterior probability

$$p(C_j|\vec{s}) = \frac{p(\vec{s}|C_j)p(C_j)}{p(\vec{s})} \tag{2.40}$$

of an observation $\vec{s}$ to belong to the ith class C_j.[180] Here, $p(C_j)$ is the prior probability that the observation belongs to the jth class, $p(\vec{s}|C_j)$ the likelihood of an observation $\vec{s}$ given class j, and

$$p(\vec{s}) = \sum_{j=1}^{c} p(\vec{s}|C_j)p(C_j) \tag{2.41}$$

the marginal probability of $\vec{s}$. The prior probability and the likelihood are estimated in the training phase of the algorithm. In this work, we assumed a

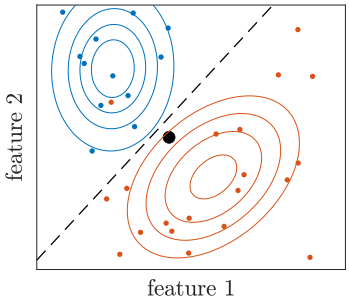

Fig. 2.28: Illustration of the Bayes classifier. The contour lines indicate the posterior class, while the dashed black line is the decision boundary.

multivariate Gaussian distribution for the class likelihood function

$$p(\vec{s}|C_j) = \frac{1}{\sqrt{(2\pi)^M \det(\Sigma_j)}} \exp\left[-\frac{1}{2}(\vec{s}-\vec{\mu}_j)^{\mathsf{T}}\Sigma_j^{-1}(\vec{s}-\vec{\mu}_j)\right] \tag{2.42}$$

with M being the number of features or variables and $\det(\Sigma_j)$ is the determinant of Σ_j. This was chosen because the estimate of the likelihood then boiled down to the calculation of the mean vector $\vec{\mu}_j$ and the covariance matrix Σ_j for each class. Subsequently, an observation is mapped to the class resulting in the highest posterior probability. An example of the Bayes classifier applied to a data set of two classes (blue and red dots) represented in a two-dimensional (2D) feature space is given in Fig. 2.28. The contour lines illustrate the posterior probability for each class, while the dashed line indicate the decision boundary, *i.e.* where the two probabilities are equal. Hence, the new input data point (black dot) is classified as "red".

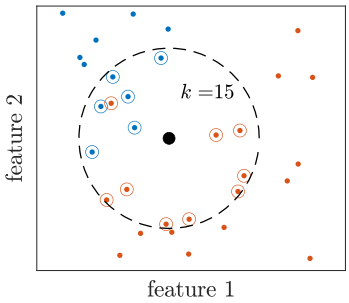

Fig. 2.29: Illustration of the k-NN classifier. The circled points are the k nearest neighbors to the new observation (black dot). The dashed line is the decision boundary.

The *k* Nearest Neighbors (*k*-NN) is a simple classification algorithm, which stores all the training data and has as such no training phase. Because the algorithm does not develop a model with adjustable parameters, it is said to be non-parametric. Instead, the *k*-NN classifier calculates the geometrical distance from each stored observation to the new observation $\vec{s}$ and, subsequently, classifies it identically to the majority of the k nearest neighboring observations. The classifier can of course be controlled by choosing different values of k. Intuitively, the classifier becomes more robust for large k, while small k will give more flexible decision boundaries, which are prone to outliers. The other parameter of the algorithm is the metric (distance function) between observations. In our studies we utilized the Euclidean distance metric, while we generally matched k to the number of training observations in the smallest class. This should give an estimate of the separation between classes as well as the within-class distribution. In Fig. 2.29 the *k*-NN algorithm is applied to the same data set as in Fig. 2.28 using $k = 15$. Similarly, the new observation (black dot) is labeled "red" as the nine of the fifteen nearest neighbors are red.

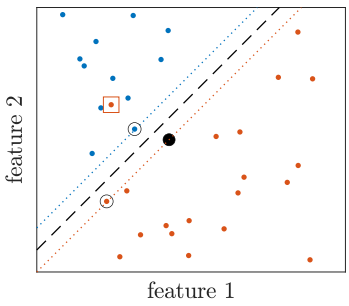

Fig. 2.30: Illustration of SVM classifier. The circled points are support vectors used to establish the margins (dotted lines). The dashed line is the decision boundary (hyperplane). The squared red point violates the hyperplane. Thus, a soft margin SVM is required.

The Support Vector Machine (SVM) algorithm searches for a hyperplane

$$\mathcal{H}: \quad \vec{w} \cdot \vec{s} + b = 0, \tag{2.43}$$

where $\vec{w}$ is a normal vector and b is an arbitrary constant determining its location, which separates the observations of two classes with maximum margin.[193, 194] When an optimal hyperplane is found, it serves as a decision boundary, and a new observation is classified to which side of the boundary it belongs. Fundamentally, SVM is binary but can be extended to a multiclass modality by evaluating the separability between every classes pair-wise (one-versus-one) or by considering each class compared to the remaining

(one-versus-all). Therefore, let us consider the same binary classification task as previously given in Fig. 2.28 and Fig. 2.29. Here, we only consider linear SVM. For now, we disregard the red dot marked by the square in Fig. 2.30. Hence, the two classes has no outliers and are linearly separable. The outermost observations of one class with respect to the second class are referred to as support vectors. In Fig. 2.30 such two are marked by circles. For a given direction or normal vector $\vec{w}$, an unique margin (dotted lines) can be found based on the support vectors. We can define the margin by a positive (blue dotted) and negative (red dotted) hyperplane, *i.e.*

$$\mathcal{H}^+: \quad \vec{w}\cdot\vec{s}+b=1 \quad \text{and} \quad \mathcal{H}^-: \quad \vec{w}\cdot\vec{s}+b=-1. \tag{2.44}$$

This constraint ensures an uniquely pair of $\vec{w}$ and b. Furthermore, it allows us to label each observation $\vec{s}_n$ as either positive or negative ($y_n = \pm 1$). However, it also implies a hard margin, where no observations are allowed to violate the boundary, that requires linearly separable classes (no outliers). The relations in Eq. (2.44) can be collapsed into the single condition

$$y_n(\vec{w}\cdot\vec{s}_n+b)\geq 1, \tag{2.45}$$

which should be fulfilled in order to classify every observation correctly. Additionally, we see that the classification rule for a new observation $\vec{s}$ writes

$$y=\operatorname{sgn}(\vec{w}\cdot\vec{s}+b). \tag{2.46}$$

Here, sgn is the sign function. We obtain the optimal (centered) hyperplane $\mathcal{H}$ orthogonal to the given direction $\vec{w}$ by choosing b such that $\vec{w}\cdot\vec{s}+b=0$. The hyperplane $\mathcal{H}$ is plotted by the dashed line in the illustration. The margin $\mathcal{M}$ is the perpendicular distance between $\mathcal{H}^+$ and $\mathcal{H}^-$. If we let $\vec{s}^+ \in \mathcal{H}^+$ and $\vec{s}^- \in \mathcal{H}^-$, the margin is simply found by projecting the points onto the unit normal vector $\vec{w}/\|\vec{w}\|$ and using the relations in Eq. (2.44), *i.e.*

$$\mathcal{M}=|\vec{s}^+-\vec{s}^-|\cdot\frac{\vec{w}}{\|\vec{w}\|}=\frac{2}{\|\vec{w}\|}. \tag{2.47}$$

Bringing everything together, we arrive at the constrained optimization problem

$$\underset{y_n(\vec{w}\cdot\vec{s}_n+b)\geq 1}{\arg\max}\left\{\frac{2}{\|\vec{w}\|}\right\} \quad \text{for} \quad n=1,\ldots,N \tag{2.48}$$

or equivalently

$$\underset{y_n(\vec{w}\cdot\vec{s}_n+b)\geq 1}{\arg\min}\left\{\frac{1}{2}\|\vec{w}\|^2\right\} \quad \text{for} \quad n=1,\ldots,N, \tag{2.49}$$

which is ensured to have a unique global solution [194], because both the object function (quadratic) and the set of constraints are convex. Similarly as

for PCA and LDA, we can apply the method of Lagrange multipliers. The Lagrangian function for the multiple constraints is

$$\mathcal{L}(\vec{w}, b, \vec{\lambda}) = \frac{1}{2}\|\vec{w}\|^2 - \sum_{n=1}^{N} \lambda_n \left(y_n(\vec{w} \cdot \vec{s}_n + b) - 1\right). \tag{2.50}$$

The stationary points are found be equating the partial derivatives to zero, *i.e.*

$$\frac{\partial \mathcal{L}}{\partial \vec{w}} = \vec{w} - \sum_{n=1}^{N} \lambda_n y_n \vec{s}_n = 0 \quad \text{and} \quad \frac{\partial \mathcal{L}}{\partial b} = \sum_{n=1}^{N} \lambda_n y_i = 0. \tag{2.51}$$

Furthermore, the Karush-Kuhn-Tucker (KKT) conditions apply [194], *i.e.*

$$\lambda_n \left(y_n(\vec{w} \cdot \vec{s}_n + b) - 1\right) = 0, \qquad \lambda_n \geq 0, \qquad y_n(\vec{w} \cdot \vec{s}_n + b) \geq 1 \tag{2.52}$$

for all $n = 1, \ldots, N$. Generally, this optimization problem must be solved by numerical methods. However, it can be instructive to study the relations in Eqs. (2.51) and (2.52). The partial derivative $\partial_{\vec{w}} \mathcal{L} = 0$ implies that the optimal direction $\vec{w}$ is a linear combination of the training vectors, *i.e.*

$$\vec{w} = \sum_{n=1}^{N} \lambda_n y_n \vec{s}_n. \tag{2.53}$$

Further, when $\vec{s}_n$ is an interior point (*i.e.* $y_n(\vec{w} \cdot \vec{s}_n + b) > 1$), the first KKT condition requires that $\lambda_n = 0$. This means that the optimal $\vec{w}$ is confined to be a linear combination of the support vectors, since only these satisfy $y_n(\vec{w} \cdot \vec{s}_n + b) = 1$.

As mentioned, this is the hard margin SVM, which does not allow outliers like the observation marked by the square in Fig. 2.30. However, in real-world applications data is most likely linearly inseparable. In this case, we can instead apply a soft margin approach, which allows outliers to violate the hyperplane at the cost of a penalty. Typically, soft margin SVMs are better at generalizing to unseen data because wider margins can be chosen. Mathematically, this is done by introducing positive slack variables ξ_n to the constraints in Eq. (2.45). Then, the new constraints can be written

$$y_n(\vec{w} \cdot \vec{s}_n + b) \geq 1 - \xi_n \quad \text{with} \quad \xi_n \geq 0 \tag{2.54}$$

for all $n = 1, \ldots, N$. This implies that for $0 < \xi_n < 1$, a given observation $\vec{s}_n$ lies within the margin on the proper side of the decision boundary (the optimal hyperplane), whereas for $\xi_n > 1$ it violates the boundary. If an observation lies on the correct side of the boundary and outside the margin as ideally in the hard margin case, there should be no penality and $\xi_n = 0$. Hence, the number of training errors are bound by the sum over all ξ_n. Thus,

we can naturally extend the optimization problem in Eq. (2.49) to

$$\underset{y_n(\vec{w}\cdot\vec{s}_n+b)\geq 1}{\arg\min}\left\{\frac{1}{2}\|\vec{w}\|^2+\gamma\sum_n \xi_n\right\} \quad \text{for} \quad n=1,\ldots,N, \tag{2.55}$$

to include the penalties. The soft margin problem is solved in a similar fashion [194] and the optimal $\vec{w}$ takes the same form as before but the support vectors now include any point with $\xi_n > 0$. Here, $\gamma > 0$ is a tuning parameter chosen prior to training by the programmer. Evidently, a larger γ value will introduce stronger penalties leading to a smaller margin and vice versa. In practice, the optimal value of γ can be hard to determine and is typically found through cross-validation.[179] Here, the data set is randomly partitioned into a number of subsets of equal size. The subsets are, in turn, chosen as the test set and the algorithm is trained on the remaining data for a certain value of the tuning parameter. The average test score is then compared to that of other parameter values. The value, which result in the highest average test score, is then chosen as the optimal one.

4.3 Summary of Results

Recently, Park *et al.* [189] pointed out the difficulties of attaining enough data, when studying MLAs for THz applications, and the ensuing challenges. Evidently, the set of training data must be sufficiently comprehensive for the MLA to learn the characteristics of the overall system. However, even when the training set is adequate for building a model, it may not be generic. Then, the model can possibly learn specific characteristics of the training data, that are not representative of the total system, or even fit to noise patterns. This is known as overfitting. [179] The MLA will hence not generalize well to unseen data. Since THz data sets are not generally publicly available, studies are typically based on one or few hundreds of measurements spread over several sample classes [104, 182, 183, 188]. Thereby each class only comprise some tens of observations, which in turn are divided into a training and a test set.

During the DETRIS project, we recorded more than 8000 frequency-domain THz reflection spectra in the range from 0.09 to 1.2 THz of seven compound materials, commonly found in the literature. These measurements has been published as the *Database of Frequency-Domain Terahertz Reflection Spectra for the DETRIS Project* (appended Publication C [195]). The experimental setup utilized for the measurements was built upon a CW THz-FDS spectrometer from Toptica AG (TeraScan 1550). The experimental scheme is illustrated in Fig. 2.31. The entire THz path was enclosed in a custom-made humidity chamber enabling measurements to be done in a controlled humidity environment. More details of the setup are given in the appended Publications A

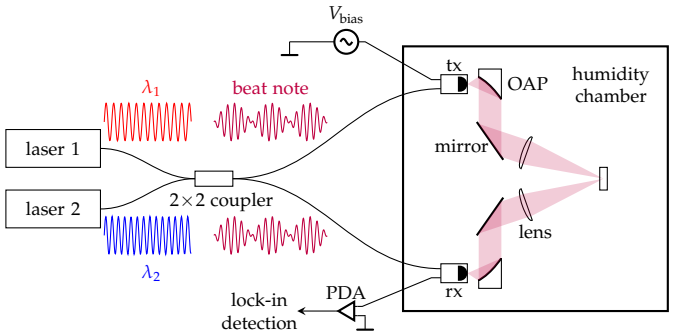

Fig. 2.31: Experimental scheme used for the reflection measurements comprised in the database. The angle of incidence was approx. 11°.

and C. The seven measured compounds included polyethylene (PE), galactitol, L-tartaric acid (L-TA), 4-aminobenzoic acid (PABA), hexogen (RDX), theophylline, and α-lactose monohydrate. PE was chosen due to its flat response in the THz spectral range and, hence, makes a convenient binder matrix for other active compounds [196, 197]. The remaining six materials were selected based on their unique spectroscopic fingerprints in the considered frequency range. The reflection coefficients of the seven compounds are plotted in Fig.

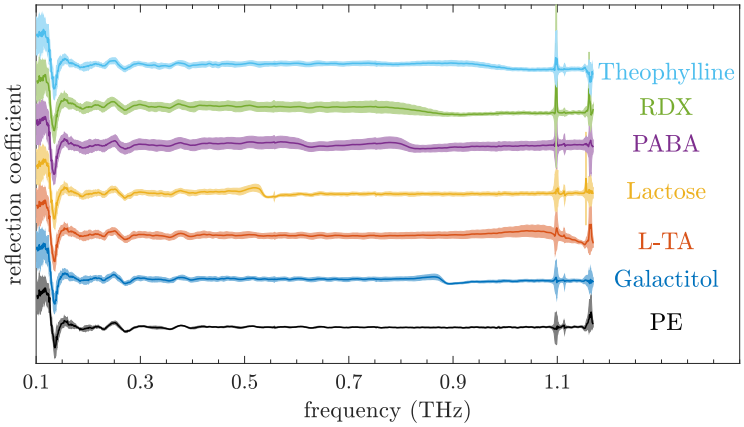

Fig. 2.32: Reflection coefficients of the seven compounds measured under ambient conditions. The continuous lines and the filled areas represents the means and the standard deviations of 480 spectra, respectively. Further, the reflection spectra have been offset vertically for a better readability.

2.32. The spectra show weak and broad spectroscopic characteristics in contrast to the sharp and distinct absorption lines well-known from transmission

spectroscopy. This is due to the dependency of the reflection coefficient on the refractive index, whereas transmission spectra depend on the absorption coefficient.[36] Below 0.15 THz, all the spectra exhibit a big dip due standing waves patterns. Around 1.1 and 1.15 THz, the spectra are noisy due to a strong absorption by atmospheric water vapor. Otherwise, the fingerprints of the different materials spread from 0.2 to 1.2 THz with several overlaps because of their broad extent. As mentioned, PE is generally flat and exhibits only tiny oscillations around 0.25 and 0.375 THz. Thus, it merely adds a constant background to the spectra of the sample materials and does not interfere with their respective characteristics. The database consists of three data sets. The first set (data set I) includes 3190 measurements recorded under ambient conditions of the compounds mixed with PE at weight-percentages of 20%, 50% and 80%, respectively, including samples of pure PE. The second set (data set II) contains 2337 measurements of the same samples recorded under controlled humidity conditions at a relative humidity (RH) of 10%, 50% and 90%, respectively. The third set (data set III) includes 2940 measurements of the compounds at 80% sample material by weight and samples of pure PE covered by various barrier materials and recorded under ambient conditions. The measuring details can be found in the appended Publications A and C.

With the database established, we could properly investigate various aspects of MLAs. In Publication A, we investigated the performance of the most common unsupervised and supervised linear DRMs (*i.e.* PCA and LDA, respectively) for analysis and classification of THz reflection spectra. Here, we will only summarize the main findings of the paper related to classification. Please see Publication A for the capabilities of PCA and LDA to provide visualization of high dimensional THz spectra. The performances of the two methods were quantified using the three classifiers described in the previous section. For the k-NN classifier, we chose k comparable to the number of observations in the smallest class of the training set. The SVM classifier employed a soft margin with a 10-fold cross-validation to determine the optimal value of the tuning parameter γ. The spectra were truncated to include only the range from 0.3 to 1.15 THz, where the six sample materials have unique characteristics. Moreover, the noise interval from 1.08 to 1.12 THz was excluded. Hence, we were left with spectra of 817 frequency components. Throughout the study, we applied a stratified random sampling to divide any given data subset into a training and a test set at a 4:1 ratio, respectively. The study comprised four experiments based on the first two data sets of the database. First, we included only the 1117 spectra of the samples with highest material concentration (*i.e.* 80% by weight). The respective training and test sets included 893 and 224 observations (roughly 128 and 32, respectively, from each class) The dimensionality of the data was reduced from 817 frequencies down to just two features. The classification scores (*i.e.* the percentages of correct predictions also known as accuracies)

	PCA		LDA		RLDA	
	Train	Test	Train	Test	Train	Test
Bayes	0.9843	0.9955	1.0000	0.9509	1.0000	1.0000
125-NN	0.9742	0.9732	1.0000	0.9509	0.9966	1.0000
SVM	0.9888	0.9732	1.0000	0.9464	1.0000	1.0000

Table 2.1: Classification scores of the PCA-, LDA- and RLDA-processed spectra of samples with 80% material by weight and samples of pure PE. Adapted from Publication A [198].

are given in Table 2.1. Both PCA and LDA yielded high classification scores for all three classifiers. Notably, PCA provided a better generalization to the unseen test data (superior test scores) compared to LDA. However, because the number of observations in the training set was comparable to the number of dimensions (a poorly-posed problem), the within-class scatter matrix (to be inverted in LDA) became almost-singular [199]. This caused the LDA algorithm to overfit the training data, which in turn implied the inferior generalization to the test data. This is also evident from the perfect classification scores of the training data together with the lower scores of the test data. Particularly, we found that LDA fitted to the noise in the training data instead of the spectral characteristics Therefore, we applied regularized-LDA (RLDA) using a 10-fold stratified cross-validation to obtain the optimal regularization value $\beta = 0.5$ [198]. The RLDA algorithm returned almost perfect classification scores of the train data and a perfect generalization to the test data for all three classifiers (see Table 2.1). Overall, RLDA thus outperformed PCA at preprocessing the data for optimal classification.

Next, the full data set I containing 3036 spectra of samples with various material concentrations and samples of pure PE was introduced. The respective training and test sets included 2428 and 608 observations. *"Since the samples are mixtures of the active material and PE, the obtained reflection coefficient is an intermediate value between the spectra of the two components. As the concentration of the active material decreases, the material-specific spectral features become less pronounced. Furthermore, for materials having a significantly higher refractive index than PE, e.g., PABA and theophylline, the reflection coefficient drops over the entire spectral range with decreasing concentration."*[198] To accommodate the higher complexity of the data, we retained three features of both the PCA and LDA algorithms. Furthermore, the material concentrations were discarded from the class labels fed to the LDA algorithm as the principal scope was to identify the sample material. The classification scores are given in Table 2.2. Evidently, LDA obtains superior train scores and generalized much better to the test data than PCA. The larger size of the training set prevents LDA from overfitting to the train data. The poor performance of PCA can be understood by recalling that PCA is unsupervised and aims to maximize

	PCA		LDA	
	Train	Test	Train	Test
Bayes	0.8871	0.8914	0.9975	0.9868
125-NN	0.9090	0.9145	0.9975	0.9885
SVM	0.8937	0.9046	0.9975	0.9868

Table 2.2: Classification scores of the PCA- and LDA-processed spectra of samples with various material concentrations and samples of pure PE. Adapted from Publication A [198].

the overall variance in the data. Hence, the PCA separates the data according to the hidden patterns. In that sense, samples of identical material but with various concentrations are regarded different, which complicates the classification task. On the other hand, LDA is supervised and aims to minimize the intra-class variance while maximizing the inter-class distance. Thus, samples of identical materials are clustered regardless of concentration, which facilitates classification. Hence, the near-perfect classification scores of LDA for all three classifiers.

Subsequently, we studied data set II, which included 2280 spectra of the same samples measured under various humidity conditions at 10%, 50% and 90% RH. We simulated a real-world application like stand-off spectroscopy, where a proper reference spectrum can be impossible to achieve, by only measuring the reference spectra at 50% RH. In consequence, the weaker water

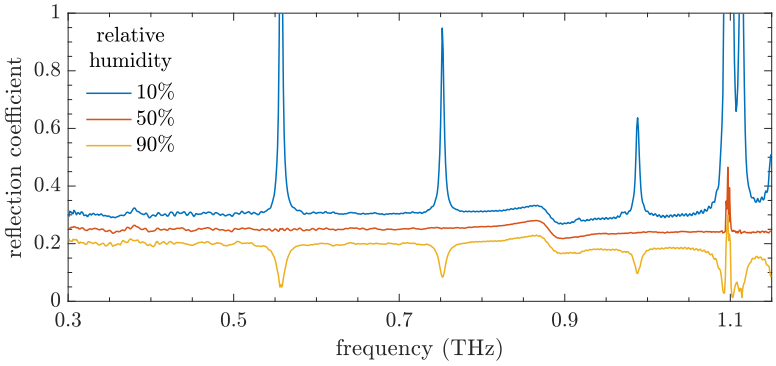

Fig. 2.33: Reflection spectra of the 80% galactitol by weight measured at various humidity conditions of 10%, 50% and 90% RH. The blue and yellow curves have been offset by ± 0.05 for clarity.

vapor absorption lines around 0.55, 0.75 and 0.98 THz, respectively, were not properly removed from the spectra measured at 10% and 90% RH. In the former measurements, this resulted in positive peaks, while the latter exhibited negative peaks, as seen in Fig. 2.33. The training and test sets contained 1824 and 456 observations, respectively. As before, we projected

	PCA		LDA	
	Train	Test	Train	Test
Bayes	0.6612	0.6316	1.0000	0.9868
95-NN	0.7007	0.6908	1.0000	0.9912
SVM	0.6321	0.6053	1.0000	0.9868

Table 2.3: Classification scores of the PCA- and LDA-processed spectra of samples with various material concentrations and samples of pure PE measured under various humidity conditions. Adapted from Publication A [198].

	PCA		LDA	
	Train	Test	Train	Test
Bayes	0.7648	0.7747	1.0000	1.0000
383-NN	0.7467	0.7500	1.0000	1.0000
SVM	0.8361	0.8322	1.0000	1.0000

Table 2.4: Classification scores of the PCA- and LDA-processed spectra of samples with various material concentrations, labeled according to their severity of hazard. Adapted from Publication A [198].

the THz spectra onto three features using both PCA and LDA, respectively. The classification scores obtained for the PCA- and LDA-preprocessed data are given in Table 2.3. Once again, we see an inferior performance of PCA with scores reaching only up to 0.70, while LDA yields unity train scores and very high test scores showing a good generalization. The additional peaks induced by water vapor due to the improper reference increased the variance of the data. Following a similar chain of reasoning as above, this led to a further overall spread of the data in the PCA feature space hampering classification. Again, this does not affect the LDA algorithm as the supplied class labels only contains information about the material type. Thus, LDA clusters the data accordingly regardless of the additional peaks due water vapor.

Lastly, we demonstrated how supervised DR methods like LDA can provide control of the classification algorithms by manipulating the class labels. This experiment was conducted on data set I. In view of security screening, we labeled galactitol, lactose, L-TA, PABA and PE as "Safe". Clearly, RDX being an explosive material was labeled "Danger". Theophylline is pharmaceutical for respiratory diseases and is toxic at high doses. Hence, it was labeled "Warning". With a total of three classes, LDA could at most retain two features. Similarly, the data dimensionality was reduced to two features using PCA for comparison. The results of PCA- and LDA-processed data classified using the new class labels are listed in Table 2.4. As expected, all of the classifiers performs perfectly on the LDA-processed data, which also

exhibit superior generalization on the test data. Yet again, the PCA algorithm was outperformed by LDA in terms of preprocessing for efficient classification with train and test scores of approx. 0.75.

The experiment on data set II of measurements under various humidity conditions, led us to the hypothesis that MLAs could render deconvolution by a reference spectrum redundant for classification of THz reflection spectra. *Viz.*, supervised DRMs can facilitate excellent accuracy scores in classification tasks of non-referenced THz reflection spectra, compared to unsupervised methods. Hence, we studied the classification of non-referenced vs. referenced terahertz spectra preprocessed by PCA and LDA, respectively, in Publication B. For the analysis, we employed only the spectral interval from 0.4 to 1.05 THz, free of the noise induced by strong water vapor absorption above 1.05 THz. Furthermore, the referenced spectra were each deconvoluted by an ideal reference spectrum to get rid of any water vapor absorption. To visualize the difference between the two types of spectra, the non-referenced (spectral amplitude $A(\nu)$) and referenced (reflection coefficient $r(\nu)$) spectra measured under ambient conditions (data set I) are shown in Fig. 2.34. For

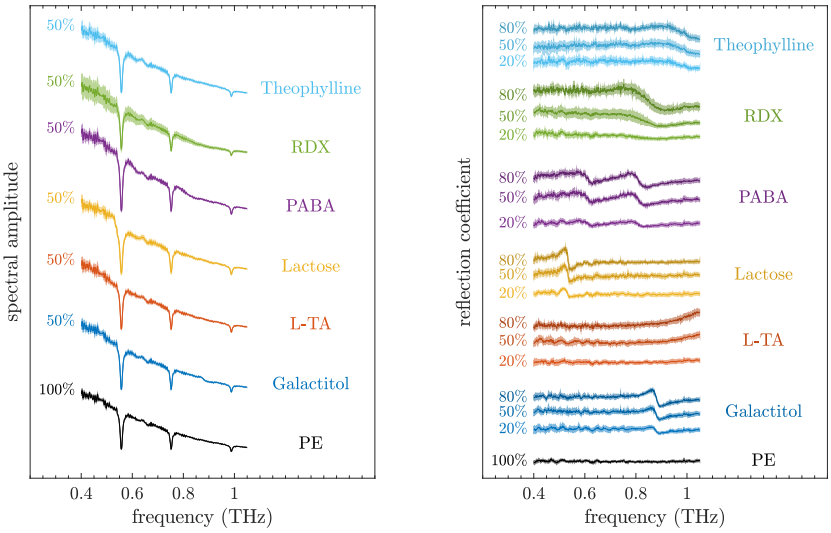

Fig. 2.34: Non-referenced (left) and referenced (right) THz reflection spectra of samples with 50% compound material by weight and samples pure PE. Both the non-referenced and referenced spectra have been offset vertically for better readability. The continuous lines and the filled areas represents the mean and the standard deviation, respectively, of 160 spectra of the given compound.

clarity, the non-referenced spectra have only been plotted for samples of 50% material by weight and samples of pure PE. In Publication B, the experiments were conducted on the basis of data set II. However, due to political reasons,

		PCA		LDA	
		Train	Test	Train	Test
Bayes	Referenced	0.9844	0.9870	1.0000	0.9974
	Non-referenced	0.9368	0.9245	1.0000	0.9974
384-NN	Referenced	0.7474	0.7448	0.9375	0.9349
	Non-referenced	0.6836	0.6615	0.9375	0.9349
SVM	Referenced	0.9980	1.0000	1.0000	0.9974
	Non-referenced	0.9258	0.9115	1.0000	0.9948

Table 2.5: Classification scores of the referenced and non-referenced spectra preprocessed by PCA and LDA, respectively. Adapted from Publication B.

measurements on the explosive compound RDX were edited out. Thereby, the data included 1920 observations that were divided into a train and a test set using stratified random sampling at a 4:1 ratio. Hence, the two data set contained 1536 and 384 observations, respectively. With six different classes, LDA can project the data onto at most five features. The spectra contained 649 discrete frequency components and were thus projected onto five features by both DRMs, respectively, to keep as much information as possible. The same three classifiers as before were used for classification of the processed data. The number of nearest neighbors was chosen equal to number of observations within each class, *i.e.* $k = 384$. Hence, the k-NN classifier will serve as a quantifier of how well the DRMs are at intra-class clustering. The results are shown in Table 2.5. Overall, the LDA-processed data yields superior classification scores as expected. Surprisingly, LDA performs equally well on the non-referenced and referenced data with perfect train scores for the Bayes and SVM classifiers and excellent test scores >99.4%. In particular, it is worth noting the very high Bayes classifier, which is a much simpler approach compared to the SVM. Reasonable classification scores are also obtained by the Bayes and SVM classifiers working on the PCA-processed data due to larger number of features as compared to the results of Publication A. However, the non-referenced score are slightly lower compared to the referenced data. The 384-NN classifier shows the worst performance for both DRMs because of our choice of k. Evidently, the higher scores for LDA proves its superior ability of clustering the data, which in turn facilitates classification. In conclusion, we see that our hypothesis was correct.

Finally, let us end this summary by addressing Hypothesis III of the DETRIS project. The hypothesis claimed that the necessary SNR required for identification of explosives can be reduced by use of MLAs. Further, these

algorithms should allow identification of explosives even when masked by various barrier materials. To investigate the effect of the SNR, the PCA, LDA

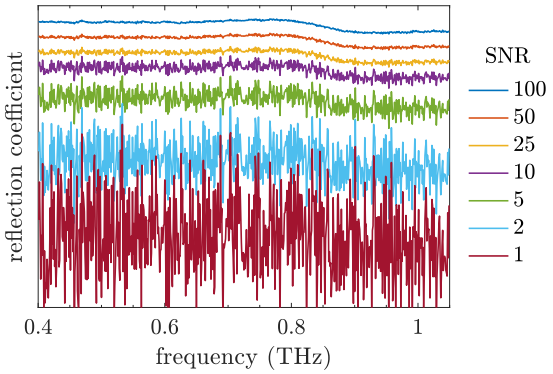

Fig. 2.35: Spectrum of an 80% RDX sample measured at 50% RH for various simulated SNRs.

and RLDA algorithms were trained using data set II and a similar methodology as above. The maximum number of six features were retained for all methods. The results presented below are based on the referenced data but similar results are achieved using the non-referenced data. White Gaussian noise was in turn added to the test data to synthesize SNRs from 100 to 1. A spectrum of an 80% RDX sample measured at 50% RH from test data set is plotted in Fig. 2.35 for the various SNRs. Clearly, the broad characteristic of RDX at 0.85 THz is hidden in noise and becomes difficult to recognize by eye as the SNR drops to values less than 10. The classification scores of the Bayes

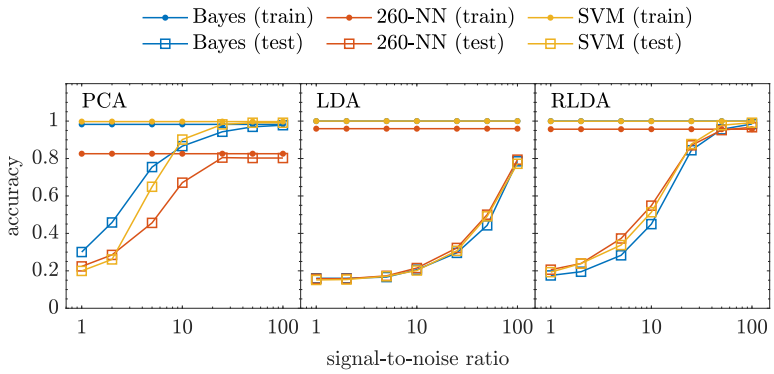

Fig. 2.36: Classification scores of PCA-, LDA- and RLDA-preprocessed data, respectively, as a function of the test data SNR. The Bayes train scores coincide with the SVM train scores for LDA and RLDA. Hence, the blue lines are hidden behind the yellow lines in these plots.

classifier, *k*-NN and SVM are plotted as a function of the SNR in Fig. 2.36. Because noise was only added to the test data, the classification scores of the train data remains constant in all cases. Generally, all three classifiers follow the same trend for all three DRMs with slight variations for the same reasons as discussed above. The classification scores diminish quickly as the SNR was decreased, starting from a SNR of 50. It is abundantly clear that LDA is overfitting (perfect train accuracy, poor test scores that rapidly drops with the SNR) due to a poorly posed problem. This is solved by the RLDA algorithm, which yields good test accuracies for SNRs better than 25. PCA appears more robust and retains test scores of approx. 90% at a SNR of 10. Subsequently, we investigated if it would help to train the algorithms on noisy data as well. Therefore, we added white Gaussian noise at the given SNRs to the full data set (train and test data) and retrained the algorithms. The results are seen in Fig. 2.37. Both PCA, LDA and RLDA yield almost constant train and test

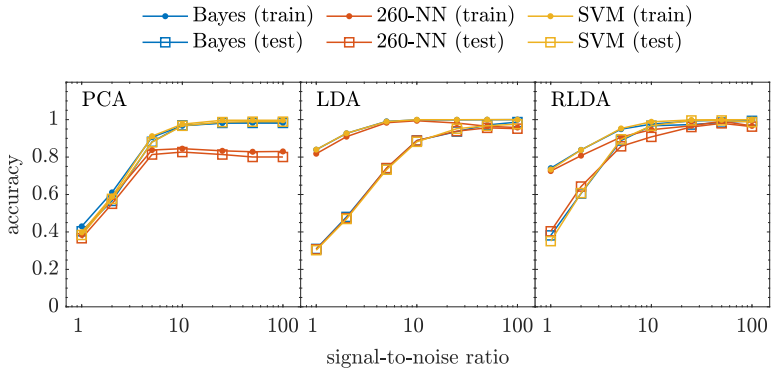

Fig. 2.37: Classification scores of PCA-, LDA- and RLDA-preprocessed data, respectively, as a function of the overall data SNR. For LDA and RLDA, the blue lines are generally hidden behind the yellow lines as the train scores of the Bayes classifier coincides with that of the SVM

scores for SNRs larger than 10. However, LDA fits to noise pattern in the train data and thus starts to generalize poorly when the SNR decreases to values below 25. Meanwhile, RLDA retained train and test accuracies of 95% and 85%, respectively, at a SNR of 5. PCA performed slightly worse with scores of 91% and 88%, respectively, at the same SNR. Therefore, we concluded that MLAs can enable detection of explosives a reduced SNRs. However, the algorithms must be trained on data with a similar SNR. Further, a certain SNR is required to maintain proper classification accuracies. Supervised methods proved to be preferable once gain. Here, RLDA maintained the highest accuracies >96.7% at a SNR of 10.

Lastly, we trained the LDA algorithm on data set III containing 2800 spectra of the 80% samples covered by various barrier materials and measured

	Referenced		Non-referenced	
	Train	Test	Train	Test
Bayes	1.0000	0.9929	1.0000	0.9964
320-NN	1.0000	0.9893	1.0000	0.9946
SVM	1.0000	0.9911	1.0000	0.9946

Table 2.6: Classification scores of the LDA-processed referenced and non-referenced spectra of 80% samples covered by various barrier materials.

under ambient conditions. The barriers included bubble foil, cotton, duct tape, low density PE, polyethylene terephthalate (PET), paper, a paper and a plastic bag, polyamide and polystyrene. The details can be found in Publication C. The train and test sets included 2240 and 560 observations, respectively. The resulting classification accuracies for both the referenced and non-referenced data are given in Table 2.6. All three classifiers obtain flawless training scores and impressively accurate test scores, better than 99% in all cases except for the 320-NN of the referenced data set. Notably, the best test scores >99.4% are yielded for non-referenced data. Thus, we can as well confirm the second claim of Hypothesis III that explosives masked by various barriers can be identified using MLAs.

5 Conclusions of the DETRIS Project

The goal of the DETRIS project was to improve the stand-off distance for detection of explosives using THz spectroscopy. At the time the project began, detection of explosives using THz radiation at distances of more than a few meters was deemed unlikely. Thus, the goal was to increase the maximum distance to more than 10 m.

First, we examined how a monochromatic CW FDS spectrometer performed compared to a more common broadband pulsed TDS system. At the time the project started, such CW system was the state-of-the-art of commercially available THz spectrometers. Needless to say, the propagation losses are similar in both approaches. Thus, we found that CW systems are better suited for stand-off spectroscopy, simply because the pertinent THz sources deliver output powers typically an order of magnitude higher. Next, we investigated experimentally the use of THz photomixer arrays for improved output power and directivity of the emitted THz waves as well as improved detector sensitivity. In this pursue, we characterized four identical, commercially available, PIN diode THz photomixers with an extended bowtie antenna structure. This was done by mapping out the two-dimensional radiation patterns in the far-field for various frequencies. A rather substantial variance of the patterns between the individual photomixers was observed.

However, the overall trend was a strong central spot with weak concentric rings. We showed that these Airy-like patterns most likely originated from the THz waves being diffracted by the circular aperture of the Si lenses. The mutually coherent THz emitters were subsequently configured in a 2×2 array and characterized in a similar way. A clear interference pattern was observed in the recorded array beam pattern but the four array elements were easily distinguished, and the expected array gain was absent. We attributed the difference between the recorded and calculated beam patterns to the rather different radiation patterns of the individual elements. However that may be, both the experimental and theoretical beam patterns were impacted by the array spacing much larger than the wavelength, which resulted in grating lobes. Therefore, we concluded that photomixer phased arrays must be implemented on-chip in order to achieve a proper array gain (output power or sensitivity) and improved directivity. Finally, we demonstrated a stand-off CW THz spectrometer based on transmitting and receiving focal plane arrays of mutually coherent photomixers, respectively. At 10 m stand-off distance, we retained a 2:1 SNR at 0.8 THz using a reflecting sample. Unfortunately, the coherent summation of the multiple detected signals did not increase the sensitivity as expected. In fact, we found that the recorded spectra principally corresponded to transmitter/receiver pair that included the best performing THz emitter. Furthermore, we showed that focal plane emitter arrays are not suitable for stand-off spectroscopy, as the beams only overlap in the target plane, which, in the worst case, can lead to destructive interference at the receiver. Nonetheless, detector arrays might still be beneficial if the measured object scatters the incident THz waves due to surface irregularities causing a non-line-of-sight setting.

Second, we studied how machine learning algorithms (MLAs) can be developed and trained to identify the spectra of explosives under various conditions. Contrary to our first hypothesis, MLAs will not reduce the necessary SNR required for identification of explosives and other compounds with spectral characteristics in the THz region. We particularly examined principal component analysis (PCA) and linear discriminant analysis (LDA). The two dimensionality reduction methods represented an unsupervised and supervised approach, respectively. Our work demonstrated that LDA is superior at preprocessing THz reflection spectra for classification compared to PCA. Especially, LDA facilitated classification accuracies better than 99% under normal measuring conditions. Additionally, we found that MLAs make the deconvolution of THz reflection spectra by a precise reference spectrum redundant. This is a very substantial result, as precise reference spectra can be problematic or even unobtainable in applications outside the laboratory, and not least adds to the complexity of the required system. Finally, MLAs proved themselves very efficient for detection of specific materials retaining classification scores >99% even under unfavorable conditions (*e.g.*, samples

covered by various barrier materials or in severe humidity conditions).

In conclusion, the maximum stand-off distance for detection of explosives is limited to 10 m at the time of writing due to the maturity of the applied technology. However, our ML-based approach can most likely help facilitating THz stand-off spectroscopy at several tens of meters as more powerful THz sources become available at the relevant frequencies.

Chapter 3

Terahertz Generation through Optical Rectification

A few years prior to my research stay at IMEP-LAHC, Prof. Coutaz had proposed that THz images of nonlinear dielectric materials including biological samples can be produced with sub-wavelength resolution through OR THz generation in the sample [200]. It is well-known that second-order nonlinear optical processes, *i.e.* , second-harmonic generation (SHG) and OR, can be induced at the surface of noncentrosymmetric media by intense light [201]. SHG imaging is excellent for reproducing crystalline inhomogeneties of samples and a frequently employed in both hospitals and laboratories [202]. In fact, various nonlinear optical modalities are applied for imaging, and recently, Zhang *et al.* [203] reviewed the advances in nonlinear optics for bio-imaging applications. Several techniques including two-photon excited fluorescence (TPEF), SHG, third-harmonic generation (THG), coherent anti-Stokes Raman scattering (CARS), stimulated Raman scattering (SRS), and pump-probe imaging are describe. Surprisingly, THz generation is not mentioned at all, even though it is generated simultaneously to SHG, and it should therefore be possible to record a THz image every time a SHG image is recorded. As a proof-of-principle of the technique, Coutaz' group recorded a THz image of a caster sugar grain in transmission [200], a nonlinear material also used for SHG [204–206]. They named the technique ORTI, *i.e. Optical Rectification Terahertz Imaging*. However, the conversion efficiencies of SHG and OR depend on the optical parameters of the sample medium at both the laser as well as the generated SH and THz frequencies. That is, sample media could be transparent or opaque at both frequencies, or even transparent/opaque and vice versa at the respective frequencies, like *e.g.* water. Furthermore, Groma *et al.* [207] have demonstrated that OR can be used to study the molecular response of biological samples. Therefore, ORTI could

be complementary to SHG imaging and could contribute with additional information that will be of great interest. Only a very limited number of experiments regarding OR in reflection can be found in the literature, and none in view of microscopy. A small review is given in our recent paper [208] (appended Publication D): *"Generation of THz pulses through OR in reflection has only been studied to a lesser extent. In 2005, Reid* et al.[9] *have reported OR THz generation from a semi-conductor recorded in reflection at 45° incidence. They pumped an InAs sample below its bandgap at 800 nm and by a proper polarimetric study of both THz generation and second-harmonic generation (SHG), they were able to discriminate the respective contributions of the bound and free photo-excited electrons. Later in 2007, Zinov'ev* et al.[10,11] *and Bakunov* et al.[12,13] *developed theoretical models of THz generation through OR including a field generated in the backward direction (reflection). Zinov'ev* et al. *presented a thorough description of all the THz pulses generated when an optical pulse propagates through a slab of nonlinear material. Their theoretical calculations clarify that the THz radiation is generated at the surfaces due to the instantaneous creation and acceleration of polarization charge at the front surface, and subsequent deceleration and extinction at the back surface. They supported their theory by experiments measured in transmission. Bakunov* et al. *extended the usual Fresnel formulas for transmission and reflection of free-propagating electromagnetic pulses to forced pulses generated in a nonlinear crystal and showed that the free and forced waves obey different boundary conditions at the crystal surfaces.*[12] *In the second paper*[13]*, they expanded their model to include the focusing of the pump beam and calculate the Cherenkov angular spreading of the generated THz waves. Later on, Hargreaves* et al.[14] *published a detailed modeling on THz OR generation versus the crystal orientation in view of clearly discriminating OR and photo-induced current transient contributions. Finally, Schneider*[15] *performed a complete analysis of the THz pulses generated in a nonlinear slab considering dispersion, absorption of both optical and terahertz waves, and multiple reflections. Furthermore, OR THz generation in reflection has been performed when dealing with metals.*[16] *Most of these publications focused on the theoretical description of the OR THz generation and experimental results were either performed in transmission*[11,17] *or under oblique incidence.*[9,16]*"* However, aspects of OR needs to be studied and understood before ORTI can be implemented in real-world scenarios. For example, THz OR generation in reflection under normal incidence, as studied here, is preferable in regards to microscopy.

1 The Nonlinear Plane Wave Model

In this work, we confine ourselves to the case of normal incidence as illustrated in Fig. 3.1. Here the laboratory referential is (xyz), and the exciting laser beam propagates normally to the crystal surface along the z-direction. When the laser beam is not strongly focused onto the sample, *i.e.* when the

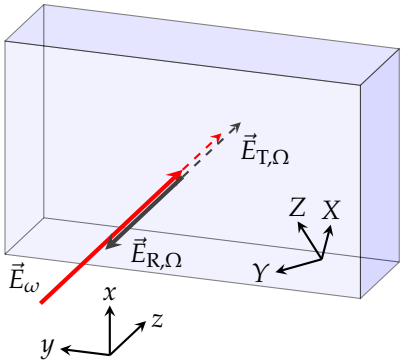

Fig. 3.1: A zinc blende crystal with crystal frame (XYZ) and a laser beam $\vec{E}_\omega$ incident normal to the crystal frame along the z-direction and the generated THz fields $\vec{E}_{R,\Omega}$ and $\vec{E}_{T,\Omega}$ in the laboratory referential frame (xyz).

laser Rayleigh length is larger than the crystal thickness d, it can be approximated with a plane wave. We will assume that the exciting plane wave consists of two spectral components ω and $\omega + \Omega$ with ω and Ω being the optical and THz angular frequencies, respectively. In air, we choose the notation of the electric field as

$$\vec{E}_{o,\omega}(z,t) = \vec{E}_{o,\omega}(z)e^{-j\omega t} = \vec{E}_{o,\omega}\, e^{jk_{o,\omega}z}e^{-j\omega t}, \tag{3.1}$$

where $\vec{k}_{o,\omega} = \frac{\omega}{c}\vec{u}_z$ is the incident wave vector, c the speed of light in vacuum, and $\vec{u}_z$ the unit vector along the z-direction of the laboratory frame. The laser field inside the crystal writes

$$\vec{E}_\omega\,(z) = \vec{E}_\omega\, e^{j\tilde{k}_\omega z} = \tilde{t}_\omega \vec{E}_{o,\omega}\, e^{j\tilde{k}_\omega z} \tag{3.2}$$

with wave vector $\vec{\tilde{k}}_\omega = \frac{\omega}{c}\tilde{n}_\omega\vec{u}_z$ and transmission coefficient $\tilde{t}_\omega$ at the crystal surface. The tilde is employed to indicate complex values except for complex fields. The complex refractive index of the crystal at the laser frequency is $\tilde{n}_\omega = n_\omega + j\kappa_\omega$. The electromagnetic fields are governed by Maxwell's equations, *viz.*

$$\vec{\nabla}\cdot\vec{D} = \rho, \tag{3.3}$$

$$\vec{\nabla}\cdot\vec{B} = 0, \tag{3.4}$$

$$\vec{\nabla}\times\vec{E} = -\frac{\partial\vec{B}}{\partial t}, \tag{3.5}$$

$$\vec{\nabla}\times\vec{H} = \frac{\partial\vec{D}}{\partial t} + \vec{J} \tag{3.6}$$

with the constitutive relations $\vec{D} = \varepsilon_o\vec{E} + \vec{P}$ and $\vec{B} = \mu_o\mu\vec{H}$. Here ρ is the free charge density andε_o the permittivity of vacuum. If we separate the

polarization

$$\vec{P} = \varepsilon_o \sum_m \vec{\vec{\chi}}^{(m)} : \vec{E}^m \tag{3.7}$$

into a linear ($m = 1$) and a nonlinear ($m > 1$) part, *i.e.* $\vec{P} = \vec{P}^L + \vec{P}^{\mathrm{NL}}$, the displacement field can be written

$$\vec{D} = \varepsilon_o \vec{\vec{\varepsilon}} \cdot \vec{E} + \vec{P}^{\mathrm{NL}}. \tag{3.8}$$

Furthermore, neglecting any anisotropy of the crystal, the permittivity tensor $\vec{\vec{\varepsilon}}$ reduces to a scalar $\tilde{\varepsilon}$. Additionally, in a nonmagnetic ($\mu = 1$) dielectric medium, there are no free charges ($\rho = 0$) and no free currents ($\vec{J} = 0$). Thus, by taking the curl of Eq. (3.5), changing the order of the curl and the time-derivative on the left-hand side, and substituting Eq. (3.6) and the constitutive relations, we get

$$\vec{\nabla} \times \vec{\nabla} \times \vec{E} = -\mu_o \varepsilon_o \tilde{\varepsilon} \frac{\partial^2 \vec{E}}{\partial t^2} - \mu_o \frac{\partial^2 \vec{P}^{\mathrm{NL}}}{\partial t^2}. \tag{3.9}$$

The right-hand side of Eq. (3.9) can be rewritten using the identity

$$\vec{\nabla} \times \vec{\nabla} \times \vec{E} = \vec{\nabla} \left(\vec{\nabla} \cdot \vec{E} \right) - \nabla^2 \vec{E}.$$

from vector calculus. Furthermore, since we approximate the electric field by a plane wave, we have $\vec{\nabla} \cdot \vec{E} = 0$. Substituting into Eq. (3.9) and applying $\mu_o = 1/\varepsilon_o c^2$, we obtain the nonlinear Helmholtz propagation equation

$$-\nabla^2 \vec{E} + \frac{1}{c^2} \tilde{\varepsilon} \frac{\partial^2 \vec{E}}{\partial t^2} = -\frac{1}{\varepsilon_o c^2} \frac{\partial^2 \vec{P}^{\mathrm{NL}}}{\partial t^2}. \tag{3.10}$$

Let us recall from Eq. (3.1) that the electric field has a harmonic time dependence $e^{-i\omega t}$. Similarly, we can apply this notation to the nonlinear polarization, *i.e.*

$$\vec{P}^{\mathrm{NL}} = \vec{P}^{\mathrm{NL}}(z) e^{-i\omega t}. \tag{3.11}$$

Thereby, we calculate the time derivatives in Eq. (3.10) and multiply by $e^{i\omega t}$ to obtain the expression

$$\nabla^2 \vec{E}(z) + \frac{\omega^2}{c^2} \tilde{\varepsilon} \vec{E}(z) = -\frac{\omega^2}{\varepsilon_o c^2} \vec{P}^{\mathrm{NL}}(z). \tag{3.12}$$

The THz wave at frequency Ω is generated through OR, which is described by the second-order nonlinear susceptibility tensor $\vec{\vec{\chi}}^{(2)}$. Therefore, the nonlinear polarization writes

$$\vec{P}^{\mathrm{NL}}_{\Omega}(z) = \varepsilon_o \vec{\vec{\chi}}^{(2)} : \vec{E}_{\omega+\Omega}(z) \cdot \vec{E}^*_{\omega}(z), \tag{3.13}$$

where the asterisk denotes the complex conjugate. Finally, we obtain the nonlinear Helmholtz propagation equation for the THz field $\vec{E}_\Omega$ by combining Eqs. (3.12) and (3.13):

$$\nabla^2\vec{E}_\Omega(z) + \frac{\Omega^2}{c^2}\tilde{\varepsilon}_\Omega\vec{E}_\Omega(z) = -\frac{\Omega^2}{c^2}\vec{\vec{\chi}}^{(2)} : \vec{E}_{\omega+\Omega}(z)\cdot\vec{E}^*_\omega(z). \tag{3.14}$$

Entering expression (3.2) of the laser field into Eq. (3.14) leads to

$$\nabla^2\vec{E}_\Omega(z) + \frac{\Omega^2}{c^2}\tilde{\varepsilon}_\Omega\vec{E}_\Omega(z) = -\vec{S}e^{j\Delta\tilde{k}z} \tag{3.15}$$

with $\Delta\tilde{k} \equiv \tilde{k}_{\omega+\Omega} - \tilde{k}^*_\omega$ and the source term $\vec{S} = \frac{\Omega^2}{c^2}\vec{\vec{\chi}}^{(2)} : \vec{E}_{\omega+\Omega}\cdot\vec{E}^*_\omega$. The angular wave number difference can be written

$$\begin{aligned}\Delta\tilde{k} &= \frac{\omega+\Omega}{c}(n_{\omega+\Omega} + j\kappa_{\omega+\Omega}) - \frac{\omega}{c}(n_\omega - j\kappa_\omega)\\ &= \frac{\omega+\Omega}{c}n_{\omega+\Omega} - \frac{\omega}{c}n_\omega + j\frac{\omega}{c}\left(\left(1+\frac{\Omega}{\omega}\right)\kappa_{\omega+\Omega} + \kappa_\omega\right).\end{aligned} \tag{3.16}$$

Within the hypothesis $\Omega \ll \omega$, we can develop the refraction index and the extinction coefficient as

$$n_{\omega+\Omega} \approx n_\omega + \Omega\frac{\partial n_\omega}{\partial\omega} \quad \text{and} \quad \kappa_{\omega+\Omega} \approx \kappa_\omega + \Omega\frac{\partial\kappa_\omega}{\partial\omega}, \tag{3.17}$$

respectively. Inserting these approximations into Eq. (3.16), we get

$$\begin{aligned}\Delta\tilde{k} &\approx \frac{\omega+\Omega}{c}\left[n_\omega + \Omega\frac{\partial n_\omega}{\partial\omega}\right] - \frac{\omega}{c}n_\omega + j\frac{\omega}{c}\left(\left(1+\frac{\Omega}{\omega}\right)\left[\kappa_\omega + \Omega\frac{\partial\kappa_\omega}{\partial\omega}\right] + \kappa_\omega\right)\\ &= \frac{\Omega}{c}\left(n_\omega + (\omega+\Omega)\frac{\partial n_\omega}{\partial\omega} + j\left[\left(2\frac{\omega}{\Omega}+\Omega\right)\kappa_\omega + (\omega+\Omega)\frac{\partial\kappa_\omega}{\partial\omega}\right]\right)\end{aligned} \tag{3.18}$$

If we apply the optical group refractive index

$$n_{\mathrm{G},\omega} = n_\omega + \omega\frac{\partial n_\omega}{\partial\omega} \tag{3.19}$$

and neglect the terms proportional to Ω^2 (these terms will be very small compared to the other terms within our hypothesis $\Omega \ll \omega$), the wave number difference $\Delta\tilde{k}$ simplifies as

$$\Delta\tilde{k} \approx \frac{\Omega}{c}\left(n_{\mathrm{G},\omega} + j\left[2\frac{\omega}{\Omega}\kappa_\omega + \omega\frac{\partial\kappa_\omega}{\partial\omega}\right]\right). \tag{3.20}$$

The second term of the imaginary part is much smaller than first term. Thus, we arrive at

$$\Delta\tilde{k} \approx \frac{\Omega}{c}n_{\mathrm{G},\omega} + j\frac{2\omega}{c}\kappa_\omega = \frac{\Omega}{c}n_{\mathrm{G},\omega} + j\alpha_\omega \equiv \frac{\Omega}{c}\tilde{n}_{\mathrm{G},\omega}. \tag{3.21}$$

Here $\alpha_\omega = 2\omega\kappa_\omega/c$ is the absorption coefficient at the optical laser frequency. Let us notice with

$$\tilde{n}_{G,\omega} \equiv n_{G,\omega} + j\kappa_{G,\omega} = n_{G,\omega} + j\frac{c}{2\omega}\alpha_{G,\omega}, \tag{3.22}$$

we can deduce from Eq. (3.21) that

$$\kappa_{G,\omega} = \frac{c}{\Omega}\alpha_\omega \quad \Rightarrow \quad \alpha_{G,\omega} = \frac{2\omega}{\Omega}\alpha_\omega. \tag{3.23}$$

With some typical numbers $\lambda_\Omega = 2\pi c/\Omega = 300\,\mu$m and $\lambda_\omega = 800$ nm, we see that $2\omega/\Omega = 750$. Hence, the group absorption is 750$\sim$1000 times larger than the laser absorption, which is enormous.

Inside the crystal, the solution of nonlinear Helmholtz Eq. (3.15) is the sum of free and forced waves, that is

$$\vec{E}_\Omega(z) = \vec{E}_{\text{free},\Omega}\, e^{j\tilde{k}_\Omega z} + \vec{E}_{\text{forc},\Omega}\, e^{j\Delta\tilde{k}z}. \tag{3.24}$$

Entering the forced wave expression into the right-hand side of Eq. (3.15), we get

$$\nabla^2\vec{E}_{\text{forc},\Omega}\, e^{j\Delta\tilde{k}z} + \frac{\Omega^2}{c^2}\tilde{\varepsilon}_\Omega\vec{E}_{\text{forc},\Omega}\, e^{j\Delta\tilde{k}z} = \left(-\Delta\tilde{k}^2 + \frac{\Omega^2}{c^2}\tilde{\varepsilon}_\Omega\right)\vec{E}_{\text{forc},\Omega}\, e^{j\Delta\tilde{k}z}, \tag{3.25}$$

and thus,

$$\vec{E}_{\text{forc},\Omega} = \frac{\vec{S}}{\Delta\tilde{k}^2 - \tilde{k}_\Omega^2} \tag{3.26}$$

with $\tilde{k}_\Omega^2 = \frac{\Omega^2}{c^2}\tilde{\varepsilon}_\Omega = \frac{\Omega^2}{c^2}\tilde{n}_\Omega^2$. Outside the crystal, *i.e.* in air or vacuum, the propagation equation is similar to Eq. (3.15) but the nonlinear source term $\vec{S}$ is null. The solution is a forward or backward propagating free plane wave. Because no THz beam illuminates the crystal, only the THz backward wave, *i.e.* the reflected THz field, must be considered:

$$\vec{E}_{R,\Omega}(z) = \vec{E}_{R,\Omega}\, e^{-jk_{R,\Omega}z} \tag{3.27}$$

with $k_{R,\Omega}^2 = \frac{\Omega^2}{c^2}$. At the crystal surface in $z = 0$, the tangential components of the electric and magnetic fields must conserved, *i.e.*

$$\vec{u}_z \times \left(\vec{E}_{R,\Omega}(z) - \vec{E}_\Omega(z)\right)\Big|_{z=0} = 0, \tag{3.28}$$

$$\vec{u}_z \times \left(\vec{H}_{R,\Omega}(z) - \vec{H}_\Omega(z)\right)\Big|_{z=0} = 0. \tag{3.29}$$

The Maxwell-Faraday Eq. (3.5) and $\vec{B} = \mu_o\vec{H}$ can be utilized to rewrite the magnetic fields in terms of the electric fields:

$$\vec{\nabla}\times\vec{E} = -\frac{\partial\vec{B}}{\partial t} = j\Omega\mu_o\vec{H} \quad \Rightarrow \quad \vec{H} = \frac{j}{\Omega\mu_o}\vec{\nabla}\times\vec{E}. \tag{3.30}$$

Then Eqs. (3.28) and (3.29) take the forms

$$\begin{pmatrix} -E_{\mathrm{R},\Omega,y} + E_{\Omega,y} \\ E_{\mathrm{R},\Omega,x} - E_{\Omega,x} \end{pmatrix} = \begin{pmatrix} -E_{\mathrm{R},\Omega,y} + E_{\mathrm{free},\Omega,y} + E_{\mathrm{forc},\Omega,y} \\ E_{\mathrm{R},\Omega,x} - E_{\mathrm{free},\Omega,x} - E_{\mathrm{forc},\Omega,x} \end{pmatrix} = 0 \quad (3.31)$$

$$\frac{\partial}{\partial z}\Big(-\vec{E}_{\mathrm{R},\Omega}(z) + \vec{E}_{\Omega}(z)\Big)\Big|_{z=0} = k_{\mathrm{R},\Omega}\vec{E}_{\mathrm{R},\Omega} + \tilde{k}_{\Omega}\vec{E}_{\mathrm{free},\Omega} + \Delta\tilde{k}_{\Omega}\vec{E}_{\mathrm{forc},\Omega} = 0 \quad (3.32)$$

after entering the expressions of the THz electric fields Eqs.(3.24) and (3.27), which leads to the system of equations

$$\begin{bmatrix} 1 & -1 \\ k_{\mathrm{R},\Omega} & \tilde{k}_{\Omega} \end{bmatrix} \begin{pmatrix} E_{\mathrm{R},\Omega,i} \\ E_{\mathrm{free},\Omega,i} \end{pmatrix} = \begin{pmatrix} 1 \\ -\Delta\tilde{k} \end{pmatrix} E_{\mathrm{forc},\Omega,i} \quad \text{for} \quad i = x, y. \quad (3.33)$$

With a little algebra, we find the solutions:

$$\begin{pmatrix} E_{\mathrm{R},\Omega,i} \\ E_{\mathrm{free},\Omega,i} \end{pmatrix} = \frac{1}{\tilde{k}_{\Omega} + k_{\mathrm{R},\Omega}} \begin{bmatrix} \tilde{k}_{\Omega} & 1 \\ -k_{\mathrm{R},\Omega} & 1 \end{bmatrix} \begin{pmatrix} 1 \\ -\Delta\tilde{k} \end{pmatrix} E_{\mathrm{forc},\Omega,i} \quad (3.34)$$

Thereby, we have obtained the full expressions of Eqs. (3.19) and (3.22) for the THz fields that propagate backwards and forwards, respectively:

$$\vec{E}_{\mathrm{R},\Omega}(z) = \frac{\tilde{k}_{\Omega} - \Delta\tilde{k}}{\tilde{k}_{\Omega} + k_{\mathrm{R},\Omega}} \frac{\vec{S}}{\Delta\tilde{k}^2 - \tilde{k}_{\Omega}^2} e^{-jk_{\mathrm{R},\Omega}z}, \quad (3.35)$$

$$\vec{E}_{\Omega}(z) = \frac{\vec{S}}{\Delta\tilde{k}^2 - \tilde{k}_{\Omega}^2} \left(e^{j\Delta\tilde{k}z} - \frac{\Delta\tilde{k} + k_{\mathrm{R},\Omega}}{\tilde{k}_{\Omega} + k_{\mathrm{R},\Omega}} e^{j\tilde{k}_{\Omega}z} \right). \quad (3.36)$$

As expected, the reflected signal does not depend on the crystal thickness, and thus, it exists even if the crystal thickness tends towards zero: The generation in reflection is a pure surface effect. Let us notice that the coefficient in front of the second exponential in Eq. (3.36) is equal to 1 when the reflected field is neglected. It follows that the transmitted field is not null even if the sample thickness is zero, because of the surface-effect generation, while it is null when one makes the hypothesis of no signal at the entrance face of the crystal.

To get the THz field transmitted through the crystal ($z > d$) at the rear surface, we need to multiply Eq. (3.31) by the THz transmission coefficient $\tilde{t}_{\Omega}$:

$$\vec{E}_{\mathrm{T},\Omega}(z) = \vec{E}_{\Omega}(d)\tilde{t}_{\Omega}e^{jk_{\mathrm{R},\Omega}(z-d)}. \quad (3.37)$$

Finally, when we enter the expressions for the angular wave numbers, the THz fields writes

$$\vec{E}_{\mathrm{R},\Omega}(z) = -\frac{\vec{\vec{\chi}}^{(2)} : \vec{E}_{\omega+\Omega} \cdot \vec{E}_{\omega}^{*}}{(\tilde{n}_{\Omega} + 1)(\tilde{n}_{\mathrm{G},\omega} + \tilde{n}_{\Omega})} e^{-jk_{\mathrm{R},\Omega}z} \quad (3.38)$$

and

$$\vec{E}_{\mathrm{T},\Omega}(z) = \frac{2\tilde{n}_\Omega}{1+\tilde{n}_\Omega}\frac{\vec{\vec{\chi}}^{(2)} : \vec{E}_{\omega+\Omega}\cdot\vec{E}^*_\omega}{\tilde{n}^2_{\mathrm{G},\omega}-\tilde{n}^2_\Omega}\left(e^{j\Delta\tilde{k}z} - \frac{\tilde{n}_{\mathrm{G},\omega}+1}{\tilde{n}_\Omega+1}e^{j\tilde{k}_\Omega z}\right). \tag{3.39}$$

The field magnitudes normalized to nonlinear source terms can be written as

$$\left|\vec{E}_{\mathrm{R},\Omega}\right| / \left|\overleftrightarrow{\tilde{\chi}}^{(2)} : \vec{E}_{\omega+\Omega}\cdot\vec{E}^*_\omega\right| = \left|\left(\tilde{n}_\Omega+1\right)\left(\tilde{n}_{\mathrm{G},\omega}+\tilde{n}_\Omega\right)\right|^{-1} \tag{3.40}$$

and

$$\left|\vec{E}_{\mathrm{T},\Omega}\right| / \left|\overleftrightarrow{\tilde{\chi}}^{(2)} : \vec{E}_{\omega+\Omega}\cdot\vec{E}^*_\omega\right| = \left|\frac{2\tilde{n}_\Omega}{1+\tilde{n}_\Omega}\right|\left|\frac{2\left(e^{j\Delta\tilde{k}d} - \frac{\tilde{n}_{\mathrm{G},\omega}+1}{\tilde{n}_\Omega+1}e^{j\tilde{k}_\Omega d}\right)}{\left(\tilde{n}_\Omega+1\right)\left(\tilde{n}^2_{\mathrm{G},\omega}-\tilde{n}^2_\Omega\right)}\right|. \tag{3.41}$$

The ratio

$$\left|\frac{\vec{E}_{\mathrm{R},\Omega}}{\vec{E}_{\mathrm{T},\Omega}}\right| = \left|\frac{\left(\tilde{n}_\Omega+1\right)\left(\tilde{n}_{\mathrm{G},\omega}-\tilde{n}_\Omega\right)}{4\tilde{n}_\Omega\left(e^{j\Delta\tilde{k}d} - \frac{\tilde{n}_{\mathrm{G},\omega}+1}{\tilde{n}_\Omega+1}e^{j\tilde{k}_\Omega d}\right)}\right|, \tag{3.42}$$

is independent of the crystal nonlinearity, and thus, on the polarization of the laser and THz beams. Expressions (3.40) and (3.41) are plotted in Fig. 3.2(a) and (b), respectively, using $\lambda = 800$ nm, $f = 1$ THz, $n_{\mathrm{G},\omega} = 2.5$, $n_\Omega = 3$, and $d = 1.52$ mm versus the absorption coefficients α_ω and α_Ω. We see that the

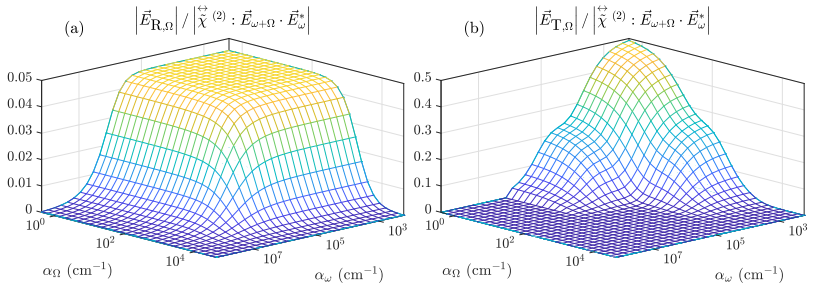

Fig. 3.2: Maps of the THz field magnitudes normalized to the nonlinear source term for generation in reflection (a) and and transmission (b) versus the optical and THz absorption coefficients α_ω and α_Ω, respectively. The figure is adapted from the appended Publication D [208]

reflected field magnitude depends weakly on the refractive index of the crystal and, thus, contains all the spectral information related to both the linear and nonlinear crystal properties at the laser and THz frequencies including phonons resonances at THz frequencies. Additionally, the magnitude of the reflected field is almost constant up to $\alpha_\omega \approx 10^6$ cm^{-1} and $\alpha_\Omega \approx 10^3$ cm^{-1} forming the yellow plateau, whereupon it quickly goes to zero. In contrast, the magnitude of the transmitted field decreases strongly when either the

laser or THz absorption increases and is almost null when $\alpha_\Omega > 10^3$ cm^{-1} or $\alpha_\omega > 10^7$ cm^{-1}, because the laser and/or THz fields does no longer propagate inside the crystal. In particular, the reflected field will naturally be stronger than the transmitted field for large absorption at laser frequencies For weak absorption, either at visible or THz frequencies, cumulative generation inside the crystal is possible and, thus, the transmitted THz field is much stronger ($\sim$ 10 times) than the reflected field. The difference between

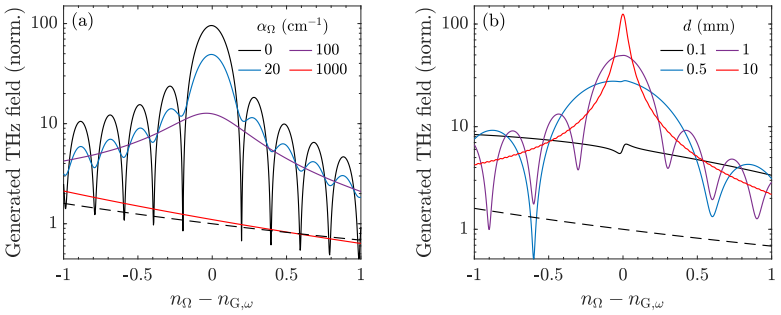

Fig. 3.3: Magnitude of the transmitted (continuous lines) and reflected (dashed line) THz field versus $n_{G,\omega} - n_\Omega$. (a) Calculation for different THz absorption values α_Ω for a 1.52-mm thick crystal assumed to be transparent at the laser wavelength $\lambda = 800$ nm. (b) Calculation for different crystal thicknesses for an assumed THz absorption $\alpha_\Omega = 20$ cm^{-1}. The curves are normalized to the reflected signal at $n_{G,\omega} - n_\Omega = 0$. The figure is taken from the appended Publication D [208].

the two fields can be emphasized by plotting the field magnitudes versus the difference $n_{G,\omega} - n_\Omega$, which is seen in Fig. 3.3 for a crystal transparent at the laser wavelength $\lambda = 800$ nm with $n_{G,\omega} = 3$ and $f = 1$ THz. The reflected field is only plotted for $\alpha_\Omega = 0$ cm^{-1} since dependency on the THz absorption is weak. In Fig. 3.3(a) the transmitted field is plotted for several values of α_Ω and normalized to the reflected signal at $n_{G,\omega} - n_\Omega = 0$. The transmitted field exhibits clear phase-match oscillations, which are attenuated and eventually erased with increasing THz absorption. Indeed, the reflected field is free of such phase-matching features. In case of strong THz absorption or the minima of the phase-match oscillations, the transmitted field becomes comparable to the reflected field. Typical values are $n_\Omega = 3.2$ and $n_{G,\omega} = 3.16$ at 1 THz and, thus, we see that $|E_R/E_T| \approx 1/90$. In Fig. 3.3(b) the transmitted field is calculated for different crystal thicknesses and $\alpha_\Omega = 20$ cm^{-1}. Here, we see that the oscillations in the transmission curves exhibit a shorter pseudo-periodicity for thinner crystals because of the phase-matching phenomenon. When phase-matching is realized, the transmitted field is 1-2 orders of magnitude stronger than the reflected field and overall the increasing crystal thickness makes up for the THz absorption. We can

conclude that THz generation by OR in transmission is the most efficient for common materials. However, the reflected THz field only has a weak dependency on the loss in the material, even for materials with strong absorption at both the laser and the THz frequencies, and does only vanish for opaque samples. Therefore, THz generation by OR in reflection can be useful only if the sample or the experiment does not allow for a measurement of the field generated in transmission. This could be the case if the sample has a rough rear face, is covered by nontransparent or diffracting layers, or in case of microscopy. Additionally, OR in reflection is requested if one wants to study any physical or chemical phenomena at the surface.

The generated THz fields in Eqs. (3.38) and (3.39) depend on the nonlinear source term $\overleftrightarrow{\tilde{\chi}}^{(2)} : \vec{E}_{\omega+\Omega} \cdot \vec{E}^{*}_{\omega}$ related to $\vec{P}^{\mathrm{NL}}_{\Omega,xyz}$, in which the nonlinear tensor $\overleftrightarrow{\tilde{\chi}}^{(2)}$ is known in the crystal frame (XYZ). A first rotation by θ around y followed by a second rotation by ϕ around z is required to switch from the laboratory to the crystal frame [209]. The associated rotation matrices are

$$R_y(\theta) = \begin{bmatrix} \cos\theta & 0 & \sin\theta \\ 0 & 1 & 0 \\ -\sin\theta & 0 & \cos\theta \end{bmatrix} \tag{3.43}$$

and

$$R_z(\phi) = \begin{bmatrix} \cos\phi & -\sin\phi & 0 \\ \sin\phi & \cos\phi & 0 \\ 0 & 0 & 1 \end{bmatrix}, \tag{3.44}$$

which can be simplified by the total rotation matrix $R(\phi,\theta) = R_z(\phi)R_y(\theta)$, *i.e.*

$$R\left(\phi,\theta\right) = \begin{bmatrix} \cos\phi\cos\theta & -\sin\theta & \cos\phi\sin\theta \\ \sin\phi\cos\theta & \cos\theta & \sin\phi\sin\theta \\ -\sin\theta & 0 & \cos\theta \end{bmatrix}. \tag{3.45}$$

The expression of the nonlinear polarization $\vec{P}^{\mathrm{NL}}_{\Omega,XYZ}$ is obtained with the expression of the laser field in the crystal frame, *i.e.*

$$\vec{E}_{\omega,XYZ} = R\left(\phi,\theta\right)\vec{E}_{\omega,xyz}. \tag{3.46}$$

Then, in order to get the nonlinear polarization in the laboratory frame, it is multiplied by the inverse rotation matrix $R^{-1}(\phi,\theta) = R_y(-\theta)R_z(-\phi)$, that is

$$R^{-1}(\phi,\theta) = \begin{bmatrix} \cos\theta & \sin\theta\sin\phi & -\sin\theta\cos\phi \\ 0 & \cos\phi & \sin\phi \\ \sin\theta & -\cos\theta\sin\phi & \cos\theta\cos\phi \end{bmatrix}. \tag{3.47}$$

Thus, we get

$$\vec{P}^{\mathrm{NL}}_{\Omega,xyz} = R^{-1}\left(\phi,\theta\right)\varepsilon_o\overleftrightarrow{\tilde{\chi}}^{(2)} : \left(R\left(\phi,\theta\right)\vec{E}_{\omega+\Omega,xyz}\right) \cdot \left(R\left(\phi,\theta\right)\vec{E}^{*}_{\omega,xyz}\right), \tag{3.48}$$

which must be calculated for each crystallographic class and each orientation of the crystal. Here, we address only cubic crystals (432, $\bar{4}3m$, 23) and the nonlinear susceptibility tensor takes the form [201]

$$\overleftrightarrow{\tilde{\chi}}^{(2)} = \begin{pmatrix} 0 & 0 & 0 & \tilde{\chi}_{14}^{(2)} & 0 & 0 \\ 0 & 0 & 0 & 0 & \tilde{\chi}_{14}^{(2)} & 0 \\ 0 & 0 & 0 & 0 & 0 & \tilde{\chi}_{14}^{(2)} \end{pmatrix}. \tag{3.49}$$

For the most common crystal cuts $\langle 100 \rangle$, $\langle 110 \rangle$ and $\langle 111 \rangle$, the rotation are

$$\theta = \frac{\pi}{2}, \phi = 0, \qquad \theta = \frac{\pi}{2}, \phi = \frac{\pi}{4} \qquad \theta = \arccos\left(\frac{1}{\sqrt{3}}\right), \phi = \frac{\pi}{4},$$

respectively. Gaborit *et al.* [209] has shown that this leads to the following dependence of the THz field on the laser polarization angle ψ:

$$\langle 110 \rangle \quad \rightarrow \quad \vec{E}_{\mathrm{R},\Omega}, \vec{E}_{\mathrm{T},\Omega} \propto \frac{1}{4} \begin{pmatrix} \cos 2\psi - 1 \\ -2 \sin 2\psi \\ 0 \end{pmatrix} \tag{3.50}$$

$$\langle 111 \rangle \quad \rightarrow \quad \vec{E}_{\mathrm{R},\Omega}, \vec{E}_{\mathrm{T},\Omega} \propto \frac{1}{\sqrt{6}} \begin{pmatrix} \cos 2\psi \\ -\sin 2\psi \\ -1/\sqrt{2} \end{pmatrix} \tag{3.51}$$

No generated THz signal propagates outside the $\langle 100 \rangle$ crystal at normal incidence.

2 Summary of Results

The experimental work on THz generation through OR in reflection was initiated at IMEP-LAHC in Chambéry and afterwards continued at Aalborg University. The work resulted in the appended Publication D published in the Journal of Applied Physics.

2.1 Experimental Work at IMEP-LAHC

The initial experimental setup for THz generation in reflection is depicted in Fig. 3.4. The setup resembled a traditional THz-TDS spectrometer. A beam of 45-fs polarized laser pulses at 1 kHz repetition rate was delivered by an amplified Ti:sapphire laser system from Coherent (Libra 7). The laser wavelength was centered at 800 nm, and the pulse energy was 4.7 mJ. A beam splitter (BS) divided the pulses into a reflected pump and a transmitted probe branch. A half-wave plate (HWP) and a mechanical chopper in the pump

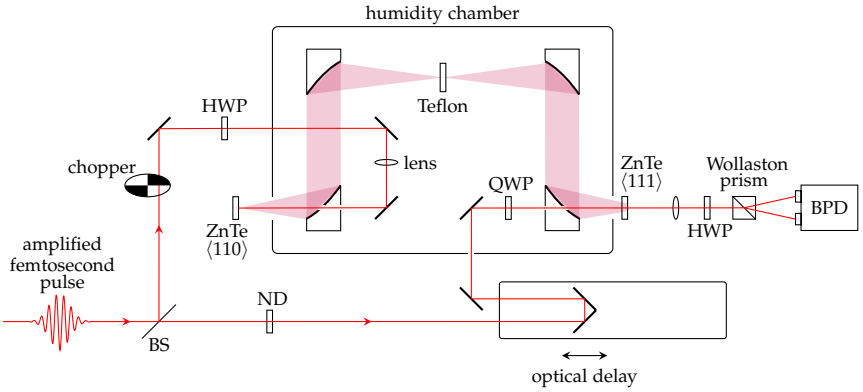

Fig. 3.4: Illustration of the initial experimental setup. BS, beam splitter; ND, neutral density filter; HWP, half-wave plate; QWP, quarter-wave plate; BPD, balanced two-photodiode.

beam controls the pump polarization and triggers the lock-in detection, respectively. The pump beam was focused by a 200-mm focal lens on a 1.52-mm thick ⟨110⟩-cut ZnTe crystal at normal incidence through a hole in an off-axis parabolic mirror (OAP). At the emitter crystal, the pump beam diameter was 1 mm and the average power was approximately 50 mW. The reflected THz radiation generated by OR was then collected by the same parabolic mirror, sent through a four OAP configuration and focused onto a 1-mm thick ⟨111⟩-cut ZnTe crystal for detection via electro-optic (EO) sampling. The majority of the THz path was placed in a humidity chamber and the measurements were performed at 5% relative humidity and room temperature. To block the back-reflected pump beam, a Teflon slab was placed at the THz waist. Before the EO crystal, the >1 mW probe beam was circularly polarized by a quarter-wave plate (QWP). In consequence of the THz induced birefringence in the EO crystal, the probe beam became elliptically polarized. Subsequently, the probe was sent through a Wollaston prism splitting it in two perpendicular polarizations, which were focused onto a balanced two-photodiode system (model Nirvana, New Focus). The signal from the balanced two-photodiode system was, in turn, recorded using a lock-in amplifier from Stanford Research Systems. The EO detection system was initially calibrated by placing a THz polarizer (Purewave Polarizers) in the THz path while optimizing the angle of the HWP, whereafter the former was removed. Hence, the EO detection scheme was ensured to be only sensitive to horizontally polarized THz radiation.

Fig. 3.5(a) shows two THz pulses separated by $\Delta t \approx 32.8$ ps (peak to peak). The first THz pulse R was generated by OR in reflection at the front surface of the crystal, while the later pulse T was generated in transmission. However, the T pulse could either be generated in transmission by the for-

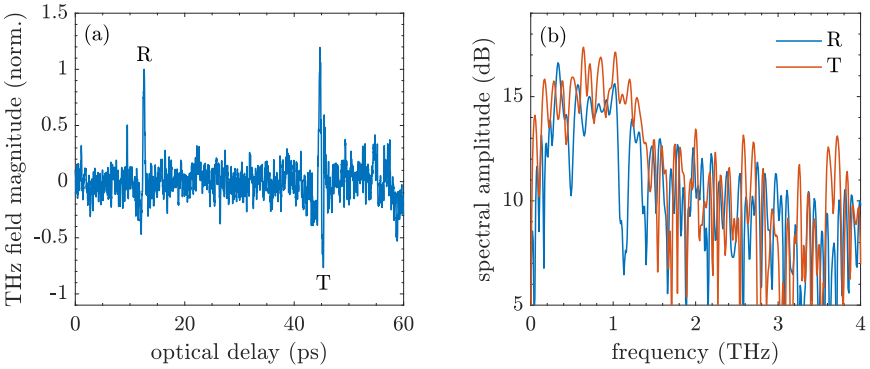

Fig. 3.5: (a) THz waveforms R and T of pulses generated by OR in reflection and transmission, respectively. The measurement has been normalized to maximum of the R pulse. (b) Spectra of the R and T waveforms.

ward going laser beam and, in turn, be reflected at the rear crystal surface and then transmitted through the front surface, or the laser pulse could propagate through the crystal, be reflected at the rear surface and then generate the T pulse as it counter propagates the crystal. In the former case, the time delay Δt between the two THz pulses is equal to $\Delta t = 2dn_{\mathrm{G},\Omega}/c \approx 2dn_{\Omega}/c$, because the additional optical path length of the T pulse is two times the crystal thickness times the THz group index compared to the R pulse. Using crystal thickness $d = 1.52$ mm and $n_{\Omega} = 3.20$ as measured around 1 THz, we get $\Delta t = 32.4$ ps by setting $n_{\mathrm{G},\omega} = 3.16$ in agreement with the measured delay. Let us compare the magnitude of the R and T pulses using Eq. (3.42). We must, however, multiply the transmitted THz field by $\tilde{r}_{\Omega}e^{-\alpha_{\Omega}d/2}$ to include the back reflection at the rear crystal surface and propagation through the crystal. For now, we assume that THz absorption inside the crystal is negligible (*i.e.* $\alpha_{\Omega} \approx 0$). The Fresnel reflection coefficient at normal incidence is $\tilde{r}_{\Omega} = (n_{\Omega} - n_{\mathrm{air}})/(n_{\Omega} + n_{\mathrm{air}}) \approx 0.52$ around 1 THz. In the previous section, we saw that $|E_{\mathrm{R}}/E_{\mathrm{T}}| \approx 1/90$ for the given values of n_{Ω} and $n_{\mathrm{G},\omega}$. When we take the reflection coefficient into account, we get $|E_{\mathrm{R}}/E_{\mathrm{T}}|_{\mathrm{calc}} \approx 1/47$ in contrast to the measured $|E_{\mathrm{R}}/E_{\mathrm{T}}| \approx 1/1.2$. In the latter case, the laser pulse and THz pulse each propagates through the crystal once. Hence, the time delay $\Delta t'$ between the two THz pulses is equal to $\Delta t' = \frac{d}{c}(n_{\mathrm{G},\omega} + n_{\mathrm{G},\Omega}) \approx \frac{d}{c}(n_{\mathrm{G},\omega} + n_{\Omega})$. Inserting the same values as before, we get $\Delta t' \approx 32.8$ ps, which is in perfect agreement with our measurement. In this case, we must multiply the transmitted THz field in Eq. (3.42) by $|\tilde{r}_{\omega}\tilde{t}_{\omega}e^{-\alpha_{\omega}d/2}|^2$ to take into account the transmission, reflection and propagation of the laser beam in the crystal. Similarly, if we assume that the crystal is transparent at the laser frequencies (*i.e.* $\alpha_{\omega} \approx 0$), we get $\tilde{r}_{\omega} = (n_{\mathrm{G},\omega} - n_{\mathrm{air}})/(n_{\mathrm{G},\omega} + n_{\mathrm{air}}) \approx 0.52$ and $\tilde{t}_{\omega} = 2n_{\mathrm{air}}/(n_{\mathrm{G},\omega+n_{\mathrm{air}}}) = 0.48$,

and thus the calculated ratio is $|E_R/E_T|_{calc} \approx 1/6$, which is still much smaller than the measured ratio. However, since the time delay agreed perfectly and the calculated ratio was closer to the measured ratio, we initially concluded that the T pulse was generated in transmission by the counter propagating laser pulse reflected at the rear surface inside the crystal.

Evidently, the recorded THz signals in Fig. 3.5 are very noisy. Hence, it was not possible to perform meaningful experiments regarding efficiency and polarimetry. The signal-to-noise ratio (SNR) could, however, readily be improved by several means. Obviously, the experimental setup was not explicitly designed for generation in reflection and could, thus, be improved by removing half of the OAPs to reduce the THz path. But even more importantly, there was a mismatch between the repetition rate of the laser and the available recording system (the lock-in amplifier). The 45-fs amplified laser system operates at 1 kHz. Thus, the resulting duty cycle of 4.5×10^{-11} is extremely low. The lock-in amplifier measures continuously in time throughout the on-time of the square-wave reference signal produced by the mechanical chopper. This implies that noise is recorded for most of the duration (the measured signal between the laser pulses) and, hence, results in a low SNR. In fact, boxcar averaging should be utilized for such a low duty cycle system for an optimal SNR. Here, the signal is recorded only during the laser pulse duration and the time intervals in-between are ignored. This corresponds to multiplying the signal by an rectangular pulse train (*i.e.* a boxcar function) with a period matched to the repetition rate of the laser. The signal can then be integrated over the duration of the boxcar width and, subsequently, be averaged over M periods. Alternatively, an improved SNR can be achieved using a lock-in amplifier by switching to a high repetition rate laser system like a Ti:sapphire oscillator typically operating at 100 MHz.

2.2 Experimental Work at AAU

Following the research stay at IMEP-LAHC, the experimental work was continued at AAU. A new experimental setup was build from scratch optimized for generation in reflection as illustrated in Fig. 3.6. To achieve an improved SNR by lock-in detection, a Ti:sapphire oscillator from Spectra-Physics operating at 80 MHz repetition rate was delivering a beam of linearly polarized 100-fs laser pulses. The laser wavelength was centered around 786 nm, and the pulse energy was 12.5 nJ. Similarly, a beam splitter divided the pulses into a pump and a probe branch. The optical delay was employed in the pump branch together with a mechanical chopper for lock-in detection and a HWP to control the pump polarization. The pump beam was focused by a 150-mm focal lens on the same $\langle 110 \rangle$-cut ZnTe crystal as utilized at IMEP-LAHC at normal incidence through a hole in an OAP. The spotsize diameter was measured using the knife-edge method and approx. 37 μm at the crys-

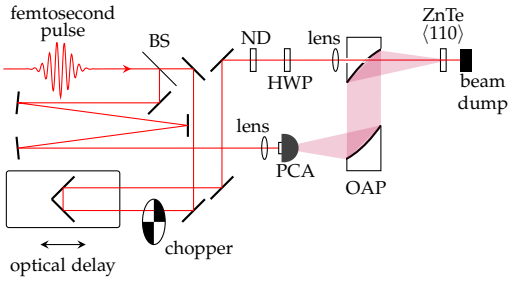

Fig. 3.6: Illustration of the experimental setup employed at AAU. BS, beam splitter; ND, neutral density filter; HWP, half-wave plate; PCA, photoconductive antenna.

tal. Additionally, the maximum average laser power was approx. 440 mW at the crystal without the chopper and could be controlled by a variable neutral density filter (ND). The THz path was simplified using only two OAPs. A first one to collect the generated THz fields and a second one to focus the THz fields onto a bow-tie PC antenna detector from BATOP GmbH. The detector was oriented to be sensitive to vertically polarized THz radiation. The measurements were all done under ambient conditions.

Fig. 3.7(a) shows THz waveforms recorded using the optimized setup. Immediately, the improved SNR is noticed but surprisingly the T pulse was

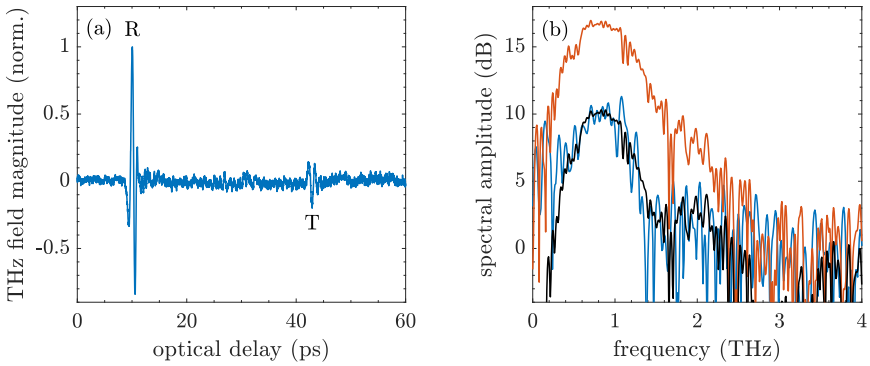

Fig. 3.7: (a) THz waveforms R and T of pulses generated by OR in reflection and transmission, respectively. (b) Spectra of the R (red) and T (blue) waveforms. The black curve is the calculated T spectra.

much weaker than the R pulse contrary to the theoretical expectations. The two pulses were again separated by $\Delta t \approx 32.8$ ps (peak to peak). Furthermore, we clearly notice that the T pulse was phase-inverted as it should be according to Eqs. (3.38)-(3.39). However, in opposition to our initial conclusion and as we shall see below, it seems more likely that the T pulse was

generated in transmission by the forward going laser beam and, in turn, reflected at the rear crystal surface and then transmitted through the front surface. In this case, we calculate the time delay as before $\Delta t \approx 2dn_\Omega/c \approx 32.4$ ps using $d = 1.52$ mm and $n_\Omega = 3.20$ as measured around 1 THz. This is still in good agreement with the measured delay, and the difference of 0.4 ps corresponds to an 1% error in the refractive index n_Ω. Let us recall that $|E_R/E_T|_{calc} \approx 1/47$. In Fig. 3.7(a), we find that the THz peak-to-peak magnitude of R relative to T is $|E_R/E_T| \approx 7$ in strong contrast to what we found in Fig. 3.5. After fruitful discussions with Prof. F. Laurell and Prof. V. Pasiskevicius from the Department of Applied Physics at Royal Institute of Technology in Stockholm (Sweden), we realized that this could be related to the much higher repetition rate of the Ti:sapphire oscillator compared to the amplified laser system. The photogenerated carrier lifetime of ZnTe is $\tau_{ZnTe} = 25$ ns [210], while the pulse period of the Ti:sapphire oscillator is 12.5 ns. Thus, a steady-state population of photogenerated free carriers could build up through a two-photon absorption (TPA) process, which could decrease the THz generation through the crystal and, in turn, absorb the THz radiation reflected at the rear crystal surface.

Let us estimate the TPA-induced THz absorption $\alpha_\Omega = 2\Omega\kappa_\Omega/c$. First, in the experiment the laser peak power density at the crystal is

$$D \approx \frac{E_{pulse}}{\tau_{pulse}\phi_s} \tag{3.52}$$

with E_{pulse} being the laser pulse energy, τ_{pulse} the pulse duration and ϕ_{pulse} the spotsize. Here, the laser pulse energy is modeled to be uniform during the pulse duration. The pulse energy is proportional to the average power $\bar{P}$ and the laser repetition rate f_{rep}, *i.e.* $E_{pulse} = \bar{P}/f_{rep}$. Let us now develop the laser intensity inside the crystal as

$$I(z + dz) - I(z) = -\left(\alpha I(z) + \beta I^2(z)\right) dz, \tag{3.53}$$

where α and β are the linear and TPA absorption coefficients at the laser frequency, respectively. Eq. (3.55) is equivalent to the differential equation

$$\frac{dI(z)}{dz} = -\alpha I(z) - \beta I^2(z), \tag{3.54}$$

which is solved by integration:

$$\int \frac{dI}{\alpha I + \beta I^2} = -\int dz = -z. \tag{3.55}$$

The fraction under the left hand side integral can be rewritten as

$$\frac{1}{\alpha I + \beta I^2} = \frac{1}{\alpha}\left(\frac{1}{I} - \frac{\beta}{\alpha + \beta I}\right). \tag{3.56}$$

Hence, we have

$$\frac{1}{\alpha}\left(\int \frac{\mathrm{d}I}{I} - \beta \int \frac{\mathrm{d}I}{\alpha + \beta I}\right) = \frac{1}{\alpha}\left(\ln(I) - \ln(\alpha + \beta I)\right) + C = -z, \tag{3.57}$$

where C is the integration constant. Rearranging Eq. (3.57), we get

$$\ln\left(\frac{I}{\alpha + \beta I}\right) = \alpha C - \alpha z \quad \Rightarrow \quad \frac{I}{\alpha + \beta I} = A e^{-\alpha z}. \tag{3.58}$$

The coefficient A is determined at crystal entrance (at $z = 0$), *i.e.*

$$\frac{I(z)}{\alpha + \beta I(z)} = \frac{I(0)}{\alpha + \beta I(0)} e^{-\alpha z} \quad \Rightarrow \quad I(z) = \frac{I(0) e^{-\alpha z}}{1 + \frac{\beta}{\alpha} I(0)\left(1 - e^{-\alpha z}\right)}. \tag{3.59}$$

Since the ZnTe is transparent at the laser frequency, we can neglect the linear absorption, thus,

$$I(z) = \lim_{\alpha \to 0} \frac{I(0) e^{-\alpha z}}{1 + \frac{\beta}{\alpha} I(0)\left(1 - e^{-\alpha z}\right)} = \frac{I(0)}{1 + \beta I(0) z}. \tag{3.60}$$

Here, we have applied L'Hôpital's rule from calculus, *i.e.*

$$\lim_{x \to 0} \frac{f(x)}{g(x)} = \lim_{x \to 0} \frac{f'(x)}{g'(x)}. \tag{3.61}$$

The absorbed laser intensity due to the TPA effect is therefore

$$\Delta I = I(0) - I(d) = \frac{\beta I(0) d}{1 + \beta I(0) d} I(0). \tag{3.62}$$

The laser intensity at the crystal entrance is $I(0) = T_\omega D$ with transmission coefficient $T_\omega = (2/(n_{\mathrm{G},\omega} + 1))^2$. The number of absorbed photons for each pulse is proportional to the absorbed intensity, thus, we can write

$$\frac{\Delta I}{I(0)} = \frac{N_{\mathrm{abs}}}{N_{\mathrm{pulse}}(0)} \quad \Rightarrow \quad N_{\mathrm{abs}} = \frac{\Delta I}{I(0)} N_{\mathrm{pulse}} = \frac{\Delta I}{I(0)} \frac{E_{\mathrm{pulse}}}{\hbar\omega} \tag{3.63}$$

with $E_{\mathrm{pulse}} = N_{\mathrm{pulse}} \hbar\omega$. Let us assume that the corresponding generated carrier density is uniform throughout the crystal, which can then be written as

$$n_{\mathrm{TPA}} = \frac{N_{\mathrm{abs}}}{\phi_{\mathrm{s}} d}. \tag{3.64}$$

Here, we are only interested in the mean carrier density and, hence, we will not consider dynamics of the TPA carrier density. Due to the laser pulse train effect, the carrier density accumulates over time. When a second pulse hits the crystal, the carrier density from the former pulse is down by $e^{-\Delta\tau}$, where

$\Delta\tau = \tau_{\text{rep}}/\tau_{\text{rc}}$ is the ratio of the time delay between two consecutive laser pulses $\tau_{\text{rep}} = 1/f_{\text{rep}}$ and the free carrier lifetime τ_{rc}. After M pulses, we have

$$\begin{aligned} s_M = \sum_{m=1}^{M} e^{-m\Delta\tau} &= e^{-\Delta\tau} + \cdots + e^{-M\Delta\tau} \\ &= e^{-\Delta\tau}\left(1 + e^{-\Delta\tau}\cdots + e^{-(M-1)\Delta\tau}\right) \\ &= e^{-\Delta\tau}\left(1 + s_M - e^{-M\Delta\tau}\right), \end{aligned} \tag{3.65}$$

which implies

$$s_M = \frac{e^{-\Delta\tau} - e^{-(M-1)\Delta\tau}}{1 - e^{-\Delta\tau}} \quad \rightarrow \quad \frac{e^{-\Delta\tau}}{1 - e^{-\Delta\tau}} \quad \text{for} \quad M \rightarrow \infty. \tag{3.66}$$

Thus, the mean density is

$$\bar{n}_{\text{TPA}} = n_{\text{TPA}} \frac{e^{-\Delta\tau}}{1 - e^{-\Delta\tau}} = n_{\text{TPA}} \frac{1}{e^{\Delta\tau} - 1}. \tag{3.67}$$

We can now apply the Drude model

$$\tilde{\varepsilon}_\Omega = \varepsilon_\infty - \frac{\omega_{\text{p}}^2}{\Omega(\Omega + j\Gamma)} \quad \text{with} \quad \omega_{\text{p}}^2 = \frac{\bar{n}_{\text{TPA}} e^2}{m_{\text{eff}} \varepsilon_o}. \tag{3.68}$$

to determine κ_Ω. Here, $\tilde{\varepsilon}_\Omega = (n_\Omega + j\kappa_\Omega)^2$ is the complex permittivity, ω_{p}^2 the plasma frequency, n_{TPA} the TPA photocarrier density, m_{eff} the effective mass of the free electrons, Γ the damping angular frequency, and e the electron charge. From Eq. (3.68) we can deduce the real and imaginary parts of the complex permittivity,

$$\varepsilon_{\text{r}} = \epsilon_\infty - \frac{\omega_{\text{p}}^2}{\Omega^2 + \Gamma^2} = n_\Omega^2 - \kappa_\Omega^2 \quad \text{and} \quad \varepsilon_{\text{i}} = -\frac{\omega_{\text{p}}^2 \Gamma}{\Omega(\Omega^2 + \Gamma^2)} = 2 n_\Omega \kappa_\Omega, \tag{3.69}$$

using the identities $\text{Re}\{z\} = \frac{1}{2}(z + z^*)$ and $\text{Im}\{z\} = \frac{1}{2j}(z - z^*)$. Substituting $n_\Omega = \varepsilon_{\text{i}}/(2\kappa_\Omega)$ into $\varepsilon_{\text{r}} = n_\Omega^2 - \kappa_\Omega^2$, it follows that

$$\kappa_\Omega^4 + \epsilon_{\text{r}} \kappa_\Omega^2 - \frac{\varepsilon_{\text{i}}^2}{4} = 0 \quad \Rightarrow \quad \kappa_\Omega = \sqrt{\frac{\sqrt{\varepsilon_{\text{r}}^2 + \varepsilon_{\text{i}}^2} - \varepsilon_{\text{r}}}{2}}. \tag{3.70}$$

Finally, we can estimate the TPA-induced THz absorption $\alpha_\Omega = 2\Omega\kappa_\Omega/c$. Using the TPA coefficient $\beta \approx 5$ cm/GW [211], $\tau_{\text{rc, ZnTe}} \approx 25$ ns [210], $\epsilon_\infty = n_\Omega^2$ with $n_\Omega = 3.2$ as measured at $f = 1$ THz, $\Gamma = 20$ THz [212] and $m_{\text{eff}} = 0.15 \times m_e$ [213] together with the experiment parameters, we obtain $\alpha_\Omega \approx 80$ cm^{-1}. Likewise, we can fit the modified Eq. (3.42) (multiplied by $\tilde{r}_\Omega e^{-\alpha_\Omega d/2}$

in the denominator) to the measured ratio $|E_R/E_T| \approx 7$. In this case, we find $\alpha_\Omega \approx 77$ cm^{-1} in good agreement with our estimate. The slightly lower measured absorption coefficient is expected, because we do not take into account the change in THz transmission and reflection due to the increased THz absorption, as well as a non-uniform distribution of the free carriers in the sample.

The THz spectra associated with waveform R and T are shown in Fig. 3.7(b). When disregarding water vapor absorption lines, the R spectrum (red) is fairly smooth, while the T spectrum (blue) exhibits the well-known sinc function pattern with a first zero at ∼1.5 THz, which agrees with the cut-off frequency $f_{\mathrm{cut-off}} = c/\pi d(n_\Omega - n_{G,\omega}) \approx 1.57$ THz related to non-optimal phase-matching. Therefore, the T spectrum is also narrower than the R spectrum. The lower SNR of the T spectrum is due to the attenuated intensity by linear and TPA absorption when propagating backwards in the crystal as explained above. The R spectrum extending up to 2.7 THz is limited by the bandwidth (-20 dB limit) of the bow-tie PC antenna detector. The actual R spectrum may be directly proportional to laser pulse spectral width, since the THz pulse generated in reflection is only weakly dependent on the crystal absorption. Thus, it could reach some tens of THz with sub-100 fs laser pulses. However, detection of such broadband R pulses would require a very sensitive detector because of the inherent weak magnitude of the R pulses. Typically, sensitive detectors like bolometers exhibit a long response time. This could be overcome by performing an interferometric measurement as is developed for SHG spectroscopy in the appended Publication E. In that case, the recorded signal will be the autocorrelation trace of the generated THz pulses. Previously, we concluded that the T waveform originates from a THz pulses generated in transmission and subsequently reflected at the rear crystal surface. Thereby, the T spectrum should be equal to the R spectrum multiplied by the calculated ratio $\tilde{r}_\Omega e^{-\alpha_\Omega d/2} \left| E_{T,\Omega} / E_{R,\Omega} \right|$, which takes into account the the reflection and absorption through the crystal. In particular, this is true since both the R and T waveforms are recorded by the same detector and, hence, it allow us to get rid of the setup's spectral response. As before, we apply the Drude model to calculate the TPA-induced THz absorption, but this time the only adjustable variable is the free carrier density. The black curve plotted in Fig. 3.7(b) is the calculated T spectrum, which evidently makes an excellent fit to the measured T spectrum for a carrier density of 1.19×10^{15} cm^{-3}. Conversely, we can estimate the photogenerated carrier density through Eq. (3.64) and laser power applied for the measurement, in which case we obtain a carrier density of 6.49×10^{15} cm^{-3}. The agreement between the two values is reasonable, when we take into account that we neglect the TPA effect in nonlinear propagation equation, which if included would result in a higher estimate of the carrier density from the fitted T spectrum.

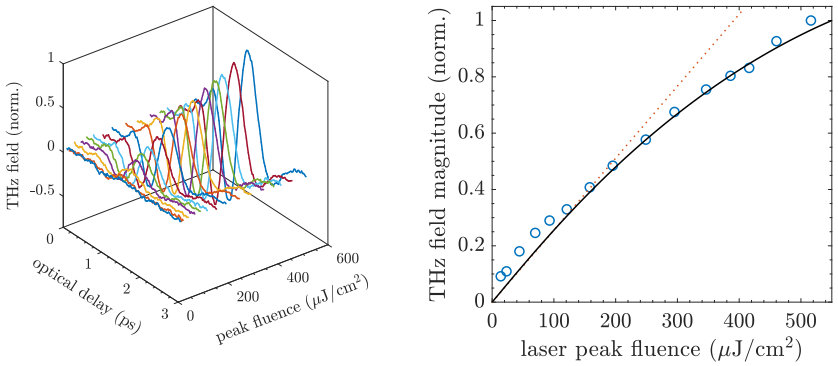

Fig. 3.8: Measured R pulse waveforms and peak magnitude (circles) versus laser peak fluence, respectively. The dotted straight line is a linear fit, while the continuous black curve is calculated taking into account the TPA effect.

Next, we studied the efficiency of THz generation in reflection via OR. The recorded THz waveforms and corresponding THz field maxima (circles) of the R pulse are plotted versus pump laser fluence in Fig. 3.8, respectively. Additionally, a linear fit (dotted) and a TPA-induced saturation fit (black) are calculated for the maximum THz field magnitudes on the right. The efficiency is linear for low pump laser fluences and TPA-induced saturation is seen from 200 μJ/cm^2 in good agreement with published results on THz generation in transmission through OR in ZnTe [214]. In accordance with the discussion above, this saturation is explained by the TPA-induced THz absorption. It is a comprehensive task to carry out an stringent analysis of this phenomena, which requires one to solve the coupled nonlinear propagation equations including the TPA effect. In particular, propagation equations are typically solved in the frequency-domain, while carrier population dynamics generally are treated in the time-domain. Thus, it is beyond the framework of this thesis. Nevertheless, we can evaluate the order of magnitude of the TPA effect. Notice that both refractive indices $\tilde{n}_\Omega$ and $\tilde{n}_{G,\omega} \propto \tilde{n}_\omega$ at the THz and the laser frequencies, respectively, are modified by the TPA photocarrier population. Let us recall the magnitude of the reflected THz field given in Eq.(3.40):

$$\left|\vec{E}_{R,\Omega}\right| / \left|\overleftrightarrow{\chi}^{(2)} : \vec{E}_{\omega+\Omega} \cdot \vec{E}^*_\omega\right| = \left|\left(\tilde{n}_\Omega + 1\right)\left(\tilde{n}_{G,\omega} + \tilde{n}_\Omega\right)\right|^{-1}.$$

Evidently, TPA-induced changes will affect the reflected field as well. The Kerr effect the TPA effect can respectively cause variations Δn_ω and $\Delta\kappa_\omega$ in the real and imaginary parts of $\tilde{n}_{G,\omega}$. The related coefficients are $n_2 \approx 5 \times 10^{-18}$ m^2/W and $\beta = 5$ cm/GW in ZnTe[215]. Using Eq. (3.52), we find that the maximum laser intensity in the experiment is $I_{max} \approx 5.5$ GW/cm^2

and, thus, we obtain $\Delta n_\omega \approx 2.5 \times 10^{-4}$ and $\Delta \kappa_\omega \approx 2 \times 10^{-4}$. Therefore, we conclude that photoinduced variation of $\tilde{n}_{G,\omega}$ is too small to explain the saturation seen in Fig. 3.8. To address the variation of THz refractive index $\tilde{n}_\Omega$, we will once again employ the Drude model to include the influence of the TPA photocarrier population using the optical parameters of ZnTe determined by Constable and Lewis [213] ($m_{\text{eff}} = 0.151 \times m_e$, $\varepsilon_\infty = 7.3$ and $\Gamma = 0.3$ THz). The real and imaginary parts of the resulting refractive index

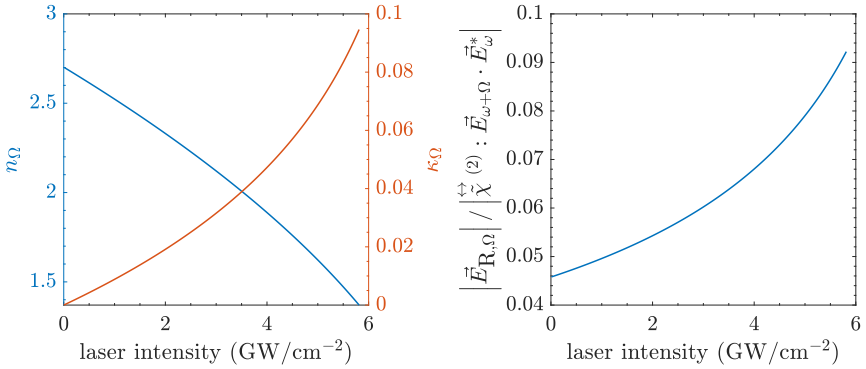

Fig. 3.9: Calculated variations of photoinduced variation of $\tilde{n}_\Omega = n_\Omega + j\kappa_\Omega$ (left) and the effect on the THz field generated in reflection (right) versus laser intensity.

$\tilde{n}_\Omega$ together with the magnitude of the reflected THz field normalized to the source term are plotted versus the laser intensity in Fig. 3.9 We see that TPA induces both a decrease in the refractive index and an increase of absorption at THz frequencies. Further, we see that the decrease in refractive index has a greater impact on the generated THz field than the increased absorption, which results in a slight increase of the reflected field with increasing laser intensity. Thus, the explanation of the saturation effect is neither to be found here. Consequently, the saturation must be related to photoinduced modifications of the nonlinear susceptibility. In a classical model for the nonlinear susceptibility [201, 216], the magnitude of the nonlinear susceptibility $\overleftrightarrow{\tilde{\chi}}^{(2)}$ is proportional to the magnitudes of the linear susceptibilities at ω and Ω, *i.e.*

$$\begin{aligned}\left|\overleftrightarrow{\tilde{\chi}}^{(2)}\right| &\propto \left|\left(\overleftrightarrow{\tilde{\chi}}_\omega^{(1)}\right)^2 \overleftrightarrow{\tilde{\chi}}_\Omega^{(1)}\right| \\ &= \left|\left(\tilde{\varepsilon}_\omega - 1\right)^2 \left(\tilde{\varepsilon}_\Omega - 1\right)\right| \\ &= \left|\left((n_\omega + j\kappa_\omega)^2 - 1\right)^2 \left((n_\Omega + j\kappa_\Omega)^2 - 1\right)\right|.\end{aligned} \tag{3.71}$$

Let us modify Eq.(3.64) in the Drude model to include the coefficient η, *i.e.*

$$n_{\mathrm{TPA}} = \eta \frac{N_{\mathrm{abs}}}{\phi_{\mathrm{s}} d}, \tag{3.72}$$

which accounts for the dynamics of the photocarrier population including carrier lifetime, diffusion inside the sample, *etc.*. Using the same parameters for the Drude model as previously, we can calculate the term $\left|\overleftrightarrow{\tilde{\chi}}^{(2)}\right| I_\omega$ of Eq. (3.38). The continuous black curve in Fig. 3.8 is the normalized result. Here, we used η as the only adjustable parameter. The excellent fit with our experimental data is obtained for $\eta = 0.259$, meaning that roughly a quarter of the photoexcited carriers interact with the THz pulse generated in reflection. As mentioned in our paper [208] (appended Publication D) *"The reason could be that they both recombine and diffuse inside the sample (Dember effect, both longitudinal and transversal[33,34]) in between two successive laser pulses."* It should be emphasized that this model is crude and the explanations must be validated by an exhaustive study as mentioned above. Nonetheless, the change in the nonlinear susceptibility seems to be the predominant consequence of the strong TPA effect.

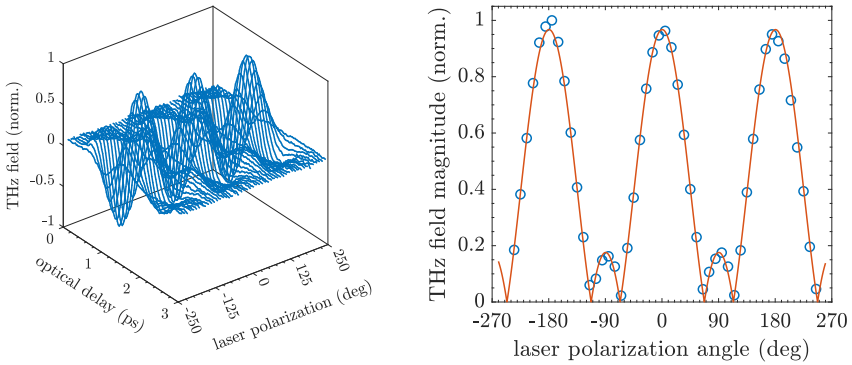

Fig. 3.10: Polarimetric pulse trace measurements of the R pulse (left). The peak THz field magnitudes are plotted versus laser polarization angle as circles and fitted with the model by the red continuous line (right).

In Fig. 3.10, we see the recorded THz waveforms of the R pulse versus the pump laser polarization angle $\psi = 2\psi_{\mathrm{HWP}}$, which is scanned 360° in 5° steps by adjusting the half-wave plate angle ψ_{HWP}. The peak of the THz field magnitudes are plotted as circles versus ψ in the figure to the right. Since the PC antenna used for detection does not completely discriminate the perpendicular polarization due to its bow-tie antenna geometry, we must fit a weighted expression

$$(1-\gamma) E_{\mathrm{R},\Omega,x} + \gamma E_{\mathrm{R},\Omega,y} \tag{3.73}$$

of the field components given in Eqs. (3.50) and (3.51). Further, the fit considers the disorientation of the crystal axes compared to the laboratory frame via an angular shift $\delta\psi$. The best fit as shown in Fig. 3.10 (the red continuous line) is found for $\gamma = 0.34$ and $\delta\psi = 66.5°$, which corresponds to a cross polarization sensitivity of 10%, within the specifications given by BATOP GmbH. This shows that information of the crystalline orientation of sample is embedded in the reflected THz signal.

3 Conclusion

As concluded in the published paper [208] (appended Publication D), *"we experimentally demonstrated the generation of a reflected THz signal at normal incidence through OR in a ZnTe crystal. The reflected signal originates in the boundary conditions for the nonlinear fields at the crystal surface. All the characteristics of THz OR generation in the crystal (polarization symmetry, spectral features...) are retrieved in the reflected signal. Its bandwidth is wider than in transmission, because it is not limited by absorption losses in the crystal. At high laser power excitation, the reflected THz signal from ZnTe saturates: It seems that its origin is the effect of TPA, which reduces the magnitude of the second order nonlinear susceptibility. However, for crystals of common mm-thickness that are transparent or exhibit moderate absorption in both the THz and visible domains, the THz reflection magnitude is much smaller than the one in transmission. When dealing with crystals that are opaque in one or both of these spectral domains, or whose rear surface is rough or covered by opaque films like metals, the reflected THz signal is of great interest since the transmitted THz signal is weak or even zero. This could be applied to THz microscopy of opaque materials, like humid biological samples, e.g. when performing sub-wavelength OR THz imaging.[7,8]"*

Chapter 4

Outlook

In the following sections, we will outline some perspectives of future directions of THz stand-off spectroscopy and THz generation through OR in reflection, respectively.

1 Prospects of Terahertz Stand-Off Detection

THz stand-off detection of explosives is still current, whether it is in relation to the safety of critical infrastructure like airports or to prevent improvised explosive devices and roadside bombs.

It is clear from the DETRIS project that the technology is still not mature for field applications. This is mainly due to lack of powerful THz emitters and sensitive THz receivers. However, tremendous progress have been made in the development of both THz emitters and receivers since the project started. For example, commercial electronic THz sources based on frequency multipliers[a] are now able to operate above 3 THz. Similarly, compact quantum cascade lasers (QCLs) with cryogenic free cooling[b] can now produce powerful THz radiation at multiple discrete frequencies in the 2.5 - 5 THz range have become commercially available. In Fig. 4.1 we have plotted the power spectrum of a PC antenna as estimated from TDS (see Sec. 2) together with typical power levels of THz photomixers based on PIN photodiodes (PDs), electronic sources and QCLs for comparison. Generally, the high output power of the monochromatic CW electronic sources comes at the cost of limited tuneability. Several individual sources are, hence, required to cover the spectral region up to 3.2 THz. There are, however, still a few dead regions, *e.g.* , from 0.74-0.8 THz, 1.17-1.32 THz, 1.54-1.71 THz and 2.15-2.48 THz. The

[a] See, *e.g.* , the custom transmitters made by Virginia Diodes Inc.

[b] *e.g.* , the TeraCascade 2000 series by Lytid SAS.

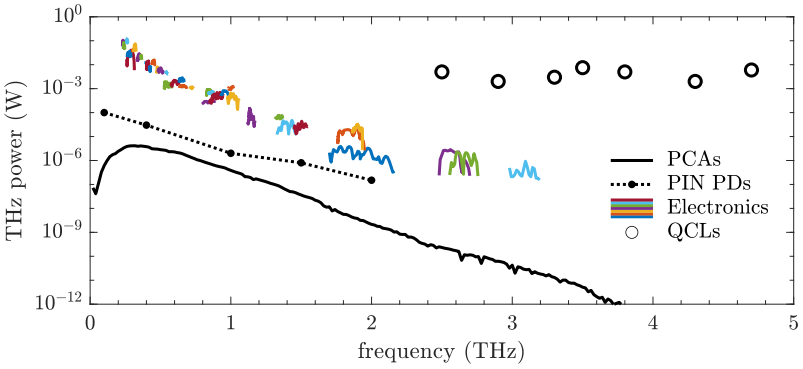

Fig. 4.1: Comparison of available output power from different THz sources. The colored continuous lines are power spectra adapted from custom electronic transmitters by Virginia Diodes Inc. The QCL data is adapted from Lytid SAS's TeraCascade 2000 series.

same apply for the QCLs operating in the upper THz band from 2.5 THz.

Very recently, Murate *et al.* [217] investigated how feature selection ML algorithms can applied to THz spectroscopic imaging of reagents hidden by thick shielding materials. In contrast to the feature extraction algorithms, which we applied in this thesis, feature selection algorithms select a subset of the original frequency components containing the most relevant information and discard the remaining ones. The study by Murate *et al.* included 852 transmission spectra of lactose, maltose and glucose. Each spectrum consisted of 70 frequency components between 1.1 and 1.8 THz. They found that the materials could be identified with almost 100% accuracy using only seven of the 70 frequency components. The seven selected frequency components were chosen according to the largest contribution ratios (calculated by the ML algorithm). As intuitively expected, the largest contributions came from the frequency components near the absorption peaks. Concurrently, we have investigated the performance of different feature selection algorithms on THz reflection spectra. Here, we will not discuss our work in details (manuscript in preparation). However, our main result shows that we can retain $\geq$ 95% accuracy by retaining only 10 of the >800 initial frequency components. Furthermore, the frequency components selected by the ML algorithms were not strictly chosen according to the absorption features of the samples. This is a remarkable result as it allows for identification of substances using only a few THz sources emitting at selected discrete frequencies. That is, broad spectra are not necessarily requisite in order to accurately identify different compounds via THz spectroscopy. This together with powerful monochromatic sources (*e.g.*, electronic sources or QCLs) could in particular pave the way for THz stand-off detection of explosives and other hazardous substances, in contrast to Kemp's conclusions in Ref. [159].

2 Future Studies of Optical Rectification

As mentioned in Chapter 3, a long-term perspective for ORTI is to achieve sub-wavelength THz images of biological samples through OR, like it is commonly done using SHG and THG. It should however be noted that it is not without challenges to apply ORTI to biological samples. First of all due to much weaker nonlinear conversion (3 orders of magnitude) compared to SHG due to the Manley-Rowe energy conservation law. Second, there exists no detectors which can facilitate photon-counting of the weak THz signal, as for SHG and THG. Nonetheless, THz generation via OR must be further studied, while the technology certainly develops and matures. Clearly, it is pertinent to demonstrate ORTI microscopy in reflection, which is needed for, *e.g.*, opaque samples. Additionally, THz generation in reflection does not suffer from dispersion and/or attenuation effects related to propagation through the crystal. Thus, the THz bandwidth is expected to be directly proportional to the laser bandwidth (*i.e.*, inversely proportional to the laser pulse duration). Therefore, laser pulses of sub 100-fs duration should produce very large broadband THz pulses. A natural next step would be to record these ultra broadband THz pulses generated in reflection. In common THz-TDS systems, the bandwidth is limited by the receiver response. Using a PC antenna receiver, the bandwidth is roughly limited to 6 THz. Electro-optic (EO) sampling can facilitate larger bandwidths (up to 40-50 THz [218]) using very thin EO crystals, however, at the cost of sensitivity (and vice versa). We learned that THz signals generated in reflection are rather weak. Thus, broad bandwidth EO sampling using a thin insensitive crystal is neither adequate. Instead, we can apply the Fourier transform approach, we developed in Publication E for SHG. This methodology will allow us to use a slow but very

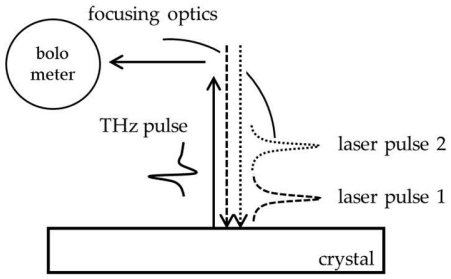

Fig. 4.2: Experimental scheme for time-resolved broadband measurements based on the Fourier transform approach in Publication E.

sensitive detector (*e.g.*, a bolometer), as illustrated in Fig. 4.2. Here, two delayed laser pulses are used for THz generation. The temporal resolution

is then achieved by controlling the delay between the two pulses. Of course, varioius experiments can be conducted using this approach. The scheme illustrated in Fig. 4.2 assumes normal incidence of the lasers pulses but a similar setup can be designed for oblique incidence. Furthermore, the THz generation can be studied at normal incidence in view of different polarizations of the two laser pulses.

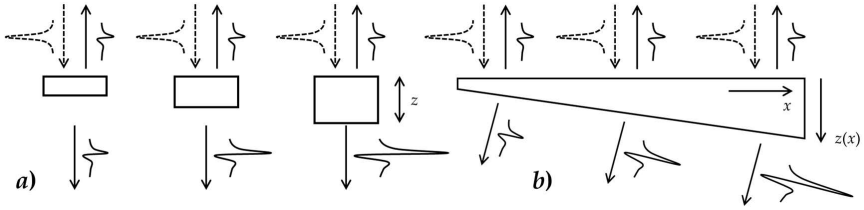

Fig. 4.3: THz generation through OR versus sample thickness. a) With different samples and b) with a single wedged-shaped sample. The dashed line indicates the laser pulse, while the THz pulses are drawn with continuous lines.

Another obvious experiment would be to study the THz generation versus the crystal thickness. This could either be examined with samples of different thicknesses [Fig. 4.3 a)] or with a single wedged-shaped sample [Fig. 4.3 b)], which can be continuously scanned laterally to change the effective crystal thickness. In both experiments, the reflected signal should remain constant, while the THz signal generated transmission is expected to follow the well-known sinc-dependence. Evidently, the wedged sample will refract the transmitted THz signal at the angled crystal rear face. However, if the wedge angle is small and large aperture optics are used to collect the THz signal, it should be possible to measure the back-reflection of the transmitted THz from the rear crystal face, as we did in Publication D.

These are just a few examples of future experiments. Other very interesting studies include, *e.g.*, the effect of a surface layer, which alters the boundary conditions, from which the reflected field originates, and to scan the pump laser over a polycrystalline or inhomogeneous sample to obtain a two-dimensional map of the reflected THz signal.

References

[1] Jean-Louis Coutaz, Frederic Garet, and Vincent P. Wallace. *Principles of Terahertz Time-Domain Spectroscopy*. Pan Stanford Publishing, 2018.

[2] Yun-Shik Lee. *Principles of Terahertz Science and Technology*. Springer, 2009.

[3] Daniel M. Mittleman. *Sensing with Terahertz Radiation*. Ed. by Daniel M. Mittleman. 1st ed. Springer, 2003.

[4] C. H. Townes and A. L. Schawlow. *Microwave Spectroscopy*. Second. Dover Publications, 2012.

[5] Peter R. Griffiths and James A. De Haseth. *Fourier Transform Infrared Spectrometry*. Second. Wiley, 2007.

[6] P. U. Jepsen, D. G. Cooke, and M. Koch. "Terahertz spectroscopy and imaging - Modern techniques and applications". In: *Laser and Photonics Reviews* 5.1 (2011), pp. 124–166.

[7] Frank C. De Lucia. "Spectroscopy in the Terahertz Spectral Region". In: *Sensing with Terahertz Radiation*. Ed. by Daniel M. Mittleman. 1st ed. Springer, 2003, pp. 39–115.

[8] Mira Naftaly, Nico Vieweg, and Anselm Deninger. "Industrial applications of terahertz sensing: State of play". In: *Sensors (Switzerland)* 19.19 (2019).

[9] Ryan M. Smith and Mark A. Arnold. "Selectivity of Terahertz Gas-Phase Spectroscopy". In: *Analytical Chemistry* 87.21 (2015), pp. 10679–10683.

[10] R. A. Lewis. "A review of terahertz sources". In: *Journal of Physics D: Applied Physics* 47.37 (2014).

[11] R. A. Lewis. "A review of terahertz detectors". In: *Journal of Physics D: Applied Physics* 52.43 (2019).

[12] K. Sakai. *Terahertz Optoelectronics*. Ed. by K. Sakai. Springer, 2005.

[13] Jens Neu and Charles A. Schmuttenmaer. “Tutorial: An introduction to terahertz time domain spectroscopy (THz-TDS)”. In: *Journal of Applied Physics* 124.23 (2018).

[14] Hichem Guerboukha, Kathirvel Nallappan, and Maksim Skorobogatiy. “Toward real-time terahertz imaging”. In: 10.4 (2018), pp. 843–938.

[15] E. R. Brown et al. “Photomixing up to 3.8 THz in low-temperature-grown GaAs”. In: *Applied Physics Letters* 285.1995 (1995), p. 285.

[16] Dennis Stanze et al. “Compact cw terahertz spectrometer pumped at 1.5 μm wavelength”. In: *Journal of Infrared, Millimeter, and Terahertz Waves* 32.2 (2010), pp. 225–232.

[17] Anselm J. Deninger et al. “2.75 THz tuning with a triple-DFB laser system at 1550 nm and InGaAs photomixers”. In: *Journal of Infrared, Millimeter, and Terahertz Waves* 36.3 (2015), pp. 269–277.

[18] D. Stanze et al. “Coherent CW terahertz systems employing photodiode emitters”. In: *34th International Conference on Infrared, Millimeter, and Terahertz Waves, IRMMW-THz 2009* (2009), pp. 6–8.

[19] Axel Roggenbuck et al. “Using a fiber stretcher as a fast phase modulator in a continuous wave terahertz spectrometer”. In: *Journal of the Optical Society of America B* 29.4 (2012), p. 614.

[20] A. Roggenbuck et al. “Coherent broadband continuous-wave terahertz spectroscopy on solid-state samples”. In: *New Journal of Physics* 12 (2010), pp. 1–13.

[21] Dominik Walter Vogt and Rainer Leonhardt. “High resolution terahertz spectroscopy of a whispering gallery mode bubble resonator using Hilbert analysis”. In: *Optics Express* 25.14 (2017), p. 16860.

[22] Dominik Walter Vogt, Miro Erkintalo, and Rainer Leonhardt. “Coherent Continuous Wave Terahertz Spectroscopy Using Hilbert Transform”. In: *Journal of Infrared, Millimeter, and Terahertz Waves* (2019), pp. 524–534. arXiv: 1810.10026.

[23] Julius O. Smith. *Mathematics of the Discrete Fourier Transform (DFT) with Audio Applications*. Second. W3K Publishing, 2007.

[24] De-Yin Kong et al. “High resolution continuous wave terahertz spectroscopy on solid-state samples with coherent detection”. In: *Optics Express* 26.14 (2018), p. 17964.

[25] Max Born and Emil Wolf. *Principles of Optics*. Seventh. Cambridge University Press, 1999.

[26] Milton Abramowitz and Irene A Stegun. *Handbook of mathematical functions with formulas, graphs, and mathematical tables*. ninth. Dover Publications, 1972.

[27] E. R. Brown et al. “On the strong and narrow absorption signature in lactose at 0.53 THz”. In: *Applied Physics Letters* 90.6 (2007), pp. 1–4.

[28] M.C. Kemp et al. “Security applications of terahertz technology”. In: *Terahertz for Military and Security Applications* 5070.July 2003 (2003), p. 44.

[29] M.C. Kemp, C. Baker, and I. Gregory. *Stand-off explosives detection using terahertz technology*. 2006, pp. 151–165.

[30] D.L. Woolard et al. *Terahertz science and technology for military and security applications*. 2007, pp. 1–260.

[31] National Research Council. *Assessment of millimeter-wave and terahertz technology for detection and identification of concealed explosives and weapons*. Tech. rep. 2007, pp. 1–71.

[32] H.-B. Liu et al. “Terahertz spectroscopy and imaging for defense and security applications”. In: *Proceedings of the IEEE* 95.8 (2007), pp. 1514–1527.

[33] T. Coty and A. Fuller-Tedeschi. “The role of THz and submillimeter wave technology in DHS”. In: *Proceedings of SPIE - The International Society for Optical Engineering*. Vol. 8031. 2011.

[34] X.-C. Zhang et al. “THz Wave Technology for Stand-Off Detection of Explosives and Other Military and Security Applications”. In: *NATO RTO-TR-SET-124* (2011).

[35] R. Beigang et al. “THz Technology for Stand-Off Detection of Explosives : From Laboratory Spectroscopy to Detection in the Field”. In: *NATO RTO-TR-SET-193* (2018).

[36] Yaochun Shen, Philip F. Taday, and M.C. Kemp. “Terahertz spectroscopy of explosive materials”. In: *Passive Millimetre-Wave and Terahertz Imaging and Technology* 5619 (2004), p. 82.

[37] Y. C. Shen et al. “Detection and identification of explosives using terahertz pulsed spectroscopic imaging”. In: *Applied Physics Letters* 86.24 (2005), pp. 1–3.

[38] William R. Tribe et al. “Hidden object detection: security applications of terahertz technology”. In: *Terahertz and Gigahertz Electronics and Photonics III* 5354.April 2004 (2004), p. 168.

[39] C. Baker et al. “People screening using terahertz technology”. In: *Proceedings of SPIE - The International Society for Optical Engineering*. Vol. 5790. May 2005. 2005, pp. 1–10.

[40] C. Baker et al. “Detection of concealed explosives at a distance using terahertz technology”. In: *Proceedings of the IEEE* 95.8 (2007), pp. 1559–1565.

[41] Kohji Yamamoto et al. “Noninvasive inspection of C-4 explosive in mails by terahertz time-domain spectroscopy”. In: *Japanese Journal of Applied Physics, Part 2: Letters* 43.3 B (2004).

[42] F. Huang et al. “Terahertz study of 1,3,5-trinitro-s-triazine by time-domain and Fourier transform infrared spectroscopy”. In: *Applied Physics Letters* 85.23 (2004), pp. 5535–5537.

[43] Yunqing Chen et al. “Spectroscopic characterization of explosives in the far-infrared region”. In: *Terahertz for Military and Security Applications II* 5411 (2004), p. 1.

[44] M.J. Fitch et al. “Time-domain terahertz spectroscopy of bio-agent simulants”. In: *Proceedings of SPIE - The International Society for Optical Engineering*. Vol. 5584. 2004, pp. 16–22.

[45] M.K. Choi, A.D. Bettermann, and D.W. Van der Weide. “Biological and chemical sensing with electronic THz techniques”. In: *Proceedings of SPIE - The International Society for Optical Engineering*. Vol. 5268. 2004, pp. 27–35.

[46] M.K. Choi et al. “Potential for detection of explosive and biological hazards with electronic terahertz systems”. In: *Philosophical Transactions of the Royal Society A: Mathematical, Physical and Engineering Sciences* 362.1815 (2004), pp. 337–349.

[47] Y. Chen, H. Liu, and X.-C. Zhang. “THz spectra of 4-NT and 2, 6-DNT”. In: *Proceedings of SPIE - The International Society for Optical Engineering*. Vol. 6212. 2006.

[48] J. Chen et al. “Absorption coefficients of selected explosives and related compounds in the range of 0.1-2.8 THz”. In: *Optics Express* 15.19 (2007), p. 12060.

[49] M. R. Leahy-Hoppa et al. “Wideband terahertz spectroscopy of explosives”. In: *Chemical Physics Letters* 434.4-6 (2007), pp. 227–230.

[50] Michael J. Fitch et al. “Molecular absorption cross-section and absolute absorptivity in the THz frequency range for the explosives TNT, RDX, HMX, and PETN”. In: *Chemical Physics Letters* 443.4-6 (2007), pp. 284–288.

[51] N. Palka. “Spectroscopy of explosive materials in the THz Range”. In: *Acta Physica Polonica A* 118.6 (2010).

[52] E.M. Witko et al. “Terahertz spectroscopy of energetic materials”. In: *Proceedings of SPIE - The International Society for Optical Engineering*. Vol. 8023. 2011.

[53] Yunqing Chen et al. “THz spectroscopic investigation of 2,4-dinitrotoluene”. In: *Chemical Physics Letters* 400.4-6 (2004), pp. 357–361.

[54] Y. Chen, H. Liu, and X.-C. Zhang. "Experimental and density functional theory study on THz spectra of 4-NT and 2, 6-DNT". In: *International Journal of High Speed Electronics and Systems* 17.2 (2007), pp. 283–291.

[55] Zhijin Yan and Wei Shi. "Detection of aging in the common explosive RDX using terahertz time-domain spectroscopy". In: *Journal of the Optical Society of America B* 39.3 (2022), A9.

[56] H. Zhong, A. Redo-Sanchez, and X.-C. Zhang. "Identification and classification of chemicals using terahertz reflective spectroscopic focalplane imaging system". In: *Optics Express* 14.20 (2006), pp. 9130–9141.

[57] A. Sengupta et al. "THz reflection spectroscopy of C-4 explosive and its detection through interferometric imaging". In: *Proceedings of SPIE - The International Society for Optical Engineering*. Vol. 6120. 2006.

[58] Y. Dikmelik et al. "Examining explosive residues on surfaces with terahertz technology". In: *Proceedings of SPIE - The International Society for Optical Engineering*. Vol. 6549. 2007.

[59] N. Palka. "THz Reflection spectroscopy of explosives measured by time domain spectroscopy". In: *Acta Physica Polonica A* 120.4 (2011), pp. 713–715.

[60] V.A. Trofimov et al. "Efficiency of the detection and identification of ceramic explosive using the reflected THz signal". In: *Proceedings of SPIE - The International Society for Optical Engineering*. Vol. 8363. 2012.

[61] Kyujin Choi et al. "Reflection terahertz time-domain spectroscopy of RDX and HMX explosives". In: *Journal of Applied Physics* 115.2 (2014).

[62] N. Palka and Mateusz Szala. "Transmission and Reflection Terahertz Spectroscopy of Insensitive Melt-Cast High-Explosive Materials". In: *Journal of Infrared, Millimeter, and Terahertz Waves* 37.10 (2016), pp. 977–992.

[63] Andrei A Plekhanov et al. "Study of terahertz reflection spectra of optically thin RDX samples by terahertz imaging with spectral resolution". In: *Optical Engineering* 62.March (2023), pp. 1–13.

[64] H. Zhong et al. "THz wave standoff detection of explosive materials". In: *Proceedings of SPIE - The International Society for Optical Engineering*. Vol. 6212. 2006.

[65] H. Zhong, A. Redo-Sanchez, and X.-C. Zhang. *Standoff sensing and imaging of explosive related chemical and bio-chemical materials using THz-TDS*. 2007, pp. 47–57.

[66] H. Liu et al. "Detection and identification of explosive RDX by THz diffuse reflection spectroscopy". In: *Optics Express* 14.1 (2006), p. 415.

[67] Yamac Dikmelik et al. “Effects of surface roughness on reflection spectra obtained by terahertz time-domain spectroscopy”. In: *Optics Letters* 31.24 (2006), p. 3653.

[68] M. Ortolani et al. “Surface roughness effects on the terahertz reflectance of pure explosive materials”. In: *Applied Physics Letters* 93.8 (2008).

[69] M. Herrmann et al. “The influence of surface roughness on THz reflection measurements”. In: *34th International Conference on Infrared, Millimeter, and Terahertz Waves, IRMMW-THz 2009*. 2009.

[70] S.C. Henry et al. “Measurement and modeling of rough surface effects on terahertz spectroscopy”. In: *Proceedings of SPIE - The International Society for Optical Engineering*. Vol. 7601. 2010.

[71] Mark J. Rosker and H. Bruce Wallace. “Imaging through the atmosphere at terahertz frequencies”. In: *IEEE MTT-S International Microwave Symposium Digest* 2 (2007), pp. 773–776.

[72] Carter M Armstrong. “The truth about terahertz”. In: *IEEE Spectrum* september (2012).

[73] Yihong Yang, Mahboubeh Mandehgar, and D. Grischkowsky. “Broadband THz pulse transmission through the atmosphere”. In: *IEEE Transactions on Terahertz Science and Technology* 1.1 (2011), pp. 264–273.

[74] Yihong Yang, Mahboubeh Mandehgar, and D. Grischkowsky. “Broadband THz signals propagate through dense fog”. In: *IEEE Photonics Technology Letters* 27.4 (2015), pp. 383–386.

[75] Eom Bae Moon, Tae In Jeon, and D. Grischkowsky. “Long-Path THz-TDS Atmospheric Measurements between Buildings”. In: *IEEE Transactions on Terahertz Science and Technology* 5.5 (2015), pp. 742–750.

[76] Gyeong-Ryul Kim, Tae-In Jeon, and D. Grischkowsky. “910-m propagation of THz ps pulses through the Atmosphere”. In: *Optics Express* 25.21 (2017), p. 25422.

[77] Gyeong-Ryul Kim et al. “ Remote N 2 O gas sensing by enhanced 910-m propagation of THz pulses ”. In: *Optics Express* 27.20 (2019), p. 27514.

[78] T. Kürner, D. M. Mittleman, and T. Nagatsuma, eds. *THz Communications*. Vol. 234. Springer, 2022, pp. 1–531.

[79] C. Baker et al. “Developments in people screening using terahertz technology”. In: *Proceedings of SPIE - The International Society for Optical Engineering*. Vol. 5616. 2004, pp. 61–68.

[80] Jianming Dai, Jingle Liu, and X.-C. Zhang. “Terahertz wave air photonics: Terahertz wave generation and detection with laser-induced gas plasma”. In: *IEEE Journal on Selected Topics in Quantum Electronics* 17.1 (2011), pp. 183–190.

[81] B. Clough, J. Dai, and X.-C. Zhang. “Laser air photonics: Beyond the terahertz gap”. In: *Materials Today* 15.1-2 (2012), pp. 50–58.

[82] H. Hamster et al. “Subpicosecond, electromagnetic pulses from intense laser-plasma interaction”. In: *Physical Review Letters* 71.17 (1993), pp. 2725–2728.

[83] H. Hamster et al. “Short-pulse terahertz radiation from high-intensity-laser-produced plasmas”. In: *Physical Review E* 49.1 (1994), pp. 671–677.

[84] D.J. Cook and Hochstrasser R. M. “Intense terahertz pulses by four-wave rectification in air”. In: *Optics Letters* 25.16 (2000), pp. 1210–1212.

[85] T. Löffler, F. Jacob, and H. G. Roskos. “Generation of terahertz pulses by photoionization of electrically biased air”. In: *Applied Physics Letters* 77.3 (2000), pp. 453–455.

[86] Xu Xie, J. Dai, and X.-C. Zhang. “Coherent control of THz wave generation in ambient air”. In: *Physical Review Letters* 96.7 (2006), pp. 1–4.

[87] N. Karpowicz and X. C. Zhang. “Coherent terahertz echo of tunnel ionization in gases”. In: *Physical Review Letters* 102.9 (2009), pp. 1–4.

[88] J. Dai, N. Karpowicz, and X.-C. Zhang. “Physics and potential applications of terahertz air photonics”. In: *34th International Conference on Infrared, Millimeter, and Terahertz Waves, IRMMW-THz 2009*. 2009.

[89] J. Dai, Xu Xie, and X.-C. Zhang. “Detection of broadband terahertz waves with a laser-induced plasma in gases”. In: *Physical Review Letters* 97.10 (2006), pp. 8–11.

[90] N. Karpowicz et al. “Coherent heterodyne time-domain spectrometry covering the entire "terahertz gap"”. In: *Applied Physics Letters* 92.1 (2008).

[91] N. Karpowicz et al. “Coherent millimetre wave to mid-infrared measurements with continuous bandwidth reaching 40 THz”. In: *Electronics letters* 44.8 (2008).

[92] X. Xie et al. “Ambient air used as the nonlinear media for THz wave generation”. In: *International Journal of High Speed Electronics and Systems* 17.2 (2007), pp. 261–270.

[93] J. Dai and X.-C. Zhang. “Method and applications of intense terahertz wave radiation from laser-induced air plasma”. In: *Optics InfoBase Conference Papers*. 2008.

[94] J. Dai, X. Guo, and X.-C. Zhang. “Terahertz air photonics for stand-off explosive detection”. In: *2009 IEEE Conference on Technologies for Homeland Security, HST 2009*. 2009, pp. 461–464.

[95] X. Lu et al. “Recent progress of THz generation and detection in ambient air or Gases”. In: *Proceedings of SPIE - The International Society for Optical Engineering*. Vol. 7917. 2011.

[96] J. Dai and X.-C. Zhang. “Terahertz wave generation from gas plasma using a phase compensator with attosecond phase-control accuracy”. In: *Applied Physics Letters* 94.2 (2009).

[97] J. Dai and X.-C. Zhang. “Standoff terahertz wave generation from two-color laser-induced plasma at 30 meters in ambient air”. In: *IRMMW-THz 2011 - 36th International Conference on Infrared, Millimeter, and Terahertz Waves*. 2011.

[98] K. Liu and X.-C. Zhang. *Toward standoff sensing of CBRN with THz waves*. Vol. PartF1. 2017, pp. 3–10.

[99] J. Liu et al. “Broadband terahertz wave remote sensing using coherent manipulation of fluorescence from asymmetrically ionized gases”. In: *Nature Photonics* 4.9 (2010), pp. 627–631.

[100] F. Buccheri, K. Liu, and X.-C. Zhang. “Terahertz radiation enhanced emission of fluorescence from elongated plasmas and microplasmas in the counter-propagating geometry”. In: *Applied Physics Letters* 111.9 (2017).

[101] B. Clough, J. Liu, and X.-C. Zhang. “Encoding terahertz signatures into laser-induced plasma acoustic waves”. In: *Proceedings of SPIE - The International Society for Optical Engineering*. Vol. 7938. 2011.

[102] Benjamin Clough, Jingle Liu, and X.-C. Zhang. ““All air–plasma” terahertz spectroscopy”. In: *Optics Letters* 36.13 (2011), p. 2399.

[103] J. Liu and X.-C. Zhang. “Terahertz radiation-enhanced-emission-of-fluorescence”. In: *Frontiers of Optoelectronics* 7.2 (2014), pp. 156–198.

[104] K. Liu, P. Huang, and X.-C. Zhang. “Terahertz wave generation from ring-Airy beam induced plasmas and remote detection by terahertz-radiationenhanced- emission-of-fluorescence: a review”. In: *Frontiers of Optoelectronics* 12.2 (2018), pp. 117–147.

[105] Chia-Yeh Li et al. “Broadband field-resolved terahertz detection via laser induced air plasma with controlled optical bias”. In: *Optics Express* 23.9 (2015), p. 11436.

[106] Meng Ku Chen et al. “Terahertz generation in multiple laser-induced air plasmas”. In: *Applied Physics Letters* 93.23 (2008), pp. 2006–2009.

[107] M. Chateauneuf et al. “Detection of explosives using THz time domain spectroscopy”. In: *Proceedings of SPIE - The International Society for Optical Engineering*. Vol. 6796. 2008.

[108] F. Blanchard et al. “Generation of high-power terahertz pulses at the advanced laser light source (ALLS)”. In: *Conference on Lasers and Electro-Optics, 2007, CLEO 2007* (2007), pp. 31–32.

[109] M. Chateauneuf and Jacques Dubois. “Canadian TeraWatt portable laser”. In: *Femtosecond Phenomena and Nonlinear Optics III* 6400.September 2006 (2006), 64000F.

[110] F. Meyer et al. “Milliwatt-class MHz repetition-rate THz source driven by a sub-100 fs high-power thin-disk laser”. In: *Optics Express* 27.21 (2019), pp. 30340–30349.

[111] F. Meyer et al. “Single-cycle, MHz repetition rate THz source with 66 mW of average power”. In: *Optics Letters* 45.9 (2020), pp. 2494–2497.

[112] Tobias Olaf Buchmann et al. “High-power few-cycle THz generation at MHz repetition rates in an organic crystal”. In: *APL Photonics* 5.10 (2020).

[113] Tobias Olaf Buchmann et al. “MHz-repetition-rate, sub-mW, multi-octave THz wave generation in HMQ-TMS”. In: 28.7 (2020), pp. 9631–9641.

[114] József András Fülöp, Stelios Tzortzakis, and Tobias Kampfrath. “Laser-Driven Strong-Field Terahertz Sources”. In: *Advanced Optical Materials* 8.3 (2020), pp. 1–25.

[115] T. Edwards et al. “Compact source of continuously and widely-tunable terahertz radiation.” In: *Optics Express* 14.4 (2006), p. 1582.

[116] D. J.M. Stothard et al. “Line-narrowed, compact, and coherent source of widely tunable terahertz radiation”. In: *Applied Physics Letters* 92.14 (2008), pp. 10–13.

[117] D. Walsh et al. “Injection-seeded intracavity terahertz optical parametric oscillator”. In: *Journal of the Optical Society of America B* 26.6 (2009), p. 1196.

[118] G.P.A. Malcolm, D.A. Walsh, and M. Chateauneuf. “Physics and applications of T-rays”. In: *Springer Series in Optical Sciences*. Ed. by M. Perenzoni and D. J. Paul. Vol. 173. 2014, pp. 149–175.

[119] N. Hempler et al. “Intracavity terahertz optical parametric oscillator for standoff spectroscopy applications”. In: *Applied Industrial Optics: Spectroscopy, Imaging and Metrology, AIO 2012*. 2012.

[120] M Squared Lasers Ltd. *Firefly THz*. 2022.

[121] M. A. Piestrup, R. N. Fleming, and R. H. Pantell. “Continuously tunable submillimeter wave source”. In: *Applied Physics Letters* 26.8 (1975), pp. 418–421.

[122] Kodo Kawase et al. “Coherent tunable THz-wave generation from LiNbO3 with monolithic grating coupler”. In: *Applied Physics Letters* 68.18 (1996), pp. 2483–2485.

[123] Kodo Kawase et al. “Non-destructive terahertz imaging of illicit drugs using spectral fingerprints”. In: *Optics Express* 11.20 (2003), p. 2549.

[124] D. Molter, M. Theuer, and R. Beigang. “Nanosecond terahertz optical parametric oscillator with a novel quasi phase matching scheme in lithium niobate”. In: *Optics Express* 17.8 (2009), p. 6623.

[125] Kosuke Murate et al. “A High Dynamic Range and Spectrally Flat Terahertz Spectrometer Based on Optical Parametric Processes in LiNbO3”. In: 4.6 (2014), pp. 749–752.

[126] Shin’Ichiro Hayashi et al. “Ultrabright continuously tunable terahertz-wave generation at room temperature”. In: *Scientific Reports* 4 (2014), pp. 3–7.

[127] Mikiya Kato et al. “Non-destructive drug inspection in covering materials using a terahertz spectral imaging system with injection-seeded terahertz parametric generation and detection”. In: *Optics Express* 24.6 (2016), p. 6425.

[128] Kosuke Murate, Shinichiro Hayashi, and Kodo Kawase. “Expansion of the tuning range of injection-seeded terahertz-wave parametric generator up to 5 THz”. In: *Applied Physics Express* 9.8 (2016), pp. 5–8.

[129] Kosuke Murate, Shin’ichiro Hayashi, and Kodo Kawase. “Multiwavelength terahertz-wave parametric generator for one-pulse spectroscopy”. In: *Applied Physics Express* 10.3 (2017).

[130] K. Murate and K. Kawase. “Perspective: Terahertz wave parametric generator and its applications”. In: *Journal of Applied Physics* 124.16 (2018).

[131] Kouji Nawata et al. “Tunable Backward Terahertz-wave Parametric Oscillation”. In: *Scientific Reports* 9.1 (2019), pp. 1–6.

[132] Yuma Takida, Kouji Nawata, and Hiroaki Minamide. “Security screening system based on terahertz-wave spectroscopic gas detection”. In: *Optics Express* 29.2 (2021), p. 2529.

[133] Wei Shi and Yujie J. Ding. “Fingerprinting molecules based on direct measurement of absorption spectrum by frequency-tuning monochromatic THz source”. In: *Laser Physics Letters* 1.11 (2004), pp. 560–564.

[134] Wei Shi and Yujie J. Ding. “A monochromatic and high-power terahertz source tunable in the ranges of 2.7-38.4 and 58.2-3540 μm for variety of potential applications”. In: *Applied Physics Letters* 84.10 (2004), pp. 1635–1637.

[135] Wei Shi and Yujie J. Ding. “Tunable coherent radiation from terahertz to microwave by mixing two infrared frequencies in A 47-MM-long GaSe crystal”. In: *International Journal of High Speed Electronics and Systems* 16.2 (2006), pp. 589–595.

[136] Yujie J. Ding. “High-power tunable terahertz sources based on parametric processes and applications”. In: *IEEE Journal on Selected Topics in Quantum Electronics* 13.3 (2007), pp. 705–720.

[137] Hongqian Sun, Yujie J. Ding, and Ioulia B. Zotova. “THz spectroscopy by frequency-tuning monochromatic THz source: From single species to gas mixtures”. In: *IEEE Sensors Journal* 10.3 (2010), pp. 621–629.

[138] Yujie J. Ding. “Progress in terahertz sources based on difference-frequency generation [Invited]”. In: *Journal of the Optical Society of America B* 31.11 (2014), p. 2696.

[139] T. Bach et al. “Tunable THz source with less than 100 GHz bandwidth”. In: *2011 Conference on Lasers and Electro-Optics Europe and 12th European Quantum Electronics Conference, CLEO EUROPE/EQEC 2011*. 2011.

[140] Z.-M. Huang et al. “Down-converters with doped solid solution crystals GaSe1-xSx for THz spectrometry”. In: *Proceedings of SPIE - The International Society for Optical Engineering*. Vol. 10173. 2017.

[141] Z.-M. Huang et al. “Long bases standoff THz spectrometer: State-of-the-art and prospective”. In: *International Conference on Infrared, Millimeter, and Terahertz Waves, IRMMW-THz*. 2017.

[142] Ruixiang Guo et al. “Highly sensitive coherent detection of terahertz waves at room temperature using a parametric process”. In: *Applied Physics Letters* 93.2 (2008), pp. 2006–2009.

[143] R. Beigang et al. “Comparison of terahertz technologies for detection and identification of explosives”. In: *Proceedings of SPIE - The International Society for Optical Engineering*. Vol. 9102. 2014.

[144] Naofumi Shimizu et al. “Stand-off gas sensing system based on Terahertz spectroscopy”. In: *Journal of the National Institute of Information and Communications Technology* 55.1 (2008), pp. 165–170.

[145] Atsushi Wakatsuki, Yoshifumi Muramoto, and Tadao Ishibashi. “Development of terahertz-wave photomixer module using a uni-traveling-carrier photodiode”. In: *NTT Technical Review* 10.2 (2012).

[146] Satoshi Kohjiro et al. “A 0.2-0.5 THz single-band heterodyne receiver based on a photonic local oscillator and a superconductor-insulator-superconductor mixer”. In: *Applied Physics Letters* 93.9 (2008).

[147] Naofumi Shimizu et al. “Remote detection of hazardous gases in full-scale simulated fire by using terahertz electromagnetic waves”. In: *NTT Technical Review* 10.2 (2012).

[148] S. Preu et al. “Interference between two coherently driven monochromatic terahertz sources”. In: *Applied Physics Letters* 92.22 (2008).

[149] S. Preu et al. “Coherent superposition of terahertz beams”. In: *Millimetre Wave and Terahertz Sensors and Technology*. Vol. 7117. 2008, 71170S.

[150] S. Bauerschmidt et al. “Coherent superposition of terahertz beams from a phased linear photomixer array”. In: *Proceedings - TERA-MIR 2009, NATO Advanced Research Workshop Terahertz and Mid Infrared Radiation: Basic Research and Practical Applications* November (2009), pp. 75–76.

[151] S. Bauerschmidt et al. “Continuous wave terahertz emitter arrays for spectroscopy and imaging applications”. In: *Terahertz Physics, Devices, and Systems IV: Advanced Applications in Industry and Defense* 7671 (2010), p. 76710D.

[152] S. Bauerschmidt et al. “Arrayed free space continuous-wave terahertz photomixers”. In: *Optics Letters* 38.18 (2013), pp. 3673–3676.

[153] A. Bandyopadhyay et al. “Terahertz interferometric and synthetic aperture imaging”. In: *Journal of the Optical Society of America A: Optics and Image Science, and Vision* 23.5 (2006), pp. 1168–1178.

[154] L. Mo et al. “Nine wave-length THz spectrum for identification using Backward Wave Oscillator”. In: *Proceedings of SPIE - The International Society for Optical Engineering*. Vol. 7512. 2009.

[155] H. Richter et al. “Development of a THz heterodyne receiver with quantum cascade laser and hot electron bolometer mixer for stand-off detection of explosive material”. In: *Proceedings of SPIE - The International Society for Optical Engineering*. Vol. 7311. 2009.

[156] J. Chen et al. “Wavelength beam-combining of terahertz quantum-cascade laser arrays”. In: *Optics Letters* 46.8 (2021), pp. 1864–1867.

[157] B. Schulkin et al. “Progress toward handheld THz sensing”. In: *IRMMW-THz 2011 - 36th International Conference on Infrared, Millimeter, and Terahertz Waves*. 2011.

[158] M.C. Kemp. “Millimetre wave and terahertz technology for the detection of concealed threats - A review”. In: *Proceedings of SPIE - The International Society for Optical Engineering*. Vol. 6402. 2006.

[159] M.C. Kemp. “Explosives detection by terahertz spectroscopy - A bridge too far?” In: *IEEE Transactions on Terahertz Science and Technology* 1.1 (2011), pp. 282–292.

[160] Enrique Castro-Camus et al. “On the reliability of power measurements in the terahertz band”. In: *Communications Physics* 5.1 (2022), pp. 6–8.

[161] Björn Globisch et al. “Absolute terahertz power measurement of a time-domain spectroscopy system”. In: *Optics Letters* 40.15 (2015), p. 3544.

[162] Randy L. Haupt and Yahya Rahmat-Samii. “Reflector Antenna Developments: A Perspective on the Past, Present and Future”. In: *IEEE Antennas and Propagation Magazine* 57.2 (2015), pp. 85–95.

[163] Probir K. Bondyopadhyay. “First application of array antenna”. In: *IEEE International Symposium on Phased Array Systems and Technology* (2000), pp. 29–32.

[164] K. F. Braun. “Electrical Oscillations and Wireless Telegraphy”. In: *Nobel Lecture, December* 11.1909 (1909), pp. 226–245.

[165] G. Marconi and F. Braun. *The Nobel Prize in Physics 1909*. 2023.

[166] S. Preu et al. “Arrayed Telecom-Wavelength Compatible THz n-i-pn-i-p Superlattice Photomixers for Spectroscopy Applications”. In: *Terahertz and Mid Infrared Radiation: Generation, Detection and Applications*. Vol. NATO Scien. 2011.

[167] E. R. Brown. “THz Generation by Photomixing in Ultrafast Photoconductors”. In: *International Journal of High Speed Electronics and Systems* 13.2 (2003), pp. 497–545.

[168] S. Preu et al. “Highly collimated and directional continous-wave Terahertz emission by photomixing in semiconductor device arrays”. In: *Millimeter-Wave and Terahertz Photonics* 6194 (2006), 61940F.

[169] Naofumi Shimizu and Tadao Nagatsuma. “Photodiode-integrated microstrip antenna array for subterahertz radiation”. In: *IEEE Photonics Technology Letters* 18.6 (2006), pp. 743–745.

[170] Ming Che et al. “Arrayed Photomixers for THz Beam-Combining and Beam-Steering”. In: *Journal of Lightwave Technology* 40.20 (2022), pp. 6657–6665.

[171] Alejandro Rivera-Lavado et al. “Arrays and new antenna topologies for increasing THz power generation using photomixers”. In: *Journal of Infrared, Millimeter, and Terahertz Waves* 34.2 (2013), pp. 97–108.

[172] Daniel Headland et al. “Tutorial: Terahertz beamforming, from concepts to realizations”. In: *APL Photonics* 3.5 (2018).

[173] Yasuaki Monnai, Xuyang Lu, and Kaushik Sengupta. “Terahertz Beam Steering: from Fundamentals to Applications”. In: *Journal of Infrared, Millimeter, and Terahertz Waves* (2023).

[174] C. A. Balanis. *Antenna theory; analysis and design*. Vol. 72. 7. 2008, pp. 989–990.

[175] Simon Nellen et al. "Radiation pattern of planar optoelectronic antennas for broadband continuous-wave terahertz emission". In: *Optics Express* 29.6 (2021), p. 8244.

[176] Jessica Smith et al. "Beam profile characterisation of an optoelectronic silicon lens-integrated pin-pd emitter between 100 ghz and 1 thz". In: *Applied Sciences (Switzerland)* 11.2 (2021), pp. 1–12.

[177] Eugene Hecht. *Optics*. Fourth. Addision Wesley, 2002.

[178] David Tse and Viswanath Pramod. *Fundamentals of wireless communication*. Vol. 9780521845. 2005, pp. 1–564.

[179] Christopher M. Bishop. *Pattern Recognition and Machine Learning*. Springer, 2006.

[180] Ethem Alpaydin. *Introduction to Machine Learning Second Edition*. second. Vol. 1107. The MIT Press, 2010.

[181] Y. Watanabe et al. "Component spatial pattern analysis of chemicals using terahertz spectroscopic imaging". In: *Applied Physics Letters* 83.4 (2003), pp. 800–802.

[182] Can Cao et al. "Terahertz spectroscopy and machine learning algorithm for non-destructive evaluation of protein conformation". In: *Optical and Quantum Electronics* 52.4 (2020), pp. 1–18.

[183] Maciej Roman Nowak et al. "Recognition of pharmacological bi-heterocyclic compounds by using terahertz time domain spectroscopy and chemometrics". In: *Sensors (Switzerland)* 19.15 (2019).

[184] Wei Liu et al. "Discrimination of geographical origin of extra virgin olive oils using terahertz spectroscopy combined with chemometrics". In: *Food Chemistry* 251.August 2017 (2018), pp. 86–92.

[185] Jinnuo Zhang et al. "Identification of Bacterial Blight Resistant Rice Seeds Using Terahertz Imaging and Hyperspectral Imaging Combined With Convolutional Neural Network". In: *Frontiers in Plant Science* 11.June (2020), pp. 1–15.

[186] Kaiqiang Wang, Da Wen Sun, and Hongbin Pu. "Emerging non-destructive terahertz spectroscopic imaging technique: Principle and applications in the agri-food industry". In: *Trends in Food Science and Technology* 67 (2017), pp. 93–105.

[187] Wei Liu et al. "Application of terahertz spectroscopy imaging for discrimination of transgenic rice seeds with chemometrics". In: *Food Chemistry* 210 (2016), pp. 415–421.

[188] Anastasia I. Knyazkova et al. “Paraffin-Embedded Prostate Cancer Tissue Grading Using Terahertz Spectroscopy and Machine Learning”. In: *Journal of Infrared, Millimeter, and Terahertz Waves* 41.9 (2020), pp. 1089–1104.

[189] Hochong Park and Joo Hiuk Son. “Machine learning techniques for thz imaging and time-domain spectroscopy”. In: *Sensors (Switzerland)* 21.4 (2021), pp. 1–25.

[190] Rasmus Bro and Age K. Smilde. “Centering and scaling in component analysis”. In: *Journal of Chemometrics* 17.1 (2003), pp. 16–33.

[191] Rasmus Bro and Age K. Smilde. “Principal component analysis”. In: *Analytical Methods* 6.9 (2014), pp. 2812–2831.

[192] Ian T. Jolliffe and Jorge Cadima. “Principal component analysis: A review and recent developments”. In: *Philosophical Transactions of the Royal Society A: Mathematical, Physical and Engineering Sciences* 374.2065 (2016).

[193] Corinna Cortes and Vladimir Vapnik. “Support-Vector Networks”. In: *Journal of Physics: Conference Series* 20 (1995), pp. 273–297.

[194] Christopher J.C. Burges. “A Tutorial on Support Vector Machines for Pattern Recognition”. In: *Data Mining and Knowledge Discovery* 2 (1998), pp. 121–167.

[195] Paweł Piotr Cielecki, Mathias Hedegaard Kristensen, and Esben Skovsen. “Database of frequency-domain terahertz reflection spectra for the DETRIS project”. In: *Zenodo* (2021).

[196] Yuefang Hua and Hongjian Zhang. “Qualitative and quantitative detection of pesticides with terahertz time-domain spectroscopy”. In: *IEEE Transactions on Microwave Theory and Techniques* 58.7 PART 2 (2010), pp. 2064–2070.

[197] Hankyu Namkung et al. “Impact of pellet thickness on quantitative terahertz spectroscopy of solid samples in a polyethylene matrix”. In: *Analytical Chemistry* 85.7 (2013), pp. 3674–3681.

[198] Paweł Piotr Cielecki, Mathias Hedegaard Kristensen, and Esben Skovsen. “Analysis and Classification of Frequency-Domain Terahertz Reflection Spectra Using Supervised and Unsupervised Dimensionality Reduction Methods”. In: *Journal of Infrared, Millimeter, and Terahertz Waves* 42.9-10 (2021), pp. 1005–1026.

[199] Jerome H. Friedman. “Regularized discriminant analysis”. In: *Journal of the American Statistical Association* 84.405 (1989), pp. 165–175.

[200] Federico Sanjuan, Gwenaël Gaborit, and Jean Louis Coutaz. “Subwavelength terahertz imaging through optical rectification”. In: *Scientific Reports* 8.1 (2018), pp. 2–8.

[201] Robert W. Boyd. *Nonlinear Optics*. Fourth. Academic Press, 2020.

[202] F. S. Pavone and P. J. Campagnola. *Second Harmonic Generation Imaging*. 1st. CRC Press, 2013.

[203] Si Lu Zhang et al. "Recent advances in nonlinear optics for bio-imaging applications". In: *Opto-Electronic Advances* 3.10 (2020), pp. 1–18.

[204] S. K. Kurtz and T. T. Perry. "A powder technique for the evaluation of nonlinear optical materials". In: *Journal of Applied Physics* 39.8 (1968), pp. 3798–3813.

[205] J. M. Halbout and Chung L. Tang. "Phase-Matched Second-Harmonic Generation in Sucrose". In: *IEEE Journal of Quantum Electronics* 18.3 (1982), pp. 410–415.

[206] Mark J. Rosker and Chung L. Tang. "Evaluation of second-harmonic generation of various sugars in the powder form". In: 4 (1984), pp. 334–336.

[207] Géza I. Groma et al. "Resonant optical rectification in bacteriorhodopsin". In: *Proceedings of the National Academy of Sciences of the United States of America* 101.21 (2004), pp. 7971–7975.

[208] Mathias Hedegaard Kristensen et al. "Terahertz generation through optical rectification in reflection". In: *Journal of Applied Physics* 133 (2023), p. 173103.

[209] G. Gaborit, F. Sanjuan, and J.-L. Coutaz. "Second order nonlinear optical processes in [111] cubic crystals for terahertz optoelectronics". In: *Lithuanian Journal of Physics* 58.1 (2018), pp. 24–37.

[210] D. N. Bose, R. K. Ahrenkiel, and S. Bhunia. "Steady-state and time-resolved photoconductivity measurements of minority carrier lifetime in ZnTe". In: *Journal of Applied Physics* 86.11 (1999), pp. 6599–6601.

[211] Z. Y. Zhao et al. "THz generation by optical rectification and competition with other nonlinear processes". In: *Chinese Physics Letters* 25 (2008), pp. 189–192.

[212] M. Schall and P. Uhd Jepsen. "Above-band gap two-photon absorption and its influence on ultrafast carrier dynamics in ZnTe and CdTe". In: *Applied Physics Letters* 80.25 (2002), pp. 4771–4773.

[213] E. Constable and R. A. Lewis. "Optical parameters of ZnTe determined using continuous-wave terahertz radiation". In: *Journal of Applied Physics* 112.6 (2012).

[214] Federico Sanjuan, Gwcnael Gaborit, and Jean Louis Coutaz. "Influence of Two-Photon Absorption Anisotropy on Terahertz Generation in < 111 > Zinc Blende Crystals". In: *International Conference on Infrared, Millimeter, and Terahertz Waves, IRMMW-THz* 2018-Septe (2018), pp. 378–386.

[215] Wei-Qiang He, Chun-Ming Gu, and Wen-Zhong Shen. “Direct evidence of Kerr-like nonlinearity by femtosecond Z-scan technique”. In: *Optics Express* 14.12 (2006), p. 5476.

[216] N. Bloembergen. *Nonlinear Optics*. World Scientific, 1996.

[217] Kosuke Murate, Hiroki Kanai, and Kodo Kawase. “Application of Machine Learning to Terahertz Spectroscopic Imaging of Reagents Hidden by Thick Shielding Materials”. In: *IEEE Transactions on Terahertz Science and Technology* 11.6 (2021), pp. 620–625.

[218] P. Y. Han and X. C. Zhang. “Coherent, broadband midinfrared terahertz beam sensors”. In: *Applied Physics Letters* 73.21 (1998), pp. 3049–3051.

Publication A

Analysis and Classification of Frequency-Domain Terahertz Reflection Spectra using Supervised and Unsupervised Dimensionality Reduction Methods

List of authors:

Paweł Piotr Cielecki
Mathias Hedegaard Kristensen
Esben Skovsen

The paper has been published in the
Journal of Infrared, Millimeter, and Terahertz Waves Vol. 42, pp. 1005, 2021.

Journal of Infrared, Millimeter, and Terahertz Waves (2021) 42:1005–1026
https://doi.org/10.1007/s10762-021-00810-w

Analysis and Classification of Frequency-Domain Terahertz Reflection Spectra Using Supervised and Unsupervised Dimensionality Reduction Methods

Paweł Piotr Cielecki[1] · Mathias Hedegaard Kristensen[1] · Esben Skovsen[1]

Received: 31 March 2021 / Accepted: 15 August 2021 / Published online: 25 September 2021

Abstract
The unique properties of terahertz (THz) spectroscopy show a great potential for security and defense applications such as safe screening of persons and objects. However, a successful implementation of THz screening systems requires a development of reliable and efficient identification algorithms. Dimensionality reduction (DR) methods aim to reduce the dimensionality of the multivariate data and are therefore commonly used as a preprocessing step for classification algorithms and as an analytical tool allowing data visualization. In this paper, we compare the use of unsupervised and supervised DR methods for analysis and classification of THz reflection spectra based on their most widespread linear representatives, namely principal component analysis and linear discriminant analysis, respectively. To this end, both methods were applied to more than 5000 THz reflection spectra acquired from six active materials mixed at three different concentrations with polyethylene and measured at various humidity conditions. While considering scenarios with different levels of complexity, we found that the supervised approach provides better results because it enables efficient grouping despite intra-class variability. Furthermore, we showed that manipulating labels introduced into the supervised DR algorithm allows conditioning the data for a desired classification task such as security screening. Presented classification results show that simple machine learning algorithms are sufficient for highly accurate classification (>98.6%) of THz spectra, which will be suitable for many real-life applications of THz spectroscopy based on material identification.

Keywords THz spectroscopy · THz screening · Frequency-domain · Dimensionality reduction · Classification · Machine learning

✉ Esben Skovsen
es@mp.aau.dk

[1] Department of Materials and Production, Section for Physics and Mechanics, Aalborg University, Skjernvej 4A, DK-9220 Aalborg East, Denmark

1 Introduction

Terahertz (THz) spectroscopy exhibits a unique potential for security and defense applications [1–6], which, along with wireless communication [7–10] and quality control applications [6, 11–14], has been the main stimuli for a rapid development of THz technology during the past decades. Many hazardous substances including pure and military-grade explosives [1–4, 15, 16], illicit drugs [1, 2, 17, 18], and toxic gasses [19–21] possess distinctive spectral fingerprints in the THz region allowing their identification. Furthermore, THz radiation penetrates most nonpolar dielectric covering materials such as paper, cardboard, plastic, and textiles (e.g., cotton and polyester) with only moderate absorption losses enabling identification of concealed objects [4, 22–24]. Finally, THz radiation is nonionizing. Therefore, at reasonable intensities, it is considered safe for scanning persons and objects [5, 24]. This exceptional set of features makes it possible to implement a nondestructive and noninvasive THz security screening, which can be used to improve safety in public places such as airports and subway stations [25–27], and monitor the content of mails and parcels [4, 5, 28, 29].

Despite being overshadowed by the more popular pulsed time-domain technology, THz continuous-wave(CW)frequency-domain spectroscopy (FDS) offers numerous advantages desired in security screening applications. Spectral selectivity associated with this technology enables measurements within water transmission windows. This limits water absorption losses that are unavoidable for broadband time-domain systems. Consequently, CW technology has a potential for measurements at stand-off distances. Furthermore, a high spectral resolution of FDS makes it suitable for detection of gasses, which usually have very narrow absorption lines [19, 30, 31]. Modern THz CW spectrometers based on photomixing technology and highly reliable distributed-feedback 1.5 μm lasers offer a wide range of frequency tuning and high signal-to-noise ratio even at relatively short exposure times [32–34]. In comparison to time-domain systems that require femtosecond lasers and delay lines, CW spectrometers are cheaper and more robust. Furthermore, their compact size and low weight allow development of portable systems, which can be mounted on vehicles or drones enabling a myriad of new applications [35, 36].

Nevertheless, a successful implementation of THz screening systems requires a development of reliable and efficient identification algorithms. A variety of machine learning techniques has been fostered for classification of THz spectra. This includes Bayesian models [37, 38], artificial neural networks [39–41], support vector machines [42–44], and random forests [37, 39, 43]. Dimensionality reduction (DR) methods play an important role in that process [37, 43, 45–49]. They transform the data into a lower dimensional space, while preserving most of the relevant information. This allows lowering the computational requirements of the machine learning algorithm and increasing the speed of learning. Therefore, DR is commonly used as a preprocessing step for classification [37, 43–50]. Furthermore, DR often allows visualization of the data, which is an important analytical tool that facilitates the interpretation of the data.

In this work, we compare the use of unsupervised and supervised DR methods in the analysis of THz spectra. To this end, we used principal component analysis (PCA) and linear discriminant analysis (LDA), which are the most commonly used linear representatives of each approach, respectively [51, 52]. We analyzed spectra of six compounds, measured in a reflection configuration using a THz CW FDS. While analyzing the spectra, we focused on two main applications of DR, namely data visualization and preprocessing the data for classification. To test the visualization ability of the featured methods, we have reduced the

dimensionality of the data to at most three dimensions. Furthermore, we have classified the DR-processed data using three different classifiers, namely k-Nearest Neighbors (k-NN), Bayesian classifier, and support vector machines (SVM). We considered four different scenarios with different levels of complexity. In Section 3.1, we focused on samples with only a single concentration of each active material. In Section 3.2, we analyzed spectra of the samples that contain three different concentrations of the active material (80%, 50%, and 20%). Section 3.3 investigates an impact of atmospheric conditions, namely water vapor absorption. For that purpose, we analyzed THz spectra measured under controlled humidity conditions at a relative humidity of 90%, 50%, and 10%. Finally, we considered a real-life example related to THz security screening (in Section 3.4). For that purpose, we arbitrarily divided the samples according to the threat they pose. This included RDX that is an active component in several military explosives [3]. This approach allowed us to test whether the DR methods are able to properly condition the data for this specific classification task.

This paper explains the differences between the use of unsupervised and supervised DR methods in the analysis of THz spectra. It shows that DR methods are a useful tool that allows the visualization of multidimensional spectra and that they are able to ensure high classification accuracy when used even with simple classification algorithms. Our results are highly relevant for applications that rely on the classification or identification of THz spectra such as security screening.

2 Experimental Details and Methods

2.1 Sample Fabrication

We selected six compounds with discernible spectral features in the THz regime, namely galactitol, L-tartaric acid (L-TA), 4-aminobenzoic acid (PABA), hexogen (RDX), theophylline, and α-lactose monohydrate. All the materials were purchased from Sigma-Aldrich except for L-TA that was purchased from MERCK and RDX that was supplied by the courtesy of the Danish Ministry of Defence Acquisition and Logistics Organisation. We mixed each of the materials with polyethylene (PE) powder, which functions as a binder [53], at weight percentages of 80%, 50%, and 20% of the active material, respectively. Since PE does not have any features in the observed spectral range, it does not affect the measured spectrum other than providing a constant background [54]. To facilitate easy handling of the samples, the mixtures were subsequently compressed into cylindrical pellets with a diameter of 25 mm and weight of 7 g using a hydraulic press. The applied pressure was approximately 4 tons. To prevent interference arising between the front and the back surface reflections, we fabricated an inset to the hydraulic press that made the back surface at an angle of 15° relative to the front surface. As a result, we produced truncated cylindrical samples as shown in the inset of Fig. 1. After pressing the samples, no additional surface treatment such as polishing was performed. We fabricated two samples for each material composition and two additional samples of a pure PE. Table 1 provides an overview of all samples used in this study. Due to the relatively large crystal size of galactitol and L-TA, we were unable to fabricate satisfactory pellets, especially for the compositions with a high content of the active material. The samples were brittle and had a tendency to break when removed from the press. Furthermore, their surface was rough, following the crystal size, which promoted

light scattering. Therefore, before mixing with PE, galactitol and L-TA were ground into a fine powder using mortar and pestle.

2.2 Terahertz Setup and Measurements

We characterized the samples by means of THz-FDS using the reflection setup shown in Fig. 1. The setup is based on a TeraScan 1550 system (Toptica Photonics), which operates in a coherent detection scheme. A combined output of two tunable distributed-feedback diode lasers creates a heterodyne (beat pattern), which illuminates two InGaAs photomixers (emitter and receiver, respectively) modulating their conductivity. Applying a bias voltage to the emitter induces a photocurrent oscillating at the difference frequency of the lasers, which is then outcoupled into free space by an integrated antenna. The emitted THz radiation covers the spectral range from 0.09 to 1.19 THz. A 1″ diameter off-axis parabolic mirror collimates the THz beam, which is then reflected towards the sample at an angle of approximately 11° and focused onto the sample's surface by a TPX lens. A symmetrical optical system collects the reflected THz signal and focuses it onto the receiver. The total optical path length of the THz beam is approximately 1 m. The detected THz signal superimposed with the optical beat induces a photocurrent in the receiver. The photocurrent is amplified by a lock-in amplifier, recorded by the DLC smart controller for the TeraScan system and analyzed by a computer.

First, we performed measurements under ambient conditions. Each sample was measured 80 times over the entire spectral range using a frequency step of 80 MHz and 3 ms integration time. Using these parameters, the time per scan was around 45 s. A computer-controlled two-axis translation stage moved the sample after each measurement to a random position within a 7 × 7 mm scanning area with a step resolution of 0.5 mm. Every 20 measurements, we replaced the sample with an aluminum mirror and recorded its spectrum as a reference. Subsequently, we performed measurements under controlled humidity conditions. For this purpose, a custom-built humidity chamber enclosing the terahertz setup was purged with either

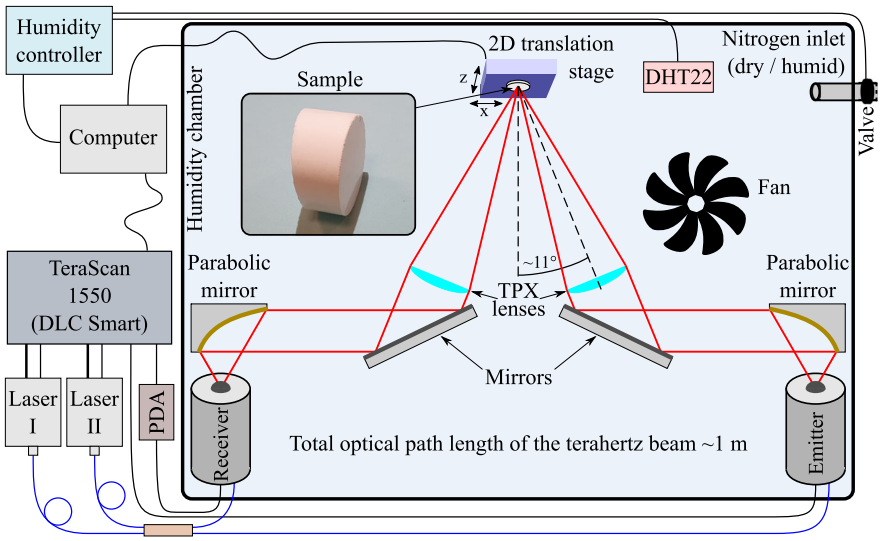

Fig. 1 Schematic drawing of the terahertz reflection setup. The inset of the figure shows a typical truncated cylindrical sample used in the experiments

Table 1 Overview of the samples used in our studies. Each filled circle represents a single sample with a given concentration of the active material

Material	Weight percentage of the active material			
	20%	50%	80%	100%
Galactitol	● ●	● ●	● ●	
Lactose	● ●	● ●	● ●	
L-TA	● ●	● ●	● ●	
PABA	● ●	● ●	● ●	
RDX	● ●	● ●	● ●	
Theophylline	● ●	● ●	● ●	
PE				● ●

dry or water vapor saturated nitrogen depending on whether the intended humidity was lower or higher than the ambient air. Based on a relative humidity readout from a DHT22 sensor, a custom-built humidity controller manages a solenoid valve, which opens and closes the nitrogen flow. A fan installed next to the nitrogen inlet ensures a uniform humidity distribution inside the chamber. The applied methodology allowed us to keep the relative humidity (RH) at the intended level with a stability better than ±0.3 percent points. We measured each sample 20 times at the RH of 90%, 50%, and 10%, respectively, using the same parameters as before. Due to a long purging time, the samples were measured in groups of two with a single reference measurement at RH of 50% used for both samples. Despite a good performance of our humidity controller, we observed a small variation in the intensity of water absorption peaks. We attribute this to changes in the room temperature, which were approximately ±0.7 °C during the measurements.

2.3 Data Processing

In the CW coherent detection scheme, the photocurrent, I_{ph}, depends on the THz electric field amplitude, E_{THz}, and the phase shift, $\Delta\varphi$, between the THz wave and the optical beat via $I_{\mathrm{ph}} \propto E_{\mathrm{THz}} \cos(\Delta\varphi = 2\pi\Delta L\nu/c)$ [55–57]. The phase difference depends, in turn, on the frequency of the THz signal, ν, and the optical path difference $\Delta L = L_{\mathrm{THz}} + L_E - L_R$, where L_{THz} is THz beam path, and L_E and L_R are optical beat paths to emitter and receiver, respectively. For setups with a fixed path length difference, which is the case here, it is possible to separate the magnitude and phase of the detected THz signal by analyzing an interference pattern (fringes) in the frequency scan [55–58]. To achieve this, we employed a well-known approach of finding fringe extrema, where the THz amplitude is directly proportional to the absolute value of the photocurrent and the THz phase is a multiple of π. This approach neglects all other measurement points. Consequently, the spacing between adjacent extrema defines the effective measurement resolution, which for our setup was around 0.9 GHz. To eliminate the possible offset in the photocurrent, instead of treating the extrema separately, the photocurrent was obtained from two adjacent extrema and used at the average frequency. The coherent detection scheme allows extraction of the phase information, but in this study, we used only the amplitude of the THz field. Therefore, the methodology presented in this paper can be also applied to THz systems using non-coherent detection. To compensate for spectral shifts of fringe extrema, the data was interpolated onto integer GHz frequencies. Finally, we determined the reflection coefficient of the sample by dividing the THz spectrum with the corresponding

reference spectrum. Due to the standing wave patterns and lack of spectral features in the low frequency regime, we only used the data in the spectral range from 0.3 to 1.15 THz.

We recorded 3040 terahertz reflection spectra of six compounds with three different weight percentages of the active material under ambient conditions. Four out of these 3040 measurements were excluded due to processing issues and not analyzed further. These spectra are used in Sections 3.1, 3.2, and 3.4. Additionally, we collected 2280 spectra under controlled humidity conditions, which are analyzed in Section 3.3. A dataset of this size constitutes a good basis for developing various machine learning classifiers, which is an important step towards a real-time identification of illegal substances, e.g., explosives or drugs, using terahertz spectroscopy. The data is available online as a part of "Database of frequency-domain terahertz reflection spectra for the DETRIS project" [59].

The datasets were arranged in $n \times d$ matrices, where n is the number of observations (measurements, also referred to as data points) and d is the number of features (dimensions). Before DR, the dataset under consideration was randomly divided into a training set and a test set at a ratio of 4:1 using stratified random sampling. Furthermore, the features were standardized so that they had a zero mean and a variance equal to unity, which is crucial for a correct operation of the PCA algorithm [60, 61]. All presented algorithms (feature standardization, DR, and classification) were only trained on the training set, and the test set was used solely for the final evaluation. We performed the data processing and implemented all DR and classification algorithms used in this study in MATLAB (MathWorks, version R2018a).

2.4 Dimensionality Reduction

As the name suggests, dimensionality reduction algorithms aim to lower the dimensionality of the multivariate data while maintaining most of the information it contains [62–64]. They can be divided into two categories, namely feature selection and feature extraction. In machine learning, the term "feature" refers to an individual measurable property of the observed object or phenomenon [65]. In our case, features correspond to discrete frequencies in THz spectra. Feature selection methods strive to select a subset of features that contain the most relevant information (for a desired task) while eliminating redundant, noisy, and irrelevant features. Common approaches for feature selection include filters such as Relief and Information Gain, and wrappers, which utilize a preselected machine learning model to evaluate relevance of considered features [62–64]. Additionally, some machine learning algorithms, such as random forests and models based on LASSO regularization, have an embedded feature selection step [62–64]. Feature extraction methods construct a new feature space with reduced dimensionality, where new features are obtained as a combination of the original features. In this work, we focus on two well-known linear feature extraction methods, namely principal component analysis and linear discriminant analysis, which represent unsupervised and supervised approach, respectively [51, 52]. Therefore, when referring to dimensionality reduction, we explicitly refer to feature extraction.

Principal component analysis is a widespread multivariate analysis and dimensionality reduction method, which has found application in various fields including image processing, pattern recognition, and chemometrics [47, 49, 63, 66, 67]. As an unsupervised method, PCA does not process class membership information (labels); therefore, its outcome depends only on the hidden patterns in the data. It transforms original features into a set of new uncorrelated (orthogonal) features, called principal components, designed to maximize the variance of the data. This should lead to separation of observations having different properties (i.e., belonging

to different classes). In practice, the variance maximization is achieved by eigendecomposition of the data's covariance matrix (or correlation matrix [60]). The obtained eigenvectors are ordered by the amount of explained variance, which is proportional to their eigenvalues, so that the first principal component represents the highest variability. Dimensionality reduction is obtained by selecting a limited number of most relevant principal components. In many cases, projecting the initial data onto a relatively small number of principal components is able to explain the vast majority of the variance. This allows for a significant reduction in dimensionality [45, 68, 69].

Linear discriminant analysis is a commonly used dimensionality reduction technique, which utilizes a supervised approach. In comparison to unsupervised methods, using class membership information offers a range of new possibilities for formulating transformation criteria. LDA seek a transformation that maximize the distance between classes, while minimizing the scatter within each class [70]. This should provide a large inter-class spacing and small intra-class separation in the new reduced feature space. Satisfying these criteria requires calculating between-class S_b and within-classS_w scatter matrices defined as:

$$S_w = \frac{1}{n}\sum_{j=1}^{m}\sum_{x\in X_j}\left(x-c^{(j)}\right)\left(x-c^{(j)}\right)^T \qquad S_b = \frac{1}{n}\sum_{j=1}^{m} n_j\left(c^{(j)}-c\right)\left(c^{(j)}-c\right)^T$$

where x is a vector representing a specific observation, c is a global centroid and $c^{(j)}$ is a centroid of jth class, and n and m are the number of observations and classes, respectively. Alternatively, a total scatter matrix S_t calculated as

$$S_t = \frac{1}{n}\sum_{i=1}^{n}(x_i-c)(x_i-c)^T = S_b + S_w$$

can be used instead of S_w. It has been shown that these two approaches yield equivalent solution [52, 71, 72]. In this work, we used second approach (calculating S_t). The desired optimization task is then reduced to eigendecomposition of $S_t^{-1}S_b$ (or $S_w^{-1}S_b$) [52, 70]. Since the rank of the S_b matrix is limited to $m - 1$ (S_b is the sum of m matrices of rank 1), the obtained solution contains at most $m - 1$ independent eigenvectors that are associated with non-zero eigenvalues [51, 72]. Consequently, LDA can project the data onto at most $m - 1$ dimensions. Since in most cases the number of original features is larger than the number of considered classes, this property alone imposes a reduced dimensionality of the new feature space. However, it is also possible to select a smaller number of most relevant features to further reduce the dimensionality.

2.5 Machine Learning–Classification Algorithms

The *Bayes classifier* is a probabilistic classification model that utilizes Bayes' theorem [51, 73, 74]. According to Bayes' formula, a posterior probability $p(C_i|\ x)$, which is the probability that the observation with value x belongs to the ith class, can be calculated as

$$p(C_i|x) = \frac{p(x|C_i)\,p(C_i)}{p(x) = \sum_i p(x|C_i)\,p(C_i)} \qquad \text{posterior} = \frac{\text{likelihood} \times \text{prior}}{\text{evidence}}$$

where $p(C_i)$ is called the prior and it is the probability that the observation, regardless of its value, belongs to the class i, and the likelihood $p(x|C_i)$ is a probability that the member of the ith class takes an observation value x. The expression in the denominator $p(x)$, called the evidence, is a marginal probability that the observation x occurs. The evidence is merely a normalization factor, which ensures that the posteriors sum up to one, and can be neglected. The prior and the class likelihood are estimated from the training data and used for computing the class-specific posterior probability. Finally, the Bayesian classifier assigns the observation to the class with the highest posterior probability. In our work, we assumed a multivariate normal (Gaussian) distribution of the class likelihood function. This limited the likelihood estimation to finding the two unknown parameters of the multivariate Gaussian, namely the mean vector and the covariance matrix. Henceforth, we refer to the method as the Gaussian Bayes classifier.

k-Nearest Neighbors is a simple, yet effective, non-parametric classification algorithm. Despite being considered a machine learning algorithm, k-NN has no model learning (training) phase (a so-called lazy learning algorithm) [75, 76]. Instead, the algorithm stores all training data and classify a new observation based on its similarity to the training instances. Here, similarity is expressed in terms of the geometrical distance, such as the Euclidean, Minkowski, Manhattan, or Chebyshev distance, between the data points [76, 77]. The algorithm assigns the new observation to the class possessed by the majority of the k closest data points called nearest neighbors. The choice of k, the number of considered nearest neighbors, is crucial as it allows for controlling the algorithm's behavior. For small k, the decision boundaries are more flexible, but the algorithm becomes prone to outliers, while higher k results in more robust boundaries [78, 79]. In this study, we used the Euclidean distance as a similarity metric in the k-NN algorithm. For each considered case, we used k comparable to the number of training examples in the smallest class ($k = 125$ in Chapters 3.1 and 3.2, $k = 95$ in Chapter 3.3, and $k = 383$ in Chapter 3.4, as indicated in the corresponding classification accuracy tables). This approach should provide a good estimate of intra-class distribution and separation between classes.

Support vector machine was introduced by Vapnik in 1995 and has been one of the most widely used classification algorithms ever since [80]. The algorithm is based on the maximal margin classification concept. It searches for a hyperplane, $h(x) = x^T\beta + \beta_0 = 0$, that separates the observations belonging to two classes and has the largest value of the minimum geometrical distance to class representatives—the margin M. The classification of new observations is based on which side of the hyperplane they are on. The maximal margin hyperplane is found by solving the following optimization problem [81–83]:

$$\max_{\beta,\beta_0,\|\beta\|=1} M \text{ subject to } y_i\left(x_i{}^T\beta+\beta_0\right)\geq M, \quad i=1,\ldots,n,$$

where β and β_0 are parameters of the optimal hyperplane, $y \in \{-1, 1\}$ are labels associated with two considered classes, and n is the number of observations. The maximal margin classifier offers the solution with $M > 0$ only when the classes are linearly separable. For non-linearly separable data, the algorithm utilizes a soft margin approach. It allows some data points to violate the margin or even be on the opposite side of the hyperplane in exchange for imposing a penalty, called the slack variable ξ_i, on the objective function. The optimization problem then becomes:

$$\max_{\beta,\beta_0,\|\beta\|=1} M \; y_i\left(x_i{}^T\beta+\beta_0\right)\geq M(1-\xi_i), \quad \xi_i\geq 0, \quad \sum_i^n \xi_i \leq C, \quad i=1,\ldots,n,$$

where C is a non-negative tuning parameter that controls the balance between the margin width and the slack (the bias-variance trade-off). In practice, finding an optimal hyperplane only requires the consideration of a small number of observations that lie on or violate the margin (so-called support vectors). Since the hyperplane has a dimensionality of $d - 1$, where d is the dimensionality of the input data, the obtained decision boundary is linear. However, SVM can also create non-linear decision boundaries. This is achieved by mapping the data into higher dimensional space using non-linear kernel functions. In this study, we used SVMs with a linear kernel. Originally, SVMs were defined for a binary classification problem. In order to perform multiclass classification, we adopted a one-versus-one approach in which a separate SVM is constructed for each pair of classes [81]. The final classification is a majority decision of all $\binom{m}{2}$ pairwise SVM classifiers. To determine the optimal value of C, we performed a 10-fold cross-validation on the training set.

3 Results and Discussion

3.1 Samples with Single Concentration of Active Materials

Some publications on material identification using THz spectroscopy consider samples with only a single concentration of active materials within each material class [40, 84]. Therefore, we first compared the performance of DR methods in this simple scenario. To this end, we used the samples with the highest content of the active material (80%), which exhibit the most pronounced spectral features, and two samples of pure PE. As shown in Fig. 2, all six active materials have distinctive spectral features in the measured frequency range, while PE is inert and exhibits an almost featureless spectrum. Since THz spectroscopy measurements were performed in a reflection configuration, the spectra depend on the refractive index of the materials [85] having smooth and relatively broad features. Consequently, there is significant spectral overlap among materials and the spectral features cover almost the entire frequency range. Two prominent absorption lines of atmospheric water vapor, located at around 1100 and 1115 GHz, respectively [4], reduce the signal measured from the sample (but not the reference) to the level comparable to the noise floor. This leads to the formation of two narrow, noisy peaks. By excluding the noisy data in the range 1086-1119 GHz (blue line in Fig. 2), we obtained 1117 spectra containing 817 discrete frequencies (dimensions / features), which we divided into training and test sets (4:1) and used for the evaluation of the DR methods.

We used PCA and LDA algorithms to reduce dimensionality of the THz spectra. To numerically verify the performance of the DR methods in terms of grouping and separating different materials, we classified the data using three different classifiers, namely a Gaussian Bayes classifier, a k-NN, and an SVM. Table 2 summarizes the obtained classification accuracies. As shown in Fig. 3, projecting the spectra onto a two-dimensional space provides good separation between materials in the training set (filled circles). For PCA (Fig. 3a), there is a small overlap between lactose, theophylline, and galactitol, while the other materials are well separated. Classification of PCA-processed data with the SVM and the Bayes classifier yielded similar training classification accuracies of 0.9888 and 0.9843, respectively. The k-NN algorithm showed slightly lower performance of 0.9742. As expected, all misclassification cases originate from confusing two of the overlapping materials. For LDA (Fig. 3b), all the

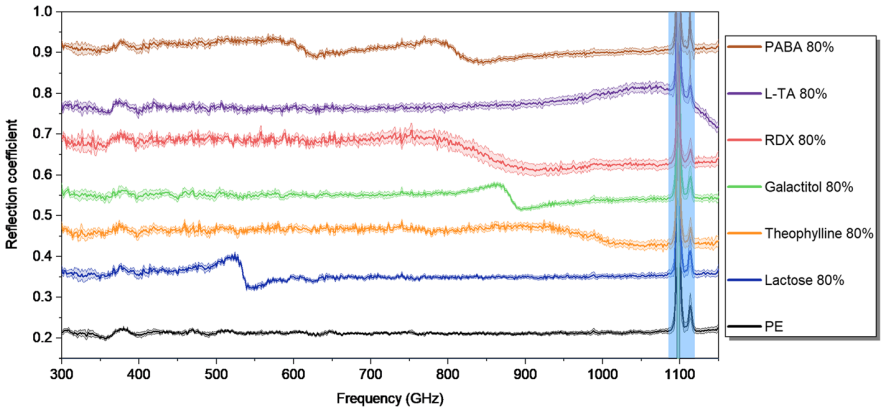

Fig. 2 THz reflection spectra of the samples with 80% of the active material and samples of pure PE. The central lines represent the mean of 160 measurements performed on two different samples, while the error bars (outer lines) represent a standard deviation of the measured spectra. For clarity, each consecutive spectrum, except PE, has been shifted upwards by 0.1. The blue line represents a spectral region excluded from simulations due to significant water absorption–related noise

materials seem to be spatially separated. Although theophylline is located close to L-TA, there is no overlap between these materials. The performed classification confirms that observation as all classifiers yielded a perfect accuracy on the training set.

Subsequently, we performed DR on the test set (empty squares in Fig. 3) using the trained PCA and LDA algorithms to verify their performance on unseen data, a so-called generalization. For PCA (Fig. 3a), the test set overlaps distinctly well with the training set and each cluster corresponding to different materials shows similar distribution for both datasets. Furthermore, the obtained test classification accuracies are comparable to those obtained on the training set, which proves a good generalization of the PCA algorithm. However, as shown in Fig. 3b, LDA does not generalize as well as PCA. Data points corresponding to the specific material are more scattered in the test set than it is the case for the training set. Classifying the LDA-processed test data, we obtained a relatively poor classification accuracy of around 0.9509 and 0.9464 for Bayes classifier and k-NN, and for SVM, respectively. Most cases of misclassification arose from confusing theophylline and L-TA due to the increased dispersion of the test data. The observed lack of generalization together with a perfect performance on the training set suggests overfitting of the LDA algorithm [86, 87]. It has been reported that LDA is prone to overfitting if the dimensionality of the data is comparable to the size of the training set [88–90] (poorly posed problem), which applies to the considered case (817 features and 893 training spectra). The eigenvectors obtained during the training confirm that the algorithm

Table 2 Classification accuracy of DR-processed THz spectra. Only the samples with 80% of active material and samples of pure PE have been considered

	PCA		LDA		RLDA	
	Train	**Test**	**Train**	**Test**	**Train**	**Test**
Bayes	0.9843	0.9955	1.0000	0.9509	1.0000	1.0000
125-NN	0.9742	0.9732	1.0000	0.9509	0.9966	1.0000
SVM	0.9888	0.9732	1.0000	0.9464	1.0000	1.0000

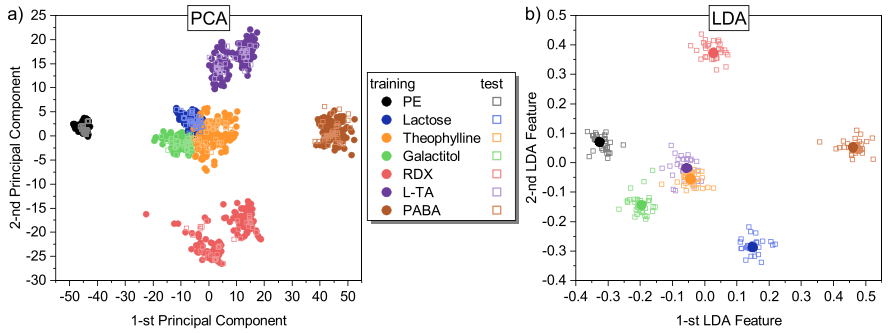

Fig. 3 THz reflection spectra (shown in Fig. 2) projected onto a two-dimensional feature space using two DR methods: **a** PCA and **b** LDA. Filled circles correspond to the training set, while empty squares to the test set

follows the noise instead of patterns (spectral features) in the data (see Fig. S1 in the supplementary material). Consequently, the algorithm performs poorly on the unseen data, which exhibit a different noise pattern.

Overfitting is a well-known problem in machine learning and is closely related to the bias/variance trade-off, where the trained model exhibits a high variance [51, 86]. Increasing the size of the training set constrains the variability of the model and thus prevents overfitting. However, performing a great number of additional measurements is usually time-consuming and costly, and in some applications, it can be impractical or even impossible. Another approach is to reduce the number of parameters to train. It can be achieved by feature selection methods, which eliminate redundant features and those that contain the least amount of information [62]. However, feature selection is a complex task and sometimes may remove essential features leading to inferior performance of the algorithm [89]. Regularization is a simple, yet effective, solution to the overfitting problem. It has been implemented in many machine learning algorithms [51, 82, 86]. It allows constraining the variance by imposing a penalty on complex models. In LDA, the simplest form of regularization is implemented by adding a regularization parameter λ to the diagonal elements of the total scatter matrix S_t following the formula: $\widehat{S}_t = S_t + \lambda I$, where $\lambda > 0$ and I is the identity matrix [52, 70, 72]. However, more sophisticated forms of regularization have also been proposed [52, 72, 87, 91]. Choosing λ is crucial for a correct operation of regularized LDA (RLDA) because it directly controls the balance between bias and variance of the model (see Fig. S2 in the supplementary information). To estimate an optimal value of λ, we performed 10-fold stratified cross-validation on the training set [81, 82, 88]. Using the classification accuracy of the Gaussian Bayes classifier as a validation criterion, we found the optimal value of λ to be 0.5. Finally, we trained the RLDA algorithm on the entire training set using the previously estimated optimal value of λ and applied the trained model to the test set.

As shown in Fig. 4, RLDA provides significantly better generalization than the classical LDA algorithm while maintaining a perfect separation between materials. There is a perfect alignment between the training and test data and material-specific clusters show similar distribution in both datasets. The SVM and the Bayes classifier had no problems with the RLDA-processed data yielding a unity accuracy on both training and test sets. The k-NN also achieved a perfect test accuracy but misclassified a few training examples yielding a training accuracy of 0.9966. Our results shows that RLDA slightly outperforms PCA in terms of preprocessing data for classification purposes. However, reducing the dimensions of the data

from 817 to two is very strict. Projecting the THz spectra onto three- instead of two-dimensional space allows obtaining a perfect separation of materials also for PCA as confirmed by the Gaussian Bayes classifier and SVM (k-NN misclassified a few training examples resulting in a training accuracy of 0.9955). In comparison to PCA, RLDA provides more efficient spatial grouping of the materials. For PCA, data points corresponding to RDX are scattered and form two separate clusters (a similar behavior can be observed for L-TA). We found that two nominally identical samples of RDX exhibit slightly different spectra, which we attribute to non-uniform distribution of the active material. Since PCA is an unsupervised method, it considers only the patterns in the data. Therefore, spectral differences between RDX samples result in spatial separation in the reduced feature space. In the case of RLDA, the provided class membership information, which is a key property of supervised learning methods, enables efficient grouping of data despite the spectral differences. A poor grouping ability of unsupervised DR methods may have a negative impact on the performance of some classification algorithms.

3.2 Samples with Various Concentrations of Active Materials

Subsequently, we considered a more realistic scenario, where the samples contain various concentrations of the active material to be identify. To this end, we characterized the samples with three different concentrations, i.e., 80%, 50%, and 20%, respectively. Additionally, we used two samples of pure PE to test whether the samples with low active material content and therefore high PE content can be distinguished from the background. Figure 5 shows the spectra of all types of samples used in this study. Since the samples are mixtures of the active material and PE, the obtained reflection coefficient is an intermediate value between the spectra of the two components. As the concentration of the active material decreases, the material-specific spectral features become less pronounced. Furthermore, for materials having a significantly higher refractive index than PE, e.g., PABA and theophylline, the reflection coefficient drops over the entire spectral range with decreasing concentration. Here, we investigate if the increased variability of the data associated with material concentration affects the performance of the DR algorithms.

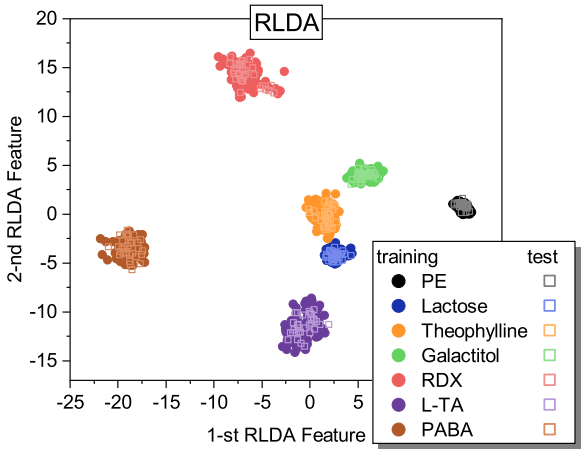

Fig. 4 THz reflection spectra (shown in Fig. 2) projected onto a two-dimensional feature space using RLDA. Filled circles correspond to the training set, while empty squares to the test set

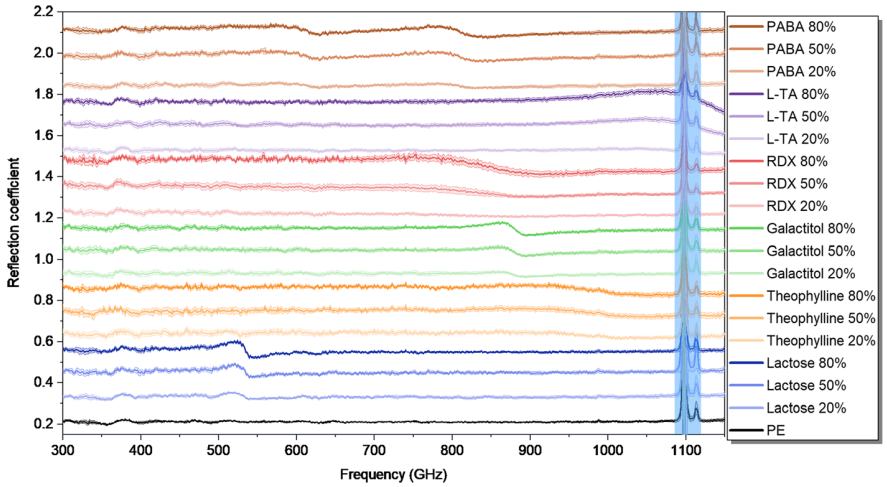

Fig. 5 THz reflection spectra of all samples used in this study. The central lines represent the mean of 160 measurements performed on two different samples, while the error bars (outer lines) represent the standard deviation of the measured spectra. For clarity, each consecutive spectrum, except PE, has been shifted upwards by 0.1. The blue line represents a spectral region excluded from simulations due to significant water absorption–related noise

While performing DR, we used the same methodology as before. First, PCA and LDA algorithms were trained on the training set containing 80% (2428) of the THz spectra. Then, we applied them to the remaining 20% (608) of the spectra, which constitute a test set. Since the aim was to identify the sample by the contained active material regardless of its concentration, the class labels used for the supervised DR contain only the information about the type of the material, while neglecting its concentration. In contrast to the simple scenario considered previously, the DR algorithms were unable to provide good separation between the materials using only two most significant features. Therefore, we projected the data onto three-dimensional space. As an unsupervised method, PCA considers only the patterns in the input data, or more precisely, its variance. Therefore, we expect that an additional variability related to material concentration is going to be transferred into a lower dimensional space as we observed for RDX in the previous section. As shown in Fig. 6a and 7, PCA processing arranged the data into a shape resembling a conical surface. At the vertex of the cone, there are data points corresponding to the pure PE, which is a component of all the samples. The data corresponding to samples with a low content of active material, and hence with a high content of PE, is located close to the pure PE and distributed around the cone's symmetry axis depending on the contained active material (Fig. 7). In this configuration, faint spectral features of the samples with low active material content correspond to a small spatial separation between samples. As the concentration of the active material increases, the data points are projected further from the vertex. Consequently, the data corresponding to each material is divided into clusters, which correspond to different material concentrations. The materials that exhibit larger concentration-related spectral changes (globally, over the entire spectra), e.g., RDX or PABA (see Fig. 5), are more scattered in the reduced feature space. Therefore, the spatial separation between the samples with high active material content, which have more pronounced spectral features, becomes larger. In other words, the greater the spectral differences between the samples, the larger the separation is in the reduced feature space. This

intuitive explanation of variance can become useful in data analysis; however, in terms of data visualization, the clarity offered by PCA is rather poor. A comparable distribution of test and training data in Fig. 6a and 7 indicates that, as in the previous case, PCA provides a good generalization on unseen data. Subsequently, we classified the PCA-processed data depending on the active material contained in the sample (Table 3). The classification accuracies obtained on the training set ranged from 0.8871 for the Bayes classifier to 0.9090 for the k-NN. For the test set, the classifiers yielded accuracies ranging from 0.8914 to 0.9145 for Bayes classifier and k-NN, respectively. Test results similar or, in that case, better than those obtained on the training set prove a good generalization of PCA. However, the concentration-related separation of data within the material class disturbs the operation of heavily biased classifiers used in this study. This, in turn, results in relatively poor classification accuracy.

The objective of LDA is to maximize the inter-class distance and minimize the scatter within each class. Figure 6b shows that the algorithm does it very well. LDA provides not only a great separation between materials but also a superior intra-class grouping than PCA. The class membership information, introduced into a supervised algorithm by labels, enables efficient grouping of data associated with the same active material despite having an additional variability related to the concentration. However, the distribution of the data in the lower dimensional subspace is not as intuitive and easy to interpret as we observed for PCA. In comparison with the simple scenario presented in the previous section, LDA shows better generalization. Since we used more THz spectra for training (2428 compared to 893 used previously), the noise is effectively averaged out and the algorithm better learns the pattern in the data. As a result, the test set shows a similar distribution compared to the training set. As shown in Table 3, all classifiers achieved a high accuracy of 0.9975 for the LDA-processed training data. For the test set, the obtained classification accuracies were 0.9868 and 0.9885 for the Bayes classifier and the SVM, and the k-NN, respectively. An inferior test performance of both classifiers may suggest that despite an increased amount of data the algorithm slightly overfits the data. It has been suggested that for the optimal performance, machine learning algorithms require at least ten times as many training examples as the number of features [92], while in our case this ratio is only around three. Nevertheless, LDA clearly outperforms PCA in terms of preprocessing the data for classification, as the efficient grouping mechanism offered by the supervised approach results in significantly better performance.

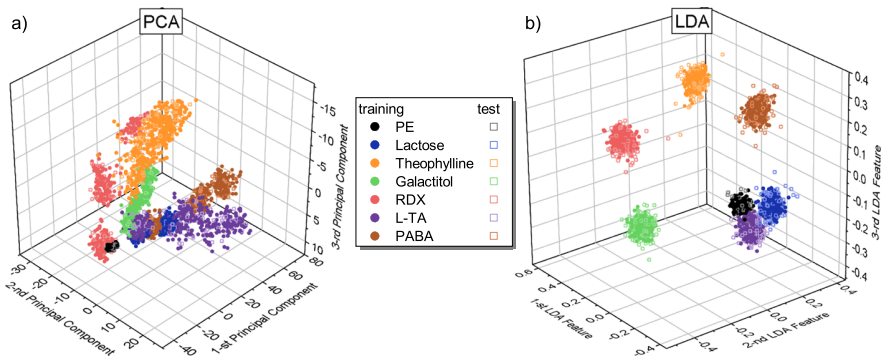

Fig. 6 THz reflection spectra of samples with various concentrations of active material (shown in Fig. 5) projected onto a three-dimensional feature space using two DR methods: **a** PCA and **b** LDA

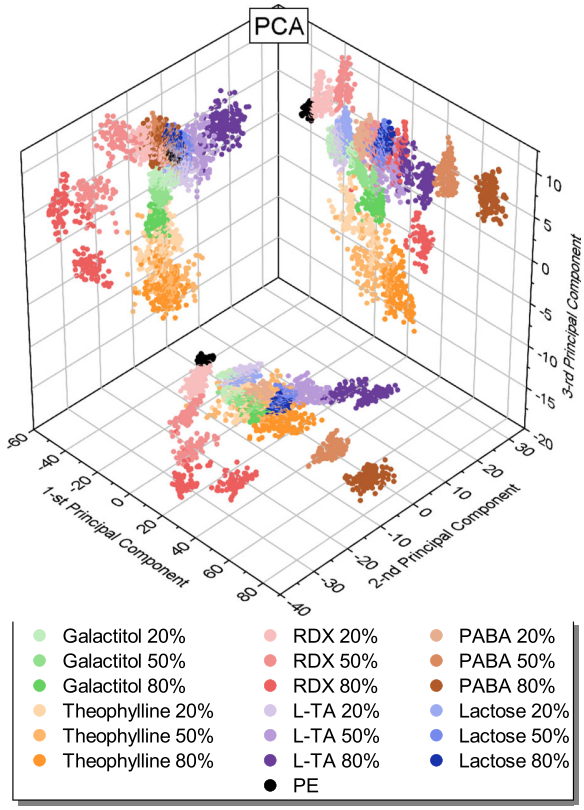

Fig. 7 PCA-processed THz spectra from Fig. 6 projected (for clarity) onto two-dimensional planes and labeled with respect to the active material and its concentration

3.3 Samples with Various Concentrations of Active Materials Under Various (Controlled) Humidity Conditions

Absorption of the atmospheric water vapor is a well-known problem in the THz technology. In Section 3.1, we observed that strong water absorption lines located around 1100 GHz and 1115 GHz almost completely attenuated the THz signal, preventing any useful measurements in the adjacent spectral range (Fig. 2 and Fig. 5). For weaker absorption lines that allow resolving the remaining THz signal, the reference measurement was able to efficiently remove the spectral features related to atmospheric water vapor (Fig. S3 in the supplementary materials). However, in many potential out-of-the-lab applications, e.g., stand-off

Table 3 Classification accuracy of DR-processed THz spectra for the samples with various concentrations of active materials

	PCA		LDA	
	Training	**Test**	**Training**	**Test**
Bayes	0.8871	0.8914	0.9975	0.9868
125-NN	0.9090	0.9145	0.9975	0.9885
SVM	0.8937	0.9046	0.9975	0.9868

identification of hazardous substances, obtaining a precise reference is difficult or even impossible to achieve. Consequently, the THz spectra may possess additional spectral features related to water absorption. To verify their impact on the performance of DR algorithms, we characterized all samples at three different RH levels of 90%, 50%, and 10%, respectively. The reference measurements were performed at RH of 50%. The obtained THz spectra have three narrow peaks corresponding to the water absorption lines located at around 557 GHz, 753 GHz, and 988 GHz (see Fig. S3 in the supplementary materials). The peaks are positive for measurements performed at RH 10% and negative for RH 90%. At RH 50%, the peaks do not occur as they were removed by the reference.

Using an unaltered methodology, we applied DR algorithms to project the THz spectra onto a three-dimensional subspace. As shown in Fig. 8a, PCA arranged the data into three distinctive clusters that correspond to RH level during the measurements. Each RH-related cluster contains smaller clusters corresponding to the active material contained in the sample and its concentration. We conclude that the additional variability related to the water absorption has an effect similar to the material concentration in Section 3.2 and leads to further separation (grouping) of data in the principal component space. This had a significant impact on classification results of PCA-processed data, presented in Table 4. The k-NN algorithm, which showed the best performance, provided an accuracy of only around 0.70 and 0.69 for the training and test set, respectively. In turn, training and test accuracies obtained with SVM were as low as 0.6321 and 0.6053. Figure 8b shows that despite the additional variability, LDA provides an excellent separation between materials and great intra-class grouping. Classification results of the LDA-threated data summarized in Table 4 prove a superior performance of the supervised method. All classification algorithms yielded a unity accuracy on the training set and a test accuracy better than 0.986. The obtained results are similar to those from the previous section showing that the additional variance originating from the water absorption does not adversely affect LDA performance.

3.4 Manipulating Class Label in Supervised Methods

Our results from previous sections show that due to using class membership information, supervised DR methods provide better separation of the materials and superior grouping in comparison to their unsupervised counterparts. However, class labels offer another important functionality. As an additional input parameter, they provide better control over the

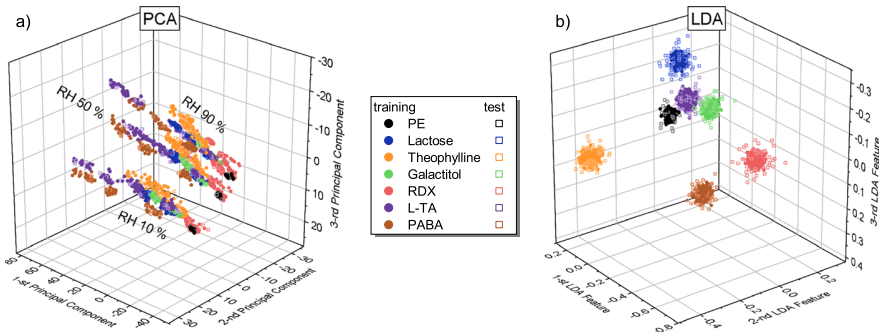

Fig. 8 Three-dimensional projections of THz spectra obtained by **a** PCA and **b** LDA. The THz spectra of samples with various concentrations of active materials were measured under various humidity conditions

Table 4 Classification accuracy of DR-processed THz spectra for the samples with various concentrations of active materials measured under various humidity conditions

	PCA		LDA	
	Training	**Test**	**Training**	**Test**
Bayes	0.6612	0.6316	1.0000	0.9868
95-NN	0.7007	0.6908	1.0000	0.9912
SVM	0.6321	0.6053	1.0000	0.9868

classification algorithm. To demonstrate this, we considered an example related to security screening, which is a potential application of THz spectroscopy. For security screening, it is not necessary to identify an exact material composition of the investigated object. Instead, it is more relevant to recognize whether the object poses any threat, to specify a type and magnitude of the threat, and to determine the proper course of action in response. Therefore, we re-labeled the spectra used in Section 3.2 based on the type of hazard that the corresponding samples represent. RDX is a common explosive compound that has been used in numerous bomb plots including terrorist attacks. It is widely used as a stand-alone explosive but also as a part of explosive mixtures such as Composition C-4, Torpex, and Semtex H [3]. Due to posing an imminent threat to multiple persons, detection of RDX requires immediate actions. Therefore, we labeled RDX as “Danger”. Theophylline is a pharmaceutical compound used to treat respiratory diseases such as asthma. It has a narrow therapeutic range and is toxic if ingested at higher doses. Nevertheless, in comparison to RDX, the threat it constitutes is minor and does not require such drastic measures. Consequently, theophylline was assigned with a “Warning” label. The rest of investigated materials (galactitol, lactose, L-TA, PABA, and PE) does not pose any hazard; hence, they were labeled as “Safe”.

Subsequently, we used the spectra with new labels to train the LDA algorithm. Since we divided the data into three classes, LDA can project the data onto a two-dimensional subspace at most. Despite this limitation, LDA provides a perfect separation between newly established classes and an efficient intra-class grouping, as shown in Fig. 9. Furthermore, LDA shows a

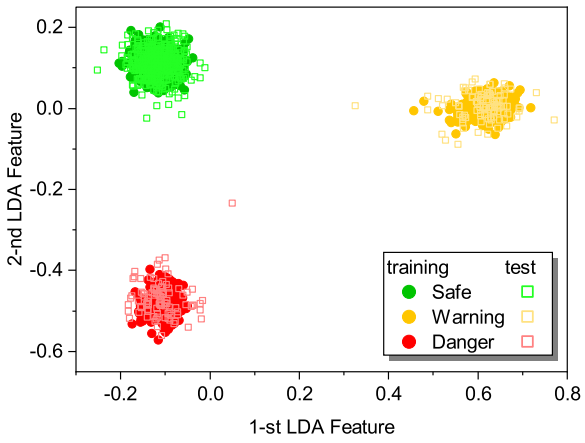

Fig. 9 THz reflection spectra projected onto a two-dimensional feature space using LDA. The labels used in supervised DR correspond to the hazard represented by the samples. Filled circles correspond to the training set, while empty squares to the test set

good generalization on the test data. As expected, none of the classifiers had any problems with LDA-processed data, yielding unity accuracy on both training and test sets. This shows that by altering the class labels, it is possible to project the data into different groups that are more suitable for the desired application. For comparison, we classified PCA-processed data using new class labels. Since the output of unsupervised methods does not depend on the class labels, we refer to the results from Section 3.2 (PC1-PC2 plane in Fig. 7). Obtained classification results, summarized in Table 5, show that PCA was not up to the task. Bayes classifier and k-NN correctly predicted only around 0.77 and 0.75 of test data, respectively. On the other hand, SVM yielded a higher, but still far from satisfactory, test classification accuracy of approximately 0.83.

4 Conclusions

In summary, we compared the use of principal component analysis and linear discriminant analysis—two linear methods that represent an unsupervised and a supervised approach, respectively, for analysis of THz CW reflection spectra. We focused on two common applications of dimensionality reduction, namely data visualization and preprocessing the data for classification. In the simple scenario, where we considered only samples with a single concentration of active materials, both approaches were able to compress 817-dimensional spectra down to a two-dimensional subspace while providing good discrimination between materials.

However, as we increased the complexity of the data by using samples with various concentrations of active materials, the performance of the unsupervised approach decreased significantly. We observed a formation of separate clusters for samples having different active material concentrations in PCA-processed data. The same effect was observed while evaluating measurements performed under various humidity conditions. Since the unsupervised methods depend only on the patterns in the data, the additional intra-class variance is transferred into the reduced lower dimensional space. This may have a negative impact on the classification accuracy, especially for highly biased classifiers as those used in this study. On the other hand, using class membership information (labels) allowed LDA to effectively group the samples with the same active material despite differences in concentration and RH. As a result, LDA provides better visualization clarity and higher classification accuracy. Therefore, if the considered application provides the labels, we strongly recommend using supervised methods, as the use of unsupervised methods in this case involves neglecting information. Furthermore, using THz security screening as an example, we demonstrated that manipulating the labels allows tuning the output of the algorithm for the desired classification task.

Table 5 Classification accuracy of DR-processed THz spectra for the samples with various concentrations of active materials, labeled according the type of hazard they represent

	PCA		LDA	
	Training	**Test**	**Training**	**Test**
Bayes	0.7648	0.7747	1.0000	1.0000
383-NN	0.7467	0.7500	1.0000	1.0000
SVM	0.8361	0.8322	1.0000	1.0000

Despite showing a better performance and more flexibility than PCA, LDA has some drawbacks that need to be considered. When the number of observations is comparable to the number of features, a so-called poorly posed problem, LDA tends to overfit the data. This can result in a significant drop in classification accuracy. Therefore, LDA requires more measurements than its unsupervised counterpart does, which in some applications may be an obstacle. We demonstrated that regularization is an effective solution for the overfitting problem; however, tuning the regularization parameter requires an additional user intervention. Since LDA aims to maximize the distance between classes and minimize the intra-class scatter, the distribution of the data in the lower dimensional subspace is not as intuitive as it is the case in PCA, which aims to maximize the variance.

Furthermore, our experiments show that simple algorithms (linear dimensionality reduction and basic classifiers such as Bayesian classifier and k-NN) are sufficient for visualization and classification of THz reflection spectra. In all presented scenarios, the obtained classification accuracy was better than 98.6% using LDA. However, we recognize that in more complex cases, such as measurements through covering materials and diffused reflection measurements, which are relevant for implementation of THz screening systems, the use of more sophisticated algorithms, e.g., neural networks, may be beneficial.

Supplementary Information The online version contains supplementary material available at https://doi.org/10.1007/s10762-021-00810-w.

Acknowledgements The project was performed in collaboration with MyDefence. The authors wish to express their gratitude to the Danish Defence and Danish Ministry of Defence Acquisition and Logistics Organisation for knowledge and assistance in measurements of explosives. Finally yet importantly, the authors are thankful to Associate Professor Torben Tvedebrink for fruitful conversations.

Code Availability The data processing as well as dimensionality reduction and classification algorithms has been implemented in MATLAB (MathWorks, version R2018a).

Author Contribution Paweł Piotr Cielecki: formal analysis, investigation, methodology (lead), software, validation, visualization, writing – original draft, writing – review and editing.
Mathias Hedegaard Kristensen: investigation, methodology, writing – review and editing.
Esben Skovsen: conceptualization, funding acquisition, methodology, supervision, writing – review and editing.

Funding This work was financed by the Innovation Fund Denmark Grand Solutions program with grant no. IFD-7076-00017B.

Data Availability The data is available upon request from the corresponding author.

Declarations

Conflict of Interest The authors declare no competing interests.

References

1. A. G. Davies, A. D. Burnett, W. Fan, E. H. Linfield, and J. E. Cunningham, Mater. Today **11**, 18 (2008).
2. J. F. Federici, B. Schulkin, F. Huang, D. Gary, R. Barat, F. Oliveira, and D. Zimdars, Semicond. Sci. Technol. **20**, S266 (2005).

3. M. R. Leahy-Hoppa, M. J. Fitch, and R. Osiander, Anal. Bioanal. Chem. **395**, 247 (2009).
4. H.-B. Liu, H. Zhong, N. Karpowicz, Y. Chen, and X.-C. Zhang, Proc. IEEE **95**, 1514 (2007).
5. A. Luukanen, R. Appleby, M. Kemp, and N. Salmon, in *Terahertz Spectrosc. Imaging. Springer Ser. Opt. Sci.*, edited by K. Peiponen, A. Zeitler, and M. Kuwata-Gonokami (Springer Berlin Heidelberg, 2012), pp. 491–520.
6. P. U. Jepsen, D. G. Cooke, and M. Koch, Laser Photon. Rev. **5**, 124 (2011).
7. S. Koenig, D. Lopez-Diaz, J. Antes, F. Boes, R. Henneberger, A. Leuther, A. Tessmann, R. Schmogrow, D. Hillerkuss, R. Palmer, T. Zwick, C. Koos, W. Freude, O. Ambacher, J. Leuthold, and I. Kallfass, Nat. Photonics **7**, 977 (2013).
8. I. F. Akyildiz, J. M. Jornet, and C. Han, Phys. Commun. **12**, 16 (2014).
9. T. Kleine-Ostmann and T. Nagatsuma, J. Infrared, Millimeter, Terahertz Waves **32**, 143 (2011).
10. D. M. Mittleman, J. Appl. Phys. **122**, 230901 (2017).
11. F. Rutz, M. Koch, S. Khare, M. Moneke, H. Richter, and U. Ewert, Int. J. Infrared Millimeter Waves **27**, 547 (2007).
12. A. A. Gowen, C. O'Sullivan, and C. P. O'Donnell, Trends Food Sci. Technol. **25**, 40 (2012).
13. A. I. Hernandez-Serrano, S. C. Corzo-Garcia, E. Garcia-Sanchez, M. Alfaro, and E. Castro-Camus, Appl. Opt. **53**, 7872 (2014).
14. F. Ellrich, M. Bauer, N. Schreiner, A. Keil, T. Pfeiffer, J. Klier, S. Weber, J. Jonuscheit, F. Friederich, and D. Molter, J. Infrared, Millimeter, Terahertz Waves **41**, 470 (2020).
15. J. Chen, Y. Chen, H. Zhao, G. J. Bastiaans, and X.-C. Zhang, Opt. Express **15**, 12060 (2007).
16. M. R. Leahy-Hoppa, M. J. Fitch, X. Zheng, L. M. Hayden, and R. Osiander, Chem. Phys. Lett. **434**, 227 (2007).
17. A. D. Burnett, W. Fan, P. C. Upadhya, J. E. Cunningham, M. D. Hargreaves, T. Munshi, H. G. M. Edwards, E. H. Linfield, and A. G. Davies, Analyst **134**, 1658 (2009).
18. K. Kawase, Y. Ogawa, Y. Watanabe, and H. Inoue, Opt. Express **11**, 2549 (2003).
19. F. Hindle, A. Cuisset, R. Bocquet, and G. Mouret, Comptes Rendus Phys. **9**, 262 (2008).
20. J. Qin, B. Zhu, Y. Du, and Z. Han, Opt. Fiber Technol. **52**, 101990 (2019).
21. N. Shimizu, T. Ikari, K. Kikuchi, K. Matsuyama, A. Wakatsuki, S. Kohjiro, and R. Fukasawa, in *2011 IEEE MTT-S Int. Microw. Symp.* (IEEE, 2011), pp. 1–4.
22. U. Puc, A. Abina, M. Rutar, A. Zidanšek, A. Jeglič, and G. Valušis, Appl. Opt. **54**, 4495 (2015).
23. C. Baker, T. Lo, W. R. Tribe, B. E. Cole, M. R. Hogbin, and M. C. Kemp, Proc. IEEE **95**, 1559 (2007).
24. M. C. Kemp, in *2007 Jt. 32nd Int. Conf. Infrared Millim. Waves 15th Int. Conf. Terahertz Electron.* (IEEE, Cardiff, 2007), pp. 647–648.
25. D. Zimdars, J. S. White, G. Stuk, A. Chernovsky, G. Fichter, and S. Williamson, Insight - Non-Destructive Test. Cond. Monit. **48**, 537 (2006).
26. G. Tzydynzhapov, P. Gusikhin, V. Muravev, A. Dremin, Y. Nefyodov, and I. Kukushkin, J. Infrared, Millimeter, Terahertz Waves **41**, 632 (2020).
27. K. Nawata, Y. Takida, Y. Tokizane, T. Notake, Z. Han, and H. Minamide, in *2019 44th Int. Conf. Infrared, Millimeter, Terahertz Waves* (IEEE, 2019), pp. 1–2.
28. H. Hoshina, Y. Sasaki, A. Hayashi, C. Otani, and K. Kawase, Appl. Spectrosc. **63**, 81 (2009).
29. K. Yamamoto, M. Yamaguchi, F. Miyamaru, M. Tani, M. Hangyo, T. Ikeda, A. Matsushita, K. Koide, M. Tatsuno, and Y. Minami, Jpn. J. Appl. Phys. **43**, L414 (2004).
30. C. Hepp, S. Luttjohann, A. Roggenbuck, A. Deninger, S. Nellen, T. Gobel, M. Jorger, and R. Harig, in *2016 41st Int. Conf. Infrared, Millimeter, Terahertz Waves* (IEEE, 2016), pp. 1–2.
31. C. Bray, A. Cuisset, F. Hindle, G. Mouret, R. Bocquet, and V. Boudon, J. Quant. Spectrosc. Radiat. Transf. **203**, 349 (2017).
32. D. Stanze, A. Deninger, A. Roggenbuck, S. Schindler, M. Schlak, and B. Sartorius, J. Infrared, Millimeter, Terahertz Waves **32**, 225 (2011).
33. A. J. Deninger, A. Roggenbuck, S. Schindler, and S. Preu, J. Infrared, Millimeter, Terahertz Waves **36**, 269 (2015).
34. S. Preu, G. H. Döhler, S. Malzer, L. J. Wang, and A. C. Gossard, J. Appl. Phys. **109**, 061301 (2011).
35. J. R. Demers, F. Garet, and J.-L. Coutaz, IEEE Sensors Lett. **1**, 1 (2017).
36. J. R. Demers, J.-L. Coutaz, and F. Garet, in *Terahertz, RF, Millimeter, Submillimeter-Wave Technol. Appl. XI*, edited by L. P. Sadwick and T. Yang (SPIE, 2018), p. 20.
37. C. Cao, Z. Zhang, X. Zhao, and T. Zhang, Opt. Quantum Electron. **52**, 225 (2020).
38. M. R. Nowak, K. Nowak, M. Grzelczak, B. Szlachetko, L. Sterczewski, E. F. Plinski, P. Swiatek, M. Strzelecka, S. Plinska, and W. Malinka, in *2017 42nd Int. Conf. Infrared, Millimeter, Terahertz Waves* (IEEE, 2017), pp. 1–2.
39. W. Liu, C. Liu, J. Yu, Y. Zhang, J. Li, Y. Chen, and L. Zheng, Food Chem. **251**, 86 (2018).
40. H. Zhong, A. Redo-Sanchez, and X.-C. Zhang, Opt. Express **14**, 9130 (2006).

41. J. Zhang, Y. Yang, X. Feng, H. Xu, J. Chen, and Y. He, Front. Plant Sci. **11**, 1 (2020).
42. K. Wang, D. W. Sun, and H. Pu, Trends Food Sci. Technol. **67**, 93 (2017).
43. W. Liu, C. Liu, X. Hu, J. Yang, and L. Zheng, Food Chem. **210**, 415 (2016).
44. A. I. Knyazkova, A. V. Borisov, L. V. Spirina, and Y. V. Kistenev, J. Infrared, Millimeter, Terahertz Waves **41**, 1089 (2020).
45. A. Pohl, N. Deßmann, K. Dutzi, and H.-W. Hübers, J. Infrared, Millimeter, Terahertz Waves **37**, 175 (2016).
46. H. Zhang, Z. Li, T. Chen, and J. Liu, Optik (Stuttg). **138**, 95 (2017).
47. J. Liu, Optik (Stuttg). **131**, 885 (2017).
48. S. Yamaguchi, Y. Fukushi, O. Kubota, T. Itsuji, T. Ouchi, and S. Yamamoto, Sci. Rep. **6**, 30124 (2016).
49. J. Bou-Sleiman, J.-B. Perraud, B. Bousquet, J.-P. Guillet, N. Palka, and P. Mounaix, in *Millimetre Wave Terahertz Sensors Technol. VIII*, edited by N. A. Salmon and E. L. Jacobs (2015), p. 965109.
50. G. Chao, Y. Luo, and W. Ding, Mach. Learn. Knowl. Extr. **1**, 341 (2019).
51. E. Alpaydin, *Introduction to Machine Learning*, 3rd ed. (MIT Press, Cambridge, MA, 2014).
52. J. Ye and S. Ji, in *Biometrics* (John Wiley & Sons, Inc., Hoboken, NJ, USA, 2009), pp. 1–19.
53. H. Namkung, J. Kim, H. Chung, and M. A. Arnold, Anal. Chem. **85**, 3674 (2013).
54. Yuefang Hua and Hongjian Zhang, IEEE Trans. Microw. Theory Tech. **58**, 2064 (2010).
55. A. Roggenbuck, H. Schmitz, A. Deninger, I. C. Mayorga, J. Hemberger, R. Güsten, and M. Grüninger, New J. Phys. **12**, 043017 (2010).
56. D. W. Vogt and R. Leonhardt, Opt. Express **25**, 16860 (2017).
57. A. Roggenbuck, K. Thirunavukkuarasu, H. Schmitz, J. Marx, A. Deninger, I. C. Mayorga, R. Güsten, J. Hemberger, and M. Grüninger, J. Opt. Soc. Am. B **29**, 614 (2012).
58. D.-Y. Kong, X.-J. Wu, B. Wang, Y. Gao, J. Dai, L. Wang, C.-J. Ruan, and J.-G. Miao, Opt. Express **26**, 17964 (2018).
59. P. P. Cielecki, M. H. Kristensen, and E. Skovsen, (2021). DOI: https://doi.org/10.5281/zenodo.5079558
60. I. T. Jolliffe and J. Cadima, Philos. Trans. R. Soc. A Math. Phys. Eng. Sci. **374**, 20150202 (2016).
61. R. Bro and A. K. Smilde, Anal. Methods **6**, 2812 (2014).
62. J. Tang, S. Alelyani, and H. Liu, in *Data Classif. Algorithms Appl.*, edited by C. C. Aggarwal, 1st ed. (Chapman and Hall/CRC, 2014), pp. 37–64.
63. S. Khalid, T. Khalil, and S. Nasreen, in *2014 Sci. Inf. Conf.* (IEEE, 2014), pp. 372–378.
64. Z. M. Hira and D. F. Gillies, Adv. Bioinformatics **2015**, 1 (2015).
65. G. Chandrashekar and F. Sahin, Comput. Electr. Eng. **40**, 16 (2014).
66. T. Chen, Z. Li, X. Yin, F. Hu, and C. Hu, Spectrochim. Acta Part A Mol. Biomol. Spectrosc. **153**, 586 (2016).
67. J. El Haddad, B. Bousquet, L. Canioni, and P. Mounaix, TrAC Trends Anal. Chem. **44**, 98 (2013).
68. W. Xu, L. Xie, Z. Ye, W. Gao, Y. Yao, M. Chen, J. Qin, and Y. Ying, Sci. Rep. **5**, 11115 (2015).
69. Y. Xie and P. Sun, Opt. Quantum Electron. **50**, 46 (2018).
70. A. Tharwat, T. Gaber, A. Ibrahim, and A. E. Hassanien, AI Commun. **30**, 169 (2017).
71. W.-K. Ching, D. Chu, L.-Z. Liao, and X. Wang, Pattern Recognit. **45**, 2719 (2012).
72. J. Ye, T. Xiong, Q. Li, R. Janardan, J. Bi, V. Cherkassky, and C. Kambhamettu, in *Proc. 15th ACM Int. Conf. Inf. Knowl. Manag. - CIKM '06* (ACM Press, New York, New York, USA, 2006), p. 532.
73. Siuly, X. Yin, S. Hadjiloucas, and Y. Zhang, Comput. Methods Programs Biomed. **127**, 64 (2016).
74. Charu C. Aggarwal, in *Data Classif. Algorithms Appl.*, edited by C. C. Aggarwal (Chapman & Hall/CRC, 2014), pp. 1–36.
75. O. Boiman, E. Shechtman, and M. Irani, in *2008 IEEE Conf. Comput. Vis. Pattern Recognit.* (IEEE, 2008), pp. 1–8.
76. P. Mulak and N. Talhar, Int. J. Sci. Res. **4**, 2101 (2015).
77. G. Bhattacharya, K. Ghosh, and A. S. Chowdhury, Pattern Recognit. Lett. **33**, 356 (2012).
78. R. O. Duda, P. E. Hart, and D. G. Stork, *Pattern Classification*, 2nd ed. (Wiley, New York, 2000).
79. M. Kubat, *An Introduction to Machine Learning*, 2nd ed. (Springer International Publishing, 2017).
80. C. Cortes and V. Vapnik, Mach. Learn. **20**, 273 (1995).
81. G. James, D. Witten, T. Hastie, and R. Tibshirani, *An Introduction to Statistical Learning* (Springer New York, New York, NY, 2013).
82. T. Hastie, R. Tibshirani, and J. Friedman, *The Elements of Statistical Learning: Data Mining, Inference, and Prediction*, 2nd ed. (Springer, New York City, 2009).
83. P.-W. Wang and C.-J. Lin, in *Data Classif. Algorithms Appl.*, edited by C. C. Aggarwal (Chapman & Hall/CRC, 2014), pp. 187–204.
84. J. Huang, J. Liu, K. Wang, Z. Yang, and X. Liu, Spectrochim. Acta Part A Mol. Biomol. Spectrosc. **198**, 198 (2018).
85. N. Palka, Acta Phys. Pol. A **120**, 713 (2011).

86. C. M. Bishop, *Pattern Recognition and Machine Learning*, 1st ed. (Springer-Verlag New York, 2006).
87. K. Z. Mao, Feng Yang, and Wenyin Tang, in *2011 IEEE Symp. Comput. Intell. Bioinforma. Comput. Biol.* (IEEE, 2011), pp. 1–7.
88. J. H. Friedman, J. Am. Stat. Assoc. **84**, 165 (1989).
89. E. Neto, F. Biessmann, H. Aurlien, H. Nordby, and T. Eichele, Front. Aging Neurosci. **8**, 273 (2016).
90. C. Su, F. Tu, X. Zhang, B. Shia, and T. Lee, J. Data Sci. **17**, 1 (2019).
91. Y. Guo, T. Hastie, and R. Tibshirani, Biostatistics **8**, 86 (2007).
92. R. Liu and D. F. Gillies, Pattern Recognit. **53**, 73 (2016).

Supplementary Materials

Analysis and Classification of Frequency-domain Terahertz Reflection Spectra Using Supervised and Unsupervised Dimensionality Reduction Methods

Journal of Infrared, Millimeter, and Terahertz Waves

Paweł Piotr Cielecki, Mathias Hedegaard Kristensen and Esben Skovsen*

Department of Materials and Production, Section for Physics and Mechanics, Aalborg University, Skjernvej 4A, DK-9220 Aalborg East, Denmark

*es@mp.aau.dk

An analysis of eigenvectors obtained from the optimization task provides insight into the operation of the DR algorithm. Fig. S1 shows that PCA eigenvectors follow spectral features of the measured material (population / global characteristics); whereas LDA overfits the data as its eigenvectors reproduce the noise pattern (sample / local characteristics). Consequently, LDA performed poorly on the unseen data, while PCA showed good generalization ability.

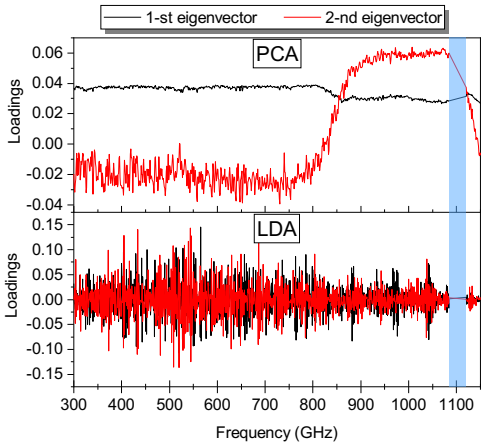

Fig. S1 Eigenvectors obtained during dimensionality reduction using PCA (top panel) and LDA (bottom panel). The blue line represent a spectral region excluded from simulations due to water absorption-related noise.

Overfitting of the LDA algorithm can be overcome by regularization. In this study, we performed regularization by adding a regularization parameter λ to diagonal elements of the total scatter matrix. Adjusting λ allows controlling the balance between bias and variance of the model. Fig. S2 shows eigenvectors obtained by RLDA for three different values of λ, including the optimal solution $\lambda = 0.5$ determined by means of 10-fold stratified cross validation. As λ increases, the eigenvectors become less noisy and more similar to the spectral features of the measured samples.

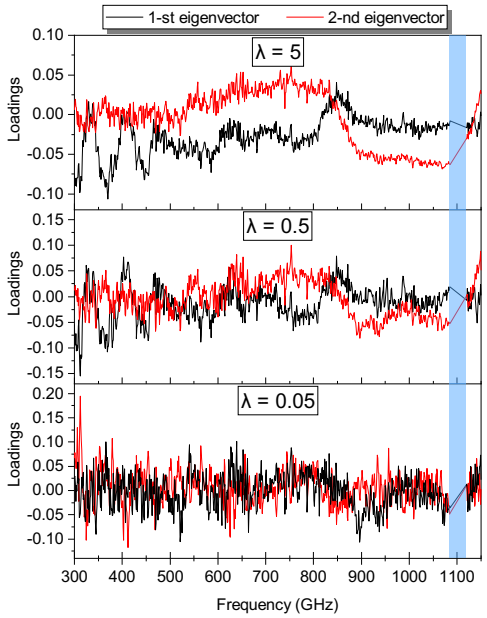

Fig. S2 RLDA eigenvectors obtained for different values of the regularization parameter $\boldsymbol{\lambda}$. The blue line represent a spectral region excluded from simulations due to water absorption-related noise.

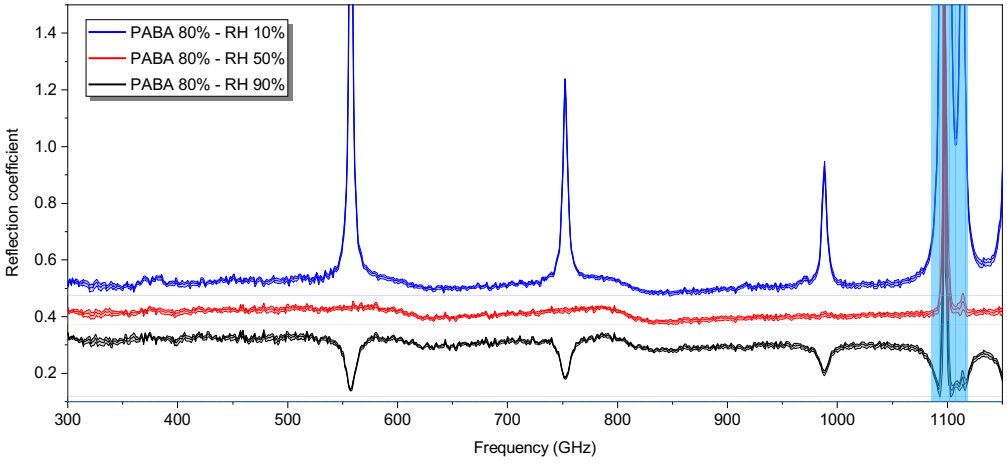

Fig. S3 THz spectra of PABA measured at relative humidity of 10 %, 50 % and 90 %, respectively. The measurements were referenced with a spectra of aluminum mirror recorded at RH = 50 %. For clarity, each consecutive spectrum, except RH 90 %, has been shifted upwards by 0.1. The blue line represent a spectral region excluded from simulations.

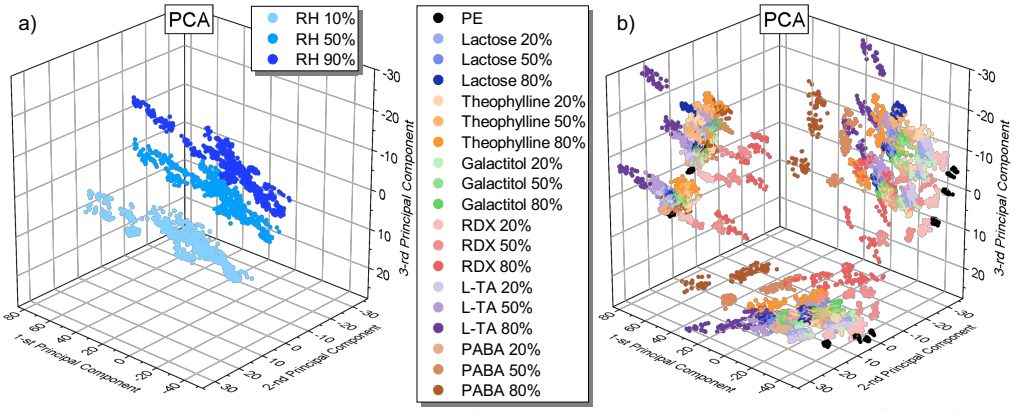

Fig. S4 THz spectra of samples with various concentrations of active material measured under various humidity conditions projected onto three-dimensional space using PCA. Data points are labeled with respect to a) relative humidity b) active material and its concentration (for clarity shown as projections onto 2D planes).

Publication B

Classification of Non-Referenced Terahertz Reflection Spectra using Machine Learning Algorithms

List of authors:

Mathias Hedegaard Kristensen
Paweł Piotr Cielecki
Esben Skovsen

The paper has been submitted to
APL Machine Learning, June 2023.

Classification of Non-Referenced Terahertz Reflection Spectra using Machine Learning Algorithms

Mathias Hedegaard Kristensen,[1] Paweł Piotr Cielecki,[1] and Esben Skovsen[1]
Department of Materials and Production, Section for Physics and Mechanics, Aalborg University, Skjernvej 4A, DK-9220, Aalborg East, Denmark

(*Electronic mail: mhkr@icloud.com)

(Dated: 23 June 2023)

Commonly, a terahertz spectrum is deconvoluted by a reference spectrum to remove the water vapor absorption lines and other system related responses. However, in real-life applications obtaining reference spectra can be problematic and adds to the complexity of the system. In this letter, we study how typical machine learning algorithms for classification of terahertz reflection spectra perform on non-referenced spectra, *i.e.* spectra which have not been deconvoluted by reference spectra, compared to referenced spectra. Prior to classification, the dimensionality of the spectra is reduced from 649 frequencies to five features by either the unsupervised principal component analysis or the supervised linear discriminant analysis. We apply three different classification algorithms; namely a Gaussian Bayes model, the k nearest neighbors, and a support vector machine. Especially, if the terahertz spectra are preprocessed using linear discriminant analysis, very high classification scores (> 99.7%) can be retained for the non-referenced spectra. Thus, this could be of great importance for real-world material identification applications based on terahertz spectroscopy.

I. INTRODUCTION

Terahertz (THz) spectroscopy has proven to be a promising technology for security, defense, safety, and quality control, applications[1,2] since many compound materials exhibit unique spectroscopic characteristics. Including hazardous substances such as explosives, commercial and illicit drugs, and toxic gasses, *e.g.*, ammonia or carbon monoxide. Concurrently, terahertz radiation allows for non-invasive screening as many non-polar and non-metallic materials are transparent within the terahertz frequency band. In addition, the low photon energy inherent to terahertz radiation results in a non-ionizing nature to biological samples. Hence, terahertz spectroscopy is not only desired but also safe for screening of personnel and objects.

For many real-world applications of THz spectroscopy, it is necessary to be able to distinguish different substances in an efficient and reliable manner. Additionally, many applications require the THz spectroscopic measurements to be done in a reflection scheme. The weak and broad spectroscopic characteristics of substances inherent to reflection spectra, caused by the dependence on the refraction index[3], complicates things further. Reflection spectra of some materials commonly found in the literature, measured under ambient conditions, are seen in Fig. 1. The center line of each curve is the mean of 80 measurements, while the filled area represents the standard deviation. The curves are shifted vertically for a better readability. Each spectrum shows clear absorption lines of atmospheric water vapor around 0.55, 0.75, and 0.99 THz, while the spectral characteristics intrinsic to the studied materials are much harder to recognize. If the same spectra are deconvoluted with appropriate reference spectra to obtain the reflection coefficients of the samples (Fig. 2), the material specific characteristics are easily recognized. However, when the weight percentage of the active material in a sample drops to from 50% to 20%, it suddenly becomes difficult to distinguish or identify materials like theophylline, L-TA and PE. Several rather complex machine learning techniques including Bayesian models[4,5], artificial neural networks[6–8], support vector machine[9–11], and random forests[4,6,10] have previously been utilized for classification of terahertz spectra. To make such identification algorithms more efficient, the data is typically preprocessed using dimensionality reduction (DR) methods. This lowers the computational requirements, increases the learning speed of the machine learning algorithm, and allows for visualization of the data for easier interpretation.

Recently, we compared the performance of two unsupervised and supervised linear DR methods[12]; Principal Component Analysis (PCA) and Linear Discriminant Analysis (LDA). We showed that simple machine learning algorithms are sufficient for highly accurate classification (>98.6%) of terahertz spectra. The results relied on deconvolution of the measured reflection spectra with non-ideal reference measurements. Nevertheless, the need for reference spectra can be very inconvenient or even impossible to fulfill in a real-world scenario.

In this letter, we present the classification results of non-referenced vs. referenced terahertz spectra preprocessed using either PCA or LDA for three different classifiers: Bayesian, k nearest neighbors (k-NN), and support vector machines (SVM). These classifiers represent a probabilistic, a non-parametric, and a finely tuned linear algorithm, respectively.

II. METHODS AND MATERIALS

A thorough description of the experimental setup and measuring procedure can be found in[12].

A. Experimental Setup, Samples, and Measurements

The samples were characterized in a reflection geometry by continuous wave (CW) terahertz frequency-domain spec-

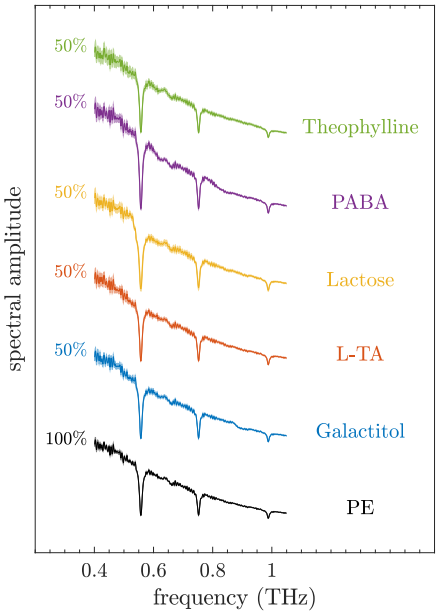

FIG. 1. Non-referenced THz reflection spectra of the samples with 50% of active material and pure PE measured at 50% RH. The dark colored center line of each curve is the mean of 80 measurements, while the light colored fill represents the standard deviation. The curves of each material are shifted vertically for a better readability.

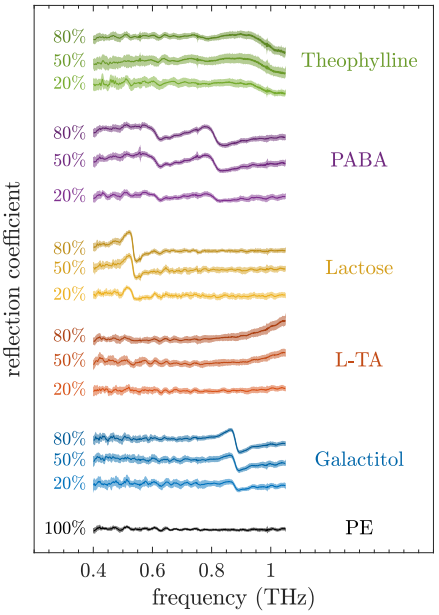

FIG. 2. Referenced THz reflection spectra of the samples with 20%, 50% and 80% of active material and pure PE measured at 50% RH. The dark colored center line of each curve is the mean of 80 measurements, while the light colored fill represents the standard deviation. The curves of each material are shifted vertically for a better readability.

troscopy (THz-FDS) using a TeraScan 1550 system manufactured by Toptica Photonics working from 0.09 to 1.19 THz. The complete setup was enclosed by a custom-built humidity chamber that could be purged with either dry or water vapor saturated nitrogen to achieve relative humidity (RH) levels below or above the ambient air level. Five compound materials with spectral features in the frequency range of the TeraScan 1550 were selected for the study. Including galactitol, L-tartaric acid (L-TA), 4-aminobenzoic acid (PABA), theophylline, and alpha-lactose monohydrate. Six pellets from each compound were fabricated in pairs at weight percentages of 20%, 50%, and 80% of active material mixed with polyethylene powder. The flat response of PE in the spectral band of interest makes it a convenient binder matrix for the active compounds[13]. Furthermore, the sample pellets were shaped as a 15° wedge to avoid interference between the front and the back surface reflections. Each sample was measured over the entire spectral range in 80 MHz increments integrated for 3 ms at 20 random positions in 0.5 mm steps within the scanning area of the sample surface. A reference spectrum was recorded for every 40 measurements replacing the sample with an aluminum mirror. The acquisition procedure was repeated under controlled conditions of 10%, 50%, and 90% RH, respectively. The data includes more than 1900 spectra and is available online as a part of the "Database of frequency-domain terahertz reflection spectra for the DETRIS project"[14].

B. Data Processing and Machine Learning

The CW THz-FDS setup operates in a coherent detection scheme, which causes phase oscillations in the recorded photocurrent $I_{\mathrm{ph}}(\nu)$ as the THz frequency ν is scanned. In this study, the instantaneous amplitude $A(\nu)$ and instantaneous phase $\phi(\nu)$ were calculated by applying the Hilbert transformation $\mathscr{H}$ to the oscillating photocurrent proportional to the THz electric field[15,16]. The resulting complex-valued analytic signal

$$I_{\mathrm{a}}(\nu) = I_{\mathrm{ph}}(\nu) + i\mathscr{H}\left\{I_{\mathrm{ph}}(\nu)\right\} = A(\nu)\exp\left[i\phi(\nu)\right]$$

was then Fourier transformed into the time-domain, in which it was filtered for any reflections in the experimental setup causing Fabry-Pérot interference, and inversely Fourier transformed back into the frequency-domain.[17] The data was cropped to an interval from 0.4 to 1.05 THz to include only the spectral region containing spectroscopic characteristics of

samples and achieving a proper signal to noise ratio. In coherence to our previous study[12], we used only the spectral amplitude $A(\nu)$ of the THz field in the further processing. Nonetheless, the same unique material information is contained in the spectral phase $\phi(\nu)$ as for THz time-domain spectroscopy (TDS)[15,16]. Prior to the calculation of the reflection coefficient

$$R(\nu) = A_{\text{sample}}(\nu)/A_{\text{reference}}(\nu),$$

the data was interpolated onto integer GHz-frequencies to ensure a proper deconvolution of the individual spectral components. In the remaining part of this paper, we categorize the spectral data $A(\nu)$ and $R(\nu)$ plotted in Fig. 1 and Fig. 2 as *non-referenced* and *referenced*, respectively.

The referenced and non-referenced data sets were both standardized *i.e.*, each feature was normalized to zero mean and unity variance, which is crucial for PCA to operate correctly[18,19]. Next, the two data sets were individually divided into training and test sets at a 4:1 ratio using stratified random sampling. Each spectrum in the data sets spanned 649 discrete frequencies. In machine learning, such individual measurable properties of the observed object are referred to as features. We restricted ourselves to two well-established linear feature extraction methods to reduce the dimensionality of our multivariate data. Principal Component Analysis maximizes the variance of the data by eigendecomposition of the covariance matrix[20]. The resulting orthogonal eigenvectors or principal components are ranked by the respective eigenvalues, which are proportional to the amount of explained variance, such that the first principal component represents the highest variability. The dimensionality of the data can be reduced while maintaining most of the information by retaining only a relative few of the most significant principal components. The PCA algorithm does not include any class membership information and relies solely on hidden patterns in the data. Hence, this method is unsupervised. A supervised counterpart to PCA is Linear Discriminant Analysis, which includes class membership information to calculate the distance between class means and the variance within each class. Here, each material (and/or weight percentage of the active material) can be viewed as a different class. Through e.g. eigendecomposition a lower-dimensional space is constructed such that the inter-class distances are maximized while the intra-class variance is minimized. Contrary to PCA, at most $N-1$ non-zero eigenvalues exist, where N is the total number of classes, meaning that LDA reduces the dimensionalty to at most $N-1$ features[20,21].

For classification, three different algorithms were applied. First, a probabilistic classification model based on Bayes' theorem. The Bayes classifier calculates the posterior probability $p(C_i|x)$ of an observation with value x to belong to the ith class C_i as the product of the prior probability that the observation belongs to the ith class $p(C_i)$ and the likelihood $p(x|C_i)$ of an observation value x given class i normalized by the marginal probability of x. That is[20],

$$p(C_i|x) = \frac{p(x|C_i)p(C_i)}{p(x)}, \qquad p(x) = \sum_i p(x|C_i)p(C_i)$$

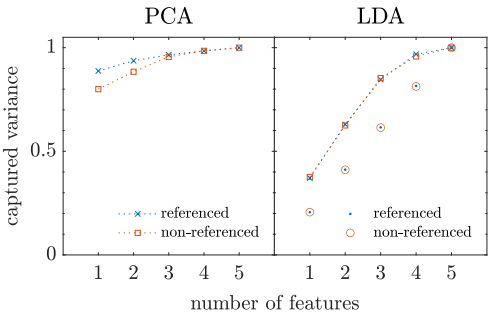

FIG. 3. The cumulative captured variance (cross and square) vs. the number of included features in the reduced feature space computed by PCA (left) and LDA (right). For LDA, the ratio of the cumulative sum over the total sum of eigenvalues (dot and circle) is plotted as well.

Accordingly, the Bayes classifier appoints the observation to the class with the highest posterior probability. Here, we assumed the class likelihood function to follow a multivariate normal distribution. Second, the simple non-parametric k Nearest Neighbors algorithm. This classification algorithm stores all training data, calculates the geometrical distance to a new observation, and subsequently, classifies the new observation identically to the majority of the k nearest neighboring data points. In our study we utilized the Euclidean distance metric and $k = 384$ equal to the total number of observations in each class. Choosing such a large value of k means that the k-NN algorithm will be an indicator of how well PCA and LDA are at intra-class grouping. The final approach was the support vector machine. The algorithm searches for a hyperplane separating observations of two classes with maximal margin, i.e. the maximum geometrical distance to both classes. A new observation is classified according to the half-space it is belonging. Real-world data is often linearly inseparable, wherefore a soft margin is often applied. It allows data points to violate the hyperplane at the cost of a penalty. This results in a wider margin that generalizes better to unseen data. We utilized a linear kernel and a soft margin approach together with a 10-fold cross-validation on the training set. The data processing was performed in MATLAB (MathWorks, R2020b).

III. RESULTS AND DISCUSSION

The referenced and non-referenced data sets consisted of 1920 reflection spectra of samples prepared as pellets of polyethylene with 20%, 50%, and 80% by weight of active materials, respectively, measured under various controlled humidity conditions (10%, 50%, and 90% RH). The dimensionality of each THz spectrum was reduced by either PCA or LDA for comparison. In Fig. 3, we plot the captured variance (cross and square), *i.e.* the cumulative variance along

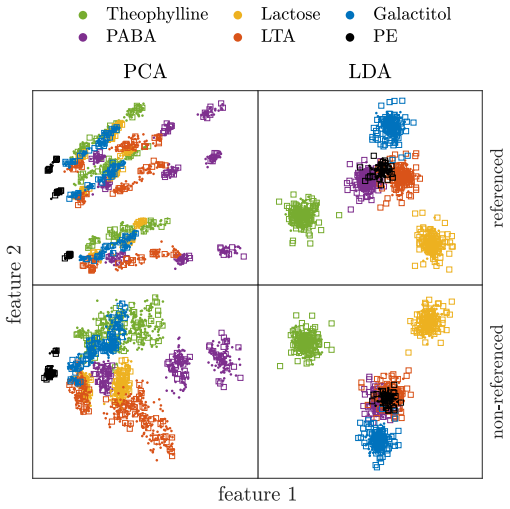

FIG. 4. Projections of the referenced (top) and non-referenced (bottom) spectra to a two-dimensional feature space processed by PCA (left) and LDA(right), respectively.

each new feature normalized to the total variance in the reduced feature space, computed for the principal component and linear discriminant analyses of the train sets. For PCA, the captured variance is equivalent to the proportion of explained variance (the ratio of the cumulative sum and the total sum of eigenvalues) as the eigenvalues are proportional to the total variance[19]. This is not true for LDA, for which the eigenvalues are related to the between-class and within-class variance and, hence, reflect the robustness and the ability to discriminate between different classes[21]. For the sake of comparison, we plot the cumulative eigenvalue ratio (dot and circle) of LDA as well. In terms of captured variance, the LDA algorithm performs almost equally well, whether the input data is referenced or not, while there is a slight difference in performance of the PCA algorithm up to three features. Interestingly, more than 90% of the variance is explained by including just three features of the PCA, whereas three LDA features capture 85% of the variance and achieve 61% robustness. To retain most of the information in the data, the dimensionality of the THz spectra was reduced from 649 frequencies to five features. In Fig. 4 the referenced (top) and non-referenced (bottom) spectra are projected onto a two-dimensional feature space by PCA (left) and LDA(right), respectively. The training and test sets of the data are displayed with dots and open squares, respectively. Overall, the test data fits very well with the train data indicating that both PCA and LDA provide a good generalization to unseen data. As we have previously shown for referenced data using a non-ideal reference[12], PCA clusters the data according to the sample material and further by the material concentration as the algorithm aims to maximize the overall variance. Thus, PCA results in poor intra-class grouping, which is also evident from the poor classification score of k-NN in Table I. LDA, on the other hand, includes the class labels to cluster each type of material regardless of concentration.

		PCA		LDA	
		Train	Test	Train	Test
Bayes	Referenced	0.9844	0.9870	1.0000	0.9974
	Non-referenced	0.9368	0.9245	1.0000	0.9974
384-NN	Referenced	0.7474	0.7448	0.9375	0.9349
	Non-referenced	0.6836	0.6615	0.9375	0.9349
SVM	Referenced	0.9980	1.0000	1.0000	0.9974
	Non-referenced	0.9258	0.9115	1.0000	0.9948

TABLE I. Classification accuracy scores of the PCA- and LDA-processed referenced and non-referenced spectra.

The Bayes, k-NN, and the SVM classification algorithms are applied to quantify the performance of the DR methods on the referenced and non-referenced spectra, respectively. The classification scores is given in Table I. At first glance, we see that the classification scores of the referenced and non-referenced are astonishingly similar for all three classifiers. This clearly indicates that THz reflection spectra can be accurately classified without deconvolution by an precise reference measurement. Furthermore, it is clear from the exceptional agreement of the train and the test scores that our algorithms generalize very well. Among the three classifiers, the performance of the 384-NN classifier is inferior. Particularly, for the PCA-processed data with classification scores around 70%. This is related to our choice of k equal to the total number of observations within each class, that was intended to verify the inter-class grouping. As expected, LDA exhibits superior performance due to the clustering of the data contrary to the splitting in case of PCA evident from Fig. 4. Finally, it is worth noting the identical, almost perfect performance of the Bayes classifier and the SVM. We shall, however, bear in mind that SVM is the most computationally complex classifier of the three and requires fine-tuning of the slack variable through cross-validation. Thus, the performance of the Bayes classifier is remarkable taking its simplicity into account.

IV. CONCLUSION

In conclusion, we demonstrated that terahertz reflection spectra do not need to be deconvoluted with a reference spectrum to achieve highly accurate classification. The performance of the classification algorithms was improved when the data was preprocessed by LDA compared to PCA. Especially, LDA secured almost perfect classification (> 99.7%) of the non-referenced data. This could be of great importance for real-world applications of terahertz spectroscopy based on material identification.

REFERENCES

[1] P. Jepsen, D. Cooke, and M. Koch, "Terahertz spectroscopy and imaging – modern techniques and applications," Laser & Photonics Reviews **5**, 124–166 (2011).

[2] M. Naftaly, N. Vieweg, and A. Deninger, "Industrial applications of terahertz sensing: State of play," Sensors **19** (2019), 10.3390/s19194203.

[3] N. Palka, "THz Reflection Spectroscopy of Explosives Measured by Time Domain Spectroscopy," Acta Physica Polonica A **120**, 713–715 (2011).

[4] C. Cao, Z. Zhang, X. Zhao, and T. Zhang, "Terahertz spectroscopy and machine learning algorithm for non-destructive evaluation of protein conformation," Optical and Quantum Electronics **52**, 225 (2020).

[5] M. R. Nowak, R. Zdunek, E. Pliński, P. Świątek, M. Strzelecka, W. Malinka, and S. Plińska, "Recognition of pharmacological bi-heterocyclic compounds by using terahertz time domain spectroscopy and chemometrics," Sensors **19** (2019), 10.3390/s19153349.

[6] W. Liu, C. Liu, J. Yu, Y. Zhang, J. Li, Y. Chen, and L. Zheng, "Discrimination of geographical origin of extra virgin olive oils using terahertz spectroscopy combined with chemometrics," Food Chemistry **251**, 86–92 (2018).

[7] H. Zhong, A. Redo-Sanchez, and X.-C. Zhang, "Identification and classification of chemicals using terahertz reflective spectroscopic focal-plane imaging system," Opt. Express **14**, 9130–9141 (2006).

[8] J. Zhang, Y. Yang, X. Feng, H. Xu, J. Chen, and Y. He, "Identification of bacterial blight resistant rice seeds using terahertz imaging and hyperspectral imaging combined with convolutional neural network," Frontiers in Plant Science **11** (2020), 10.3389/fpls.2020.00821.

[9] K. Wang, D.-W. Sun, and H. Pu, "Emerging non-destructive terahertz spectroscopic imaging technique: Principle and applications in the agri-food industry," Trends in Food Science & Technology **67**, 93–105 (2017).

[10] W. Liu, C. Liu, F. Chen, J. Yang, and L. Zheng, "Discrimination of transgenic soybean seeds by terahertz spectroscopy," Scientific Reports **6**, 35799 (2016).

[11] A. I. Knyazkova, A. V. Borisov, L. V. Spirina, and Y. V. Kistenev, "Paraffin-embedded prostate cancer tissue grading using terahertz spectroscopy and machine learning," Journal of Infrared, Millimeter, and Terahertz Waves **41**, 1089–1104 (2020).

[12] P. P. Cielecki, M. H. Kristensen, and E. Skovsen, "Analysis and classification of frequency-domain terahertz reflection spectra using supervised and unsupervised dimensionality reduction methods," Journal of Infrared, Millimeter, and Terahertz Waves **42**, 1005 – 1026 (2021).

[13] Y. Hua and H. Zhang, "Qualitative and quantitative detection of pesticides with terahertz time-domain spectroscopy," IEEE Transactions on Microwave Theory and Techniques **58**, 2064–2070 (2010).

[14] P. P. Cielecki, M. H. Kristensen, and E. Skovsen, "Database of Frequency-Domain Terahertz Reflection Spectra for the DETRIS Project," (2021).

[15] D. W. Vogt and R. Leonhardt, "High resolution terahertz spectroscopy of a whispering gallery mode bubble resonator using hilbert analysis," Opt. Express **25**, 16860–16866 (2017).

[16] D. W. Vogt, M. Erkintalo, and R. Leonhardt, "Coherent continuous wave terahertz spectroscopy using hilbert transform," Journal of Infrared, Millimeter, and Terahertz Waves **40**, 524–534 (2019).

[17] D.-Y. Kong, X.-J. Wu, B. Wang, Y. Gao, J. Dai, L. Wang, C.-J. Ruan, and J.-G. Miao, "High resolution continuous wave terahertz spectroscopy on solid-state samples with coherent detection," Optics Express **26**, 17964 (2018).

[18] R. Bro and A. K. Smilde, "Principal component analysis," Anal. Methods **6**, 2812–2831 (2014).

[19] I. T. Jolliffe and J. Cadima, "Principal component analysis: a review and recent developments," Philosophical Transactions of the Royal Society A: Mathematical, Physical and Engineering Sciences **374** (2016).

[20] E. Alpaydin, *Introduction to Machine Learning*, 3rd ed., Adaptive Computation and Machine Learning (MIT Press, 2014).

[21] A. Tharwat, T. Gaber, A. Ibrahim, and A. E. Hassanien, "Linear discriminant analysis: A detailed tutorial," AI Communications **30**, 169 (2017).

Publication C

Database of Frequency-Domain Terahertz Reflection Spectra for the DETRIS Project

List of authors:

Paweł Piotr Cielecki
Mathias Hedegaard Kristensen
Esben Skovsen

The dataset has been published on
Zenodo.org, 2021.

Database of frequency-domain terahertz reflection spectra for the DETRIS project

Paweł Piotr Cielecki, Mathias Hedegaard Kristensen and Esben Skovsen

Department of Materials and Production, Section for Physics and Mechanics, Aalborg University, Skjernvej 4A, DK-9220 Aalborg East, Denmark

Hereby, we present a database of frequency-domain terahertz reflection spectra for the project Detection of explosives using terahertz radiation at improved standoff-distances (DETRIS) conducted at Aalborg University in collaboration with MyDefence and with help from Danish Defence and Danish Ministry of Defence Acquisition and Logistics Organisation, and financial support from The Innovation Fund Denmark.

1.1 Samples

Terahertz (THz) reflection spectra contained in the database were acquired from solid-state samples in form of truncated cylinders with a diameter of 25 mm and weight of 7 g shown in the inset of Fig. 1. The angle of 15° between the back and the front surface of the sample was introduced to prevent interference. We selected six compounds with discernible spectral features within the investigated THz range. This includes:

Compound	***Name in the Database***
4-Aminobenzoic acid	PABA
Galactitol	Galactitol
Hexogen	RDX
L-tartaric acid	LTA
Theophylline	Theophylline
α-Lactose monohydrate	Lactose

We mixed each of the materials with a spectrally inert polyethylene (PE) powder, which functions as a binder, at weight percentages of the active material of 80%, 50% and 20%, respectively. PE was purchased from Micro Powders, LTA from MERCK, and RDX was supplied by the Danish Ministry of Defence Acquisition and Logistics Organisation. The remaining materials were purchased from Sigma Aldrich. The mixtures were compressed into samples under the pressure of approximately 4 tons using a hydraulic press. Galactitol and LTA were ground into a fine powder using mortar and pestle before mixing with PE. Otherwise, the obtained samples were brittle and had a tendency to break during removal from the press due to relatively large crystal size of these compounds. The obtained samples were used as is without any additional surface treatment like, e.g. polishing. In total, we fabricated 38 samples: Two samples for each material composition and two samples made of a pure PE, as summarized in following table:

Material	*Weight percentage of the active material*			
	20%	50%	80%	100%
Galactitol	● ●	● ●	● ●	
Lactose	● ●	● ●	● ●	
L-TA	● ●	● ●	● ●	
PABA	● ●	● ●	● ●	
RDX	● ●	● ●	● ●	
Theophylline	● ●	● ●	● ●	
PE				● ●

1.2 Terahertz setup and measurements

The setup used for THz characterization is based on the commercially available frequency-domain spectrometer TeraScan 1550 (Toptica Photonics) operating in a coherent detection scheme. The setup was arranged using 1" optics in the reflection configuration as shown in Fig. 1. The incidence angle was approx. 11° and the total path length of the THz beam was approximately 1 m. We performed all measurements using the parameters listed below:

- frequency scanning range – 0.09 – 1.19 THz,
- frequency step – 80 MHz,
- integration time – 3ms.

After each measurement, a computer-controlled two-axis translation stage with a fixed step of 0.5 mm moved the sample to a new (random) position within a 7 x 7 mm scanning area allowing measurements of different spots on the sample.

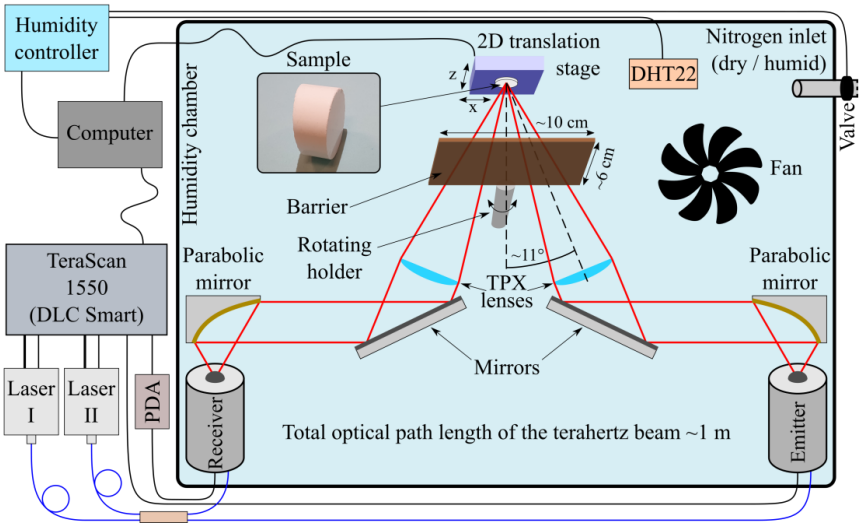

Fig. 1 Schematic drawing of the THz setup.

We conducted THz measurements under various experimental conditions divided into three datasets, as described below:

Datasheet I: Measurements performed under ambient conditions. We measured each sample 80 times in the series of 20 measurement. A single reference was recorded before each series of measurements. For that purpose, we replaced the sample with an aluminum mirror.

Datasheet II: Measurements performed under controlled humidity conditions. To this end, a custom-built humidity chamber that encloses the THz setup was purged with either dry or water vapor saturated nitrogen to lower or increase the humidity, respectively. A custom-built humidity controller opens and closes the nitrogen flow based on the readout from a DHT22 sensor, which allowed maintaining the relative humidity inside the chamber within ±0.3 percent points of the intended level. To ensure a uniform humidity distribution, a fan was installed next to the nitrogen inlet. We measure each sample 20 times at a relative humidity of 90%, 50% and 10%, respectively. Due to a long purging time, we measured the samples in groups of two and, at each relative humidity, we recorded a single reference measurement intended for both samples.

Datasheet III: Measurements performed under ambient conditions through various barrier materials described in the table below. The barrier was placed in a rotating holder with a clearance of ~10 cm by 6 cm located approximately 3.7 cm in front of the sample. In this configuration, the barrier blocks both the incoming and reflected THz beam, as it would be the case in real-world applications. Due to the large number of investigated barriers, these measurements were performed only on samples with the highest concentration of active material (80%) and PE samples. For each barrier material, we measured each of the considered samples 20 times. Each such measurement series was preceded by a reference measurement. The barrier was kept parallel to the sample surface for the first six measurements in the series. For the remaining measurements, a stepper motor coupled to the barrier holder rotated the barrier (around z-axis) by a fixed step in the range of approx. −32° to 32°.

Name of the barrier	***Description***
BubbleFoil	Two layers of packaging 'bubble foil'
Cotton	Plain 100% cotton fabric obtained from a T-shirt
Duct	Plastic shopping bag (the same as in *PlasticBag*) with a single layer of a 0.23 mm thick duct tape (3M, Duct Tape 3939)
LDPE	Low-density polyethylene packaging foam with a thickness of approx. 5.3 mm
Paper	A sheet of office paper
PaperBag	Shopping bag made of recycled paper
PET	Polyethylene terephthalate (PET) obtained from a plastic bottle
PlasticBag	Plastic shopping bag made of low-density polyethylene
Polyamide	A plain fabric made of 96% polyamide and 4% elastane obtained from a T-shirt
Polystyrene	polystyrene sheets with thickness of approx. 4.5 mm and approx. 6.5 mm were used interchangeably

1.3 Database structure and file details

The database consists of raw .txt files obtained from a frequency-domain THz spectrometer. The files contain three tab-delimitated columns. The first column represents a set frequency expressed in GHz. The second column contains the values of the measured photocurrent in nA. The third column contains the actual frequency given in GHz. The set frequency represents an expected frequency value and may differ from the actual frequency. Therefore, it is recommended to use the actual frequency (v) listed in the third column. For more information, we refer to Toptica's manual for TeraScan 1550 system.

The database contains 8467 files (8118 measurements and 349 references) arranged into three datasets described earlier. **Dataset I** contains 3190 files (3038 measurements and 152 references) categorized by the active material and in the next directory level by material concentration. As with all the datasets, the reference files are always in the same folder as the corresponding measurement files. Noteworthy, there are 160 measurements for each material composition except of Lactose80 and PABA80. For these material compositions, only 159 have been performed due to a processing error. **Dataset II** consists of 2337 files (2280 measurements and 57 references). As with **Dataset I**, the files are arranged by the active material in the first directory level and by material concentration in the second. Finally, **Dataset III** contains 2.940 files (2800 measurements and 140 references) arranged by the barrier material.

The measurement files in the database are named according to the following scheme:

$$\overbrace{2020\_07\_17}^{date}\_\underbrace{Theophylline80}_{sample\ details}\_\overbrace{BubbleFoil}^{conditions}\_\underbrace{0023}_{number}.txt \quad (1)$$

The filename starts with the *date* of the measurement followed by *sample details*, experimental *conditions*, and ends with the measurement's *number*. The *date* is in the format of YYYY_MM_DD. *Sample details* consist of two parts: The name of the active material and a numeric value corresponding to its weight percentage in the sample. For samples made of pure PE, which do not contain any active material, the second part of *sample details* is omitted. In this case, *sample details* are only 'PE'. Experimental *conditions* describe either relative humidity given in form of 'RHxx', where xx is the percentage value of the relative humidity (this applies to **Dataset II**) or a name of the barrier material used in the measurement (this applies to **Dataset III**). For **Dataset I**, which contains measurements under ambient conditions and without any barrier materials, the experimental *conditions* field is not used. Since we performed multiple measurements of each sample at a given set of experimental conditions, similar measurements were given consecutive *number*s. The *number* has form of four digits padded with zeros before the value. Hence, the sample measurement filename from (1) corresponds to the 23rd measurement recorded on the sample with 80% weight percentage of Theophylline through BubbleFoil.

The reference files are named in a similar fashion:

$$\overbrace{2020\_07\_17}^{date}\_reference\_for\_\underbrace{Theophylline80}_{sample\ details}\_\overbrace{BubbleFoil}^{conditions}\_\underbrace{0021-0040}_{range}.txt \quad (2)$$

At the beginning of the filename, the *date* when the reference was recorded is given followed by '*reference_for*'. Subsequently, there is information about the measurement files, which the reference is intended for. This includes *sample details*, experimental *conditions*, and the *range* of measurements' numbers, which are analogous to the parts of measurement filenames. *Sample details* is the name of the active material and its weight percentage in the sample. For the measurements from **Dataset III,** experimental *conditions* correspond to the applied barrier material used, while for measurements from the **Dataset I**, this field is unused. Because we intended to use references and measurements recorded at different humidity levels with each other, reference files in **Dataset II** are named differently. We did not state the relative humidity during sample measurements in the experimental *conditions* field as the reference is not limited for use with measurements performed at a single relative humidity. Instead, we specified the relative humidity level during recording the reference. To this end, we replaced '*reference_for*' with '*reference_RHxx_for*', where xx is the percentage value of the relative humidity. Based on the above description, the sample reference filename from (2) is intended for measurements 21 to 40 performed on the sample containing 80% weight percentage of Theophylline with a BubbleFoil used as a barrier material. This includes the measurement with name (1).

1.4 Data processing and MATLAB repository

Due to characteristics of the coherent detection scheme, the measured photocurrent depends both on the amplitude of the THz electric field (E_{THz}) and the phase shift ($\Delta\varphi$) between the THz wave and the laser beat signal via $I_{ph} \propto E_{THz}\cos(\Delta\varphi = 2\pi\Delta L\nu/c)$. The phase difference depends on the THz frequency (ν) and the optical path difference $\Delta L = L_{THz} + L_E - L_R$, where L_{THz} is THz beam path, and L_E and L_R are optical beat paths to emitter and receiver, respectively. To obtain the THz spectrum, $E_{THz}(\nu)$, it is necessary to extract the amplitude of the detected THz signal from the interference pattern (also known as fringes) in the frequency scan [1–3]. A common approach is to find the fringe extrema, where the THz amplitude is directly proportional to the absolute value of the photocurrent ($\Delta\varphi$ is a multiple of π), and neglect the remaining data points. Consequently, the effective spectral resolution of the measurement is determined by the spacing between adjacent extrema, which in our case was around 0.9 GHz. Instead of analyzing the extrema separately, we calculated the THz amplitude and corresponding THz frequency based on the information contained in two adjacent extrema (maximum and minimum). This approach should compensate for a possible offset in the photocurrent. The obtained data points were then interpolated onto integer GHz frequencies to compensate for spectral shifts of the fringes. As the low frequency regime exhibited no material-related spectral features and was dominated by standing wave patterns, we cropped the spectra to range from 0.3 to 1.17 THz. All data processing was performed in MATLAB (version 2020b).

We saved the processed data together with the raw data in the .mat file named **Main**. There are two variables in the **Main** file: The structure array named **Database** and a vector named **Frequency**. The **Database** contains both raw and processed data from the THz measurements. Each row of the array corresponds to a single .txt file (either measurement or reference). The **Database** structure have the following fields:

Name of the field	*Description*
'FileName'	The name of the corresponding .txt file
'Folder'	Path to the folder containing the .txt file
'Frequency_raw'	Actual frequency, which corresponds to the third column in the .txt file (*raw data*)
'Photocurrent'	Measured photocurrent, which corresponds to the second column in the .txt file (*raw data*)
'E_THz'	Amplitude of the THz electric field extracted from the measured photocurrent (*processed data*)
'Reference'	The field indicates whether the file is a reference or the measurement. For reference this field is 'true'
'Dataset'	Indicates the dataset to which the file belongs, $\in\{1, 2, 3\}$

The **Frequency** vector contains discrete frequencies (GHz) onto which the electric field amplitude THz has been interpolated. This vector is common for all the data. In order to obtain THz spectra one should plot E_THz of the considered measurement or reference versus the **Frequency** vector.

1.5 Contact information

In case of any questions related to the database, please contact us:

Paweł Piotr Cielecki pawel.cielecki@yahoo.com

Esben Skovsen es@mp.aau.dk

1.6 Acknowledgements

This work was financed by the Innovation Fund Denmark Grand Solutions program with grant no. IFD-7076-00017B. The project was performed in collaboration with MyDefence. The authors wish to express their gratitude to the Danish Defence, and Danish Ministry of Defence Acquisition and Logistics Organisation for knowledge and assistance in measurements of explosives.

1.7 References

[1] A. Roggenbuck, H. Schmitz, A. Deninger, I.C. Mayorga, J. Hemberger, R. Güsten, M. Grüninger, Coherent broadband continuous-wave terahertz spectroscopy on solid-state samples, New J. Phys. 12 (2010) 043017. doi:10.1088/1367-2630/12/4/043017.

[2] D.W. Vogt, R. Leonhardt, High resolution terahertz spectroscopy of a whispering gallery mode bubble resonator using Hilbert analysis, Opt. Express. 25 (2017) 16860. doi:10.1364/OE.25.016860.

[3] A. Roggenbuck, K. Thirunavukkuarasu, H. Schmitz, J. Marx, A. Deninger, I.C. Mayorga, R. Güsten, J. Hemberger, M. Grüninger, Using a fiber stretcher as a fast phase modulator in a continuous wave terahertz spectrometer, J. Opt. Soc. Am. B. 29 (2012) 614. doi:10.1364/JOSAB.29.000614.

Known issues:

- PABA20 measurements 101-160 in the Dataset I, the date in the filename is 2019_08_21 while it should be 2019_08_22

Publication D

Terahertz Generation through Optical Rectification in Reflection

List of authors:

Mathias Hedegaard Kristensen
Emilie Herault
Dongwei Zhai
Esben Skovsen
Jean-Louis Coutaz

The paper has been published in
Journal of Applied Physics Vol. 133, pp. 173103, 2023.

Journal of Applied Physics

RESEARCH ARTICLE | MAY 01 2023

Terahertz generation through optical rectification in reflection

Mathias Hedegaard Kristensen ✉; Emilie Herault; Dongwei Zhai; ... et. al

Journal of Applied Physics 133, 173103 (2023)
https://doi.org/10.1063/5.0144433

AIP Publishing

Journal of Applied Physics ARTICLE scitation.org/journal/jap

Terahertz generation through optical rectification in reflection

Cite as: J. Appl. Phys. **133**, 173103 (2023); doi: 10.1063/5.0144433
Submitted: 30 January 2023 · Accepted: 17 April 2023 ·
Published Online: 1 May 2023

Mathias Hedegaard Kristensen,[1,a)] Emilie Herault,[2] Dongwei Zhai,[2,3] Esben Skovsen,[1] and Jean-Louis Coutaz[2]

AFFILIATIONS

[1]Department of Materials and Production, Section for Physics and Mechanics, Aalborg University, Skjernvej 4A, DK-9220 Aalborg East, Denmark
[2]IMEP-LAHC, UMR CNRS 5130, Université Savoie Mont Blanc, 73 376 Le Bourget du Lac Cedex, France
[3]College of Physics, Qingdao University, Qingdao 266071, China

[a)]**Author to whom correspondence should be addressed:** mhkr@icloud.com

ABSTRACT

In this paper, we study terahertz generation through optical rectification in reflection at normal incidence in a dielectric nonlinear crystal. We first analyze, with a nonlinear optical model, the sample parameters (thickness, absorption at both laser and terahertz wavelengths, etc.) for which a terahertz optical rectification reflection scheme is preferable to the common transmission scheme. Then, we report our experimental observations of a reflected terahertz signal generated at the surface of a ZnTe crystal. The reflected terahertz signal shares all the characteristics of a signal generated in transmission but is not limited by absorption losses in the crystal, thereby providing a broader bandwidth. At high pump laser power, the signal exhibits saturation, which is caused by the decrease of the nonlinear susceptibility due to photocarriers generated by two-photon absorption. This reflection scheme could be of great importance for terahertz microscopy of opaque materials like, e.g., humid samples or samples exhibiting strong absorption bands or to study samples for which the transmitted signal cannot be recorded.

I. INTRODUCTION

Optical rectification (OR) is an elegant way to produce terahertz (THz) pulses by irradiating a dielectric nonlinear crystal with femtosecond laser pulses. Because of the almost instantaneous polarization of the crystal atoms or molecules, broadband THz pulses may be generated.[1] Moreover, very intense THz peak power can be delivered.[2] Actually, OR corresponds to the difference of frequencies between all the spectral components of the ultra-short laser pulse. In fact, difference-frequency generation was the first opto-electronic technique used to generate far-infrared beams.[3–5] Here, difference-frequency generation is named OR because the generated THz frequencies are much smaller than the exciting laser frequency. Usually, generation of THz waves through OR in a crystal is performed in transmission, because the generated THz field magnitude increases linearly with the crystal thickness if phase-matching between the incident laser beam and the generated THz beam is realized. Recently, Sotome *et al.*[6] employed OR in transmission to obtain THz images of ferroelectric samples, where the laser beam was scanned over the sample, and each irradiated point of the sample generated a THz signal whose magnitude was related to both the crystallinity and nonlinearity of the sample. More recently, some of us used the same technique to get THz images of a caster sugar grain with a sub-wavelength resolution.[7] We named this technique Optical Rectification Terahertz Imaging (ORTI). Then, by improving our setup, we published an ORTI image of the domains of a periodically poled KTP crystal with a lateral resolution of $\lambda/200$.[8] A next progress toward ORTI of actual samples will be to record images in reflection. It will allow one to characterize opaque or bulky samples or samples whose rear face is rough.

Generation of THz pulses through OR in reflection has only been studied to a lesser extent. In 2005, Reid *et al.*[9] have reported OR THz generation from a semi-conductor recorded in reflection at 45° incidence. They pumped an InAs sample below its bandgap at 800 nm and by a proper polarimetric study of both THz

generation and second-harmonic generation (SHG), they were able to discriminate the respective contributions of the bound and free photo-excited electrons. Moreover, they demonstrated the different contributions of both bulk and surface regions of the sample, this difference arising thanks to the surface electric-field. The effect is strong in narrow bandgap semiconductors like InAs, but insignificant in larger bandgap materials, like GaAs. Later in 2007, Zinov'ev *et al.*[10,11] and Bakunov *et al.*[12,13] developed theoretical models of THz generation through OR including a field generated in the backward direction (reflection). Zinov'ev *et al.* presented a thorough description of all the THz pulses generated when an optical pulse propagates through a slab of nonlinear material. Their theoretical calculations clarify that the THz radiation is generated at the surfaces due to the instantaneous creation and acceleration of polarization charge at the front surface and subsequent deceleration and extinction at the back surface. They supported their theory by experiments measured in transmission. Bakunov *et al.* extended the usual Fresnel formulas for transmission and reflection of free-propagating electromagnetic pulses to forced pulses generated in a nonlinear crystal and showed that the free and forced waves obey different boundary conditions at the crystal surfaces.[12] In the second paper,[13] they expanded their model to include the focusing of the pump beam and calculate the Cherenkov angular spreading of the generated THz waves. Later on, Hargreaves *et al.*[14] published a detailed modeling on THz OR generation vs the crystal orientation in view of clearly discriminating OR and photo-induced current transient contributions. Finally, Schneider[15] performed a complete analysis of the THz pulses generated in a nonlinear slab considering dispersion, absorption of both optical and terahertz waves, and multiple reflections. Furthermore, OR THz generation in reflection has been performed when dealing with opaque materials like metals.[16]

In most of these publications, the research was focused on the theoretical description of the OR THz generation. When experimental results were reported, they were performed either in transmission[11,17] or under oblique incidence.[9,16] From a practical point of view when dealing with applications like ORTI, THz OR generation in reflection under normal incidence is preferable. The goal of this paper is not to propose a highly efficient scheme for high power THz generation but to show that OR in reflection can be used to study the THz response of samples. Moreover, generation in reflection is the only available OR technique when samples are absorbing and too thick, or if their rear face does not allow a good transmission of the THz beam (rough surface, surface covered with opaque films like metallic ones, etc.). In particular, we will (1) evaluate for which samples OR in reflection supplies stronger signals than OR in transmission and, thus, should be preferred and (2) experimentally demonstrate THz OR generation in reflection under normal incidence. This study is performed with ZnTe as a dielectric nonlinear crystal.

II. MODELING

Let us recall some basic expressions of OR generated THz fields. We will deal only with the case of normal incidence. The laboratory reference frame is (xyz) and the laser beam propagates normally to the crystal surface along the z-direction. We suppose that the irradiating laser beam is a plane wave with two spectral components at ω and $\omega+\Omega$ (ω and Ω are, respectively, the optical and THz angular frequencies). The plane wave is a good approximation when the laser beam is not strongly focused onto the sample, i.e., the laser Rayleigh length is larger than the crystal thickness d. We choose the following notation for the electrical field of this plane wave in air:

$$\vec{E}_{o,\omega}(z,t)=\vec{E}_{o,\omega}(z)e^{-j\omega t}=\vec{E}_{o,\omega}\,e^{jk_{o,\omega}z}e^{-j\omega t}. \tag{1}$$

Here, $\vec{k}_{o,\omega}=\frac{\omega}{c}\vec{u}_z$ is the incident wave vector (c is the velocity of light in vacuum and $\vec{u}_z$ is the unit vector along direction z). We neglect the anisotropy of the crystal. Inside the crystal, the laser field is

$$\vec{E}_{\omega}(z)=\vec{E}_{\omega}\,e^{j\tilde{k}_{\omega}z}=\tilde{t}_{\omega}\vec{E}_{o,\omega}\,e^{j\tilde{k}_{\omega}z}, \tag{2}$$

with wavevector $\vec{\tilde{k}}_{\omega}=\frac{\omega}{c}\tilde{n}_{\omega}\vec{u}_z$ and transmission coefficient $\tilde{t}_{\omega}$ at the crystal surface (we employ a tilde to indicate complex values except for complex fields). Here, $\tilde{n}_{\omega}=n_{\omega}+j\kappa_{\omega}$ is the complex refractive index of the crystal at the laser frequency. The THz wave at frequency Ω is generated through OR, i.e., a second order nonlinear effect. The related nonlinear polarization is

$$\vec{P}_{\Omega}^{\mathrm{NL}}(z)=\varepsilon_o\overleftrightarrow{\chi}^{(2)}:\vec{E}_{\omega+\Omega}(z)\cdot\vec{E}_{\omega}^{*}(z), \tag{3}$$

where ε_o is the permittivity of vacuum, $\overleftrightarrow{\chi}^{(2)}$ is the nonlinear OR tensor, and the asterisk denotes the complex conjugate. The nonlinear Helmholtz propagation equation for the THz field $\vec{E}_{\Omega}$ is

$$\nabla^2\vec{E}_{\Omega}(z)+\frac{\Omega^2}{c^2}\tilde{\varepsilon}_{\Omega}\vec{E}_{\Omega}(z)=-\frac{\Omega^2}{c^2}\overleftrightarrow{\chi}^{(2)}:\vec{E}_{\omega+\Omega}(z)\cdot\vec{E}_{\omega}^{*}(z). \tag{4}$$

In order to derive the THz fields reflected and transmitted outside the crystal, we neglect the rebounds of the laser and THz pulses inside the crystal. We then substitute the laser field in Eq. (4) with the expression from Eq. (2), and thus, the nonlinear term is written as follows:

$$\overleftrightarrow{\chi}^{(2)}:\vec{E}_{\omega+\Omega}(z)\cdot\vec{E}_{\omega}^{*}(z)=\overleftrightarrow{\chi}^{(2)}:\vec{E}_{\omega+\Omega}\cdot\vec{E}_{\omega}e^{j\left(\tilde{k}_{\omega+\Omega}-\tilde{k}_{\omega}^{*}\right)z}. \tag{5}$$

The wave vector difference

$$\tilde{k}_{\omega+\Omega}-\tilde{k}_{\omega}^{*}=\frac{\omega+\Omega}{c}n_{\omega+\Omega}-\frac{\omega}{c}n_{\omega}+j\frac{\omega}{c}\left(\left(1+\frac{\Omega}{\omega}\right)\kappa_{\omega+\Omega}+\kappa_{\omega}\right), \tag{6}$$

simplifies as

$$\Delta\tilde{k}=\tilde{k}_{\omega+\Omega}-\tilde{k}_{\omega}^{*}\approx\frac{\Omega}{c}n_{\mathrm{G},\omega}+j\alpha_{\omega}\equiv\frac{\Omega}{c}\tilde{n}_{\mathrm{G},\omega}, \tag{7}$$

assuming $\Omega\ll\omega$ and using the group index $n_{\mathrm{G},\omega}=n_{\omega}+\omega\frac{\partial n_{\omega}}{\partial\omega}$. In Eq. (7), $\alpha_{\omega}=\frac{2\omega}{c}\kappa_{\omega}$ is the coefficient of absorption at the laser

wavelength. It follows that

$$\tilde{n}_{G,\omega} \equiv n_{G,\omega} + j\frac{c}{2\omega}\alpha_{G,\omega} \Rightarrow \alpha_{G,\omega} = \frac{2\omega}{\Omega}\alpha_{\omega}. \quad (8)$$

Solving the boundary equations at the surface ($z = 0$) within this hypothesis, the reflected THz field is given by

$$\vec{E}_{R,\Omega}(z) = -\frac{\overleftrightarrow{\tilde{\chi}}^{(2)} : \vec{E}_{\omega+\Omega} \cdot \vec{E}^{*}_{\omega}}{(\tilde{n}_{\Omega}+1)(\tilde{n}_{G,\omega}+\tilde{n}_{\Omega})} e^{-jk_{R,\Omega}z}. \quad (9)$$

Here, $\tilde{n}_{\Omega}$ is the refractive index at the THz frequency and $k_{R,\Omega} = \Omega/c$. When dealing with ultrashort laser pulses, expression (9) must be integrated over the whole laser pulse spectrum [see, for example, Eqs. (7) and (20) in the paper by Schneider *et al.*[17]]. This is compulsory when one desires to determine the upper spectral limit of the generated THz signal or to fit the experimental spectra. Let us notice that in Eq. (9),

$$\tilde{n}_{G,\omega} + \tilde{n}_{\Omega} = n_{G,\omega} + n_{\Omega} + j\frac{c}{2\Omega}(2\alpha_{\omega} + \alpha_{\Omega}), \quad (10)$$

which is deduced from Eq. (7). As expected, the reflected field does not depend on the crystal thickness and exists even if the crystal thickness tends toward zero: The generation in reflection is a pure surface effect. The reflected field magnitude depends on the crystal nonlinearity and only slowly on the crystal refractive index. Therefore, the reflected THz signal exhibits all the spectral features related to the linear and nonlinear properties of the crystal at both laser and THz frequencies. In particular, phonon resonances at THz frequencies should be clearly observed in the reflected THz spectrum. Figure 1(a) shows the magnitude normalized to the nonlinear source, i.e.,

$$\left|\vec{E}_{R,\Omega}/\overleftrightarrow{\tilde{\chi}}^{(2)} : \vec{E}_{\omega+\Omega} \cdot \vec{E}^{*}_{\omega}\right| = \left|(\tilde{n}_{\Omega}+1)(\tilde{n}_{G,\omega}+\tilde{n}_{\Omega})\right|^{-1},$$

for $\lambda = 2\pi c/\omega = 800$ nm, $f = 1$ THz, $n_{G,\omega} = 2.5$, and $n_{\Omega} = 3$ vs the absorption coefficients $\alpha_{G,\omega}$ and α_{Ω}. We see that the reflected field magnitude is almost constant up to $\alpha_{\omega} \approx 10^6$ cm^{-1} and $\alpha_{\Omega} \approx 10^3$ cm^{-1} (the yellow plateau), whereupon it decreases strongly and becomes zero. We can conclude that for most of materials, even if they exhibit a rather large absorption at both laser and THz wavelengths, the reflected THz field does not depend so much on the loss. It vanishes only for materials that are practically opaque.

Let us now treat the transmitted THz field. At a distance z inside the crystal, the field is the sum of the propagating free and forced waves,

$$\vec{E}_{\Omega}(z) = \frac{\overleftrightarrow{\tilde{\chi}}^{(2)} : \vec{E}_{\omega+\Omega} \cdot \vec{E}^{*}_{\omega}}{\tilde{n}^2_{G,\omega} - \tilde{n}^2_{\Omega}}\left(e^{j\Delta\tilde{k}z} - \frac{\tilde{n}_{G,\omega}+1}{\tilde{n}_{\Omega}+1}e^{j\tilde{k}_{\Omega}z}\right), \quad (11)$$

with $\tilde{k}_{\Omega} = \frac{\Omega}{c}\tilde{n}_{\Omega}$. The field transmitted at the exit face of the crystal ($z > d$) must be multiplied by the THz transmission coefficient $\tilde{t}_{\Omega}$,

$$\vec{E}_{T,\Omega}(z) = \vec{E}_{\Omega}(d)\tilde{t}_{\Omega}e^{j\tilde{k}_{R,\Omega}(z-d)}. \quad (12)$$

The magnitude of the transmitted field normalized to the nonlinear source,

$$\left|\vec{E}_{T,\Omega}/\overleftrightarrow{\tilde{\chi}}^{(2)} : \vec{E}_{\omega+\Omega} \cdot \vec{E}^{*}_{\omega}\right| = \left|\frac{2\tilde{n}_{\Omega}}{1+\tilde{n}_{\Omega}}\frac{2\left(e^{j\Delta\tilde{k}d} - \frac{\tilde{n}_{G,\omega}+1}{\tilde{n}_{\Omega}+1}e^{j\tilde{k}_{\Omega}d}\right)}{(\tilde{n}_{\Omega}+1)(\tilde{n}^2_{G,\omega} - \tilde{n}^2_{\Omega})}\right|,$$

is plotted in Fig. 1(b) using similar parameter values as for the reflected field and crystal thickness $d = 1.52$ mm (this is the thickness of the sample studied in the experimental part. It corresponds to a typical value for a rather efficient and broadband THz OR generation in transmission). The transmitted THz signal decreases strongly when the visible and/or THz absorption increase. Typically, it is almost null when $\alpha_{\Omega} > 10^3$ cm^{-1} or $\alpha_{\omega} > 10^7$ cm^{-1}. Finally, let us compare the magnitudes of the reflected and transmitted THz fields,

$$\left|\frac{\vec{E}_{R,\Omega}}{\vec{E}_{T,\Omega}}\right| = \left|\frac{(\tilde{n}_{\Omega}+1)(\tilde{n}_{G,\omega} - \tilde{n}_{\Omega})}{4\tilde{n}_{\Omega}\left(e^{j\Delta\tilde{k}d} - \frac{\tilde{n}_{G,\omega}+1}{\tilde{n}_{\Omega}+1}e^{j\tilde{k}_{\Omega}d}\right)}\right|. \quad (13)$$

The ratio is independent on the crystal nonlinearity and, thus, on the polarization of the laser and THz beams. For weak visible and THz absorption, the transmitted THz signal is much stronger than the reflected signal due to cumulative generation throughout the crystal. At higher absorption, laser and/or THz beams no longer propagate inside the crystal. This appears clearly on the contour maps plotted in Fig. 1(c) for $d = 0.1$ mm, Fig. 1(d) for $d = 1.52$ mm, and Fig. 1(e) for $d = 1$ cm. The red line represents the unity ratio. For the $d = 1.52$ mm sample, the red line limit occurs at $\alpha_{\Omega} \approx 10^3$ cm^{-1} for crystals with an absorption α_{ω} at the laser frequency less than $\sim 10^3$ cm^{-1}. For large absorption values at the laser frequency, the reflected signal is of course stronger than the transmitted one at an absorption weaker than for thinner samples. In conclusion, for most of the common materials with standard thicknesses, THz generation by OR in transmission is more efficient than in reflection, and hence, the reflection technique is practically useful only if the sample or the experimental geometry does not allow to measure the transmitted signal. This is the case for samples whose exit face is rough or covered by a metallic film. For absorption values beyond this red contour, i.e., for materials like water[18] or carbon-fiber composites[19] ($\alpha_{\Omega} \sim 1000$ cm^{-1}), the reflected signal is stronger than the transmitted signal. However, we must keep in mind that its magnitude is very weak, even if stronger than the transmitted one. The difference between the reflected and transmitted signals is emphasized when plotting the field magnitudes vs the difference $n_{G,\omega} - n_{\Omega}$. Figure 2(a) shows the transmitted and reflected THz fields vs $n_{G,\omega} - n_{\Omega}$ for $n_{G,\omega} = 3$ and $f = 1$ THz. We assume that the crystal is $d = 1.52$ mm thick and transparent at the laser wavelength ($\lambda = 800$ nm). The transmitted field is plotted for different values of the THz absorption. Because the reflected field depends weakly

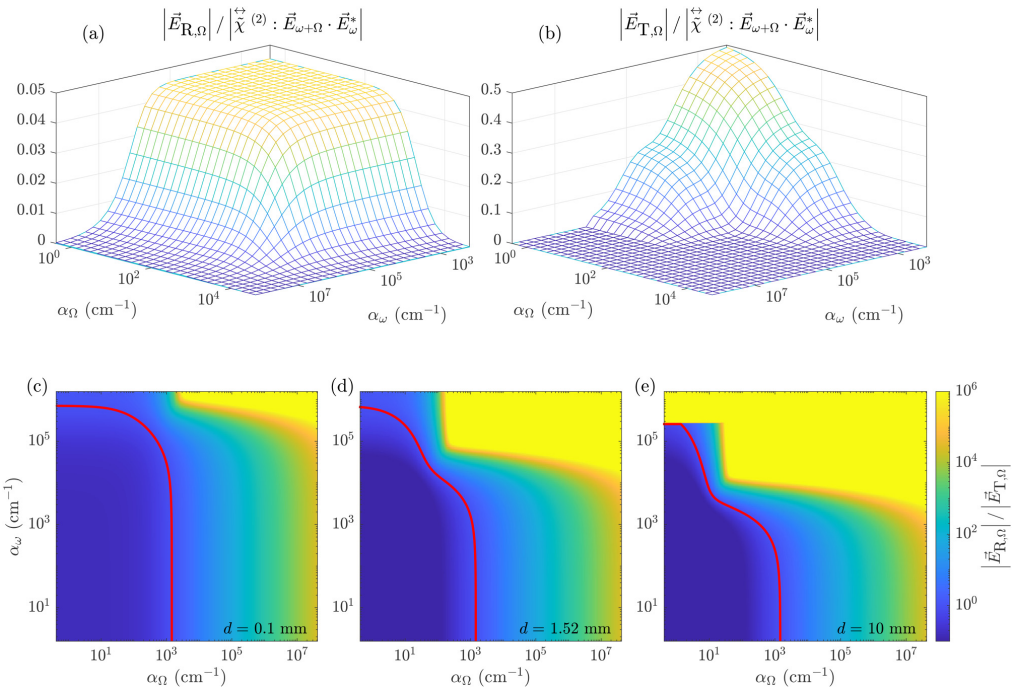

FIG. 1. Maps of the THz field magnitudes generated in reflection (a) and transmission (b) normalized to the nonlinear source using $\lambda = 2\pi c/\omega = 800$ nm, $f = 1$ THz, $n_{\mathrm{G},\omega} = 2.5$, $n_\Omega = 3$, and $d = 1.52$ mm, vs the optical and THz absorption coefficients. The contour map of the ratio [Eq. (13)] is plotted in the case of phase-matching ($n_{\mathrm{G},\omega} = n_\Omega = 3$) for $d = 0.1$ mm (c), $d = 1.52$ mm (d), and $d = 10$ mm (e). The red lines indicate the unity ratio.

on the THz absorption, we plot it only for $\alpha_\Omega = 0\,\mathrm{cm}^{-1}$. The phase-matching oscillations in transmission are clearly seen when the THz absorption is null, while the much weaker reflection curve does not show any phase-matching feature. Typically, at 1 THz with $n_\Omega = 3.2$, $n_{\mathrm{G},\omega} = 3.16$, and $d = 1.52$ mm, one obtains $E_R/E_T = 1/90$. With increasing THz absorption, the transmitted THz signal decreases and its oscillations are attenuated. However, when the sample is almost opaque to THz waves ($\alpha_\Omega = 1000\,\mathrm{cm}^{-1}$, like water[18] or carbon-fiber composites[19]), the phase-matching maximum is erased and the transmitted field is comparable to the reflected field. Figure 2(b) presents similar curves but calculated for a given THz absorption ($\alpha_\Omega = 20\,\mathrm{cm}^{-1}$) and different crystal thicknesses. Because of the phase-matching phenomenon, the transmitted curves show oscillations whose pseudo-periodicity is shorter with thinner crystals. Here, the effect of THz absorption is compensated by increasing the crystal thickness when phase-matching is realized. Thus, as before [Fig. 2(a)], the transmitted field is stronger than the reflected one by 1–2 orders of magnitude when phase-matching is realized.

Hence, it appears that, even for transparent crystals and without achieving phase-matching, the signal generated in reflection is much smaller than the one in transmission. Therefore, OR performed in reflection is not a technique that produces high power THz pulses. It should be used when studying materials that are opaque or scatter in the THz range, or whose rear face is rough, or covered by nontransparent or diffracting layers. Also, it could be of interest when a reflection scheme is easier to implement than a transmission one, for example, in microscopy. In all other cases, a transmission arrangement is more efficient.

Let us now address the error on the transmitted THz field made when the reflected THz is omitted. Instead of expression (11), one gets

$$\vec{E}_\Omega^{\,\mathrm{approx}}(d) = \frac{\overleftrightarrow{\chi}^{(2)} : \vec{E}_{\omega+\Omega} \cdot \vec{E}_{\omega}^{*}}{\tilde{n}_{\mathrm{G},\omega}^{2} - \tilde{n}_{\Omega}^{2}} \left(e^{j\tilde{\mathrm{A}}\tilde{k}d} - e^{j\tilde{k}_\Omega d}\right). \tag{14}$$

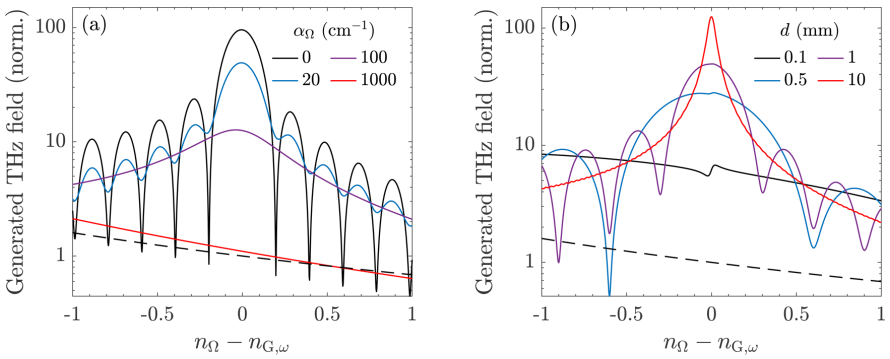

FIG. 2. Calculated transmitted (continuous lines) and reflected (dashed line) THz field magnitudes vs $n_{G,\omega} - n_\Omega$. All the curves are normalized to the reflected signal at $n_{G,\omega} - n_\Omega = 0$. (a) The sample ($d = 1.52$ mm) is assumed to be transparent at the laser wavelength and $n_{G,\omega} = 3$. (b) The THz absorption is assumed to be $\alpha_\Omega = 20$ cm^{-1}, and the curves are calculated for different crystal thicknesses, namely, $d = 0.1$, 0.5, 1, and 10 mm.

The relative error writes

$$\frac{\vec{E}_\Omega^{\text{approx}}(d) - \vec{E}_\Omega(d)}{\vec{E}_\Omega(d)} = \frac{\tilde{n}_{G,\omega} - \tilde{n}_\Omega}{(1+\tilde{n}_\Omega)e^{j(\Delta\tilde{k}-\tilde{k}_\Omega)d} - 1 - \tilde{n}_{G,\omega}}. \quad (15)$$

Typically, this error is almost constant with $\tilde{n}_\Omega - \tilde{n}_{G,\omega}$, but it depends strongly on the crystal thickness d. For a transparent crystal, and at 1 THz, the error is much less than 1% for d larger than 1 mm, and thus, it could be neglected. But, it increases to ~7% for $d = 100\,\mu$m and up to ~30% for $d = 10\,\mu$m. In such very thin crystals, used to generate very broadband THz signals,[20] generation in transmission is weak because the crystal thickness is small. Thus, the amplitudes of the reflected and transmitted THz signals become of the same order of magnitude. Therefore, the reflected field can no longer be omitted.

The generated THz fields depend on the nonlinear source term $\vec{\tilde{\chi}}^{(2)} : \vec{E}_{\omega+\Omega} \cdot \vec{E}_\omega^*$. This nonlinear term has to be calculated in the crystal frame (XYZ), in which the nonlinear tensor $\vec{\tilde{\chi}}^{(2)}$ is known. To switch from the laboratory to the crystal frame, a first rotation by θ around y is performed followed by a second rotation by ϕ around z.[21] The whole rotation matrix R is

$$R(\phi,\theta) = \begin{pmatrix} \cos\phi\cos\theta & -\sin\theta & \cos\phi\sin\theta \\ \sin\phi\cos\theta & \cos\theta & \sin\phi\sin\theta \\ -\sin\theta & 0 & \cos\theta \end{pmatrix}. \quad (16)$$

The nonlinear polarization $\vec{P}^{\text{NL}}_{\Omega,XYZ}$ in Eq. (4) is calculated in the crystal frame using

$$\vec{E}_{\omega,XYZ} = R(\phi,\theta)\vec{E}_{\omega,xyz}$$

and then multiplied by the inverse rotation matrix $R^{-1}(\phi,\theta)$ to obtain the expression in the laboratory frame

$$\vec{P}^{\text{NL}}_{\Omega,xyz} = R^{-1}(\phi,\theta)\varepsilon_o \vec{\tilde{\chi}}^{(2)} : \left(R(\phi,\theta)\vec{E}_{\omega+\Omega,xyz}\right) \cdot \left(R(\phi,\theta)\vec{E}^*_{\omega,xyz}\right). \quad (17)$$

Expression (17) must be calculated for each crystallographic class and each orientation of the crystal. In the case of cubic crystals (432, $\bar{4}3m$, 23) addressed here, the nonlinear susceptibility tensor is

$$\vec{\tilde{\chi}}^{(2)} = \begin{pmatrix} 0 & 0 & 0 & \tilde{\chi}^{(2)}_{14} & 0 & 0 \\ 0 & 0 & 0 & 0 & \tilde{\chi}^{(2)}_{14} & 0 \\ 0 & 0 & 0 & 0 & 0 & \tilde{\chi}^{(2)}_{14} \end{pmatrix}. \quad (18)$$

For the most common crystal cuts $\langle 110\rangle$ and $\langle 111\rangle$, the rotation angles are, respectively,

$$\theta = \frac{\pi}{2},\ \phi = \frac{\pi}{4} \quad \text{and} \quad \theta = \arccos\left(\frac{1}{\sqrt{3}}\right),\ \phi = \frac{\pi}{4},$$

which leads to the following dependence of the THz field on the laser polarization angle ψ:[21]

$$\langle 110\rangle \rightarrow \vec{E}_{R,\Omega}, \vec{E}_{T,\Omega} \propto \frac{1}{4}\begin{pmatrix} \cos 2\psi - 1 \\ -2\sin 2\psi \\ 0 \end{pmatrix}, \quad (19)$$

$$\langle 111\rangle \rightarrow \vec{E}_{R,\Omega}, \vec{E}_{T,\Omega} \propto \frac{1}{\sqrt{6}}\begin{pmatrix} \cos 2\psi \\ -\sin 2\psi \\ -1/\sqrt{2} \end{pmatrix}. \quad (20)$$

Here, we model the THz OR generation in the framework of plane waves interaction. However, if strongly focusing the exciting

laser beam in view of performing ORTI microscopy, the issue of focusing the pump laser beam is of utmost importance. Such an issue is very difficult to address, as both laser and THz beams encounter diffraction, and the nonlinear process in the crystal is made complicated because each spatial plane wave component of the incident laser beam exhibits a E-field polarized in a slightly different direction. A complete modeling taking into account the finite size of the exciting laser beam has already been treated by Bakunov *et al.*:[13] When the laser beam is not strongly focused, the generated THz beam is very similar to a one-dimensional beam (plane wave-like of limited radial size). On the other hand, when the laser spot size at the crystal entrance is smaller than the involved THz wavelengths, a Cherenkov cone is generated inside the crystal and both the transmitted and reflected THz beam are highly diverging outside the crystal: The excited area of the crystal behaves almost as a THz point-source. In the hypothesis of a crystal thickness that is smaller than the laser beam Rayleigh length, Schneider *et al.*[17] came to the same conclusion and gave a simple analytical expression of the generated THz beam, assuming the realization of phase-matching and no absorption at both laser and THz frequencies. THz generation by optical rectification in transmission, with a sub-wavelength Gaussian-shaped spot source, has been modeled and measured by Lin and co-workers.[22] When the laser spot size is much smaller than the THz wavelength, the THz beam is diffracted in nearly all directions from the crystal independently of the frequency, and it obeys the obliquity factor law. The main result is a decrease of the signal collected by an aperture-limited receiving system. Oppositely, for large laser spot size, the generated THz beam is almost a paraxial Gaussian-like beam. For intermediate laser spot size, the diffraction effect is more pronounced for the lower frequency range, making the corresponding signal detected with a weaker efficiency than the high frequency range. Here, a similar behavior is expected, as only the excited spot at the sample surface radiates the THz field. In the case of ORTI microscopy, as-large-as-possible aperture optics must be employed in front of the receiver in order to collect the maximum of all the THz reflected light spread in a 2π solid angle. Let us point out that, even in the case of strong focusing, all the spectral features of the THz field will be saved.

III. EXPERIMENT

The experimental setup used for THz generation through OR in reflection (Fig. 3) resembled a THz time-domain spectroscopy setup. A beam of 100-fs linearly polarized laser pulses at 80 MHz repetition rate was delivered by a Ti:sapphire oscillator (Spectra-Physics Tsunami, 786 nm center wavelength, and 12.5 nJ pulse energy). A beam splitter (BS) divided the pulses into a pump and a probe branch. A half-wave plate (HWP) and a mechanical chopper in the pump beam controlled the pump polarization and triggered the lock-in detection, respectively. The pump beam was focused by a 150-mm focal lens on a 1.52-mm thick ⟨110⟩-cut ZnTe crystal at normal incidence through a hole in an off-axis parabolic mirror (OAP). At the crystal, the spotsize diameter was 37 μm and the maximum average laser power was approximately 400 mW without the chopper. A neutral density filter (ND) was used to control the laser power at the crystal. The reflected THz

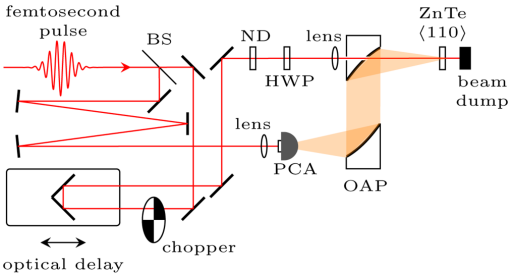

FIG. 3. Illustration of the experimental setup. ND, variable neutral density filter. BS, beam splitter; HWP, half-wave plate; PCA, photoconductive antenna; OAP, off-axis parabolic mirror.

radiation generated through OR was collected by the same parabolic mirror and focused onto a photoconductive antenna (PCA) by a second OAP. The bow-tie PCA detector (BATOP GmbH) was oriented such that it was sensitive to vertically polarized THz radiation. Finally, the measurements were done under ambient conditions.

IV. RESULTS AND DISCUSSION

Figure 4(a) shows two THz pulses separated by $\Delta t \approx 32.8$ ps (main-peak-to-main-peak). The first THz waveform R was generated through OR in reflection, while the later waveform T was generated in transmission and then reflected at the exit surface of the crystal. The time delay Δt between the two THz waveforms is thus equal to $\Delta t = 2dn_{G,\Omega}/c \approx 2dn_{\Omega}/c$. With the crystal thickness $d = 1.52$ mm and $n_{\Omega} = 3.20$ measured around 1 THz, we get $\Delta t = 32.4$ ps. Let us examine the magnitudes of the R and T pulses. Here, the T pulse is not measured in transmission but is reflected by the exit face of the crystal toward the detector. The great advantage of this scheme over the common transmission one is that both the R and T pulses are excited by the same laser pulse and are measured by the same detector and the same receiving electronics. Therefore, any error due to a difference in sensitivity of a double separated detection (one in reflection and one in transmission) is avoided. Moreover, we took a great care in the alignment of the sample in the THz beam, in such a way the T pulse is directed exactly in the same direction as the reflected one. Laser beams reflected at the entrance and exit faces of the crystal were adjusted to superimpose at the detection system, within a precision better than the laser beam size, i.e., less than 1 mm at a 30-cm distance from the crystal. The angular precision is thus better than 0.003 rad = 11 arcmin. Let us notice that, generally, crystals are supplied with a parallelism of a few arc min. The ratio of the R and T pulse can be calculated using Eq. (13). However, the transmitted THz field must be multiplied by $\tilde{r}_{\Omega}e^{-\alpha_{\Omega}d/2}$ to include the back reflection at the second crystal surface and transmission through the crystal. With $\alpha_{\Omega} \approx 0$, we get $|E_{R,\Omega}/E_{T,\Omega}|_{calc} \approx 1/47$. In the recorded trace, we unexpectedly find that the THz peak-to-peak

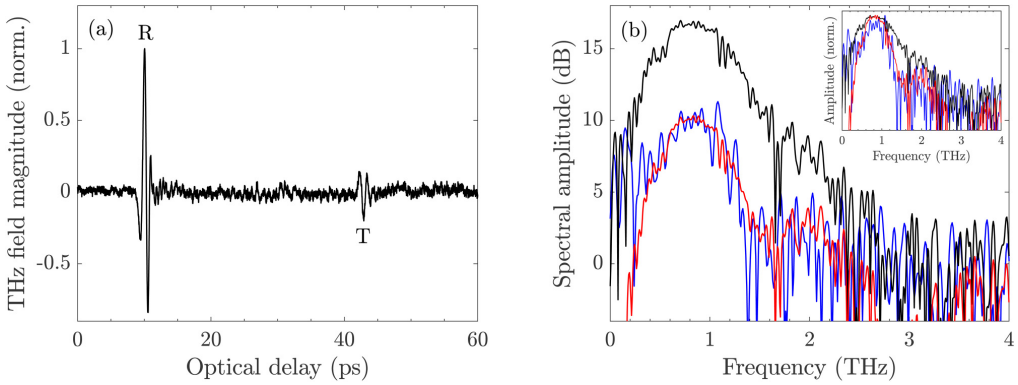

FIG. 4. (a) Waveforms of THz pulses R and T generated through OR in reflection and in transmission, respectively. (b) THz spectra of waveform R (black) and T (blue) and the calculated T spectra (red). The inset shows the R and T spectra normalized to their peak value, which points out the narrower T spectrum as compared to the R spectrum (see comments in the text).

magnitude of waveform R is 7 times stronger compared to waveform T. A possible explanation of the weak T pulse is THz absorption by free carriers generated through a two-photon absorption (TPA) process. Bose *et al.*[23] measured the photogenerated carrier lifetime of ZnTe to be $\tau_{ZnTe} = 25$ ns. The pulse period of the Ti:sapphire oscillator is 12.5 ns. Thus, TPA could lead to a steady-state free carrier population that may decrease the THz generation through the crystal and, in turn, absorb the THz radiation reflected at the exit surface. Using the TPA coefficient $\beta \approx 5$ cm/GW,[24] $\tau_{ZnTe} \approx 25$ ns, and the Drude model to determine the THz absorption by the mean density of photogenerated carriers, we obtain $\alpha_\Omega \approx 80\ \mathrm{cm}^{-1}$. Contrary, if we extract the absorption coefficient from the measurement using the modified expression (13), we get $\alpha_\Omega \approx 77\ \mathrm{cm}^{-1}$ in good agreement with the estimate. As expected, the measured absorption coefficient is slightly lower compared to our estimate, since we do not consider the change of THz transmission/reflection due to the increase of THz absorption.

The THz spectra of waveform R (black) and waveform T (blue) are plotted in Fig. 4(b). The R spectrum is rather smooth (excluding water vapor absorption lines), while the T spectrum exhibits the known sinc function shape with a first zero around 1.5 THz [$f_{\mathrm{cut-off}} = c/\pi d(n_\Omega - n_{G,\omega}) \approx 1.57$ THz] and two plateaus at 0.9 and 2 THz. The T spectrum is evidently narrower than the R spectrum due to non-perfect phase-matching and exhibits a poor signal-to-noise ratio because its intensity is degraded by linear and TPA absorption when propagating backwards in the crystal. Previously, we hypothesized that the T pulse corresponds to a THz pulse generated in transmission and reflected at the exit face of the crystal. Within this hypothesis, the T spectrum is equal to the R spectrum multiplied by the calculated ratio $|E_{T,\Omega}/E_{R,\Omega}|$ and by $\tilde{r}_\Omega e^{-\alpha_\Omega d/2}$ to include the reflection and absorption through the sample. The TPA-induced THz absorption is calculated using a Drude model with the free carrier density as the only adjustable variable. We assume that the crystal is transparent in the visible range. This allows us to get rid of the spectral response of our setup. The calculated spectrum is plotted as a red curve in Fig. 4(b). We see that it corresponds nicely to the measured T spectrum. The best fit is obtained for a carrier density of $1.19 \times 10^{15}\ \mathrm{cm}^{-3}$. The photogenerated carrier density can also be estimated from the laser power used in the measurement. Using the TPA coefficient $\beta \approx 5$ cm/GW and $\tau_{ZnTe} \approx 25$ ns, we get a carrier density of $6.49 \times 10^{15}\ \mathrm{cm}^{-3}$. This is in fairly good agreement with the above fit as we neglect the TPA effect in the nonlinear propagation equation, which would lead to a higher value of the carrier density calculated from the T spectrum fit. The recorded R spectrum spreads up to 2.7 THz, which is the upper limit (−20 dB) of the Batop bow-tie detector bandwidth. As the reflected pulse is weakly affected by absorption in the crystal, one may expect that its actual spectrum is directly proportional to the laser beam spectral width and could reach some tens of THz with sub-100 fs laser pulses. However, because of the weak magnitude of the reflected signal, detection of this latter requires very sensitive receivers that usually exhibit a long response time, like bolometers. This could be overcome by performing an interferometric measurement that will supply the autocorrelation trace of the generated THz pulses.[25]

The efficiency of the THz generation through OR in reflection vs pump laser fluence is plotted (circles) in Fig. 5(a) together with a linear fit (dotted) and a TPA-induced saturation fit (red). At weak pump laser fluence, the efficiency is linear, while TPA-induced saturation begins at $200\,\mu\mathrm{J/cm}^2$ in good agreement with published results on OR in transmission.[26] This saturation effect is explained by the absorption of the THz signal induced by the TPA photogenerated carriers in the sample. A rigorous analysis requires solving coupled propagation equations with the TPA effect. This is a rather tricky task, which is outside the scope of this paper, as the carrier population dynamics is usually treated in the time domain, while propagation equations are solved in the

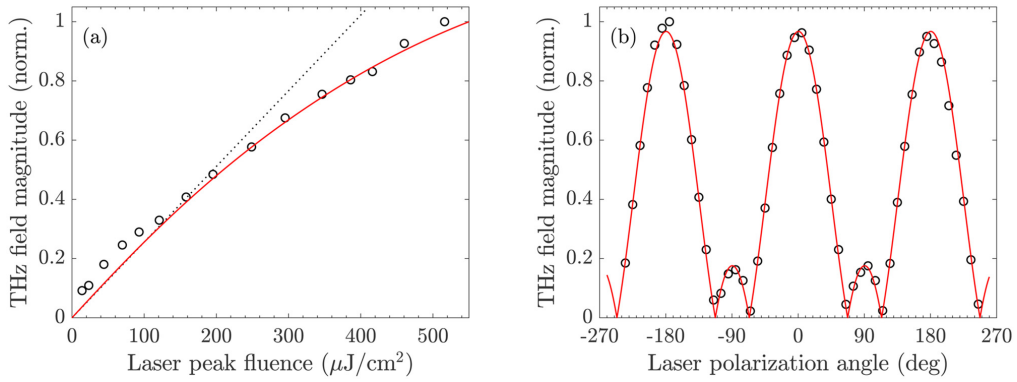

FIG. 5. (a) Measured R pulse amplitude vs laser peak fluence (circles). The dotted straight line is a linear fit while the continuous red curve is calculated taking account TPA as explained in the manuscript. (b) Polarimetric measurements of the R pulse (circles) fitted with the model (red).

frequency domain (see, for example, the pump-and-probe THz studies performed by Kužel and co-workers[27,28]). However, a simple evaluation of the order of magnitude of the influence of TPA can be performed as follows. The photocarrier population modifies both the refractive indices $\tilde{n}_\Omega$ and $\tilde{n}_{G,\omega} \propto \tilde{n}_\omega$ at THz and laser frequencies, respectively. Thus, it changes the magnitude of the reflected THz signal, whose expression is given by Eq. (9). The variation of the real part of $\tilde{n}_{G,\omega}$ is due to the Kerr effect, while its imaginary part is modified by TPA. In ZnTe, the value of the TPA absorption coefficient is $\beta = 5$ cm/GW and the Kerr coefficient is $n_2 \approx 5 \times 10^{-18}$ m^2/W.[29] In the present experiment, the maximum laser intensity is $I_\omega(\max) \approx 5.5$ GW/cm^2, therefore, the photoinduced variation of $\tilde{n}_{G,\omega}$ is $\Delta n_\omega \approx 2.5 \times 10^{-4}$ and $\Delta\kappa_\omega \approx 2 \times 10^{-4}$. We conclude that the variation of $\tilde{n}_\omega$ is too small to explain the saturation of the reflected THz field. Let us now address the variation of $\tilde{n}_\Omega$. To take into account the influence of the TPA photocarrier population, we use the Drude model

$$\tilde{\varepsilon}_\Omega = \varepsilon_\infty - \frac{\omega_p^2}{\omega(\omega + j\Gamma)} = (n_\Omega + j\kappa_\Omega)^2, \quad \omega_p^2 = \frac{N_{TPA} e^2}{m_{eff}\varepsilon_o}. \tag{21}$$

Here, N_{TPA} is the TPA photocarrier density, m_{eff} is the effective mass of the free electrons, Γ is the damping angular frequency, and e is the charge of electron. As already explained, we do not take into account the dynamics of N_{TPA}, but we simply take an averaged value in time and over the sample thickness. The absorbed laser intensity due to the TPA effect is

$$\Delta I_\omega = I_\omega\left(1 - e^{-\beta I_\omega d}\right). \tag{22}$$

The number of absorbed photons per laser pulse is

$$N_{pulse} = \Delta I_\omega \frac{\tau_{laser}}{\hbar\omega} S, \tag{23}$$

with laser pulse duration τ_{laser}, the reduced Planck constant $\hbar$, and laser spot size S. The TPA-induced photocarrier density is given by

$$N_{TPA} = \eta \frac{N_{pulse}}{Sd}. \tag{24}$$

The coefficient η (not calculated here) renders for the dynamics of the photocarrier population (carrier lifetime, diffusion inside the sample, etc.). We performed the calculation using ZnTe parameters determined by Constable and Lewis:[30] $m_{eff} = 0.151 \times m_e$, $\varepsilon_\infty = 7.3$, and $\Gamma = 0.3$ THz. The TPA induces both an increase of absorption and a decrease of the refractive index at THz frequencies. However, the effect of the refractive index decrease is stronger in Eq. (9), leading to a small increase of the reflected signal vs the laser intensity. Thus, this can neither explain the observed saturation effect. The only possible reason left for this saturation is the dependence of the nonlinear susceptibility on the carrier density. In a classical model for nonlinear susceptibility,[31,32] the magnitude of the nonlinear susceptibility $\overleftrightarrow{\tilde{\chi}}^{(2)}$ is proportional to the magnitudes of the linear susceptibilities at ω and Ω, i.e.,

$$\left|\overleftrightarrow{\tilde{\chi}}^{(2)}\right| \propto \left|\left(\overleftrightarrow{\tilde{\chi}}_\omega^{(1)}\right)^2 \overleftrightarrow{\tilde{\chi}}_\Omega^{(1)}\right| = \left|(\tilde{\varepsilon}_\omega - 1)^2(\tilde{\varepsilon}_\Omega - 1)\right|$$
$$= \left|\left((n_\omega + j\kappa_\omega)^2 - 1\right)^2\left((n_\Omega + j\kappa_\Omega)^2 - 1\right)\right|. \tag{25}$$

We calculated the term $\left|\overleftrightarrow{\tilde{\chi}}^{(2)}\right| I_\omega$ of Eq. (9) using the above-described Drude model and the ZnTe parameters by Constable and Lewis.[30] The normalized calculated curve is plotted as a continuous red curve in Fig. 5. We can see the good agreement with our experimental data. The only adjustable parameter is the coefficient η,

whose best fitting value is $\eta = 0.259$. This means that just about a quarter of the photoexcited carriers interact with the THz pulse. The reason could be that they both recombine and diffuse inside the sample (Dember effect, both longitudinal and transversal[33,34]) in between two successive laser pulses. Of course, this crude model and the related explanations must be validated by a complete rigorous analysis. Nevertheless, the variation of the nonlinear susceptibility appears to be a prevailing phenomenon when dealing with OR THz generation in a crystal exhibiting a strong TPA effect.

Finally, we perform a polarimetric study of the R pulse. The angle of the linear polarized pump beam $\psi = 2\psi_{\mathrm{HWP}}$ is scanned 360° by adjusting the half-wave plate angle ψ_{HWP} in 5° increments. The bow-tie detector is not strictly sensitive to a single polarization due to its antenna geometry. Therefore, we must fit a weighted expression

$$(1-\gamma)E_{\mathrm{R},\Omega,x} + \gamma E_{\mathrm{R},\Omega,y} \tag{26}$$

of the field components given in Eq. (19) to the data. Additionally, the fit takes into account an angular shift $\delta\psi$ due to disorientation of the crystal axes compared to the laboratory frame. Inspecting Fig. 5(b), we see an excellent agreement of the recorded THz peak magnitude (circles) and our fitted model (red, $\delta\psi = 66.5°$, $\gamma = 0.34$). This value of γ corresponds to a 10% sensitivity of the antenna to the cross polarization, which is within the specifications given by Batop GmbH. Thus, the reflected THz signal contains information of the crystalline orientation of the sample.

V. CONCLUSION

In conclusion, we experimentally demonstrated the generation of a reflected THz signal at normal incidence through OR in a ZnTe crystal. The reflected signal originates in the boundary conditions for the nonlinear fields at the crystal surface. All the characteristics of THz OR generation in the crystal (polarization symmetry, spectral features, etc.) are retrieved in the reflected signal. Its bandwidth is wider than in transmission because it is not limited by absorption losses in the crystal. At high laser power excitation, the reflected THz signal from ZnTe saturates. It seems that its origin is the effect of TPA, which reduces the magnitude of the second order nonlinear susceptibility. However, for crystals of common mm-thickness that are transparent or exhibit moderate absorption in both the THz and visible domains, the THz reflection magnitude is much smaller than the one in transmission. When dealing with crystals that are opaque in one or both of these spectral domains, or whose rear surface is rough or covered by opaque films like metals, the reflected THz signal is of great interest since the transmitted THz signal is weak or even zero. This could be applied to THz microscopy of opaque materials like humid biological samples, e.g., when performing sub-wavelength OR THz imaging.[7,8]

ACKNOWLEDGMENTS

We thank fruitful discussions with Professor F. Laurell and Professor V. Pasiskevicius, both at the Department of Applied Physics, Royal Institute of Technology, Stockholm (Sweden).

AUTHOR DECLARATIONS

Conflict of Interest

The authors have no conflicts to disclose.

Author Contributions

Mathias Hedegaard Kristensen: Data curation (lead); Formal analysis (lead); Investigation (lead); Methodology (equal); Software (lead); Validation (lead); Visualization (lead); Writing – original draft (equal); Writing – review & editing (equal). **Emilie Herault:** Funding acquisition (equal); Methodology (supporting); Resources (equal); Supervision (equal); Writing – review & editing (supporting). **Dongwei Zhai:** Writing – review & editing (supporting). **Esben Skovsen:** Funding acquisition (equal); Resources (equal); Supervision (supporting); Writing – review & editing (supporting). **Jean-Louis Coutaz:** Conceptualization (lead); Methodology (equal); Supervision (equal); Writing – original draft (equal); Writing – review & editing (equal).

DATA AVAILABILITY

Data underlying the results presented in this paper are not publicly available at this time but may be obtained from the authors upon reasonable request.

REFERENCES

[1]I. Katayama, R. Akai, M. Bito, H. Shimosato, K. Miyamoto, H. Ito, and M. Ashida, "Ultrabroadband terahertz generation using 4-N, N-dimethylamino-4'-N'-methyl-stilbazolium tosylate single crystals," Appl. Phys. Lett. **97**, 021105 (2010).
[2]J. A. Fülöp, Z. Ollmann, C. Lombosi, C. Skrobol, S. Klingebiel, L. Pálfalvi, F. Krausz, S. Karsch, and J. Hebling, "Efficient generation of THz pulses with 0.4 mJ energy," Opt. Express **22**, 20155–20163 (2014).
[3]F. Zernike and P. R. Berman, "Generation of far infrared as a difference frequency," Phys. Rev. Lett. **15**, 999 (1965).
[4]T. Yajima and K. Inoue, "Submillimeter-wave generation by optical difference-frequency mixing of ruby R1 and R2 laser lines," Phys. Lett. A **26**, 281 (1968).
[5]D. W. Faries, K. A. Gehring, P. L. Richards, and Y. R. Shen, "Tunable far-infrared radiation generated from the difference frequency between two ruby lasers," Phys. Rev. **180**, 363 (1969).
[6]M. Sotome, N. Kida, S. Horiuchi, and H. Okamoto, "Visualization of ferroelectric domains in a hydrogen-bonded molecular crystal using emission of terahertz radiation," Appl. Phys. Lett. **105**, 041101 (2014).
[7]F. Sanjuan, G. Gaborit, and J.-L. Coutaz, "Sub-wavelength terahertz imaging through optical rectification," Sci. Rep. **8**, 13492 (2018).
[8]G. Soylu, E. Hérault, B. Boulanger, F. Laurell, and J.-L. Coutaz, "Sub-wavelength THz imaging of the domains in periodically poled crystals through optical rectification," J. Infrared, Millimeter, Terahertz Waves **41**, 1144–1154 (2020).
[9]M. Reid, I. V. Cravetchi, and R. Fedosejevs, "Terahertz radiation and second-harmonic generation from InAs: Bulk versus surface electric-field-induced contributions," Phys. Rev. B **72**, 035201 (2005).
[10]N. N. Zinov'ev, A. S. Nikoghosyan, and J. M. Chamberlain, "Terahertz radiation from a nonlinear slab traversed by an optical pulse," Phys. Rev. Lett. **98**, 044801 (2007).
[11]N. N. Zinov'ev, A. S. Nikoghosyan, and J. M. Chamberlain, "Conversion of short optical pulses to terahertz radiation in a nonlinear medium: Experiment and theory," Phys. Rev. B **76**, 235114 (2007).

[12]M. I. Bakunov, A. V. Maslov, and S. B. Bodrov, "Fresnel formulas for the forced electromagnetic pulses and their application for optical-to-terahertz conversion in nonlinear crystals," Phys. Rev. Lett. **99**, 203904 (2007).
[13]M. I. Bakunov, S. B. Bodrov, A. V. Maslov, and M. Hangyo, "Theory of terahertz generation in a slab of electro-optic material using an ultrashort laser pulse focused to a line," Phys. Rev. B **76**, 085346 (2007).
[14]S. Hargreaves, K. Radhanpura, and R. A. Lewis, "Generation of terahertz radiation by bulk and surface optical rectification from crystal planes of arbitrary orientation," Phys. Rev. B **80**, 195323 (2009).
[15]A. Schneider, "Theory of terahertz pulse generation through optical rectification in a nonlinear optical material with a finite size," Phys. Rev. A **82**, 033825 (2010).
[16]F. Kadlec, P. Kužel, and J.-L. Coutaz, "Optical rectification at metal surfaces," Opt. Lett. **29**, 2674–2676 (2004).
[17]A. Schneider, M. Neis, M. Stillhart, B. Ruiz, R. U. Khan, and P. Günter, "Generation of terahertz pulses through optical rectification in organic DAST crystals: Theory and experiment," J. Opt. Soc. Am. B **23**, 1822–1835 (2006).
[18]U. Møller, D. G. Cooke, K. Tanaka, and P. U. Jepsen, "Terahertz reflection spectroscopy of Debye relaxation in polar liquids," J. Opt. Soc. Am. B **26**, A113–A125 (2009).
[19]J. Zhang, C. Shi, Y. Ma, X. Han, W. Li, T. Chang, D. Wei, C. Du, and H.-L. Cui, "Spectroscopic study of terahertz reflection and transmission properties of carbon-fiber-reinforced plastic composites," Opt. Eng. **54**, 054106 (2015).
[20]P. Han and X.-C. Zhang, "Coherent, broadband midinfrared terahertz beam sensors," Appl. Phys. Lett. **73**, 3049–3051 (1998).
[21]G. Gaborit, F. Sanjuan, and J.-L. Coutaz, "Second order nonlinear optical processes in [111] cubic crystals for terahertz optoelectronics," Lith. J. Phys. **58**, 24–37 (2018).
[22]H. Lin, C. Fumeaux, B. M. Fischer, and D. Abbott, "Modelling of subwavelength THz sources as Gaussian apertures," Opt. Express **18**, 17672–17683 (2010).
[23]D. Bose, R. Ahrenkiel, and S. Bhunia, "Steady-state and time-resolved photoconductivity measurements of minority carrier lifetime in ZnTe," J. Appl. Phys. **86**, 6599 (1999).
[24]Z.-Y. Zhao, S. Hameau, and J. Tignon, "THz generation by optical rectification and competition with other nonlinear processes," Chin. Phys. Lett. **25**, 1868 (2008).
[25]K. Kan, J. Yang, A. Ogata, S. Sakakihara, T. Kondoh, K. Norizawa, I. Nozawa, T. Toigawa, Y. Yoshida, H. Kitahara, and K. Takano, "Radially polarized terahertz waves from a photoconductive antenna with microstructures," Appl. Phys. Lett. **102**, 221118 (2013).
[26]F. Sanjuan, G. Gaborit, and J.-L. Coutaz, "Influence of two-photon absorption anisotropy on terahertz emission through optical rectification in zinc-blende crystals," J. Infrared, Millimeter, Terahertz Waves **39**, 378–386 (2018).
[27]H. Němec, F. Kadlec, S. Surendran, P. Kužel, and P. Jungwirth, "Ultrafast far-infrared dynamics probed by terahertz pulses: A frequency domain approach. I. Model systems," J. Chem. Phys. **122**, 104503 (2005).
[28]H. Němec, F. Kadlec, C. Kadlec, P. Kužel, and P. Jungwirth, "Ultrafast far-infrared dynamics probed by terahertz pulses: A frequency-domain approach. II. Applications," J. Chem. Phys. **122**, 104504 (2005).
[29]W.-Q. He, C.-M. Gu, and W.-Z. Shen, "Direct evidence of Kerr-like nonlinearity by femtosecond Z-scan technique," Opt. Express **14**, 5476–5483 (2006).
[30]E. Constable and R. A. Lewis, "Optical parameters of ZnTe determined using continuous-wave terahertz radiation," J. Appl. Phys. **112**, 063104 (2012).
[31]N. Bloembergen, *Nonlinear Optics* (World Scientific, 1996).
[32]R. W. Boyd, *Nonlinear Optics* (Academic Press, 2020).
[33]V. L. Malevich, R. Adomavičius, and A. Krotkus, "THz emission from semiconductor surfaces," C. R. Phys. **9**, 130–141 (2008).
[34]M. E. Barnes, S. A. Berry, P. Gow, D. McBryde, G. J. Daniell, H. E. Beere, D. A. Ritchie, and V. Apostolopoulos, "Investigation of the role of the lateral photo-dember effect in the generation of terahertz radiation using a metallic mask on a semiconductor," Opt. Express **21**, 16263–16272 (2013).

Publication E

Fourier Transform Second harmonic Generation for High-Resolution Nonlinear Spectroscopy

List of authors:

Mathias Hedegaard Kristensen
Peter Kjær Kristensen
Kjeld Pedersen
Esben Skovsen

The paper has been published in
Optics Communications Vol. 482, pp. 126593, 2021.

Optics Communications 482 (2021) 126593

Contents lists available at ScienceDirect

Optics Communications

journal homepage: www.elsevier.com/locate/optcom

Fourier transform second harmonic generation for high-resolution nonlinear spectroscopy

Mathias Hedegaard Kristensen *, Peter Kjær Kristensen, Kjeld Pedersen, Esben Skovsen *

Department of Materials and Production, Section for Physics and Mechanics, Aalborg University, DK 9220, Aalborg East, Denmark

ARTICLE INFO

Keywords:
Nonlinear optics
Harmonic generation
Fourier transform
Spectroscopy

ABSTRACT

In this communication we demonstrate a new characterization technique combining Fourier transform (FT) spectroscopy and second harmonic generation (SHG) that enables high spectral resolution with broadband femtosecond laser pulses. The strong and narrow exciton resonances of the wide band gap semiconductor ZnO were chosen for demonstrating the capabilities of the method. FT-SHG offers high reproducibility and high spectral resolution within the bandwidth of the input pulse.

1. Introduction

During the last decades second-order nonlinear optical (NLO) processes have become essential tools within studies of semiconductor materials [1–3]. Second-order NLO processes have different selection rules from linear optics. This has led to a wealth of applications, where valuable information on inhomogeneous structures, surfaces, interfaces, and metamaterials has been obtained. Furthermore, the NLO techniques benefit from being contact-free, applicable for layers buried in transparent media, and generally non-destructive.

Fourier transform (FT) spectroscopy is a well-established technique applied in many different fields of science such as nuclear magnetic resonance (NMR) spectrometry, optical spectroscopy, and terahertz spectroscopy. [4,5]

One of the inherent advantages of optical FT spectroscopy is the multiplex nature, i.e. all of the spectral components are measured simultaneously, known as Fellget's advantage [6], which increases the signal-to-noise ratio. This advantage cannot be exploited in the case of weak NLO signals, since detectors working in the UV range are dominated by shot noise, which equals the gain in signal-to-noise ratio. However, the single-shot feature of the technique using broadband femtosecond pulses is still beneficial in terms of scan duration. Connes' (the spectral accuracy) advantage [6] may be less well known. Nonetheless, it is very significant to the FT technique. The spectral sampling intervals are inversely proportional to the optical sampling intervals, wherefore the respective errors are directly coupled. The change in optical path difference can be tracked very precisely using the interference pattern of monochromatic light of a HeNe laser. By this approach the accuracy of the optical sampling intervals is entirely determined by the precision of the HeNe laser wavelength itself. Thus, FT spectroscopy measurements have a built-in calibration of the spectral axis giving the technique a very high spectral reproducibility. Finally, the FT approach has the advantage of practically unlimited spectral resolution. This is due to the fact that the resolution does not rely on the input pulse characteristics but is entirely determined by the maximum optical path difference of the interferometer. However, the FT method has primarily gained ground within infrared (IR) and terahertz spectroscopy. [5–7] Nevertheless, it has been demonstrated that ultrafast laser spectroscopy can take advantage of the benefits of the FT technique. This was accomplished by Bellini et al. by the demonstration of Ramsey spectroscopy with femtosecond laser pulses [8] and most recently McGuire et al. demonstrated IR–visible FT sum-frequency generation (FT-SFG) with femtosecond laser pulses, where the IR beam is modulated by an interferometer [9].

During recent years, more and more research groups have replaced their old nanosecond, picosecond, or 100 fs laser systems with modern ultrafast laser systems. The light pulses of the modern lasers are typically sub-40 fs and thus spectrally broader, which limits the achievable spectral resolution for conventional nonlinear spectroscopy.

In this communication, we present a new NLO technique combining second harmonic generation (SHG) and FT spectroscopy to circumvent this limit and give access to high spectral resolution with ultrafast laser pulses. Broadband femtosecond laser pulses are used to induce a polarization in a sample, whereupon the recorded interferogram of the response is Fourier transformed to acquire the spectral content.

An exhaustive theoretical and experimental study of the exciton resonances of the wide band gap hexagonal semiconductor ZnO in the range of 3.2–3.5 eV photon energy has previously been carried out by Lafrentz et al. [10]. Strong crystallographic SHG signals were reported for parallel p-polarized fundamental and SHG light in transmission at a sample temperature T of 1.6 K using a nanosecond-pulse-width

* Corresponding authors.
E-mail addresses: math@mp.aau.dk (M.H. Kristensen), es@mp.aau.dk (E. Skovsen).

https://doi.org/10.1016/j.optcom.2020.126593
Received 21 September 2020; Received in revised form 2 November 2020; Accepted 3 November 2020
Available online 7 November 2020
0030-4018/

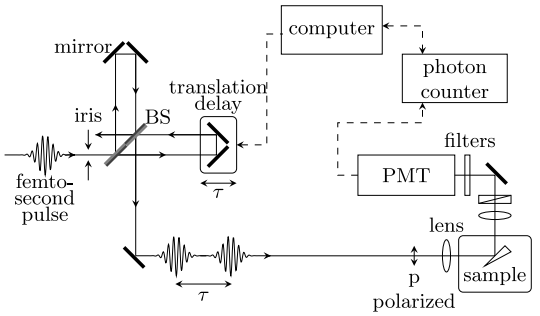

Fig. 1. Illustration of the FT-SHG setup. BS, beam splitter; PMT, photomultiplier. For details see text.

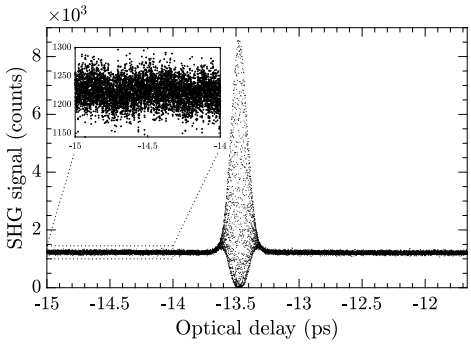

Fig. 2. SHG interferogram of the wedged ZnO crystal sample.

laser with narrow spectral bandwidth. Several sharp lines were found in the exciton spectral range from 3.37–3.44 eV. The broadening of the excitons at temperatures exceeding 20 K was found to be almost homogeneous and linearly increasing with temperature. The peak intensity and the full width at half maximum (FWHM) of the X-line and the $1s_L(C)$ exciton change slower with temperature compared to the $2p_{x,y}(A)$ states [10]. Regarding our work, the X-line at 3.407 eV is pertinent for benchmarking the FT-SHG technique due to its strong and narrow characteristics.

We find that the exciton peak can be resolved if the FT technique is applied. Furthermore, the width of the exciton peak is found to be three times smaller using the FT technique in comparison to regular SHG experiments using 100-fs laser pulses.

2. Experimental methods and materials

The FT-SHG setup is illustrated in Fig. 1. A beam of laser pulses (725 nm center wavelength, 10 nm FWHM , ~100 fs pulse width, 600 mW average power, and 80 MHz repetition rate) generated by a Ti:sapphire Tsunami femtosecond laser from Spectra-Physics, was sent through a home-built Michelson interferometer. A specially designed dielectric 50/50 beam splitter from Femto Optics obviates the need of an additional compensation plate, since each surface has a coated and uncoated section. The optical delay was established by a N-565 PiezoWalk linear stage and the appertaining E-861 controller from Physik Instrumente (PI). The N-565 stage utilizes an optical nanometrology encoder to ensure a stable, smooth, and precise linear translation of suitable length (13 mm travel range, 3 nm minimum incremental motion, and 0.5 nm resolution). Additionally, the interferometric encoder ensures the reproducibility of the spectral axis through Connes' advantage. The field leaving the Michelson interferometer, $\mathbf{E}_M$, was a superposition of two short pulses separated in time. Next, the beam was incident at 45° upon the sample mounted in a cryostat at a temperature of approx. 60 K. Prior to the sample, a long pass filter was inserted to block any previously generated SH light. The ZnO sample was cut from a (1000)-oriented ZnO single crystal and polished into a 5° wedge such that the back reflection can be avoided and the reflection from the first interface can be isolated in order to avoid Maker fringe effects [11]. The reflected SHG originates from a thin surface layer with a thickness of the order of the wavelength [12]. The signal is therefore small compared to the transmitted signal, but there is only a small effect of the linear absorption on the SH signal. It is thus expected that the spectra directly demonstrate excitonic resonances near the ZnO bandgap.

The SH signal generated at the sample was reflected into a photomultiplier tube (PMT) with proper band pass filters attached to block the fundamental and third harmonic, while transmitting the second harmonic. The signal detected by the PMT was recorded by a Stanford Research Systems SR400 gated photon counter. The SHG measured in reflection from a quartz crystal wedge was used to normalize the ZnO signal. Furthermore, the measurements were carried out for a p-to-p polarization combination. The signal was recorded by the computer as the optical delay was varied in a step-scan mode.

The output of the Michelson interferometer $\mathbf{E}_M(t,\tau)$ is the sum of two replicas of the input fields $\mathbf{E}(t) + \mathbf{E}(t-\tau)$, where

$$\mathbf{E}(t) = \int_{-\infty}^{\infty} \tilde{\mathbf{E}}(\omega) \exp[-i\omega t]\, \mathrm{d}\omega, \tag{1}$$

and $\tilde{\mathbf{E}}$ is the Fourier transform of $\mathbf{E}(t)$, and similar for the delayed replica $\mathbf{E}(t-\tau)$. Upon incidence on the sample the electric field induces a nonlinear polarization $\mathbf{P}^{(2)} = \epsilon_0 \chi^{(2)} \mathbf{E}^2$, where $\chi^{(2)}$ is the nonlinear susceptibility tensor. Hence, the reflected SHG field can be written as

$$\mathbf{E}_{\mathrm{SHG}}(\tau) \propto \chi^{(2)} \mathbf{E}_M^2(\tau) \tag{2}$$

The SHG signal of a single pulse measured by the photomultiplier is given by

$$I_{\mathrm{SHG}}(\tau) \propto \int_{-\infty}^{\infty} |\mathbf{E}_{\mathrm{SHG}}(t,\tau)|^2\, \mathrm{d}t \propto \int_{-\infty}^{\infty} |\chi^{(2)}|^2 |\mathbf{E}_M^2(t,\tau)|^2\, \mathrm{d}t. \tag{3}$$

For $\chi^{(2)} = 1$ this is the second order interferometric autocorrelation of $E(t)$ and $E(t-\tau)$. Finally, the spectrum can be achieved by Fourier transforming the measured SHG signal, i.e.

$$I_{\mathrm{SHG}}(\omega) = \mathcal{F}\left(I_{\mathrm{SHG}}(\tau)\right) \propto |\chi^{(2)}(\omega)|^2 |\tilde{\mathbf{E}}_M^2(\omega)|^2 \tag{4}$$

3. Results and discussion

Fig. 2 shows the SHG interferogram of the ZnO crystal wedge. The interferogram was recorded by scanning the optical delay by roughly 3.33 ps in 1.67 fs increments integrating for 500 ms. The magnified tail of the interferogram shown in the inset of Fig. 2 reveals a long-lasting oscillation, which indicates narrow spectral features in the signal.

Prior to the Fourier transform the recorded interferograms were baseline corrected and multiplied by an apodization function. Various apodization functions including triangular, Blackman-Harris, and Hanning were tested, however, no pronounced differences were seen in the region of interest. Therefore, the triangular apodization function was used onward. Subsequently, the data were zero padded to the next power of twice its length. Finally, in accordance to common practice [6], the signal was shifted about the maximum signal to reference the signal as close to zero phase as possible before being Fourier transformed.

The Fourier spectrum corresponding to the interferogram shown in Fig. 2 of the ZnO crystal wedge is seen in Fig. 3. The 3.33 ps optical delay in 1.67 fs increments transform to a spectral resolution of 1.2 meV and a 12.4 eV spectral range. However, the Fourier spectrum in Fig. 3

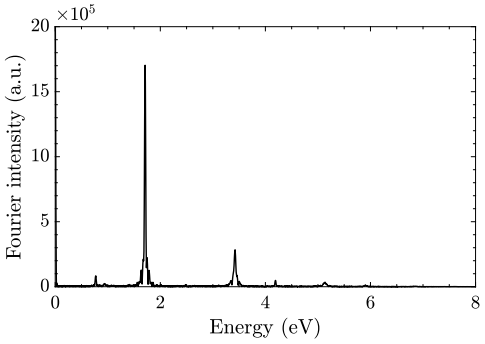

Fig. 3. The Fourier spectrum of the SHG interferogram shown in Fig. 2 cropped to 8 eV.

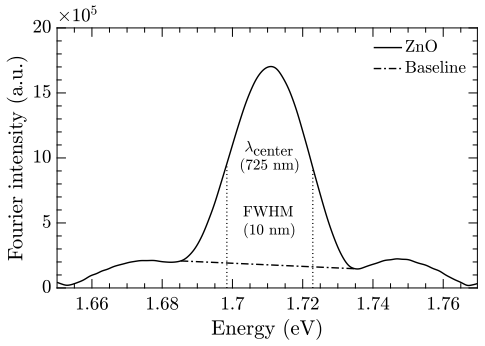

Fig. 4. Zoom-in of the fundamental peak seen in Fig. 3.

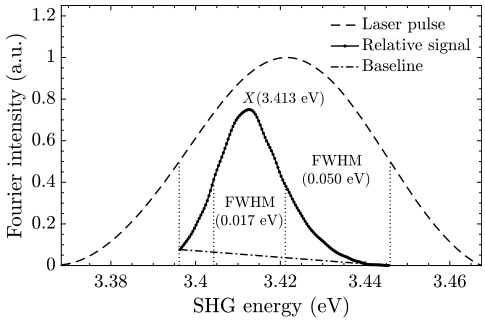

Fig. 5. The relative SHG Fourier intensity of the ZnO and quartz wedge samples measured with 10 nm FWHM laser pulses centered at 725 ± 0.5 nm.

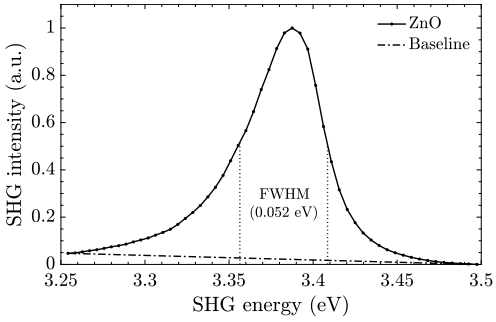

Fig. 6. The normalized SHG signal of the ZnO wedge sample measured without the Michelson interferometer.

has been cropped, since no signal nor aliasing are present above 8 eV. Distinct peaks of the Fourier intensity in Fig. 3 are seen around 1.71 and 3.42 eV corresponding to the fundamental and SHG energies of 725 nm light, respectively. The fundamental peak is an inherent part of the Fourier transformed signal even though only the SHG light reached the detector, while the incident near IR was completely blocked by filters. This is due to the interferometric nature of the probe signal. Fig. 4 shows a zoom-in of the fundamental peak. The central energy of the peak translates to a center wavelength of 725 nm while the FWHM equals 10 nm, which is in very good agreement with the expected characteristics of the laser pulses.

The interference signal has modulation components with an oscillating period corresponding to the SH signal, i.e. a period of 1.2 fs. In order to obtain a good interference signal the stability level of the interferometer should be a fraction of this period, and moreover, hold for the entire integration time in each step. The delay fluctuations of the interferometer was measured with a HeNe laser to be ± 0.048 fs, which is well below the required stability.

In Fig. 5 the normalized surface FT-SHG spectrum of ZnO at approx. 60 K (line) and the frequency-doubled squared laser spectrum (dashed) obtained from the fundamental peak are displayed for laser pulses of 10 nm FWHM centered at 725 ± 0.5 nm. The normalized FT-SHG spectrum is the ratio of seven averaged ZnO measurements and three averaged reference measurements on quartz. The bandwidth of the SHG signal is only measurable within the squared Gaussian intensity profile of the fs pulses as the SHG signal vanishes in noise towards the tails of the distribution. Hence, the spectral range has been cropped hereto. Clearly, a strong feature is seen around 3.413 eV, which is in very good agreement with the strong exciton X-line observed at 3.407 eV in [10]. The 6 meV shift of the peak in SHG energy equals a wavelength shift of 0.6 nm. This is comparable to the laser stability of ±0.5 nm. However, the measurements were recorded at a temperature of approx. 60 K compared to 1.6 K in [10], which as well contributes to the shift. The FWHM of the X-line in Fig. 5 is approximately 17 meV when the baseline is taken into account. According to [10], the magnitude of the X-line and the $1s_L(C)$ exciton decrease to approximately 20% at 50 K compared to the magnitude measured at 1.6 K, while the $2p_{x,y}(A)$ states vanish in the background above 30 K. Additionally, at 50 K the FWHM of the X-line and the $1s_L(C)$ exciton was observed to be roughly 2.2 times wider compared to the FWHM measured at 1.6 K [10]. The FWHM of the X-line can be estimated from [10] to be ~3 meV at 1.6 K resulting in a FWHM of ~7 meV at 50 K. Finally, Lafrentz et al. observed that the peaks merge into one at 3.417 eV as the temperature rise to 128 K. In the view of this, we deduce that our measurements are consistent with those in [10].

Measurements of SHG from the ZnO and quartz wedge samples were also made without the Michelson interferometer using an Optical Parametric Amplifier (Light Conversion Topas-C Model 800-fs) pumped by 100 fs pulses of an amplified Ti:sapphire laser and a PMT at the exit of a monochromator was used as detector. Careful analysis of the spectra was necessary in order to separate SHG from strong two-photon photoluminescence generated at the band gap. Fig. 6 shows normalized SHG signal extracted from the measured spectra. The width of the peak is roughly 50 meV, which is three times larger than the exciton peaks detected with FT-SHG. Evidently, the use of fs laser pulses with the FT technique allows one to distinguish the narrow individual exciton resonance peaks.

4. Conclusion

We have shown that the spectral resolution in SHG spectroscopy using femtosecond laser pulses can be efficiently improved by the FT technique to achieve high spectral resolution independent of the input pulse characteristics. This was demonstrated by resolving the strong exciton X-line at 3.407 eV in ZnO, which is much narrower than the spectral bandwidth of femtosecond laser pulses used for excitation of the resonance. Furthermore, compared to conventional methods, our FT-SHG technique benefit the high spectral reproducibility of the FT approach due to built-in calibration of the spectral axis by Connes' advantage.

The presented method is enhanced if laser pulses with even broader spectral bandwidth are utilized to excite the sample. In this case a very broad spectral band can be covered in a single scan, while retaining high spectral resolution, without prolonging the scan duration.

CRediT authorship contribution statement

Mathias Hedegaard Kristensen: Methodology (lead), Software, Validation, Investigation, Data curation (lead), Writing - original draft, Visualization, Writing - review & editing (equal). **Peter Kjær Kristensen:** Methodology, Writing - review & editing (equal). **Kjeld Pedersen:** Methodology, Resources (equal), Writing - review & editing (equal). **Esben Skovsen:** Conceptualization, Methodology, Resources (equal), Data curation, Writing - review & editing (equal).

Declaration of competing interest

The authors declare that they have no known competing financial interests or personal relationships that could have appeared to influence the work reported in this paper.

References

[1] Y.R. Shen, Wave mixing spectroscopy for surface studies, Solid State Commun. 102 (2–3) (1997) 221–229, URL https://doi.org/10.1016/S0038-1098(96)00726-0.

[2] D.R. Yakovlev, V.V. Pavlov, A.V. Rodina, R.V. Pisarev, J. Mund, W. Warkentin, M. Bayer, Exciton spectroscopy of semiconductors by the method of optical harmonics generation (review), Phys. Solid State 60 (8) (2018) 1471–1486, URL https://doi.org/10.1134/S1063783418080231.

[3] A. Prylepa, C. Reitböck, M. Cobet, A. Jesacher, X. Jin, R. Adelung, M. Schatzl-Linder, G. Luckeneder, K.-H. Stellnberger, T. Steck, J. Faderl, T. Stehrer, D. Stifter, Material characterisation with methods of nonlinear optics, J. Phys. D: Appl. Phys. 51 (4) (2018) 043001, URL http://stacks.iop.org/0022-3727/51/i=4/a=043001.

[4] D.A. Skoog, F.J. Holler, S.R. Crouch, Principles of Instrumental Analysis, seventh ed., Cengage Learning, Boston, Massachusetts, 2018.

[5] J.-L. Coutaz, F. Garet, V.P. Wallace, Principles of Terahertz Time-Domain Spectroscopy, first ed., Jenny Stanford Publishing, 2018.

[6] P.R. Griffths, J.A. de Haseth, Fourier Transform Infrared Spectrometry, second ed., John Wiley & Sons, Hoboken, New Jersey, 2007.

[7] A.P. Thorne, Fourier transform spectrometry in the ultraviolet, Anal. Chem. 63 (2) (1991) 57A–65A, URL https://doi.org/10.1021/ac00002a712.

[8] M. Bellini, A. Bartoli, T.W. Hänsch, Two-photon fourier spectroscopy with femtosecond light pulses, Opt. Lett. 22 (8) (1997) 540–542, http://dx.doi.org/10.1364/OL.22.000540, URL http://ol.osa.org/abstract.cfm?URI=ol-22-8-540.

[9] J.A. McGuire, W. Beck, X. Wei, Y.R. Shen, Fourier-transform sum-frequency surface vibrational spectroscopy with femtosecond pulses, Opt. Lett. 24 (24) (1999) 1877–1879, http://dx.doi.org/10.1364/OL.24.001877, URL http://ol.osa.org/abstract.cfm?URI=ol-24-24-1877.

[10] M. Lafrentz, D. Brunne, A.V. Rodina, V.V. Pavlov, R.V. Pisarev, D.R. Yakovlev, A. Bakin, M. Bayer, Second-harmonic generation spectroscopy of excitons in ZnO, Phys. Rev. B 88 (2013) 235207, http://dx.doi.org/10.1103/PhysRevB.88.235207, URL https://link.aps.org/doi/10.1103/PhysRevB.88.235207.

[11] J. Jerphagnon, S.K. Kurtz, Maker fringes: A detailed comparison of theory and experiment for isotropic and uniaxial crystals, J. Appl. Phys. 41 (4) (1970) 1667–1681, http://dx.doi.org/10.1063/1.1659090.

[12] N. Bloembergen, P.S. Pershan, Light waves at the boundary of nonlinear media, Phys. Rev. 128 (1962) 606–622, http://dx.doi.org/10.1103/PhysRev.128.606, URL https://link.aps.org/doi/10.1103/PhysRev.128.606.

ISSN (online): 2446-1636
ISBN (online): 978-87-7573-680-5

AALBORG UNIVERSITY PRESS